Computational Biomechanics of Diseased Arteries

Biomechanische modelvorming
van zieke slagaderen

Annette Monique Kok

Computational Biomechanics of Diseased Arteries

Biomechanische modelvorming
van zieke slagaderen

Proefschrift

ter verkrijging van de graad van doctor aan de
Erasmus Universiteit Rotterdam
op gezag van de
rector magnificus

Prof.dr. R.C.M.E. Engels

en volgens besluit van het College voor Promoties.
De openbare verdediging zal plaatsvinden op

woensdag 19 juni 2019 om 15:30 uur

Annette Monique Kok
geboren te Nijmegen

Erasmus University Rotterdam

PROMOTIECOMMISSIE

Promotor: Prof.dr.ir. A.F.W. van der Steen

Overige leden: Prof.dr.ir. H. Boersma
Dr. J. Daemen
Dr.ir. R.G.P. Lopata

Copromotor: Dr.ir. J.J. Wentzel

CONTENTS

INTRODUCTION 1

Computational modelling is widely used to obtain insight into the physical behaviour of complex systems (Melnik, 2015). Meteorologists often use computational modelling to develop and apply mathematical models that describe changes in the atmosphere. These models require meteorological measurements (e.g. temperature, air pressure, humidity, and velocity) as input (Lynch, 2008). Subsequently, computational modelling is used to simulate complex weather processes and obtain local information on the behaviour of temperature, humidity, precipitation, and wind strength and direction over time (Seyyed-abbasi et al., 2018). This information can then be used to produce the weather forecast.

Computational modelling can also be used to investigate a building's ability to withstand different forces by determining stress distributions within that building (e.g. loading, earthquakes, and wind) (Kaijima et al., 2013). Car manufacturing companies apply computational modelling during a car's design phase to develop cars with minimal fuel consumption and maximal road stability (Al-saadi et al., 2017). Therefore, engineers model the pressure and air flow around various car designs and translate this information back into energy loss. Once a car is optimally designed, computational modelling can also be used to test car safety. For this purpose, crash parameters such as impact severity and impact angle can be varied and simulated (Belytschko, 1992). In this way, engineers can investigate the effect of simple modifications in design or material on road safety; this method is more cost effective than crashing actual cars.

More recently, computational models have been developed and applied to improve or assist in healthcare; a few applications are highlighted here. Surgery simulators fully immerse physicians in a 'realistic' environment; they receive real-time feedback on the surgical procedure in the form of realistic reaction forces on and visualization of the scalpel. For this purpose, the computer must simulate the behaviour of different tissue types and their interaction with the surgeon's scalpel by computing strain and stresses in the tissue; these are directly transmitted back to the operator as resistance or force. These simulators are mostly used for training purposes (Misra et al., 2008).

Computational modelling is also applied to surgical planning of vascular access for haemodialysis in kidney disease patients. Vascular access is usually achieved in the lower arm; however, in some patients, blood flow is too low in this location, and these patients

would benefit from creation of such an access in the upper arm. In turn, vascular access in the upper arm is not suitable for all patients, since this technique in the upper arm can result in excessively high flows (Huberts et al., 2012). Currently, a large clinical trial is performed to investigate whether computational modelling can help physicians choose the location of vascular access and thereby improve long-term outcomes compared to conventional healthcare (Zonnebeld et al., 2017).

This thesis focuses on the application of computational modelling of two diseases in which the healthy arterial wall structure is disrupted: Atherosclerosis (1.1.1) and Abdominal aortic aneurysm (1.1.2). In both diseases, stresses inside the vessel wall and the shear stress of blood flow against the vessel wall are important in disease initiation, progression, and risk to cause life-threatening events.

1.1   Healthy vessels and vascular disease

The main function of arteries, with the exception of the pulmonary arteries, is to carry oxygenated blood and nutrients to organs and tissues. In addition, arteries play a role in body temperature regulation and injury healing. In the larger arteries, blood pressure within one cardiac cycle varies between 80 mmHg and 120 mmHg; the arterial wall is designed to withstand these pressures. Arteries consist of three different layers (see Figure 1.1): the intima, media, and adventitia:

Intima The intima is the innermost layer of the arterial wall and is in direct contact with the blood. It consists of endothelial cells and has many functions (Libby et al., 2011). Most importantly, it acts as a filtering system for blood components: some can pass through the intima layer into the arterial wall and some cannot.

Media The media is the mid layer of the arterial wall and mainly consists of smooth muscle cells, elastin, and collagen, which come together in a complex helical 3D structure. This structure is mostly circumferentially oriented to withstand the cyclic force of blood pressure. The smooth muscle cells in the medial can regulate the diameter of the vessel upon stimuli from the circulation (Gasser et al., 2006).

Adventitia The outermost layer, the adventitia, mainly consists of fibroblasts, fibrocytes, extracellular matrix, and collagen fibres (Gasser et al., 2006); these fibres are organized into two different helical structures. The adventitia is anchored in connective tissue and thereby increases the strength and stability of the entire artery (Hamilton, 1976).

In this thesis, two arterial diseases will be studied in which the healthy arterial wall

Figure 1.1: *A schematic view of a healthy three-layered arterial wall.*

is disrupted: coronary and carotid atherosclerosis and abdominal aortic aneurysm, see Figure 1.2.

1.1.1 Atherosclerosis

Atherosclerosis is a lipid-driven inflammatory disease that results in thickening of the arterial wall, also called a plaque. Atherosclerosis progresses slowly and remains asymptomatic for decades. The most important risk factors for atherosclerosis include: hypercholesterolemia, hypertension, tobacco use, obesity, inactive lifestyle, and age (Rafieian-Kopaei et al., 2014). Atherosclerotic plaques develop throughout the arterial system, but they have predilection sites (e.g. close to side branches in coronary and carotid arteries) (VanderLaan et al., 2004). If a plaque develops, it initially grows outward (compensatory enlargement/outward remodelling), thereby conserving the lumen (Glagov et al., 1987). In later stages of the disease, if plaque occupies approximately 40% of the cross-sectional area of the artery, the compensatory enlargement rate is no longer adequate: the plaque eventually narrows the lumen and thereby reduces blood flow (Glagov et al., 1987). Tissue located downstream from an obstruction becomes deprived of oxygen or nutrients depending on the degree to which the lumen has narrowed (stenosis). First symptoms usually appear during exercise, when oxygen (and, thus, blood) demand is higher than in a resting condition. Three locations where atherosclerotic plaques most often form are:

Legs: Atherosclerosis in the arteries that supply blood to the legs is also called intermittent claudication. The first symptom of intermittent claudication is usually leg pain during walking; later, the pain is also present during rest. In advanced stages of the disease, blood supply to the legs is diminished. If the blood flow is severely reduced, the skin may be discoloured and ulcerations can appear.
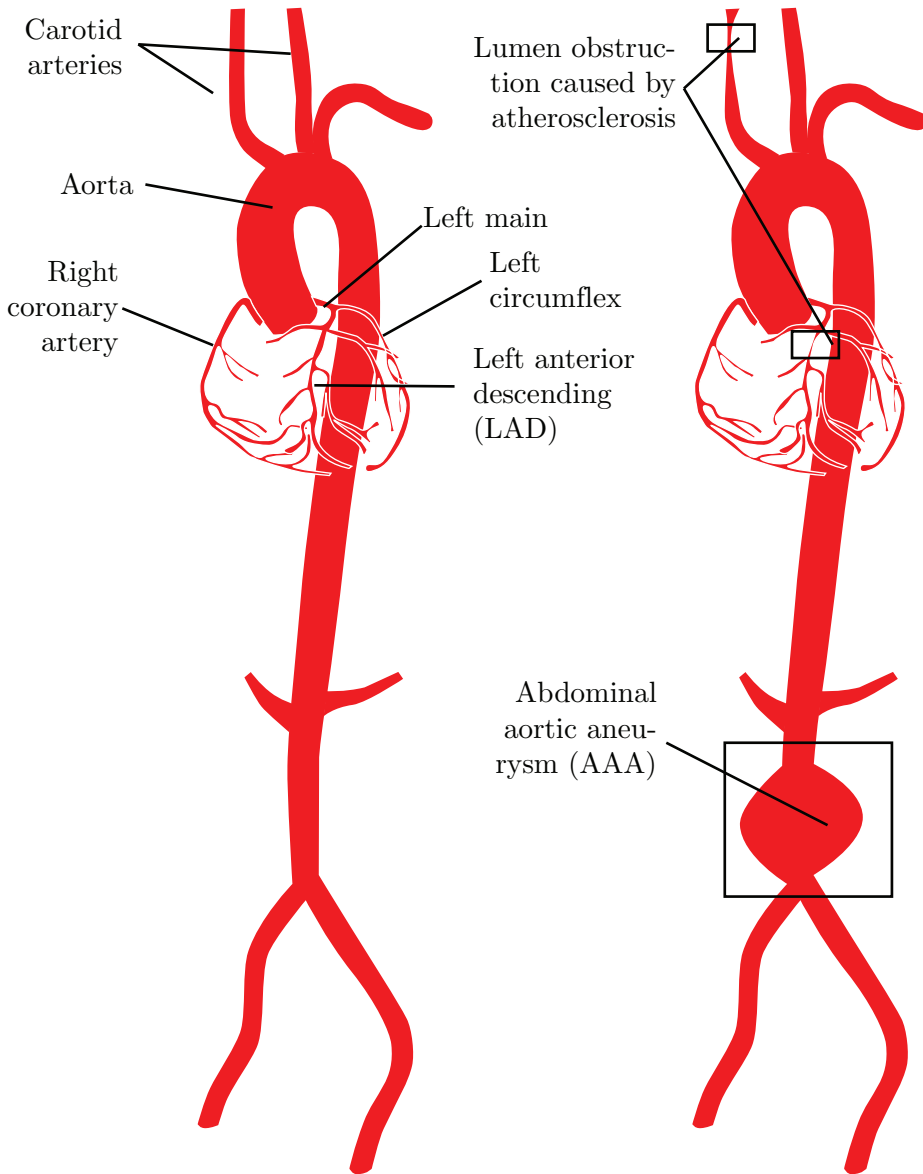
Figure 1.2: *A schematic view of the human arterial system. Left: A healthy arterial system. Right: diseased arterial system; obstructed blood flow in the coronary and carotid artery and a widening in the abdominal aorta caused by an abdominal aortic aneurysm (AAA).*

Coronary arteries: From the aorta, the left main (LM) and the right coronary artery (RCA) branch off to supply blood to the heart, see Figure 1.2. The LM coronary artery branches into the left anterior descending (LAD) artery and the left circumflex (LCX) artery. Advanced stages of coronary atherosclerosis can lead to symptoms such as chest pain during exercise, shortness of breath, fatigue, and dizziness. In the most advanced stage of the disease, a plaque may occlude an artery and deprive the distal tissue of blood: this is called a heart attack. The mortality rate of heart attack is approximately 5% (Menees et al., 2013)). If not treated quickly, the part of the heart muscle that was fed by the affected artery will die and be replaced with scar tissue.

Carotid arteries: The carotid arteries are responsible for supplying blood to the brain. Patients with carotid atherosclerosis can be either symptomatic or asymptomatic. When symptoms appear, atherosclerotic disease is already extremely advanced. These symptoms consist of stroke-related symptoms such as visual loss or impairment, contralateral weakness or numbness, hemineglect, or speech impairment (Gokaldas et al., 2015).

Atherosclerosis is usually treated with drugs that reduce lipids (e.g. statins), blood pressure (diuretics), or heart rate (beta blockers) and anticoagulants to slow down or reverse plaque formation, decrease the risk of plaque rupture by lowering blood pressure, and minimize blood clotting. In some cases, surgical intervention is preferred to remove the plaque and restore the blood supply. In general, there are three surgical approaches: bypass grafting, whereby an artery from elsewhere is used to bypass the diseased artery; balloon angioplasty, a technique to open the artery using inflation of a balloon, which is often followed by placement of a vascular mesh or stent to keep the artery open; or endarterectomy, a technology to surgically remove the plaque (not preferred for the coronaries).

Atherosclerosis results from a combination of factors including vascular biology, mechanical forces, and systemic risk factors (Morbiducci et al., 2016). Endothelial cells can become inflamed when they are subjected to agitating stimuli (e.g. shear stress or dyslipidaemia); this inflammation facilitates monocyte adhesion to the endothelial cells and migration of these cells and cholesterol into the intima (Libby et al., 2011; Tabas et al., 2007). In the intima, a monocyte develops into a macrophage, engulfs lipids and turns into a foam cell. If macrophages are present in the intima, the arterial wall displays the earliest stage of atherosclerotic plaque (Rader and Puré, 2005; Virmani et al., 2000). The pro-atherogenic environment allows a continuous influx of monocytes and lipids into the vessel wall, which in turn allows lesions to progress into advanced plaques (Libby et al.,

2011). At the same time, smooth muscle cells (SMCs) from the media migrate into the intima, proliferate, and synthesize of collagen and elastin.

In this more advanced stage of the disease, a subgroup of plaques develops a lipid-rich necrotic core (NC) resulting from dying macrophages, SMCs, and cholesterol; the NC is covered by a fibrous cap, preventing the artery from rupturing. These advanced plaques can also contain cholesterol crystals and microvessels (Libby et al., 2011). A plaque is considered a thin-cap-fibro atheroma (TCFA) when it has a thin fibrous cap infiltrated by macrophages and lymphocytes, few SMCs, and an underlying NC and it displays positive remodelling (Falk, 2006; Naghavi et al., 2003; Virmani et al., 2006). If the fibrous cap ruptures, the plaque's interior will come into direct contact with the blood, which triggers blood coagulation pathways and thrombus (blood clot) formation, see Figure 1.3. A thrombus can impede local blood flow or enter the blood stream and occlude another part further downstream. Blocking the artery may lead to myocardial infarction or stroke. However, the majority of plaque ruptures and subsequent thrombus formation do not lead to full blockage of the artery and therefore do not lead to cardiac events (Burke et al., 2001). In such cases, thrombus material becomes organized and thereby contributes to local plaque growth.
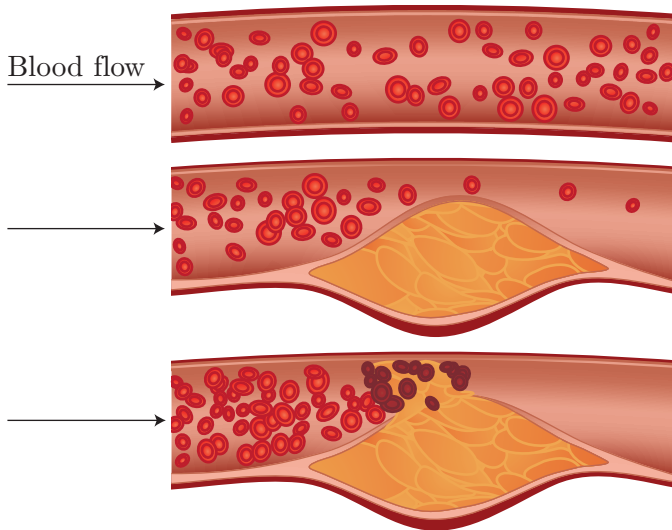
Figure 1.3: A schematic overview of the development of atherosclerosis. At the top: a healthy artery, with a three-layered wall; middle: plaque formation in the intima; bottom: rupture of plaque leading to obstruction of the blood stream (thrombosis).

According to the PROSPECT study, the presence of a TCFA, as assessed by intravascular imaging using IVUS-VH (see 1.2), predicts only 4.9% of major adverse cardiac events (MACEs) (Stone et al., 2011)(Stone et al., 2011a). Other geometric plaque features associated with increased risk of cardiovascular events include a minimal lumen area (MLA) ≤ 4 mm^2 and a plaque burden (PB) $\geq 70\%$ (Stone et al., 2011). These geometric risk factors predict 18.2% of MACEs; they are clearly insufficient to predict MACEs, and better predictors are therefore needed.

1.1.2 Abdominal aortic aneurysm

An aortic aneurysm is an enlargement of the largest artery in the human body: the aorta. In this thesis, I will focus on the most common aneurysm: the abdominal aortic aneurysm (AAA), see Figure 1.4. An AAA is diagnosed if the aorta's maximal diameter exceeds 150% of its healthy size or when maximal diameter exceeds 3 cm (Craig Kent, 2014). Unfortunately, AAA rupture is associated with extremely high mortality (80% — 90%) (Bengtsson and Bergqvist, 1993; Choksy et al., 1999).

Normal aorta   Abdominal aortic
                      aneurysm
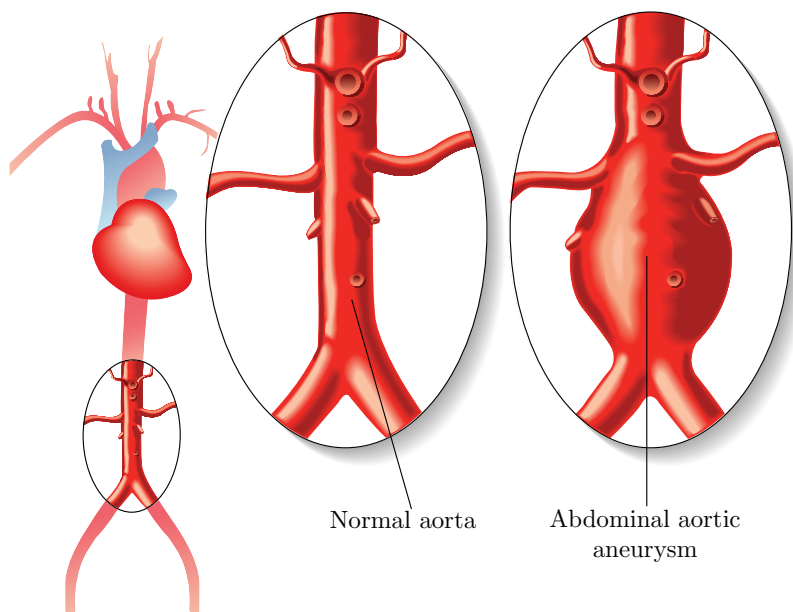
Figure 1.4: *A schematic view of the arterial system. Left: the region of interest is circled; middle: a healthy abdominal aorta; right: an abdominal aortic aneurysm (AAA).*

A patient with a AAA is usually asymptomatic, and therefore most AAAs are discovered by accident. Upon discovery of a AAA, patients are closely monitored for AAA growth. Some aneurysms grow rapidly, while others can remain stable for years (Kurvers et al., 2004). The most effective aneurysm treatment is surgery; however, surgery is not risk-free and has a mortality rate of 1% to 5% (Brewster et al., 2003). Therefore, the risk of rupture needs to be weighed against the risk of surgery. Surgical treatment is recommended when the AAA's diameter exceeds 5.5 cm (Brewster et al., 2003). This criterion is not optimal; non-ruptured aneurysms have been found above this threshold, and ruptured ones below this threshold (Conway et al., 2001; Darling et al., 1977). Therefore, there is a need for more suitable treatment criteria.

The formation of AAAs is complex and not fully understood, but a combination of different risk factors and mechanical forces is involved (Kuivaniemi et al., 2016; Tromp et al., 2010). A AAA displays obvious differences in vessel wall composition and structure compared to a healthy vessel wall; the aneurysmal wall is highly inflamed (Brophy et al., 1991; Ihara et al., 1999), which mediates elastin destruction and finally results in aneurysmal dilation, elongation, and increased tortuosity of the vessel (Campa et al., 1987; Tilson, 1988; White et al., 1993). Furthermore, AAAs contain three- to fivefold more collagen than healthy aortic tissue (Baxter et al., 1994). In later stages of AAA development, collagen degradation contributes to AAA rupture (Dobrin et al., 1984).

Furthermore, thrombus—a 3D fibrin structure—is a common phenomenon in AAAs. This fibrin structure consists of blood cells, platelets, blood proteins, and cellular debris (Li et al., 2008). In contrast to other vascular diseases such as atherosclerosis, thrombus formation generally does not cause an occlusion in AAAs (Piechota-Polanczyk et al., 2015), but prevents diffusion of oxygen and nutrients into the arterial wall. This leads to increased inflammation, neovascularisation, and hypoxia in the vessel wall, which results in a reduction of the wall's tensile strength.

1.2   Imaging

Over the years, different imaging methodologies have been developed to visualize plaque morphology and composition. The 3D shape of an artery in vivo is generally acquired via the following minimally invasive imaging techniques: computed tomography (CT), magnetic resonance imaging (MRI), or X-ray-based angiography. However, these techniques lack the required temporal and/or spatial resolution to assess plaque composition in smaller arteries such as the coronary arteries. Lately, 3D geometry acquisition with non-invasive ultrasound is being explored. Ultrasound has a relatively high resolution,

but contrast and penetration depth, and therefore the field of view, remains limited. This limitation is exacerbated when organs containing air, such as the intestines, which obstruct the view.

In addition to these 3D imaging techniques, invasive intravascular imaging techniques can be used to visualize the detailed lumen and vessel wall. These procedures use a small imaging camera (catheter) inserted into the artery. When positioned at the location of interest, the catheter visualizes cross-sections of the artery and is then pulled back at a motorized constant speed, such that longer arterial segments can be visualized. In this way, the resolution is much higher than the aforementioned 3D imaging techniques, enabling visualization of the shape and composition of atherosclerotic plaques.

The two most common invasive imaging techniques used to assess coronary plaques are intravascular ultrasound (IVUS) and optical coherence tomography (OCT). For an overview of the properties of IVUS and OCT, see Table 1.1. Each technique has advantages and disadvantages: IVUS has a large penetration depth, and therefore the full plaque thickness can be visualized; however, the resolution of IVUS is limited. The resolution of OCT is high and allows detailed visualization of superficial structures such a cap covering a lipid pool; however, the penetration depth of OCT is limited. Furthermore, since the pullback speed of OCT is very fast, it is subjected to heartbeat artefacts, whereas the IVUS pullback is slower and (can be) gated.

Table 1.1: *Properties of invasive imaging techniques: optical coherence tomography (OCT) and intravascular ultrasound (IVUS).*

	OCT	IVUS
Type	Near-infrared light	Ultrasound
Wavelength (μm)	1.3	35–80
Resolution (μm)	10–15 (axial), 40–90 (lateral)	100–200 (axial), 200–300 (lateral)
Frame rate (frames/s)	100–200	30
Pullback rate (mm/s)	10–20	0.5–1
Tissue penetration (mm)	1–2.5	10

Another IVUS-based technique is virtual histology intravascular ultrasound (VH-IVUS), which uses raw radio frequency data to identify plaque components (Nair et al., 2002) such as fibrous tissue, fibrous-fatty tissue, NC tissue, and dense calcium.

Recently, the NIRS-IVUS catheter, which combines near-infrared spectroscopy (NIRS) and IVUS, was developed for clinical use. Spectroscopy is already widely used to assess the chemical composition of any unknown substance; this new clinical NIRS-catheter is designed to detect lipids in plaques in vivo. The results of NIRS were confirmed with histology in a large autopsy study (Gardner et al., 2008). Physicians at our hospital performed the first-in-man study of this technology (Garg et al., 2010). The NIRS-catheter indicates circumferentially if there is a high probability (>60%) of cholesterol (indicated as yellow pixels) or a low probability ($\leq$ 60%) of cholesterol (indicated as red pixels). The presence of lipids is usually expressed as lipid core burden index (LCBI):

$$LCBI = 1000 * \frac{\text{\# yellow pixels}}{\text{\# yellow pixels} + \text{\# red pixels}} \qquad (1.1)$$

High NIRS-derived LCBI values in a non-culprit vessel were associated with a fourfold increase of MACE during one year of follow-up (Oemrawsingh et al., 2014). LCBI values also were associated with adverse cardiac outcomes independent of clinical risk factors or plaque burden (Schuurman et al., 2017). The potential of NIRS in addition to shear stress as possible risk factor marker for atherosclerotic progression has not been investigated.

Currently, post-processing techniques are available that allow the various non-invasive and invasive imaging modalities to be fused (van der Giessen et al., 2010). In this way, rough 3D geometry can be combined with detailed 2D information. In both techniques, side branches are visible; these can be used as landmarks for fusion purposes.

1.3   Relationship between biomechanics and vascular diseases

Mechanical forces and the resulting stresses and strains play a key role in the development and remodelling of tissues and cells. With computational modelling, we can determine these mechanical forces. In AAA or atherosclerotic arteries, we determine the stresses in force per area inside the arterial wall (with solid mechanics) or the blood flow-induced shear stresses against the arterial wall (with fluid mechanics). Using fluid mechanics, the effect of blood flow-induced shear stress on the intima (1.3.2) can be studied for plaque initiation, progression, and destabilization. Solid mechanics is used to model wall stresses and investigate rupture of the arterial wall or atherosclerotic plaque. From a

biomechanical point of view, rupture will occur when stresses exceed material strength (further explained in 1.3.1).

1.3.1 Wall stress

To understand plaque or aneurysm rupture, two things are important: arterial wall strength and arterial wall stresses. In an idealized, homogeneous, circular, straight tube, the stress (σ) can be calculated using LaPlace's Law:

$$\sigma = \frac{pr}{h} \tag{1.2}$$

where p is blood pressure, r is radius, and h is arterial wall thickness. In general, as the diameter of the artery or intraluminal pressure increases, stresses will increase. The inverse is true for wall thickness. However, arteries cannot be simplified into straight circular tubes. Arteries are geometrically highly complex: they vary in diameter, wall thickness, wall composition, curvature, and tortuosity. Therefore, LaPlace's Law does not hold, and hence the need for computational modelling.

Abdominal aortic aneurysm   AAA studies using solid mechanics to determine rupture risk have already provided some important insights. First, the presence of mural thrombus acts as a buffer and significantly decreases stresses in the wall of a AAA (Di Martino et al., 1998; Mower et al., 1997). Second, Fung et al. found that there are stresses present in arteries even without blood pressure acting on the vessel wall; these are called residual stresses or initial stresses (Fung, 1991). They may be induced in the development and remodelling phase of the arterial wall. These initial stresses have a significant effect on AAA wall stress calculations (de Putter et al., 2007; Merkx et al., 2009). Without the initial stresses, an erroneous higher volume (> 6%) of the geometry was observed when exposed to the same blood pressure (Speelman et al., 2009). Third, the maximum peak wall stress was found to be a promising predictor for AAA ruptures and therefore has potential to aid in the clinician's decision-making (Fillinger et al., 2002; Heng et al., 2008; Truijers et al., 2007; Venkatasubramaniam et al., 2004). Fourth, Speelman et al. demonstrated that the 99th peak wall stress is more robust and reproducible than peak wall stress (Speelman et al., 2008).

Atherosclerosis   Most studies on atherosclerosis that apply computational modelling focus on local stress distribution in the plaque in order to predict rupture risk. Several

studies have investigated how the shape, size, and material properties of tissue types within the plaque influence local stress distribution. In coronary arteries, wall stresses were highly dependent on the material properties of the intima (Akyildiz et al., 2011). It is very difficult to determine these material properties to simulate stress in in vivo tissues; the material properties of the intima are broadly heterogenous (Chai et al., 2013). Furthermore, geometric properties affect wall stresses (Akyildiz et al., 2016). These properties include: small irregularities in lumen and necrotic core shape and a thin intima layer near the shoulder of the NC. Next, microcalcifications, presence of haemorrhage, and macrophages were also associated with increases in wall stress (Huang et al., 2010; Hutcheson et al., 2014).

From a biomechanical point of view, an atherosclerotic plaque ruptures if plaque stresses exceed the plaque strength. Rupture typically takes place at the thin fibrous cap covering a large lipid pool (Costopoulos et al., 2017; Gao and Long, 2008; Loree et al., 1992). Cheng et al. suggested a threshold of 300 kPa of circumferential tensile stress in the cap to predict rupture risk (Cheng et al., 1993). However, this threshold is questionable since many studies suggest that there is a great variance in tissue strength (Akyildiz et al., 2014).

1.3.2 Shear stress

Atherosclerotic plaque progression is associated with shear stress (Wentzel et al., 2012), the frictional force exerted by blood shearing against the arterial wall. In a straight circular tube with fully developed flow, the flow is called Poiseuille's flow. In this case, shear stress can be calculated as a function of flow (Q), dynamic viscosity (μ) and radius (R):

$$\tau = \frac{4\mu Q}{R^3} \tag{1.3}$$

Due to the geometric complexity of blood vessels, this simple formula cannot be applied to determine local shear stress distribution. Computational modelling is used to simulate blood flow through geometric complex arteries (further explained in 1.4).

The link between atherosclerosis onset and shear stresses has been confirmed in previous studies. Predilection sites for atherosclerotic plaques include the outer wall of a bifurcation and the inner curvature, both of which experience low shear stress (VanderLaan et al., 2004). Endothelial cells are sensitive to shear stress, and both the morphology

and function of endothelial cells are related to shear stress (Davies et al., 1986; Malek et al., 1999). Endothelial cells exposed to low shear and oscillatory stress have higher rates of proliferation rate and express more inflammatory molecules than cells exposed to elevated shear stress (Davies et al., 1986),which contribute to plaque initiation.

Moreover, animal studies have demonstrated that low shear stress induces vulnerable plaques (Cheng et al., 2006). This result was confirmed by studies in a diabetic hyper-cholesteraemic pig model, in which vulnerable plaques (thin capped plaques with reduced collagen content) were most often observed at low shear stress regions (Koskinas et al., 2013b). Plaque progression has also been associated with low shear stress (Samady et al., 2011), and low shear stress has independently predicted rapid lumen narrowing and plaque burden progression (Stone et al., 2012).

As previously discussed, the lumen can become compromised in advanced atherosclerosis. When blood flow remains the same, but the lumen area decreases, blood velocity (and thus shear stress) will increase. Some studies support the hypothesis that coronary segments exposed to high time-average wall shear stress (TAWSS) are more prone to evolving a to develop into a high-risk plaque (Eshtehardi et al., 2017). Several prospective studies demonstrated that high shear stress regions experience an increase in lipid content, which leads to a more vulnerable plaque phenotype (Samady et al., 2011). Furthermore, high TAWSS regions co-localize with plaque rupture sites (Fukumoto et al., 2008; Groen et al., 2007).

In addition to the magnitude of shear stress, flow directionality affects endothelial cell morphology and function. Perpendicular flow and multidirectional flow can cause inability of cells to align in cells, which in turn is associated with the activation of inflammatory pathways (Baeyens et al., 2014; Davies et al., 1986; Wang et al., 2013). A new multidirectional shear stress parameter, transverse wall shear stress (transWSS) (Peiffer et al., 2013b), is the shear stress magnitude perpendicular to the main flow direction and, this can be interpreted as the flow direction perpendicular to endothelial cell alignment. TransWSS was a promising predictor of plaque development in a rabbit study; lipid-rich plaques were more often found at high transWSS regions than at low transWSS regions (Mohamied et al., 2015). This parameter has not yet been studied in human patients and might be helpful in better understanding atherosclerosis.

Since cholesterol levels have a major impact on plaque growth (Nissen, 2005), the combined influence of systemic cholesterol levels and shear stress was investigated in an animal study. The animals were divided into a high total cholesterol group (n=4) and a low total cholesterol group (n=5) (Koskinas et al., 2013a); animals with high total cholesterol

levels underwent the most plaque progression in areas exposed to low shear stress. This study suggests that high cholesterol greatly amplifies the effect of low shear stress on plaque growth. Lipid accumulation also contributes to the activation of local endothelial cells (Lusis, 2000); inflammation and plaque growth might be enhanced in the presence of lipids inside the plaque. Therefore, low shear stress co-localized with local lipid-rich plaques might be a better predictor for plaque progression than low shear stress and high systemic cholesterol levels.

Taken together, shear stress plays a role in the initiation and development of atherosclerosis and potentially also in plaque destabilization; this role is still largely unknown.

1.4   Computational modelling

Computational modelling is used to solve a large set of partial differential equations that describe a complex problem. These partial differential equations comply with energy, mass, and momentum conservation laws. For computational modelling (or finite element analysis), we use the continuum hypothesis, which implies that the material fills the entire space and that the behaviour of individual molecules can be ignored. In fluid mechanics, the resulting set of equations is known as the Navier-Stokes equations; these can be used to get insight in the velocity and pressure vector fields throughout the lumen of the artery for a given flow or pressure drop over the artery. From the velocity and pressure fields, other parameters such as shear stresses can be derived.

In this thesis, the deformation and stresses of the arterial wall (with or without plaque) subjected to external forces (e.g. blood pressure) are modelled by solving the mechanical force and momentum equilibrium equations through numerical approximation. The arterial wall and components thereof are modelled as elastic or hyper-elastic materials. From solid mechanics simulations, the stresses in the wall are derived and used for further study on potential wall or plaque rupture. However, to solve the large set of partial differential equations, model input is necessary.

The model input consists of geometry, material properties (e.g. blood or vessel wall), and loading conditions (e.g. blood pressure or blood velocity). A schematic overview of the input for the computational modelling is given in Figure 1.5. All input parameters are either measured or based on literature and should be set with the utmost caution. Errors can propagate or be amplified in the results, which may lead to misinterpretations of the data. These three inputs will be further explained in the following sections.
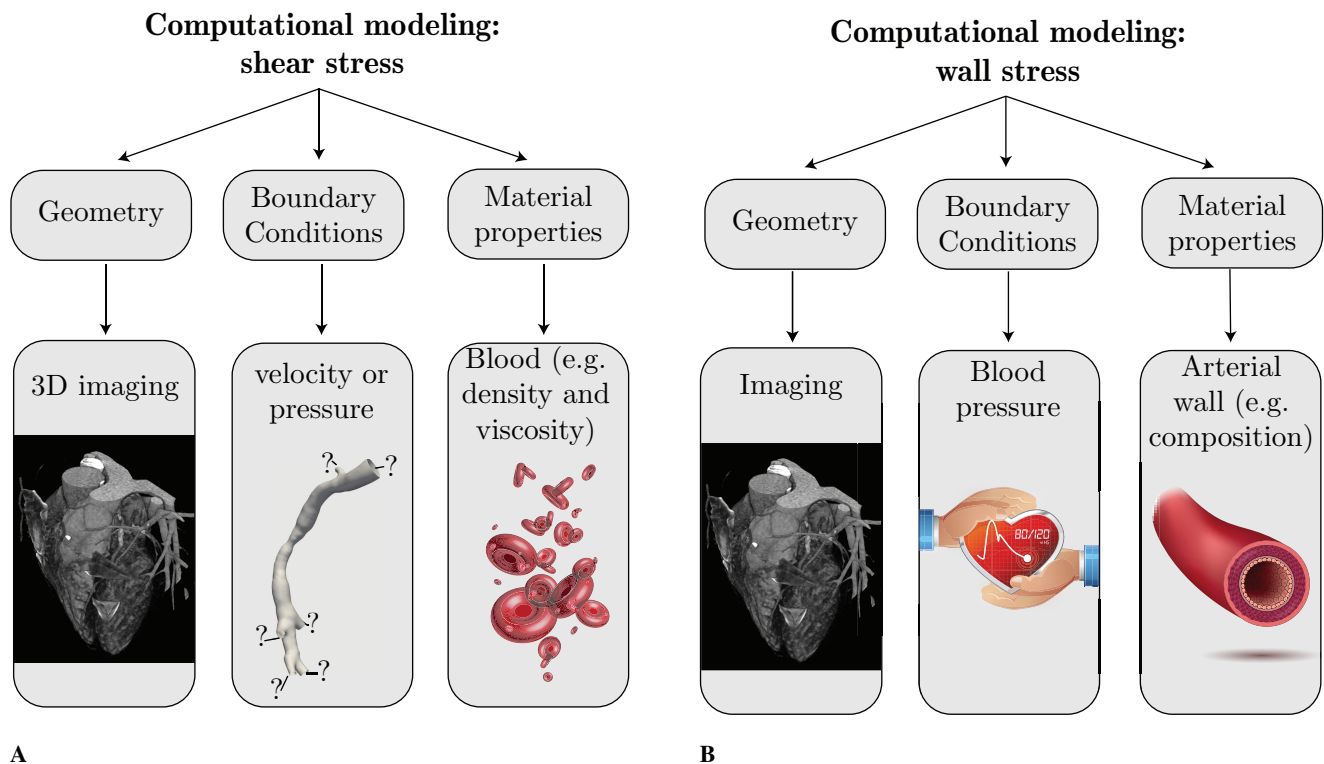
Figure 1.5: *A schematic overview of the input required for computational modeling for shear stress (A) and wall stress (B).*

For calculations of both shear stress and wall stress, geometry is very important. Shear stress calculations require an accurate description of the lumen's 3D geometry (i.e. curvature, tortuosity, and branching), including the side branches. For arterial wall stress calculations, knowledge of the lumen, the vessel wall thickness, and the composition of the arterial wall are important.

The loading specifics depend on whether the modelling type is fluid or solid. For solid mechanics, stresses in the vessel wall are calculated; here, blood pressure is a loading requirement. For fluid mechanics, the blood flow, blood velocity profile or blood pressure is required; these can be approximated but should ideally be measured. Blood flow velocity can be measured using an invasive Doppler wire or 4D phase contrast MRI (Cibis et al., 2017; Doucette et al., 1992). Many shear stress studies of coronary arteries neglect the presence of side branches. The presence of side branches affects the flow distal from the branch, since a portion of the flow will exit the system through the side branch.

Furthermore, the tissue surrounding the arteries is important. In the atherosclerotic solid mechanics studies in this thesis, it was assumed that the artery was embedded in soft tissue. The aneurysms were fixed proximally and distally. In the fluid mechanics studies, the wall was assumed to be stationary, and a non-slip boundary condition on the lumen wall was therefore assumed.

For each material that is modelled, material behaviour needs to be prescribed. Measurements of each material's behaviour would be ideal; however, this is difficult in vivo. Moreover, biological materials are often heterogeneous. In this thesis, the solid materials or plaque components were assumed to be hyper-elastic, isotropic, and incompressible. Computational fluid dynamics requires the input of blood properties such as viscosity and density. Blood is a shear-thinning fluid, meaning that viscosity decreases as a function of the shear rate. This behaviour is captured in non-Newtonian material models.

1.5   Scope and outline

The overall aim of this thesis is to investigate the impact of biomechanical stresses on the development of two arterial diseases: atherosclerosis and abdominal aortic aneurysms. Various imaging and computational methodologies were employed to assess the stress inside the wall and the blood flow-induced shear stresses acting on the wall. The influence of these stresses was investigated on changes in plaque growth and changes in composition. Furthermore, improvements on the methodologies to calculate wall stress in atherosclerotic plaques and aneurysms were investigated.

Fluid mechanics

Even though risk factors for atherosclerosis are systemic in nature (e.g. blood pressure, cholesterol), atherosclerosis was localized at certain predilection sites such as inner curvatures and near bifurcations. These predilection sites were explained by the pro-atherogenic influence of blood flow-induced shear stress at the vessel wall (VanderLaan et al., 2004). Since geometry has major impact on shear stress, multiple studies investigated the risk associated with geometric factors as an alternative to shear stress.

Chapter 2 reviews studies that investigated the relationship between geometric risk factors, shear stress and the application of geometric risk factors as predictors of atherosclerotic plaque development in coronary and carotid arteries. Additionally, helical flow is introduced as a potential surrogate marker for shear stress because helical flow was shown to be atheroprotective in carotid arteries. The association between helicity and shear stress has never been investigated in coronary arteries, which are geometrically distinct from carotid arteries. **Chapter 3** describes a study in which the association between helicity, shear stress, and geometric parameters was investigated in porcine coronary arteries.

Shear stress distribution of blood at the vessel wall largely depends on local geometry, but also changes over the cardiac cycle in both magnitude and direction. Because time-averaged wall shear stress alone is insufficient to fully predict plaque growth and destabilization, shear stress parameters that account for its multidirectionality might improve local estimations of plaque growth and destabilization. In **Chapter 4**, a study is described in which various multidirectional shear stress parameters are investigated simultaneously for the first time; this study determines their influence on plaque growth and composition changes in twenty human coronary arteries.

Lipids play a major role in atherosclerotic plaque development. A recently developed NIRS-IVUS catheter can assess plaque morphology (using IVUS) simultaneously with lipid information. In **Chapter 5**, we describe the study in which we used this new catheter to study the combined influence of a NIRS positive signal and multidirectional shear stress parameters for its ability to predict plaque progression in acute coronary syndrome (ACS) patients. In **Chapter 6**, a new porcine model to study plaque growth is introduced. In 30 coronary arteries from adult familial hypercholesteremic pigs the influence of multidirectional shear stress on plaque composition and plaque growth was investigated.

Solid mechanics

For the calculation of stresses in the vessel wall, it is imperative to know the composition and material properties of the vessel wall. In coronary arteries, detailed knowledge of plaque composition is often obtained via IVUS, OCT, or both. Although the combination of IVUS and OCT provides information on vessel wall thickness, fibrous cap thickness, and the location of the lipids, the lipid-rich NC still cannot be fully visualized. In **Chapter 7**, a methodology to reconstruct the NC based on the information that is available through IVUS and OCT is described; this method also allows calculations of stress in the vessel wall. Plaque morphology and composition in the carotid arteries are often imaged using MRI. However, the resolution of MRI is insufficient to capture the cap region of the NC, leading to an overestimation of cap thickness even by experienced MRI readers. In **Chapter 8**, a similar strategy to that described in chapter seven was applied to reconstruct the cap and complete the lipid-rich NC. Thereby, this study introduces a new methodology to improve the accuracy of computational modelling of NC geometry and of MRI-based peak cap stresses in carotid arteries.

In aneurysms, the computation of peak stresses can potentially aid in rupture risk assessment. Previously, MRI and CT images were used to create 3D models of the AAA. However, 3D ultrasound offers a higher image resolution and thus would allow a more accurate 3D reconstruction of AAA geometry. In **Chapter 9**, a study that investigated the feasibility of assessing peak stresses in AAAs based on 3D ultrasound imaging is described.

Part 1:
Shear stress

ATHEROSCLEROSIS AT ARTERIAL BIFURCATIONS

2

Based on: *Morbiducci U,* **Kok AM***, Kwak BR, Stone PH, Steinman DA., Wentzel JJ. Atherosclerosis at arterial bifurcations: Evidence for the role of haemodynamics and geometry. Thromb Haemost. 2016;115:484–492.*

ABSTRACT

Atherosclerotic plaques are found at distinct locations in the arterial system, despite the exposure to systemic risk factors of the entire vascular tree. From the study of arterial bifurcation regions, which are more prone to the initiation/progression of atherosclerosis, emerges ample evidence that haemodynamics are involved in the local onset and progression of the atherosclerotic disease. This observed co-localization of disturbed flow regions and lesion prevalence at geometrically predisposed districts such as arterial bifurcations has led to the formulation of a 'haemodynamic hypothesis', that in this review is grounded to the most current research concerning localizing factors of vascular disease. In particular, this review focuses on carotid and coronary bifurcations because of their primary relevance to stroke and heart attack. We highlight reported relationships between atherosclerotic plaque location, progression and composition, and fluid forces at vessel's wall, in particular shear stress and its 'easier-to-measure' surrogates, i.e., vascular geometric attributes (because geometry shapes the flow) and intravascular flow features (because they mediate disturbed shear stress), in order to give more insight in plaque initiation and destabilization. Analogous to Virchow's triad for thrombosis, atherosclerosis must be thought of as subject to a triad of, and especially interactions among, haemodynamic forces, systemic risk factors, and the biological response of the wall.

2.1   Introduction

Atherosclerosis is a systemic inflammatory disease of the arterial system characterized by intimal lesion formation (atherosclerotic plaques) in the vasculature. Rupture of atherosclerotic plaques is responsible for the majority of the cardiovascular events (myocardial infarction, stroke), which are leading causes of morbidity and mortality in the Western world. Atherosclerotic plaques display a variety of phenotypes: highly inflamed lesions with a large lipid pool and a thin fibrous cap are recognized as most vulnerable to rupture, whereas fibrous plaques are generally considered more stable (Ylä-Herttuala et al., 2011).

Atherosclerotic plaques develop at arterial locations with a dysfunctional endothelium and involves leukocyte recruitment, lipid accumulation, smooth muscle cell migration and proliferation, cell death and fibrosis (Libby et al., 2013; Van Vre et al., 2012). Atherosclerotic plaque development occurs preferentially at geometrically predisposed areas, like the inner curvature of the aortic arch and close to arterial branch points, despite the fact that the entire arterial tree is exposed to systemic risk factors such as hypertension, hypercholesterolemia and diabetes (Asakura and Karino, 1990; Eshtehardi et al., 2012).

There is ample evidence that haemodynamic factors are involved in the local onset and progression of atherosclerosis, often referred to as the 'haemodynamic hypothesis'. Haemodynamic factors regulate multiple aspects of vascular biology and physiology and play a key role in vascular homeostasis as well as in arterial disease development (Kwak et al., 2014). In analogy to Virchow's triad on thrombosis, Figure 2.1 shows a schematic representation of factors involved in atherosclerotic plaque formation, illustrating the complex interplay between, (1) haemodynamic factors, (2) the biological response of the arterial wall, and (3) systemic risk factors.

A haemodynamic factor that is widely recognized for its involvement in atherosclerotic plaque formation is endothelial shear stress, the frictional force per area exerted at the vessel wall by the flowing blood Figure 2.2. In general, in plaque initiation process low and oscillatory shear stress is considered atherogenic, whereas high shear stress is atheroprotective (Malek et al., 1999).

Wall shear stress can be determined by calculating the gradient of the local blood flow velocity close to the vessel wall multiplied by the blood viscosity. Physical laws determine that blood flow velocities, due to the balance of centrifugal, pressure and viscous forces, are spatially distributed such that skewed, highly asymmetric velocity profiles can be observed in bending arterial segments or at arterial branching (Asakura and Karino, 1990;
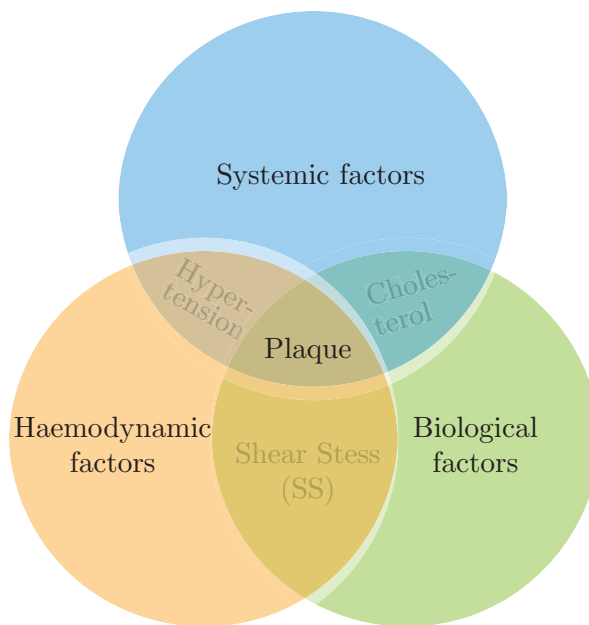
Figure 2.1: *The complex interplay among systemic risk factors, biological factors and haemodynamic factors leading to vascular pathology and atherosclerotic plaque formation may be seen as a triad in analogy to Virchow's triad of thrombosis. The systemic risk factor most influencing atherosclerosis is hypertension, whereas shear stress locally influences the endothelial function and vascular biology. In turn, endothelial function is also influenced by systemic risk factors such as cholesterol levels.*

Glagov et al., 1988) and bifurcating regions, where flow separation and reattachment can occur, consequently leading to complex distinct patterns of low and high shear stress at vessel's wall (Asakura and Karino, 1990; Zarins et al., 1983; Ku et al., 1985).

Additionally, the direction and velocity of blood flow in arteries fluctuate throughout the cardiac cycle. Vascular locations that are exposed to low, oscillatory shear stress (i.e., varying in direction, with both forward and reverse velocities) during the cardiac cycle are considered as 'disturbed' shear stress regions.

Nowadays, shear stress is most commonly assessed using advanced computational fluid dynamics (CFD) (Taylor and Steinman, 2010). However, these methods are typically limited to engineering experts and can be sensitive to assumptions and uncertainties in input parameters including blood flow rates and vessel geometry. Other methods to estimate shear stress include magnetic resonance imaging (MRI)-based velocity measurements, but these can only be applied to larger arteries such as the carotid artery and aorta. Using MRI, absolute shear stress values are typically underestimated due to MRI's low spatial and temporal resolution; however the relative distribution of low vs. high shear stress that can be obtained from the acquired phase velocities is generally correct (Cibis et al., 2014).

Researchers have also investigated whether geometric features of arteries, as easier-to-measure surrogate markers of shear stress, might be able to predict risk for atherosclerotic plaque formation, the so-called 'geometric risk hypothesis' (Friedman et al., 1983). More recently, attempts have been made to correlate specific geometric attributes of the carotid bifurcation with shear stress distribution (Lee et al., 2008; Perktold and Peter, 1990; Perktold et al., 1991; Thomas et al., 2005) and with intimal thickness location (Bijari et al., 2014). Descriptors of the intravascular flow itself, such as helical flow (which has been demonstrated to smooth out extremes of wall shear stress (Caro et al., 1996; Morbiducci et al., 2007; Gallo et al., 2012), have also been investigated as easier-to-measure surrogate markers of shear stress (Morbiducci et al., 2007; Gallo et al., 2012).

This review focuses on carotid and coronary bifurcations because of their primary relevance to stroke and heart attack. We highlight reported relationships between atherosclerotic plaque location, progression and composition and shear stress or its surrogates, i.e., vascular geometry (because geometry shapes the flow) and helical flow (because it is instrumental in suppressing flow disturbances), in order to give more insight in plaque initiation and destabilization.
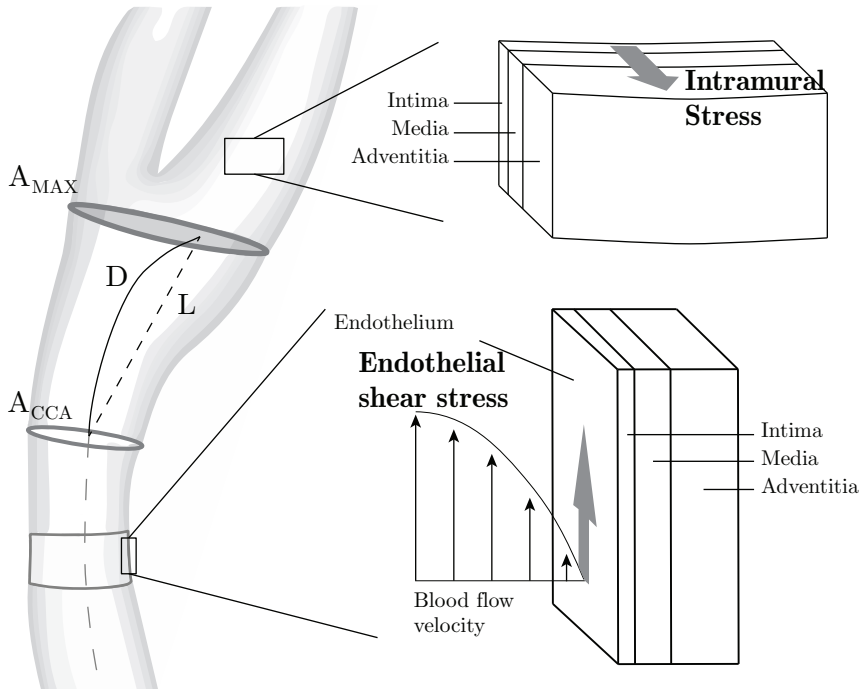
Figure 2.2: *Definition of endothelial shear stress, wall stress and geometric parame-ters in a schematic representation of carotid artery bifurcation. The shear stress is the gradient of the velocities close to the vessel wall multiplied by the viscosity, not to be confused with intramural stress (more markedly involved in plaque rupture) inside the vessel wall, also shown. The geometric parameters demonstrated for the carotid bifur-cation as 'easy-to-measure' surrogates for shear stress are the ratio of maximal area at the bifurcation region (A_{MAX}) to the area at the common carotid artery (A_{CCA}); and the ratio of the CCA centerline distance (D) to the shortest distance (L) between A_{CCA} and A_{MAX}. Also shown is the often-reported angle (α) between the two side branches.*

2.2 Vascular biology and its relationship with shear stress

The luminal side of blood vessels is lined by a monolayer of endothelial cells, which regulate leukocyte adhesion and transmigration, mass transport/permeability, platelet aggregation and smooth muscle function through the release vasoactive substances, such as nitric oxide, endothelin-1 and prostacyclin, and by the expression of specific adhesion and junctional molecules (Félétou et al., 2012; Weber et al., 2007; Zarbock and Ley, 2008). The endothelial cells are the only cell layer directly in contact with flowing blood, and shear stress influences vascular function by activating endothelial mechanoreceptors, which transmit biochemical signals in response to the shear stress. Three groups of potential shear stress sensors have been proposed over the past two decades: (1) cell membrane-associated molecules such as ion channels, receptors, adhesion molecules and the glycocalyx, (2) specific membrane microdomains, like primary cilia and caveolae, and (3) general cell supporting structures such as the cytoskeleton and the lipid bilayer membrane itself (Ando and Yamamoto, 2013). There are substantial differences in the endothelial response in straight parts of arteries that are exposed to pulsatile laminar blood flow and in regions of disturbed shear stress near arterial bifurcations, which may be initiated by different sensing mechanisms. The endothelium in regions of disturbed shear stress displays increased expression and activation of the pro-inflammatory Nuclear Factor Kappa B (NF-κB), an increased oxidant/anti-oxidant balance, activation of the unfolded protein response and endoplasmic reticulum stress as well as low expression of protective factors such as endothelial nitric oxide synthase, thrombomodulin and Krüppel-like transcription factors (KLF2, KLF4) (Boon and Horrevoets, 2009; Davies et al., 2013). These disturbed shear stress-induced changes in endothelial cell behavior result in increased susceptibility to injury and inflammation and limit the regenerative capacity of endothelial cells, this way explaining the focal nature of atherosclerotic lesion formation (Kwak et al., 2014; Schober et al., 2015).

Shear stress may not only affect the initiation of atherosclerosis, but may also directly modify plaque composition and thereby its vulnerability (Ylä-Herttuala et al., 2013). Indeed, the pattern of (imposed) shear stress disturbance appeared by itself crucial for plaque phenotype in mice (Cheng et al., 2006), *i.e.* plaques in a low shear stress region contained low amounts of smooth muscle cells and collagen, high quantities of macrophages and a large lipid core, corresponding to a vulnerable plaque phenotype in human. In contrast, oscillatory shear stress induced smaller plaques with a more stable phenotype.

The relationship between shear stress and atherosclerosis is reciprocal, since plaque formation leads to alterations in local shear stress. During early atherogenesis, outward

vessel wall remodeling can compensate for plaque growth, thus minimizing changes to the vessel lumen (Glagov et al., 1987). Since the geometry of the lumen determines blood flow patterns, this implies that shear stress will not alter significantly during this period. As a result of persisting low shear stress, plaques with a large lipid core, intense inflammation and a thin fibrous cap are found at such locations in porcine coronary arteries (Chatzizis et al., 2008). When expansive remodeling is exhausted, further plaque growth leads to narrowing of vessel lumen, resulting in marked alteration of the shear stress patterns. The upstream segment of the plaque to the point of maximal stenosis is exposed to high shear stress, whereas the downstream segment is subjected to low and oscillatory shear stress. Although defined successive alterations in shear stress patterns have not (yet) been experimentally imposed in animal models, the distribution of leukocytes in human carotid atherosclerotic lesions seems to relate to shear stress (Dirksen et al., 1998).

Upstream segments of plaques at the carotid bifurcation show enhanced macrophage accumulation and apoptosis, intraplaque hemorrhage, thinner fibrous caps and greater incidence of plaque rupture (Cicha et al., 2011; Dirksen et al., 1998). Increased smooth muscle cell and collagen content in the downstream segment seems to stabilize the plaques at this location. Several mechanisms have been proposed (Slager et al., 2005) that potentially are responsible for the high shear stress-induced fibrous cap destabilization. High shear stress leads to an increased NO production and may thereby enhance MMPs expression by macrophages, which can promote cap rupture (Death et al., 2002). Also, plasmin, which is produced by the endothelium in response to high endothelial shear stress (Kenagy et al., 2002) is a strong activator of specific MMPs (i.e. MMP-1, -3, -9, -10 and -13) (Lijnen, 2001).

It is important to note that the mechanisms governing advanced plaque progression and vulnerability are almost certainly different from those for initiation and early progression. In fact, the hypothesis that atherosclerosis initiation correlates with low and/or oscillatory shear stress cannot explain why intermediate and advanced plaques continue to grow under the elevated high shear stress condition caused by severe stenosis-driven altered flow conditions (Tang et al., 2014, 2008, 2005b).

2.3   Carotid bifurcation

2.3.1   Variation in geometry and its influence on shear stress

The carotid bifurcation is the vascular connection where arterial blood from the common carotid artery (CCA) is distributed to the intracranial and extracranial circulations via the internal (ICA) and external (ECA) carotid artery branches, respectively. The presence of this bifurcating vessel, and in particular the dilatation of the region where the ICA stems from the CCA (the so-called carotid bulb) causes complex intravascular flow structures, including flow separation and recirculation, consequently leading to low and oscillatory shear stress.

Early CFD studies using idealized geometries of the bifurcation demonstrated the impact of bulb diameter and bifurcation angle (Perktold and Peter, 1990; Perktold et al., 1991) on the size and intensity of disturbed shear stress at the carotid bulb. Later, a more systematic approach using a parametric geometry demonstrated interactions among bulb diameter, bifurcation angle, and branch diameters in predicting low shear stress (Bressloff, 2007). Investigations using patient-specific geometries showed that bifurcation planarity had only a minor influence on disturbed shear stress compared to artificially straightened counterparts (Thomas et al., 2002). A more comprehensive study of 50 young adults showed that the interaction between bifurcation area ratio and CCA tortuosity significantly predicts exposure to disturbed shear stress at the carotid bulb (Lee et al., 2008). Interestingly, in that study bifurcation angle did not show correlation with disturbed shear stress. These findings were corroborated by in vivo (MRI) imaging of blood flow in an independent cohort (Markl et al., 2010), and were later shown to be strengthened either by prudent combination of selected geometric parameters (Zhang et al., 2010), or by refining the definitions of individual geometric parameters Figure 2.2 to better reflect their influence on the shear stress distribution at the luminal surface (Bijari et al., 2012).

2.3.2   Plaque localization, growth, composition vs. shear stress

Autopsy specimens of carotid bifurcations (Ku et al., 1985; Zarins et al., 1983) have revealed that there are preferred sites for lesion location. Intimal thickening was (1) more pronounced along the outer wall, opposite of the flow divider of the bifurcation, (2) eccentric and greater than elsewhere in the carotid bulb, and (3) minimal and in general uniformly distributed at the common carotid and distal internal carotid levels.

In vitro studies on haemodynamics in adult carotid bifurcations have clarified that regions where maximum intimal thickening and atherosclerotic plaque formation occur were as-

sociated with low and oscillatory shear stress (Ku et al., 1985; Zarins et al., 1983; Ku and Giddens, 1983), whereas the minimally affected arterial lesions were exposed to high flow velocities and thus high shear stress (Zarins et al., 1983). These observations suggested that low shear stress may enhance atherogenesis in the carotid bifurcation. CFD analysis on postmortem human carotid bifurcations with early atherosclerosis have also confirmed the existence of wall alterations at low shear stress regions (Goubergrits et al., 2002).

Recent studies point to a link between shear stress and plaque composition, and thus plaque stability/rupture in carotid arteries (Lovett and Rothwell, 2003; Schulz and Rothwell, 2003). For instance, at the upstream side of the plaque, presumably exposed to high shear stress, a more vulnerable plaque phenotype is observed (Cicha et al., 2011; Dirksen et al., 1998), as is the majority of ulcerations (de Weert et al., 2009). This observation has been confirmed by using MRI-based modeling of the shear stress, showing plaque ulcers being located at the high shear stress sites of the plaque (Groen et al., 2007).

2.3.3 Geometric risk factors and plaque localization and growth

Vascular geometry might serve as a risk factor for the early development of atherosclerosis disease because of its strong influence on local haemodynamics (Friedman et al., 1983; Raso et al., 1981). Early tests of this geometric risk hypothesis were equivocal (Fisher and Fieman, 1990; Ravensbergen et al., 1998; Smedby et al., 1993; Smedby, 1996, 1998; Spelde et al., 1990; Harrison and Marshall, 1983), owing to small sample sizes (N<100) and difficulties in controlling for systemic risk factors or possible secondary effects of plaque on lumen geometry. Larger studies from the early 2000s reinvigorated the search for geometric risk factors (Schulz and Rothwell, 2001; Polak et al., 2010; Sitzer et al., 2003). In a recent study, proximal ICA radius and ICA angle were reported to be significant independent predictors of stenosis development (Phan et al., 2012), but the inclusion of cases with up to 90% stenosis makes it difficult to exclude the impact of plaque on geometry. This importance of cause vs. effect was highlighted in a recent study demonstrating that so-called 'haemodynamically-inspired' geometric risk parameters were significant independent predictors of early carotid bulb wall thickening, but only after carefully excluding cases with possibly inward remodeling (Bijari et al., 2014).

2.3.4 Helical flow velocity and plaque localization and growth

The main geometric characteristics of the carotid artery bifurcation contribute to the onset and development of helical flow patterns (i.e., pitch and torsion of the stream-

ing blood) (Morbiducci et al., 2007; Gallo et al., 2012, 2015). Recent findings on a dataset of 50 models of human carotid bifurcations showed that helical flow intensity suppress flow disturbances at the carotid bifurcation and thereby is potentially protective for atherosclerotic plaque build up (Gallo et al., 2012). Since it was demonstrated that intravascular helical flow can be reliably assessed in vivo (Morbiducci et al., 2011), the quantitative analysis of helical flow patterns could offer a practical way to predict local risk on atherosclerosis in large scale clinical studies, as already done in other arterial districts (Morbiducci et al., 2011; Frydrychowicz et al., 2012), see Figure 2.3.
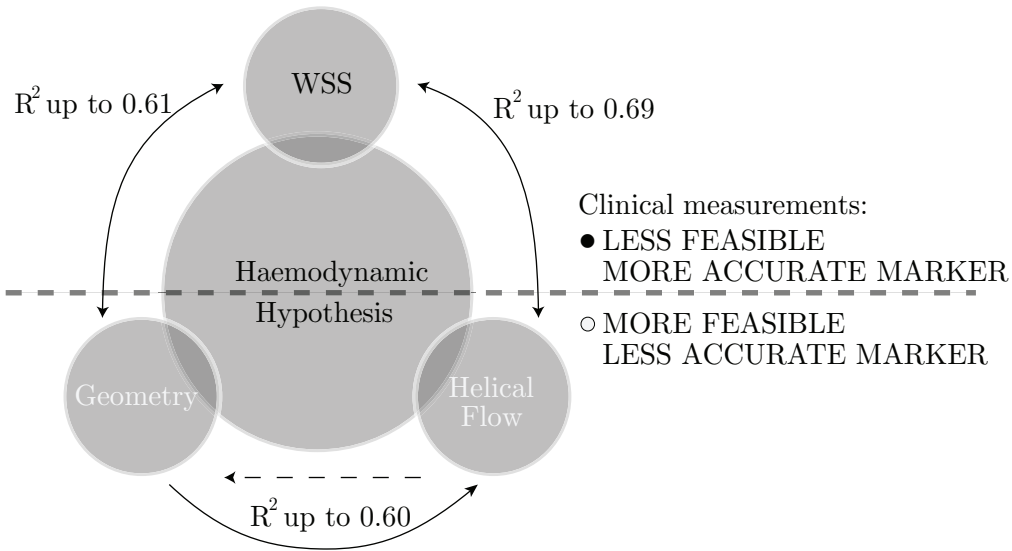
Figure 2.3: *Schematic representation of the relationship between shear stress, geometry and helical flow in carotid arteries. It is hypothesized that (1) the local shear stress is associated with either the local geometry of the bifurcation (R^2 up to 0.61) (Bijari et al., 2012) or the helical flow (R^2 up to 0.69) (Gallo et al., 2012) and that (2) local geometry and helical flow are also correlated (R^2 up to 0.60) (Gallo et al., 2015). Quantitative analysis of geometric vascular attributes and helical flow is feasible and reliable in a clinical setting. However they could be less sensitive or specific than shear stress, for inferring vascular disease.*

2.4 Coronary bifurcation

2.4.1 Variation in geometry and its influence on shear stress

The coronary circulation provides the heart with blood and, in general, it consists of two-to-three major branches: the right side of the heart is fed by the right coronary artery (RCA), whereas the left side is fed by (1) the left main coronary artery (LM), which bifurcates into the left anterior descending artery (LAD) and the left circumflex (LCx), or (2) the LAD and LCx when they stem directly from the aorta. Of all bifurcations in the coronary circulation, LM-LAD-LCx bifurcations are most often affected by disease (Boucek et al., 1980)

Data on geometrical attributes influencing shear stress in coronary artery bifurcations is limited, with the only patient data available focusing on the LM bifurcation. A recent study of LM bifurcations from eight patients showed that LM-LAD tortuosity, appeared to be a good predictor for low shear stress (Malvè et al., 2015), whereas LM-LCx tortuosity, bifurcation angle or area ratios were not predictive of shear stress. Interestingly, other studies have observed an association between LAD-LCx angle and low and oscillatory shear stress regions (Chaichana et al., 2011; Dong et al., 2015). A positive correlation between regions exposed to high shear stress and LAD-LCx and LM-LCx angles (Malvè et al., 2015) has also been observed. In addition to the bifurcation angle, the sharpness/smoothness of the artery branching off has been shown to significantly influence the local shear stress: the sharper the bifurcation the lower the shear stress (Perktold and Peter, 1990). Although the out of plane course of the coronary arteries (planarity) is potentially of influence on the local shear stress distribution, this geometric parameter has not been studied for coronary arteries.

As noted earlier, the presence of stenosis in the bifurcation region potentially changes the local well-defined shear stress distribution. As an example, a study investigated the shear stress distribution in the bifurcation region in the presence of lumen narrowing in the proximal (main) vessel, main distal vessel or side branches (Frattolin et al., 2015). Intuitively the lowest shear stress values were expected when all vessels had a significant stenosis. However, it was observed that significant stenosis in the proximal vessel in combination with stenosis in the side branch resulted in the lowest shear stress values (i.e., an intense atherogenic environment) in the side branch, in the flow recirculation zone immediately distal to the stenosis (Frattolin et al., 2015).

2.4.2 Shear stress and Plaque localization and growth

In the left coronary arteries, plaques are most commonly located at the lateral wall (Badak et al., 2003; Kimura et al., 1996; Svindland, 1983). Based on a coronary CT study, it was speculated that the plaques grow from the opposite of the flow divider (low shear stress) circumferentially towards the flow divider, presumably the high shear stress region (van der Giessen et al., 2009). Interestingly, early plaques located near bifurcations were found to be associated with high shear stress. A possible explanation for this observation is that in the bifurcation region positive remodeling is limited, leading to lumen narrowing and shear stress increase already with early disease (Gijsen et al., 2014).

Although the impact of shear stress on plaque progression has been investigated for non-bifurcated segments of the coronary arteries (Molony et al., 2015), no studies have been dedicated to the bifurcation region. The largest such plaque progression study ever, the PREDICTION study of 500 patients, showed a positive relationship between lumen area change and shear stress, and an inverse relation between plaque burden (percentage of plaque area with respect to the total vessel area) change and shear stress (Stone et al., 2012). Other studies have shown that low shear stress in combination with a plaque burden greater than 50% was a hallmark of plaque area increase over a period of 6 months (Corban et al., 2014), whereas high shear stress was found to be related to plaque area decrease (Samady et al., 2011).

2.4.3 Shear stress and Plaque composition

In a swine study, low shear stress was observed to be correlated with increased inflammation and lipid content, suggesting that low shear stress initiates plaque onset and might be involved in the generation of vulnerable plaques (Chatzizisis et al., 2008). Similar data have been obtained in a number of patient studies, suggesting a co-localization of low shear stress and vulnerable plaque composition such as necrotic core, plaque and calcium (Eshtehardi et al., 2012; Samady et al., 2011; Wentzel et al., 2013). On the other hand, plaques characterized by a plaque burden greater than 40%, at which point lumen narrowing is typically observed, showed a co-localization of high shear stress (i.e., a consequence of lumen narrowing) and the lipid core. This corroborates the hypothesis that shear stress remains low until the plaque encroaches into the lumen, leading to high shear stress exposure at the upstream side of the plaque (Wentzel et al., 2003). Interestingly, high shear stress has been associated with plaque rupture sites (Fukumoto et al., 2008; Gijsen et al., 2013).

Several studies propose strain, the wall deformation caused by wall stress Figure 2.2,

as a surrogate marker for plaque composition. Low strain or low tissue deformation presumably corresponds with 'stable' fibrous tissue and was found to be co-localized with low shear stress (Wentzel et al., 2013). In contrast high strain (or deformation), indicating weaker underlying materials such as lipid-filled macrophages was associated with high shear stress regions (Gijsen et al., 2008). In a later study, high shear stress was found to be correlated with an increase in strain over time, suggesting that high shear stress modulates plaque compositional growth (Gijsen et al., 2008). Using virtual histology, high shear stress has also been associated with increase in necrotic core area and decrease in overall plaque area, potentially leading to increase in plaque vulnerability (Corban et al., 2014).

Plaques that are located close to the bifurcation are present in the main mother vessel as well as the distal main branch. Interestingly, plaques show a clear difference in composition comparing plaques located proximal from the bifurcation versus distal from the bifurcation. Plaques containing larger lipid pools are predominantly located at the proximal site of the bifurcation, and lesions appear to be longer at this site (Papadopoulou et al., 2012) (Diletti et al., 2011; Gonzalo et al., 2009; García-García et al., 2010). In general, the thinnest caps are observed at the proximal site of the bifurcation (Diletti et al., 2011; Gonzalo et al., 2009), except for a study where the thinnest caps were found to be located at the distal site (Jia et al., 2015). Summarizing the above, one would classify atherosclerotic lesions at the proximal site of the bifurcation as vulnerable and thus more prone to rupture.

2.4.4 Geometric risk factors and plaque localization

Already in 1997, geometrical parameters were identified as possible risk factors for plaque localization (Ding et al., 1997). Based on vascular casting techniques of the left coronary artery bifurcation (LM -LAD-LCx), the presence of plaques in the LAD segment correlated best with an interaction term that included the planarity of the bifurcation and the LCx-LAD branch angle. Another study in 245 right coronary arteries correlated the shape of the coronary artery (C-shape vs. sigma shape) to the presence of disease. Although multivariate analysis showed that C-shape was an independent predictor of significant coronary artery disease (Dvir et al., 2003), the measure was not sensitive enough to be used as predictor (Demirbag and Yilmaz, 2005).

2.5   Discussion

Since atherosclerotic plaques are observed at distinct locations in the vasculature, in particular around bifurcations, a link between local haemodynamics and the initiation and progression of plaques has been suggested. For instance, in the bulb region of a carotid artery bifurcation the local flow velocity distribution and thus the local shear stress environment is complex, but well defined. This is not to imply that haemodynamic factors are the sine qua non; additionally, systemic risk factors must also be recognized in the onset and progression of atherosclerosis. As shown in Figure 2.1, the interplay among haemodynamics, systemic risk factors and vascular biology may be visualized analogously to Virchow's triad. All factors go hand in hand towards vascular pathology. For instance, the endothelial response to shear stress is modulated by systemic risk factors, such as hypercholesterolemia, influencing the endothelial function and thereby the susceptibility to atherosclerotic plaque formation (Malek et al., 1999). This synergistic effect of hypercholesterolemia on shear stress induced plaque progression was elegantly shown in an atherosclerotic animal model of plaque progression (Koskinas et al., 2013a) corroborating the interaction among the three different factors. The same risk factors are also responsible for the extent of plaque growth, as has been convincingly demonstrated in clinical studies reducing cholesterol levels and systemic inflammation by statin therapy (Goldstein and Brown, 2015).

2.5.1   Surrogate markers of 'haemodynamic risk'

Present methods to assess endothelial shear stress directly in vivo suffer from limitations of imaging technology (Cibis et al., 2014; Markl et al., 2010). On the other hand, acquisition of helical patterns or certain geometric features of vascular segments are clinically feasible and may be considered as potential surrogate markers for atherosclerosis risk, by virtue of their influence on near-wall flow patterns (Morbiducci et al., 2007; Félétou et al., 2012). Figure 2.3 shows an overview of the interplay between geometry on one hand and helical flow and the endothelial shear stress on the other, indicating the strength of associations reported by investigations of the carotid arteries. The possibility to screen risk from the bifurcation geometry or helical flow as promoters/surrogates of disturbed shear stress is attractive in terms of translation of biomechanical principles into clinical practice. However, a better understanding of the interaction of biomechanical risk factors, systemic factors and factors related to vascular biology are needed to fully capture the total risk, as visualized in Figure 2.1.

2.5.2 Coronary arteries vs carotid arteries

Geometric features dictate the local haemodynamic environment and thereby plaque initiation and progression, irrespective of the vascular bed. The geometric features the carotid and coronary bifurcations have in common, which influence low shear stress, is tortuosity (Bijari et al., 2012; Malvè et al., 2015). At the level of the bifurcation, marked differences are present: a larger area ratio was clearly associated with low disturbed shear stress for the carotid (Bijari et al., 2012), but not for coronary bifurcation (Malvè et al., 2015) owing to the dominant influence of the carotid bulb, which is unique to the carotid bifurcation. Geometric features predominantly associated with plaque in the coronary arteries were planarity and large bifurcation angle. The carotid bifurcation, on the other hand, is largely planar (Thomas et al., 2005), while the influence of bifurcation angle on haemodynamics is negated by the competing influences of area ratio and tortuosity (Zhang et al., 2010).

Identical twins studies have underlined the 'haemodynamic hypothesis' by showing plaque at similar locations even in pairs with different coronary risk profiles (Gullu et al., 2007). In twin pairs with similar anatomy the location of plaque was most often in concordance contrasting the twin pairs of which the anatomy was not in concordance (Nathoe et al., 2002). These observations highlight again the importance of geometry and thus hemodynamics in addition to genetic and systemic risk factors in the generation of plaques.

Finally, while the focus of this review paper was on wall shear stress and the haemodynamic hypothesis, it is worth making brief mention of mass transport, because it would appear that the transport of species (e.g., lipid-carrying macromolecules), their uptake into the arterial wall, as well as the adhesion of bioactive substances, can be strongly influenced by the fluid phase (Dull and Davies, 1991; Tarbell, 2003; Coppola and Caro, 2008). These observations on the existence of a mechanism involving arterial wall lipid metabolism and shear-dependent blood-wall mass transport, paralleled by the acknowledgment that blood-wall transport occurs by different routes (Tarbell, 2003), have led to the formation of the 'mass transport hypothesis', which is thought to partially underlie or at least complement the haemodynamic hypothesis.

2.5.3 Conclusions

Disturbed haemodynamics, in particular low and oscillatory shear stress, is recognized as one of the most important determinant in plaque initiation and progression. In particular, arterial bifurcations can be markedly exposed to disturbed shear and thereby affected by local plaque formation, which reflects a complex interplay among the triad of haemo-

dynamics, biological and systemic risk factors. Simply using geometrical factors or intravascular flow features might give a first indication on risk of plaque, but the interplay with biological and systemic risk factors should be taken into consideration.

ATHEROPROTECTIVE NATURE OF HELICAL FLOW

ABSTRACT

Arterial hemodynamics is markedly characterized by the presence of helical flow patterns. Previous observations suggest that arterial helical blood flow is of physiological significance, and that its quantitative analysis holds promise for clinical applications. In particular, it has been reported that distinguishable helical flow patterns are potentially atheroprotective in the carotid bifurcation as they suppress flow disturbances. In this context, there is a knowledge gap about the physiological significance of helical flow in coronary arteries, a prominent site of atherosclerotic plaque formation. This study aimed at the quantitative assessment of helical blood flow in coronary arteries, and to investigate its possible associations with vascular geometry and with atherogenic wall shear stress (WSS) phenotypes in a representative sample of 30 swine coronary arteries. This study demonstrates that in coronary arteries: (1) the hemodynamics is characterized by counter-rotating bi-helical flow structures; (2) unfavorable conditions of WSS are strongly and inversely associated with helicity intensity ($r = -0.91$; $p < 0.001$), suggesting an atheroprotective role for helical flow in the coronary tree; (3) vascular torsion dictates helical flow features ($r = 0.64$; $p < 0.001$). The findings of this work support future studies on the role of helical flow in atherogenesis in coronary arteries.

3.1 Introduction

Early observations (Frazin et al., 1990; Karino, 1986; Ku and Giddens, 1987; Sabbah et al., 1984) using in vitro models suggested that arterial hemodynamics is markedly characterized by the presence of helical flow patterns. These in vitro data were confirmed in vivo using several different imaging modalities (as summarized in Table 3.1). As an example, a recent study using Color Duplex scanning observed in a cohort of 42 healthy volunteers that: (1) helical flow was present in 90% of the cases in the common carotid artery and the infrarenal aorta, and in 81% of the cases in the internal carotid artery; (2) 97% of the subjects had more sites with helical flow (Stonebridge et al., 2016). Furthermore, phase contrast magnetic resonance imaging (MRI) has allowed to highlight that the aortic hemodynamics is markedly characterized by the presence of helical flow patterns (Table 3.1). All those observations suggest that helical flow in arteries has a physiological significance, and that its quantitative analysis holds promise for clinical applications (Liu et al., 2015).

Table 3.1: *In vivo observations of helical blood flow patterns in arteries, using several imaging modalities*

Arterial Segment	Imaging Technique	Reference
Aorta		
Thoracic Aorta	Color Doppler Ultrasound	Frazin et al. (1990)
Thoracic Aorta	4D phase contrast MRI	Kilner et al. (1993)
Thoracic Aorta	4D phase contrast MRI	Bogren and Buonocore (1994)
Thoracic Aorta	4D phase contrast MRI	Bogren et al. (1997)
Thoracic Aorta	4D phase contrast MRI	Houston et al. (2003)
Thoracic Aorta	4D phase contrast MRI	Bogren et al. (2004)
Supra-renal Aorta	MR Angiography	Houston et al. (2004)
Thoracic Aorta	4D phase contrast MRI	Markl et al. (2004)
Thoracic Aorta	4D phase contrast MRI	Hope and Herfkens (2008)
Thoracic Aorta	4D phase contrast MRI	Morbiducci et al. (2009)
Ascending Aorta	4D phase contrast MRI	Hope et al. (2011)
Thoracic Aorta	4D phase contrast MRI	Morbiducci et al. (2011)
Thoracic Aorta	4D phase contrast MRI	Bürk et al. (2012)

Table 3.1 – continued from previous page

Arterial Segment	Imaging Technique	Reference
Thoracic Aorta	4D phase contrast MRI	Frydrychowicz et al. (2012)
Thoracic Aorta	4D phase contrast MRI	Geiger et al. (2012)
Thoracic Aorta	4D phase contrast MRI	Sigfridsson et al. (2012)
Ascending Aorta	Doppler Ultrasound	Hansen et al. (2016)
Infra-renal Aorta	Color Duplex Scanning	Stonebridge et al. (2016)
Thoracic Aorta	4D phase contrast MRI	Arnold et al. (2017)
Thoracic Aorta	4D phase contrast MRI	Garcia et al. (2017)
	Carotid arteries	
Carotid bifurcation	Ultrasound Duplex Scanning	Ku et al. (1985)
Internal Carotid artery	4D phase contrast MRI	Bammer et al. (2007)
Internal Carotid artery	4D phase contrast MRI	Wetzel et al. (2007)
Internal Carotid artery	4D phase contrast MRI	Markl et al. (2010)
Common Carotid artery	4D phase contrast MRI	Knobloch et al. (2013)
External Carotid artery	4D phase contrast MRI	Knobloch et al. (2013)
Internal Carotid artery	4D phase contrast MRI	Knobloch et al. (2013)
Internal Carotid artery	4D phase contrast MRI	Meckel et al. (2013)
Common Carotid artery	Color Duplex Scanning	Stonebridge et al. (2016)
Internal Carotid artery	Color Duplex Scanning	Stonebridge et al. (2016)
	Pulmonary arteries	
Right Pulmonary artery	4D phase contrast MRI	Bogren and Buonocore (1994)
Right Pulmonary artery	4D phase contrast MRI	François et al. (2012)
Main Pulmonary artery	4D phase contrast MRI	Bächler et al. (2013)
Right Pulmonary artery	4D phase contrast MRI	Bächler et al. (2013)
Main Pulmonary artery	4D phase contrast MRI	Schäfer et al. (2017)
Right Pulmonary artery	4D phase contrast MRI	Schäfer et al. (2017)

Table 3.1 – continued from previous page

Arterial Segment	Imaging Technique	Reference
Femoral arteries		
Femoral arteries	Color Doppler Ultrasound	Stonebridge et al. (1996)
Femoral arteries	4D phase contrast MRI	Frydrychowicz et al. (2007)
Femoral arteries	Color Duplex Scanning	Stonebridge et al. (2016)
Iliac arteries		
Iliac arteries	4D phase contrast MRI	Frydrychowicz et al. (2007)
Intracranial arteries		
Basilar artery	4D phase contrast MRI	Bammer et al. (2007)

The acknowledgment of a beneficial nature to helical flow in arteries is consistent with the fundamental role recognized for helicity in the organization/stabilization of both laminar and turbulent flows by the fluid mechanics theory (Moffatt and Tsinober, 1992). In this regard, the onset of helical blood flow has been explained in terms of energy expenditure, i.e., distinguished helical blood flow patterns might be the consequence of an optimization in physiological transport process in the cardiovascular system, assuring an efficient perfusion as a result (Morbiducci et al., 2009, 2011). Furthermore, the forward-directed rotational fluid motion might stabilize blood flow, thereby minimizing flow disturbances and thus surface exposure to low and oscillatory wall shear stress (WSS), a condition which is known to influence endothelial function (Stonebridge et al., 1996) creating a pro-atherogenic environment (Malek et al., 1999). This last consideration motivated the investigation of the existence of a relationship between arterial helical flow and low and oscillatory WSS. For that purpose, in recent years hemodynamic indicators were introduced to enable the quantitative analysis of helical blood flow patterns in arteries (Morbiducci et al., 2007). Findings in the human carotid bifurcation (Gallo et al., 2015, 2012) and in the human aorta (Morbiducci et al., 2013) showed that a high helical flow intensity suppresses flow disturbances, and thereby is potentially protective for atherosclerotic plaque build-up. Moreover, numerical studies suggested that helical flow influences transport and transfer of atherogenic particles to the vessel wall, ultimately contributing to the distribution of atherosclerotic plaques at the luminal surface (Liu et al., 2010, 2009).

Until now, there is paucity of studies on the nature of helical blood flow patterns in coronary arteries. In this study we (1) assess the quantitative amount of helical blood flow, and (2) investigate if correlations exist among helical flow, vascular geometry and descriptors of disturbed shear stress in a representative sample of swine-specific computational hemodynamic models of coronary arteries. The study aims at bridging the gap of knowledge still existing on the atheroprotective nature of helical flow in coronary arteries (Morbiducci et al., 2016).

3.2 Materials and Methods

3.2.1 Animal Population and Imaging

Ten adult familial hypercholesterolemia Bretoncelles Meishan mini-pigs with a low-density lipoprotein receptor mutation were fed a high fat diet. For each animal model, the right (RCA), the left anterior descending (LAD), and the left circumflex (LCX) coronary artery were imaged at baseline using computed coronary tomography angiography (CCTA) and intravascular ultrasound (IVUS), as described in chapter 6. In each artery, blood flow velocity was measured at several locations with the ComboWire (Volcano Corp., Rancho Cardova, CA, USA).

Ethical approval was obtained to perform the pig study (EMC nr. 109-14-10) and the study was performed according to the National Institute of Health guide for the Care and Use of Laboratory animals.

3.2.2 Geometry Reconstruction

The scheme applied for coronary arteries models reconstruction is summarized in Figure 3.1. Technical details are presented in chapter 5. In short, IVUS images were segmented into lumen contours and stacked upon the 3D CCTA centerline. Additional luminal regions proximal to the IVUS segment up to the aorta and at least two diameters distal to the IVUS-based models were segmented using the CCTA images (Schaap et al., 2009).

3.2.3 Morphometric Descriptors

The vessel centerlines were extracted as the geometrical locus of the centers of the maximum inscribed spheres in the model, as given by the Vascular Modelling Toolkit software (VMTK, Orobix, Bergamo, Italy). Free-knots regression splines were then adopted (Sangalli et al., 2009) as a basis of representation for a vessel centerline to provide a
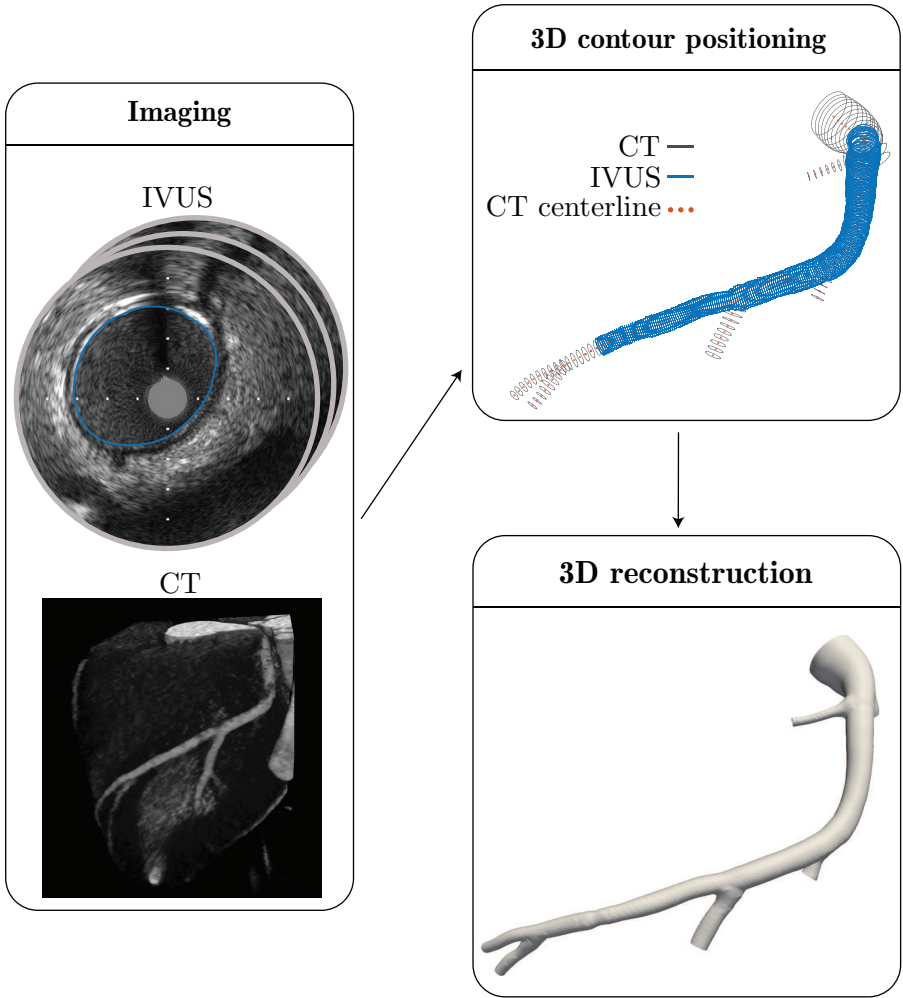
Figure 3.1: *Scheme applied for swine coronary artery geometries reconstruction for CT and IVUS images.*

continuous, noise free analytical formulation **C** with continuous derivatives. By differentiation of the free-knots regression, spline centerline representation **C**, curvature and torsion were calculated. To measure the rate of change in the tangent vector orientation along the curve the local curvature κ was determined. Local curvature κ is defined as the reciprocal of the radius of the circle lying on the osculating plane (identified by the normal and tangent vectors to the curve at that point (Equation 3.1). Local torsion τ measures the deviation of curve **C** from the osculating plane (Equation 3.2). Technically, the curvature κ and torsion τ of a centerline curve **C** along the curvilinear abscissa s were defined as:

$$\kappa(s) = \frac{|\mathbf{C}'(s) \times \mathbf{C}''(s)|}{\mathbf{C}'^3} \tag{3.1}$$

$$\tau(s) = \frac{|\mathbf{C}'(s) \times \mathbf{C}''(s)| \cdot \mathbf{C}'''(s)}{|\mathbf{C}'(s) \times \mathbf{C}''(s)|^2} \tag{3.2}$$

where $\mathbf{C}'(s)$, $\mathbf{C}''(s)$ and $\mathbf{C}'''(s)$ are the first, second and third derivative of curve **C**, respectively. In this study, the average values of curvature ($\bar{\kappa}$) and torsion ($\bar{\tau}$) along the vessel were considered, due to the known influence on arterial hemodynamics (Alastruey et al., 2012).

3.2.4 Computational Hemodynamics

The governing equations of fluid motion, the Navier-Stokes equations, were numerically solved in their discrete form by applying the finite volume method. The adopted discretization schemes are detailed in chapter 5. Blood was assumed as an incompressible, homogeneous fluid with density ρ equal to 1060 kg/m^3, and its non-Newtonian behavior was modeled assuming it as a Carreau fluid (Chiastra et al., 2017; Vorobtsova et al., 2016). Arterial walls were assumed to be rigid with no-slip condition. The derivation of boundary conditions from in vivo Doppler velocity measurements adopted here represents an accurate method to obtain personalized coronary artery computational models (Siebes et al., 2004). Technically, in each artery the instantaneous maximum blood flow velocity was measured at several locations upstream and downstream of each side branch with the ComboWire. At each measurement site, maximum velocity data were used to estimate the flow rate as proposed elsewhere (Ponzini et al., 2006). As condition at the inflow boundary, the most proximal measurement-based flow rate value was prescribed in terms of time-dependent flat velocity profile. At each side branch a flow ratio was applied as outflow boundary, based on difference between upstream and downstream

velocity-based flow rate measurements. In those vessel segments where velocity measurements were inaccurate or not available, the Huo-Kassab diameter-based scaling law (Huo and Kassab, 2012) was used to estimate the flow ratio to be prescribed.

3.2.5 Hemodynamic Descriptors

Helical flow in the 30 coronary artery models was characterized in terms of strength, size and relative rotational direction by applying different helicity-based descriptors, listed in Table 3.2. In detail, cycle-average helicity (h_1) and helicity intensity (h_2), signed (h_3) and unsigned helical rotation balance (h_4) were calculated as reported elsewhere (Gallo et al., 2012). Average helicity descriptors h_1 and h_2 indicate the net amount and the intensity of helical flow, respectively, while the helical rotation balance descriptors measure the prevalence (identified by the sign of descriptor h_3) or only the strength (h_4) of relative rotations of helical flow structures.

Table 3.2: *Definition of helicity-based intravascular hemodynamic descriptors.*

Average Helicity (h_1)	$h_1 = \dfrac{1}{TV} \int_T \int_V \boldsymbol{v} \cdot \boldsymbol{\omega} \, dV \, dt$
Average Helicity intensity (h_2)	$h_1 = \dfrac{1}{TV} \int_T \int_V \lvert \boldsymbol{v} \cdot \boldsymbol{\omega} \rvert \, dV \, dt$
Signed balance of counter-rotating helical flow structures (h_3)	$h_3 = \dfrac{h_1}{h_2} \quad -1 \leq h_3 \leq 1$
Unsigned balance of counter-rotating helical flow structures (h_4)	$h_4 = \dfrac{\lvert h_1 \rvert}{h_2} \quad 0 \leq h_4 \leq 1$

[*] $\boldsymbol{v}$ is the velocity vector; $\boldsymbol{\omega}$ is the vorticity vector; T is the period of the cardiac cycle; V is the arterial volume.

The luminal distribution of three 'established' WSS-based descriptors, namely time-averaged wall shear stress (TAWSS), oscillatory shear index (OSI) (Ku et al., 1985), and relative residence time (RRT) (Himburg et al., 2004) was computed (Appendix A). Two 'emerging' descriptors of WSS multidirectionality were also considered. The first is the transversal WSS (transWSS) (Peiffer et al., 2013b), defined as the average WSS component acting orthogonal to the time-averaged WSS vector direction, and the second is its normalized version, the Cross Flow Index (CFI) (Mohamied et al., 2017) (Appendix A). As in previous studies, (Gallo et al., 2012, 2016), data from all simulations were pooled

to define objective thresholds for 'disturbed shear stress'. From combined data, the lower tertile (i.e., the 33th percentile) for TAWSS, and the upper tertile (i.e., the 66th percentile) for OSI, RRT, transWSS, and CFI were identified. For each model, the percentage of surface area (SA) exposed to OSI, RRT, transWSS, and CFI values belonging to the upper (TAWSS lower) tertile was quantified. These areas were denoted as OSI66, RRT66, transWSS66, CFI66, and TAWSS33, respectively. Intravascular flow was investigated in terms of helical flow amount and topology.

The quantitative analysis, based on the hemodynamic descriptors in Table 3.2 and (Appendix A), was substantiated by visualizations of near-wall and intravascular quantities. The normalized internal product between local velocity and vorticity vectors Table 3.3, labeled as local normalized helicity (LNH), (Morbiducci et al., 2007) was used to visualize helical blood flow inside the coronary segments. The LNH allows to visualize left- and right-handed fluid structures in arteries (Gallo et al., 2012; Morbiducci et al., 2013) and isosurfaces of cycle average LNH values were used throughout the manuscript. Moreover, two more descriptors visualizing WSS multidirectionality were evaluated considering the cycle-average values of the projections of WSS vector respectively along (1) the 'axial direction' (WSS_{ax}), identified as the direction of the tangent to the vessel's centerline, and (2) the secondary direction (WSS_{sc}), orthogonal to the axial direction and related to secondary flow Table 3.3 (Morbiducci et al., 2015).

Table 3.3: *Definition of local normalized helicity (LNH), and of the projections of WSS vector respectively along (1) the 'axial direction' WSS_{ax}, identified as the direction of the tangent to the vessel's centerline, and (2) the secondary direction WSS_{sc}, orthogonal to the axial direction and related to secondary flow.*

Local Normalized Helicity (LNH)	$LNH = \dfrac{v \cdot \omega}{|v| \cdot |\omega|} = \cos\gamma$
Axial WSS (WSS_{ax})	$WSS_{ax} = \dfrac{WSS \cdot C'}{|C'|} \dfrac{C'}{|C'|}$
Secondary WSS (WSS_{sc})	$WSS_{sc} = \dfrac{WSS \cdot S}{|S|} \dfrac{S}{|S|}; \ S = \dfrac{C' \times R}{|C'||R|}$

[*] LNH,WSS_{ax}, and WSS_{sc} are used here for visualization purposes. v is the velocity vector; ω is the vorticity vector; γ is the angle between the velocity and vorticity; WSS is the WSS vector; C' is the vector tangent to the centerline curve C at curvilinear abscissas; R is the vector directed from the generic point at the arterial surface, lying on the vessel's cross section identified by C' at curvilinear abscissa s, and the point of application of C'.

3.2.6 Statistical analysis

Bivariate correlations among WSS-based, helicity-based and geometric descriptors were determined in Matlab environment (The MathWorks Inc., USA) by using Spearman rank ordering. Regression analysis was used to identify relationships between each pair of descriptors and reported as Spearman correlation coefficients. Significance was assumed for $p < 0.05$.

3.3 Results

The 30 reconstructed luminal surfaces of the coronary arteries (10 RCA, 10 LAD, and 10 LCX) are presented in Figure 3.2. Computational hemodynamics was performed on all models including the side branches. However, data analysis was performed in the main branch of the RCA, LAD and LCX segments only. To do that, in the post-processing step side branches were removed using the open-source Vascular Modeling Toolkit (VMTK, http://www.vmtk.org/).

Figure 3.2: *Geometry of the 30 swine coronary artery models. Labels from A to J identify the single swine model. For each swine, LAD, LCX and RCA geometries were reconstructed.*

Helical blood flow patterns were visualized using the isosurface of cycle-average LNH,

with blue and red colors indicating left-handed and right-handed helical flow rotation, respectively Figure 3.3. Notably, all 30 coronary artery models presented two distinguishable counter-rotating helical flow structures. It can be also appreciated that: (1) in most of the cases, counter-rotating cycle-average helical flow structures are distributed all along the length of the artery; (2) despite inter-individual variations, no marked differences among the coronary artery types is present.
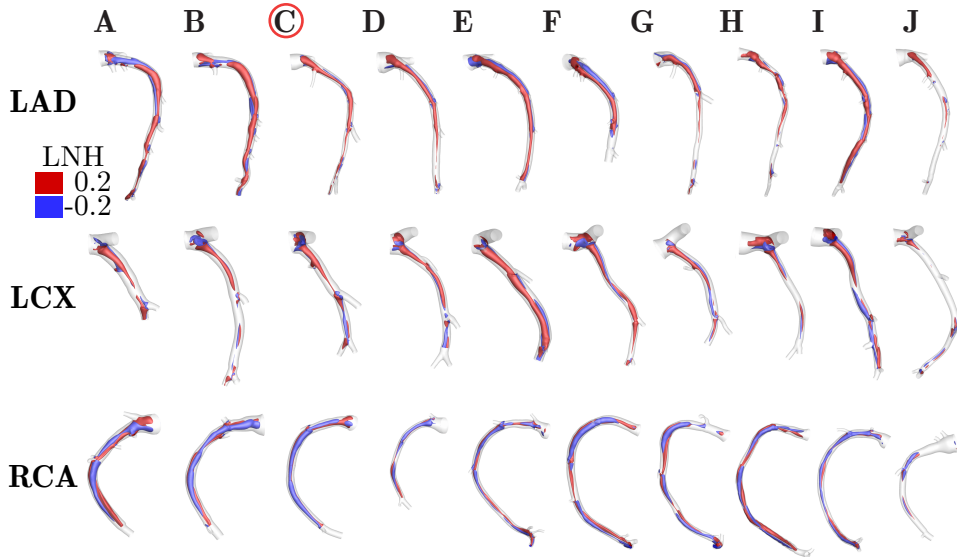
Figure 3.3: Intravascular fluid structures in the 30 coronary arteries. For each case, isosurfaces of cycle-average LNH (LNH= ± 0.2) are presented. Distinguishable left-handed (LNH<0) and right-handed (LNH>0) helical flow structures can be observed in all coronary arteries. Labels from A to J identify the single swine model. For each swine, LAD, LCX and RCA geometries were reconstructed.

Figure 3.4 shows for 3 different types of coronary arteries from animal model C (see Figure 3.2) the visualizations of the LNH cycle-average isosurfaces, and the maps of the cycle-average secondary (WSS_{sc}) and axial (WSS_{ax}) WSS vector projections. As for LNH, also for the WSS_{sc} blue and red colors identify the left and right-handed direction, respectively. For WSS_{ax} the blue and red colors identify the backward and forward flow direction, respectively. Interestingly for the LAD and RCA there was a clear match between LNH and WSS_{sc} direction of rotation, however for the LCX this was less evident. Furthermore, Figure 3.4 shows that WSS_{ax} is mainly positive, meaning that the WSS

vector is predominantly aligned with the forward flow direction. The results presented in Figure 3.5 suggests that the bi-helical arrangement of intravascular blood flow delineates the near-wall hemodynamics of coronary arteries.
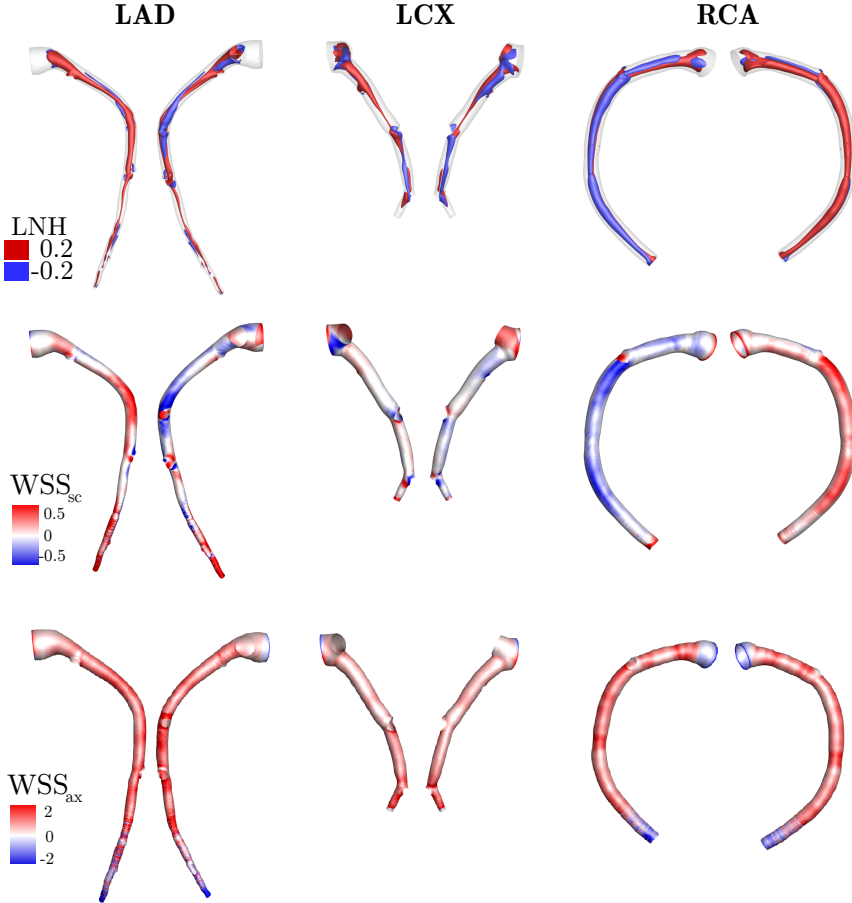
Figure 3.4: *Visualization of LNH cycle-average isosurfaces, and of maps of cycle-average secondary (**WSS$_{sc}$**) and axial (**WSS$_{ax}$**) WSS vector projections for the three different types of coronary arteries (LAD, LCX, RCA) from the representative animal model C (see Figure 3.2). As for LNH, also for the **WSS$_{sc}$** blue and red colors identify the left and right-handed direction, respectively. For **WSS$_{ax}$** the red and blue colors identify the forward and backward flow direction, respectively.*
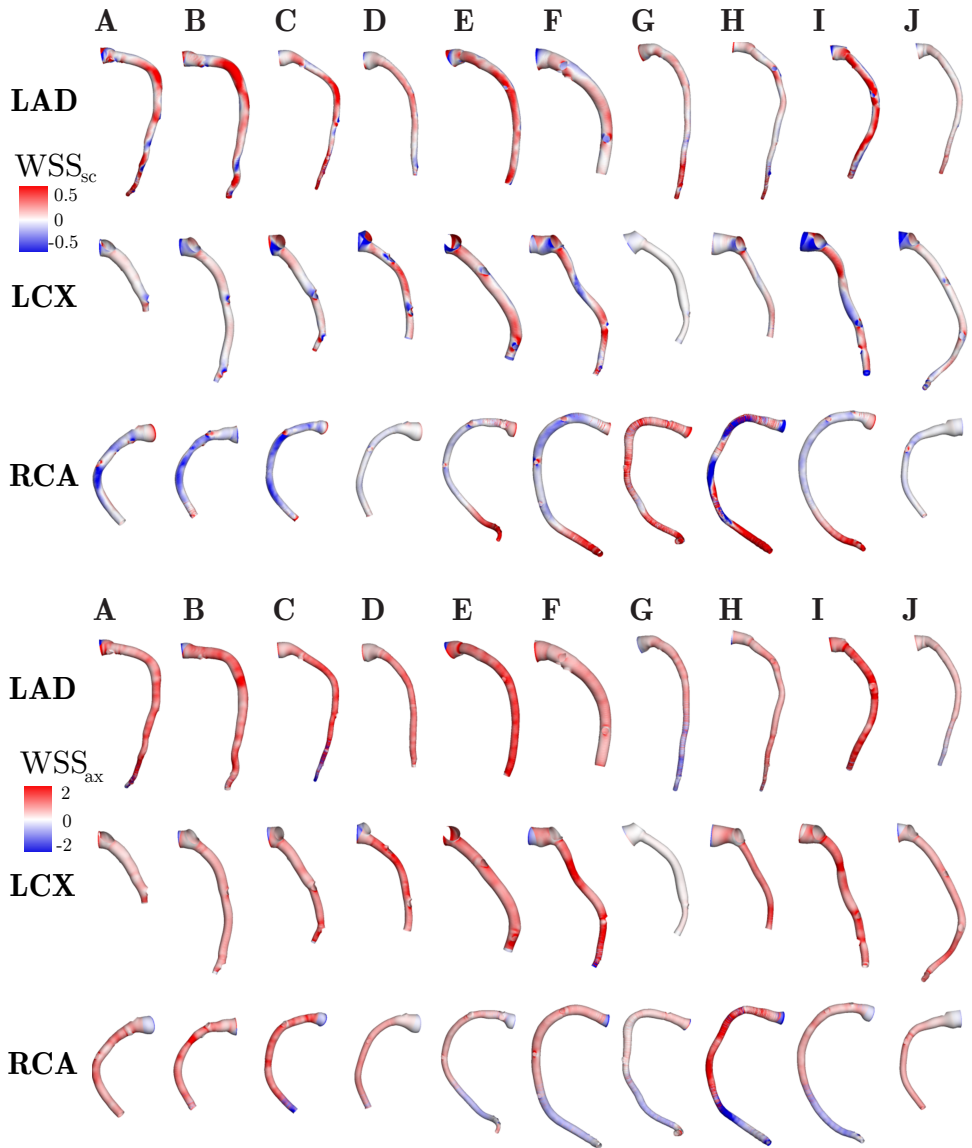
Figure 3.5: *Maps of cycle-average secondary (**WSSsc**) and axial (**WSSax**) WSS vector projections for the 30 coronary arteries. **WSSsc** blue and red colors identify the left and right-handed direction, respectively. For **WSSax** the red and blue colors identify the forward and backward flow direction, respectively.*
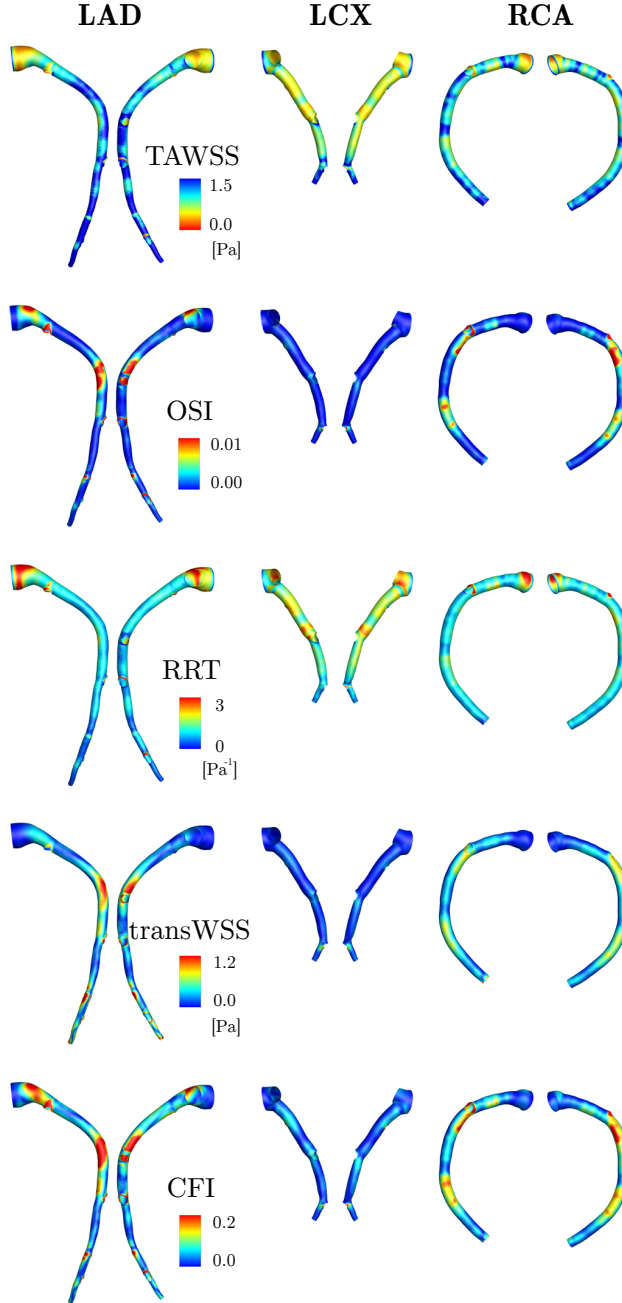
Figure 3.6: *WSS-based descriptors distribution at the luminal surface of the three different types of coronary arteries (LAD, LCX, RCA) from the representative animal model C (Figure 3.2). Red color highlights those areas exposed to low TAWSS, and high OSI, RRT, transWSS and CFI. The very low values of OSI, transWSS and CFI at the luminal surface suggest that WSS is scarcely multidirectional.*

To complete the intra-individual analysis of representative animal model C, also the luminal distribution of the other computed WSS-based descriptors were presented in Figure 3.6. Notably, OSI, transWSS and CFI values at the luminal surface were low, suggesting that WSS is scarcely multidirectional in the three different types of coronary arteries of animal C. Figure 3.6 highlights that the location of the low WSS regions in the coronary arteries was more focal in the LAD and RCA, but less in the LCX. Moreover, TAWSS and RRT showed a similar distribution, independent of coronary artery type, which was also the case for CFI and transWSS.

Table 3.4: *Correlation coefficients for percentage luminal surface areas expose to disturbed shear and helicity-based descriptors and for hemodynamic descriptors vs. geometry (average curvature(κ) and torsion(τ)).*

	h_1	h_2	h_3	h_4
%*TAWSS*33	**-0.48†**	**-0.91‡**	-0.05	-0.01
%*OSI*66	**-0.50†**	**-0.58‡**	**-0.39***	0.32
%*RRT*66	**-0.49***	**-0.90‡**	-0.02	-0.01
%*transWSS*66	**0.49†**	**0.86‡**	0.13	0.13
%*CFI*66	**0.47†**	**0.51†**	0.34	0.30
$\bar{\kappa}$	-0.12	-0.22	-0.01	0.11
$\bar{\tau}$	**-0.49†**	0.09	**0.64‡**	**0.39***

[*] Statistically significant values are in bold. [*]$P_{value} < 0.05$; [$\dagger$]$P_{value} < 0.01$; [$\ddagger$]$P_{value} < 0.001$.

Table 3.5: *Correlation coefficients for luminal surface area-averaged values of WSS-based descriptors and helicity-based descriptors.*

	h_1	h_2	h_3	h_4
$\overline{TAWSS}$	**0.54†**	**0.92‡**	0.12	0.05
$\overline{OSI}$	**0.52†**	**0.57†**	**0.38†**	0.31
$\overline{RRT}$	**-0.53†**	**-0.90‡**	-0.12	-0.07
$\overline{transWSS}$	**0.52†**	**0.86‡**	0.14	0.17
$\overline{CFI}$	**0.51†**	**0.54‡**	0.36	0.32

[*] Statistically significant values are in bold. [*]$P_{value} < 0.05$; [$\dagger$]$P_{value} < 0.01$; [$\ddagger$]$P_{value} < 0.001$
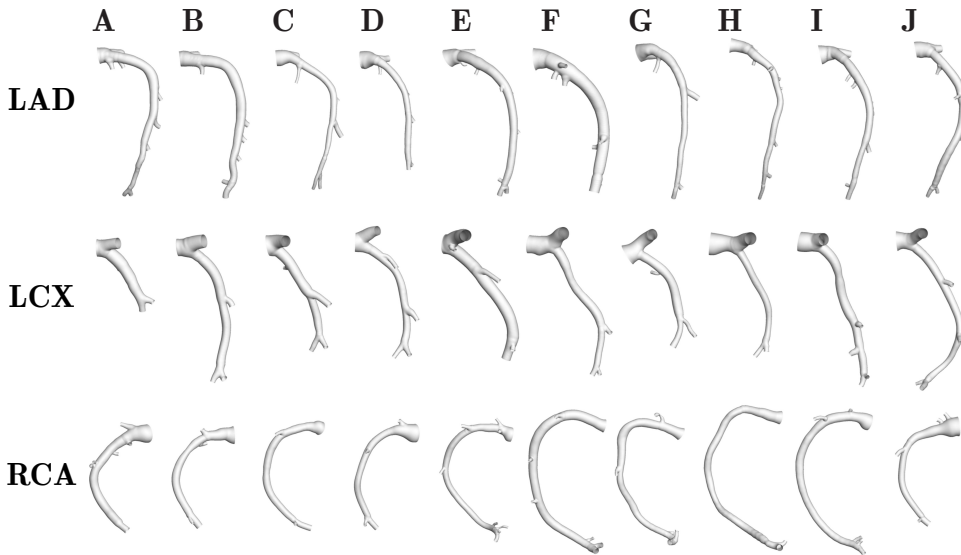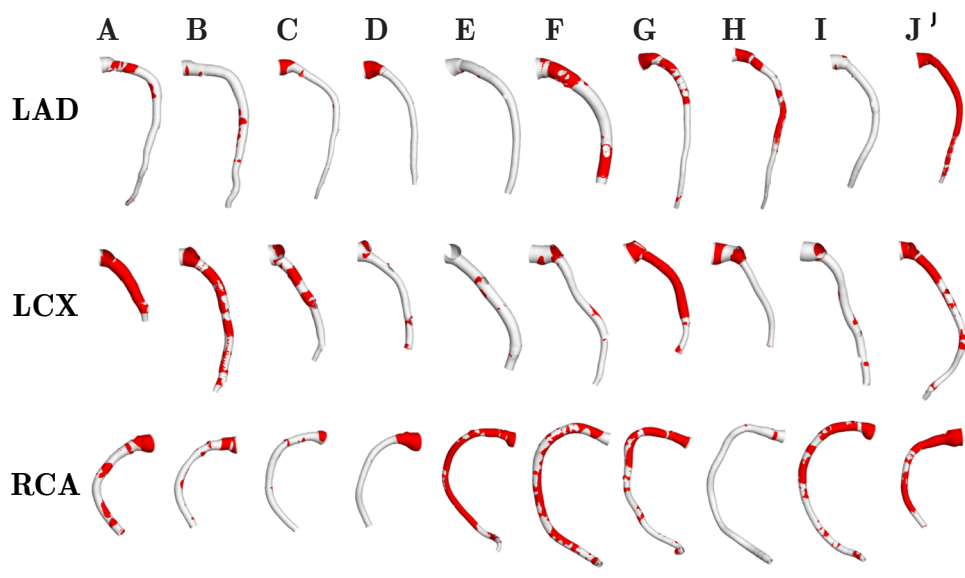
Figure 3.7: *Surface areas of the 30 swine coronary artery models exposed to TAWSS33. Labels from A to J identify the single swine model. For each swine, LAD, LCX and RCA geometries were reconstructed. Contour levels for TAWSS33 correspond to lowest tertile value of TAWSS distribution on the combined surface of all models.*
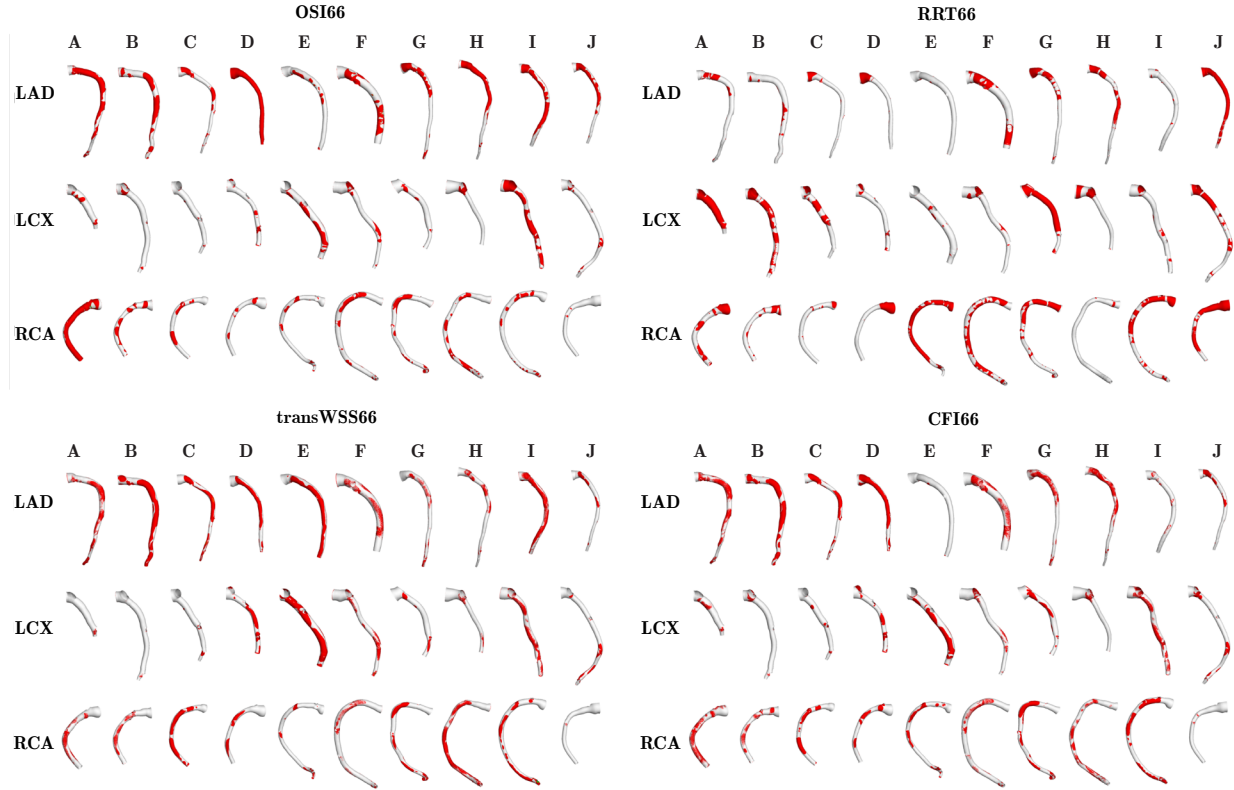
Figure 3.8: *Surface areas of the 30 swine coronary artery models exposed to OSI66 (top-left panel), RRT66 (right-left panel), transWSS66 (bottom-left panel) and CFI66 (bottom-right panel). Labels from A to J identify the single swine model. For each swine, LAD, LCX and RCA geometries were reconstructed. Contour levels for OSI66, RRT66, transWSS66, and CFI6 correspond to highest tertile value of OSI, RRT, transWSS, and CFI, distribution on the combined surface of all models, respectively.*

The visualization of SAs exposed to low WSS (TAWSS33) highlights wide inter-individual variations (Figure 3.7). In some cases the luminal surface is largely exposed to low WSS (e.g., case J-LDA, case G-LCX, case E-RCA) whereas other arteries are hardly exposed (e.g., case I-LDA, case H-RCA). The distribution of SAs exposed to OSI66, RRT66, transWSS66, CFI66 for all the 30 coronary artery models is presented in Figure 3.8.

The correlation coefficients between each possible couple of disturbed shear stress and geometry descriptors are summarized in Table 3-6. The WSS-based percentage SAs (exposed to) were significantly correlated to each other, with the sole exception of OSI66 and RRT66.

Table 3.6: *Correlation coefficients between each possible couple of disturbed shear stress parameters (% surface area exposed) and geometry (average curvature and torsion) descriptors.*

	%OSI66	%RRT66	%transWSS66	%CFI66	$\bar{\kappa}$	$\bar{\tau}$
%TAWSS66	**−0.37***	**1.00‡**	**−0.84***	**−0.39***	0.12	0.12
	%OSI66	0.34	**0.59‡**	**0.81‡**	-0.28	0.18
		%RRT66	**−0.83‡**	**−0.37***	0.13	0.14
			%transWSS66	**0.74‡**	**−0.37***	-0.5
				%CFI66	**−0.49***	0.13
					$\bar{\kappa}$	0.13

* Statistically significant values are in bold. $^{*}P_{value} < 0.05$; $^{†}P_{value} < 0.01$; $^{‡}P_{value} < 0.001$.

In this study, RRT66 was considered to be equivalent to TAWSS33. This consideration was based on the strong association that emerged between RRT66 and TAWSS33 (Table 3.6), suggesting that RRT was markedly biased by TAWSS. The definition of RRT as a combination of OSI and TAWSS (Appendix A), and the very low OSI values characterizing the investigated coronary arteries (Figure 3.8), support the observation that RRT66 is a replica of TAWSS33, in the coronary arteries investigated.

As a consequence of the low transWSS values characterizing the hemodynamics of the investigated coronary arteries, and by construction, a significant association emerged between transWSS66 and CFI66 (r=0.74, p<0.001). Interestingly, also a significant association was observed for OSI66 with transWSS66 (r=0.59, p<0.001) and CFI66 (r=-0.81, p<0.001).

Furthermore our data showed that larger SAs exposed to low WSS corresponded to

smaller SAs exposed to multidirectional WSS, as confirmed by the moderate negative associations of TAWSS33 with OSI66 (r=-0.37, p<0.05), transWSS66 (r=-0.84, p<0.05), and CFI66 (r=-0.39, p<0.05).

Low and oscillatory WSS areas were neither correlated to curvature nor torsion of the artery (Table 3.6. Since transWSS66 (r=-0.37, p<0.05) and CFI66 (r=-0.49, p<0.05) were negatively associated with curvature, our data suggest that curvature in coronary arteries serves to suppress WSS multi-directionality.

Regression analysis revealed significant associations between helicity-based vs. WSS-based descriptors (Table 3.4). Notably, h_2 was strongly and negatively associated with TAWSS33 (r=-0.91, p<0.001), indicating that the higher the h_2 is, the lower the SA of an individual coronary artery exposed to low WSS.

In contrast, positive regression coefficients were found for the significant associations of h_2 with OSI66, CFI66 and transWSS66 (Table 3.4). For clarity, it must be reported here that the threshold values (66th percentile) identified for OSI (0.002), CFI (0.066) and transWSS (0.039 Pa) are very low in the 30 coronary arteries investigated, suggesting that WSS multidirectionality is not a feature marking out their local hemodynamics (Figure 3.8 and Table 3.5).

Associations similar to h_2, although weaker, were observed for h_1 (Table 3.6). An explanation for this is that overall there is a preferential, even if moderate, cycle-average direction of rotation in the observed bi-helical blood flow patterns establishing in the 30 coronary arteries, as confirmed by the positive sign of average h_3 value and by average h_4 value ($h_4 = 0.112$).

Regarding geometric attributes, Table 3.4 also shows that neither h_1 nor h_2 were associated with curvature. Torsion was found to be positively correlated with helicity h_1 (r=0.49, p<0.01), with signed (h_3) helical rotation balance (r=0.64, p<0.001), and more weakly with its unsigned (h_4) version (r=0.49, p<0.05), suggesting an important role of vascular torsion in promoting helical flow in coronary arteries.

The nature of the association of h_2 with WSS and geometry can be better appreciated in scatter plots reported in Figure 3-10. It emerges that: (1) a non-linear decreasing trend relates h_2 with TAWSS33 (and RRT66 as well), i.e., the percentage SA exposed to low WSS; (2) an almost (positive) linear trend describes the observed association of h_2 with transWSS66; (3) trends in the observed associations are not specific for the different types of coronary arteries.

The observed associations between helicity-based descriptors and percentage of luminal
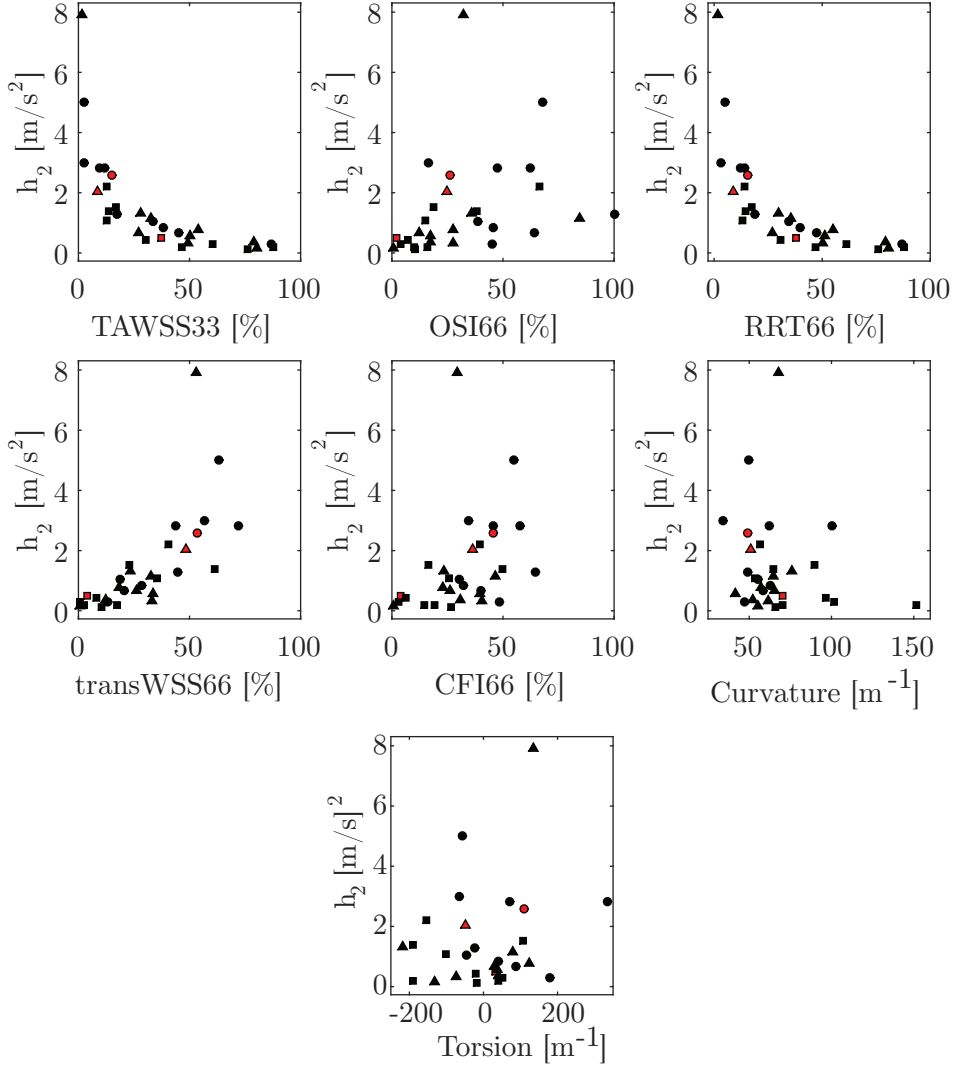
Figure 3.9: *Scatter plots of helicity intensity h2 vs. WSS-based descriptors, and aver-age curvature and values. Red color indicate case C (Figure 3.2), used as representa-tive example in Figure 3.6 and Figure 3.7.*

SAs that, based on thresholds, are subjected to more 'disturbed shear stress' (Table 3.4), are confirmed when considering luminal surface area-averaged values of the WSS-based descriptors (Table 3.5).

3.4   Discussion

In the last decade quantitative approaches have started to be massively applied to investigate the physiological significance of arterial helical flow. However, despite the qualitatively description of a relationship between helical flow and atheroma formation in coronary arteries, (Sabbah et al., 1984) only recently a patient-specific computational study on a small dataset (N=3) has suggested a link between helical flow and WSS in human coronary artery segments (Vorobtsova et al., 2016).

Here the existence of correlations among helical flow, vascular geometry and disturbed shear stress was explored in a representative dataset of 30 swine-specific models of coronary arteries. Among the main findings, it is reported for the first time that distinguishable counter-rotating helical flow patterns were present in all the models under investigation. This suggests that helical flow arrangement is a feature characterizing physiological intravascular hemodynamics in coronary arteries (Figure 3.3). Such arrangement in helical structures characterized by high helicity intensity (h_2) stabilizes blood flow imparting low WSS multidirectionality and minimizing the luminal surface exposed to low WSS, thus indicating that helical flow is instrumental in suppressing flow disturbances in coronary arteries. More in detail, since the rotating direction of helical flow patterns dictates the luminal distribution of WSS_{sc} (Figure 3.5), it emerges that bi-helical flow patterns could influence endothelial shear stress orientation, in coronary arteries. A preferential direction of rotation of the bi-helical flow structures is promoted by vascular torsion, while vascular curvature moderately suppresses an already scarcely multidirectional WSS (Table 3.6). In fact, very low values of OSI, transWSS and CFI were found (Figure 3.8 and Table 3.5), suggesting a predominant role of low WSS as hemodynamic determinant of plaque formation in coronary arteries. Previous findings support the role of low WSS in promoting endothelial dysfunction, (Chatzizis et al., 2008; Siasos et al., 2018; Stone et al., 2012; Wentzel et al., 2012) although the influence of multidirectional shear stresses on endothelial function needs to be investigated more in-depth.

In recent years, computational hemodynamics has made a remarkable contribution to highlight the physiological significance of helical blood flow naturally streaming in arteries. In particular, an in silico study on a dataset of 50 models of human carotid bifurcations showed that high helicity intensity is instrumental in suppressing flow distur-

bances, and thereby is potentially atheroprotective (Gallo et al., 2012). These findings were supported by the observation that helical flow production in the common carotid artery, reinforcing helicity in the carotid bifurcation, provides further contribution to reduce the likelihood of flow disturbances (Gallo et al., 2015). Similar findings have been reported using computational fluid dynamics in the healthy aorta, suggesting a key role for helical blood flow in (1) reducing luminal areas exposed to low and oscillatory shear stress,(Morbiducci et al., 2013) and (2) influencing near-wall transfer of atherogenic particles and oxygen (Liu et al., 2010, 2009). Moreover, computational hemodynamics findings showed that helical blood flow could be posture-dependent (Aristokleous et al., 2015). Parallel to basic studies on its physiological significance, the analysis of helical blood flow has been increasingly adopted to better understand how cardiovascular diseases, (Condemi et al., 2017; Pirola et al., 2018; Schäfer et al., 2017) or ageing, (Frydrychowicz et al., 2012) alter the arterial flow physics.

Several limitations could weaken the findings of this study. Among them, the assumption of rigid vascular wall might have affected TAWSS estimation. However, studies applying fluid-structure interaction approaches reported that TAWSS spatial distribution is preserved using rigid walls (Malvè et al., 2012). Moreover, the cardiac-induced motion of coronary arteries was neglected. This idealization was based on previous findings demonstrating that myocardial motion has a minor effect on coronary flow and WSS distribution with respect to the blood pressure pulse (Theodorakakos et al., 2008; Zeng et al., 2003). Moreover, it can markedly affect instantaneous WSS and OSI wall distribution, with minor effects on TAWSS (Torii et al., 2010). Therefore, it is expected to have minor impact on the here reported observations (Morbiducci et al., 2013). The relatively modest number (N=30) of coronary artery models investigated could limit the generality of the study. However, the existence of hemodynamic features which are common to all coronary arteries here clearly emerges as the presence of distinguishable helical blood flow patterns, and low WSS multidirectionality. Finally, here swine, not human models, have been used to characterize helical flow in coronary hemodynamics and to investigate whether a causal relationship between helical flow and shear stress exists. However, the close similarity between the human and pig coronary anatomy, in addition to the wide adoption of swine model in studies of coronary disease over the past decades, (Winkel et al., 2015) support the translation of the findings of this study to human coronary arteries. Moreover, helical flow features similar to the ones observed here were reported in a small number of image-based computational hemodynamic models of human coronary arteries, (Vorobtsova et al., 2016) confirming that swine models are representative of the human coronary circulation.

The findings of this study support the future exploration of the links between the observed helical distribution of fatty and fibrous plaques in coronary artery segments and the hemodynamic factors involved in the local onset and progression of atherosclerosis in the coronary tree. In this sense, the present findings will contribute to answer to the still open questions raised since 60s (Fox et al., 1982; Fox and Seed, 1981; Nakashima et al., 1964; Nakashima and Tashiro, 1968; Sabbah et al., 1984), regarding the observation of irregular spiral distributions of sclerotic bands in coronary arteries.

In conclusion, this study demonstrates that hemodynamics of coronary arteries is characterized by distinguishable and counter-rotating bi-helical flow structures, whose topological features are associated with geometry (in terms of average torsion of the vessel). Remarkably, it emerges that unfavorable conditions of low wall shear stress are strongly and inversely associated with helicity intensity, as already observed in other arterial districts (Gallo et al., 2012).

MULTIDIRECTIONAL SHEAR STRESS IN HUMAN CORONARY ARTERIES

4

ABSTRACT

Local wall shear stress (WSS) plays an important role in the onset of atherosclerotic plaque formation, however it does not fully explain plaque progression and destabilization. We are the first to investigate the influence of multidirectional WSS features on plaque progression and plaque composition changes in human coronary arteries. Coronary artery imaging using biplane angiography and virtual-histology intravascular ultrasound (VH-IVUS) was performed in twenty patients with coronary artery disease at baseline and after six-month follow-up. 3D surfaces of the coronary arteries were generated using the coronary imaging and together with patient-specific flow measurements different WSS features (multidirectional and conventional time-averaged WSS (TAWSS)) were determined at baseline using computational fluid dynamics (CFD). The changes in plaque component area over the six-month period were determined from VH-IVUS. Changes in plaque composition rather than plaque size were primarily associated with the (multidirectional) WSS at baseline. Interestingly, regions simultaneously exposed to low TAWSS and low multidirectional WSS showed the greatest plaque progression (p<0.001). In this patient study, several multidirectional WSS features were found to significantly contribute to coronary plaque progression and changes in plaque composition.

---

[1]Authors contributed equally

67

4.1   Introduction

Atherosclerotic plaques develop in regions exposed to low and oscillatory blood flow in-
duced wall shear stress (WSS) (Pedersen et al., 1999) (Stone et al., 2003). Low WSS
creates a pro-atherogenic environment and is therefore involved in plaque initiation by
stimulating the endothelial expression of pro-inflammatory genes and proteins (Zhou
et al., 2014). Furthermore, WSS is recognized for its role in plaque growth and changes
in plaque composition towards a high-risk vulnerable plaque (Chatzizis et al., 2011;
Samady et al., 2011; Vergallo et al., 2014).

However, the magnitude of WSS is insufficient to fully predict plaque growth or plaque
compositional changes (Stone et al., 2012). Multidirectional WSS is a measure for
change in the direction of the shear stress during the cardiac cycle. Therefore, Peiffer
et al. suggested that multidirectional WSS may be also important in lesion development
(Peiffer et al., 2013b). From the biological point of view, multidirectional WSS affects
the endothelial cell morphology and function. Upon exposure to laminar flow, the en-
dothelial cells align with the favorable main flow/WSS direction, which is related to the
induction of atheroprotective signaling pathways. In contrast, multidirectional WSS can
cause cell inability to align, which in turn is associated with induction of inflammatory
pathways (Baeyens et al., 2014; Wang et al., 2013).

Transverse WSS (transWSS), a new multidirectional WSS metric, may be important in
atherosclerosis development. TransWSS is the WSS magnitude perpendicular to the main
flow direction (Peiffer et al., 2013b). Regions with high transWSS co-localized with lipid
deposition in rabbits (Peiffer et al., 2013b), but its effect on plaque progression and plaque
composition changes is unknown. The same holds for the normalized transWSS: cross-
flow index (CFI) (Mohamied et al., 2017) and other well-known multidirectional WSS
metrics: oscillatory shear index (OSI) and relative residence time (RRT) (Himburg et al.,
2004).

To the best of our knowledge this is the first study to investigate the clinical relevance of
transWSS and other multidirectional WSS metrics on progression and destabilization of
atherosclerosis in human coronary arteries in a longitudinal study.

4.2 Methods

4.2.1 Subjects

From December 2007 to January 2009, twenty patients presented to the catheterization laboratory at Emory University Hospital with either an abnormal noninvasive stress test or stable angina syndrome. An invasive physiological evaluation of a non-obstructive lesion was performed. All patients received optimal medical therapy including 80 mg atorvastatin daily. The inclusion and exclusion criteria were previously described (Samady et al., 2011). After six months, a repeat catheterization was performed to assess changes in plaque morphology. In each patient the most proximal part of the left anterior descending (LAD) artery was investigated. The study complied with the Declaration of Helsinki and was approved by the Emory University Institutional Review Board. Each patient provided written informed consent.

4.2.2 Imaging acquisition & Reconstruction

The left coronary arteries were visualized using biplane angiography (Philips Medical Systems, Andover, USA). From these images, back projection image analysis (Qangio XA 3D RE, Medis, Leiden, NL) was used to determine the catheter path. Doppler derived velocity measurements were performed in the left main coronary artery using the ComboWire (Volcano, Corporation, Rancho Cordova, USA). To obtain detailed lumen and vessel wall composition information, virtual-histology intravascular imaging (VH-IVUS) was performed using an Eagle Eye Gold Catheter (phased-array 20 MHz Eagle Eye® Gold Catheter, Volcano Corp., Rancho Cordova, USA), see Figure 4.1. The pullback speed was 0.5 mm·s^{-1}, ECG-gating was performed at the peak of the r-wave. The VH-IVUS pullback length was at least 60 mm and contained at least two side branches, which were later used as landmarks for the 3D geometry reconstruction. In some cases a shorter region was imaged and in several cases 3D reconstruction of the full 60 mm was not possible due to severe vessel overlapping in the angiography images. Based on fusion information from the different imaging modalities, the left coronary artery was 3D reconstructed including the left main coronary artery and major side branches (Timmins et al., 2017).

4.2.3 Computational fluid dynamics and analysis

Computational fluid dynamics (CFD) was applied to perform transient WSS calculations (Fluent, Ansys 15, Ansys, Inc., Canonsburg) in this 3D reconstruction (Figure 4.1) (Timmins et al., 2015). As flow input 80% of the instantaneous peak velocity measured by the
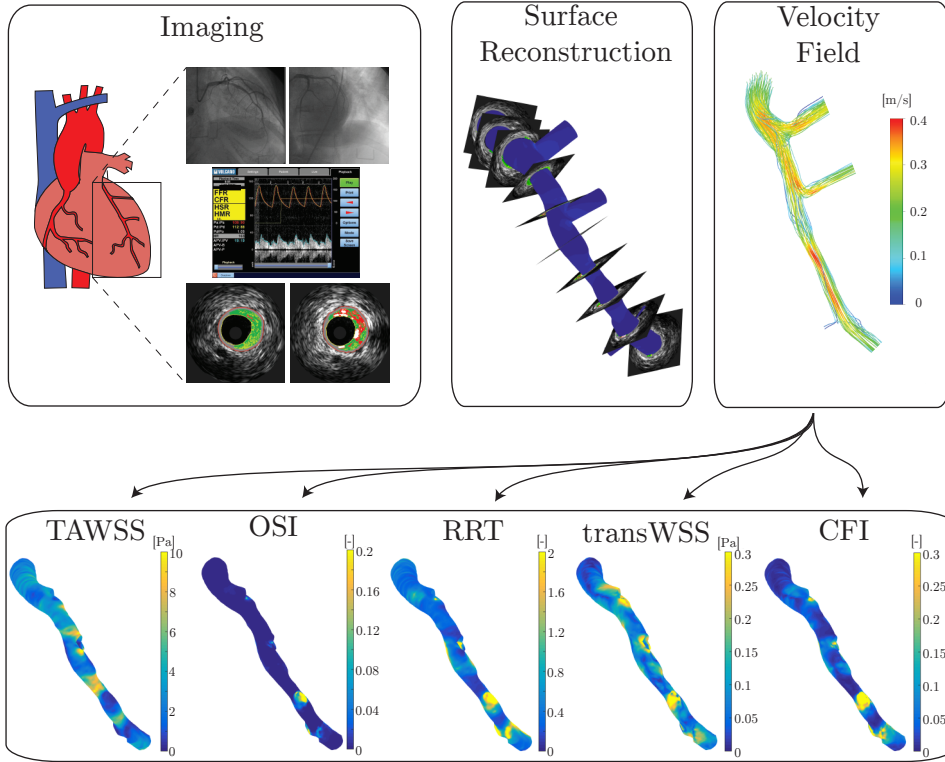
Figure 4.1: *Schematic overview of the methods.   Imaging: Biplane angiography, Doppler-derived velocity measurements and virtual-histology intravascular ultrasound (VH-IVUS). Surface reconstuction: The lumen surface 3D-reconstruction was obtained by stacking the VH-IVUS based lumen contours perpendicular to the biplane angiography derived 3D centerline. Velocity field: from the local velocities the multidirectional WSS metrics (time-averaged wall shear stress (TAWSS), oscillatory shear index (OSI), relative residence time (RRT), cross-flow index (CFI) and transverse wall shear stress (transWSS)) were determined using computational fluid dynamics.*

SS parameter	Case 1	Case 2	Case 3
TAWSS [Pa]	2	2	2
OSI [-]	0	0.07	0.12
RRT [Pa^{-1}]	0.5	0.58	0.66
transWSS [Pa]	0	0	0.8
CFI [-]	0	0	0.58
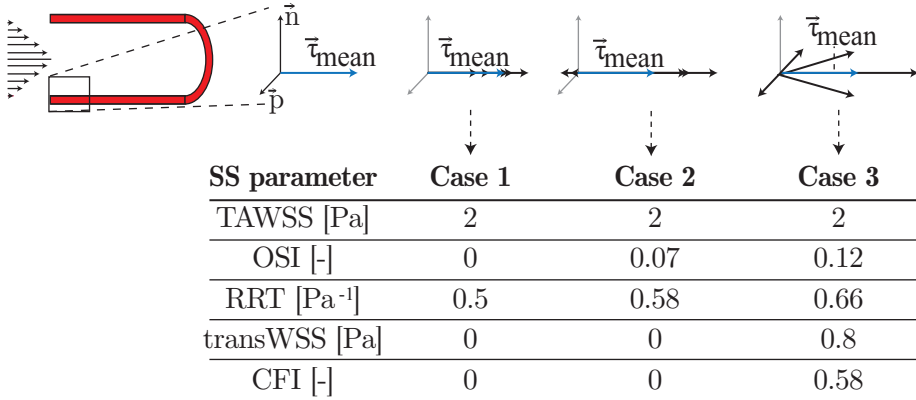
Figure 4.2: *A schematic overview of three different situation of different shear stress patterns. The blue arrow indicates the average shear stress ($\vec{\tau}_{mean}$). In each pattern the time-averaged wall shear stress (TAWSS) is 2 Pa and is therefore constant. In each pattern the oscillatory shear index (OSI), relative residence time (RRT), cross-flow index (CFI) and transverse wall shear stress (transWSS) are calculated.*

ComboWire was chosen arbitrarily, as a rounded midpoint between 50% and 100%. The flow was imposed as a plug profile at the inlet to represent the aorta plug-like velocity. All the other outlets were assumed to be pressure-free. In addition to the time-averaged WSS (TAWSS), also the oscillatory shear index (OSI), relative residence time (RRT), and transverse WSS (transWSS) and cross-flow index (CFI) were calculated (see Appendix A). The differences in these parameters are depicted in Figure 4.2.

The acquired VH-IVUS images were exported from the VH-analysis software (echoPlaque 4.0) and imported into a custom Matlab subroutine to determine the composition and plaque area. The RGB pixel values, which are distinct across the 4 VH-IVUS identified plaque components (fibrous tissue (FT), fibro-fatty tissue (FF), necrotic core (NC), and dense calcium (DC)), were identified per cross-section.

The registration of baseline and follow-up IVUS was performed by a single expert investigator (PE), who used a standardized protocol to identify landmarks (side branches and large calcific regions) (Mintz et al., 2011). Furthermore, the spacing between the IVUS images is nearly equivalent (0.5 mm) which made matching between baseline and follow-up images even more straightforward. The circumferential co-registration between baseline and follow-up was done with an automated framework which yielded excellent results (Timmins et al., 2013). The multi-directional shear stress metrics and
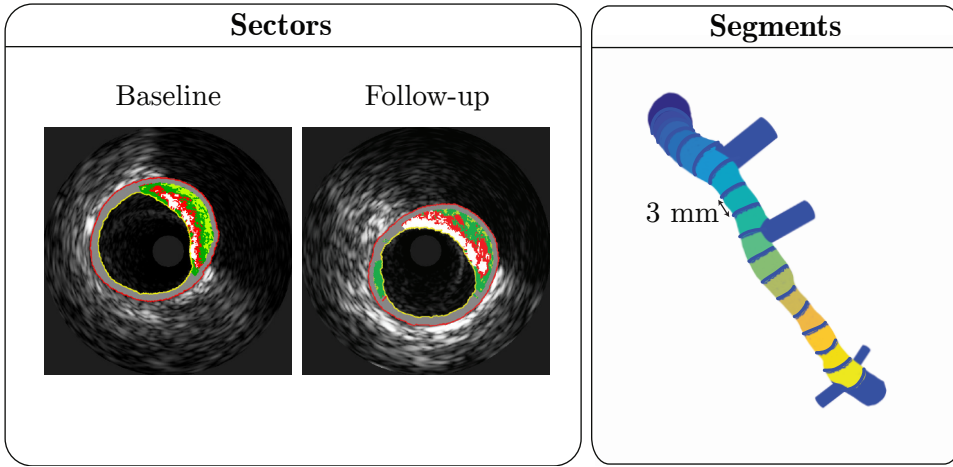
Figure 4.3: *Schematic representation of data analysis. Left: virtual-histology in-travascular ultrasound image at baseline and a matched image at follow-up. The white lines indicate the cross-sectional averaging in 8 sectors (45°). Right: 3-mm longitudinal averaging of the 8 sectors leads to regions used in the final analysis.*

plaque changes over time were quantified over 45° 3-mm regions (Figure 4.3) for further analysis (Timmins et al., 2017; Stone et al., 2012).

4.2.4   Statistics

Based on previous studies, the TAWSS data were divided into three groups: low (0-1 Pa), intermediate (1-2.5 Pa), and high (>2.5 Pa)(Samady et al., 2011). Thresholds for pathological levels of transWSS or CFI have never been explored in human coronary arteries. Therefore, we divided these metrics into 3 equally distributed groups (tertiles), this was also done for the RRT and OSI. A linear mixed-effects (LME) model was used to investigate the association between the WSS metric(s) (fixed effect) and plaque composition (dependent variable). The correlations between multiple plaque composition values are accounted for by using subject-specific random intercepts that allows for varying intercepts for each patient. In addition to fitting separate models for individual (multi-directional) shear stress features (TAWSS, OSI, RRT, TransWSS, CFI), we included the following covariates in the LME model: TAWSS, CFI and their interaction (to test for synergetic effects). The statistical analysis was performed in R (version 3.3.2, Vienna, Austria) using the LME4 package. $P<0.05$ was considered significant.

4.3 Results

4.3.1 General data

Baseline characteristics of the twenty patients was described before (Table 4.1). 1846 VH-IVUS images were analyzed with 107 (62.5–123) images per artery. From these images, 316 3-mm segments (18 (11–21) segments per artery) containing 2488 regions (141 (86.5–165) regions per artery) were used for final analysis. The average values for the low, intermediate, and high categories of the different WSS parameters is presented in Table 4.2.

4.3.2 Conventional shear stress metric: TAWSS

Plaque area progression and composition changes were greatly influenced by exposure to baseline TAWSS. A significant inverse association between TAWSS and plaque progression (p=0.006) was observed, showing more plaque regression going from low TAWSS (-0.002±0.020 mm^2) towards intermediate (-0.027 mm^2±0.018 mm^2) and high (-0.042 mm^2±0.018 mm^2) TAWSS (Figure 4.4). The other plaque constituents followed a similar significant decreasing pattern with increasing TAWSS. Significant differences were found between the low and high TAWSS groups of all the components except for FF tissue and NC.

Figure 4.4: *Plaque area and composition changes over a six-month period for plaques exposed to low, intermediate and high time-averaged wall shear stress (TAWSS). Error bars are the standard error. p<0.05: low versus intermediate (*), intermediate versus high (#) and low versus high (†).*

Table 4.1: *Patient demographic and clinical characteristics. Continuous data are reported as median (interquartile range). CAD, coronary artery disease.*

Characteristic	All patients (n=20)
age (years)	54 (46–68)
male, n (%)	13 (65)
white, n (%)	14 (70)
body mass index (kg m^{-1})	30 (27–36)
hypertension, n (%)	14 (70)
current smoking, n (%)	5 (25)
diabetes mellitus, n (%)	7 (35)
family history of CAD, n (%)	8 (40)
previous myocardial infarction, n (%)	2 (10)
e coronary flow reserve 2.35	(2.03–2.59)
fractional flow reserve	0.90 (0.82–0.96)
baseline lipid profile	
total cholesterol (mg dl^{-1})	186.0 (168.0–212.5)
triglycerides (mg dl^{-1})	115.5 (83.5–158.8)
high-density lipoprotein (mg dl^{-1})	39.5 (33.3–52.8)
low-density lipoprotein (mg dl^{-1})	118.5 (105.3–140.5)
C-reactive protein (mg l^{-1})	2.7 (1.5–7.2)
follow-up lipid profile	
total cholesterol (mg dl^{-1})	139.0 (124.3–151.3)
triglycerides (mg dl^{-1})	107.0 (75.8–138.8)
high-density lipoprotein (mg dl^{-1})	42.5 (31.3–57.3)
low-density lipoprotein (mg dl^{-1})	70.5 (54–87.5)

Table 4.2: The number of regions and the median with interquartile range of the wall shear stress (WSS) metrics for each group (low, intermediate, and high). The WSS metrics include: the time-averaged WSS (TAWSS), oscillatory shear index (OSI), relative residence time (RRT), cross-flow index (CFI) and transverse WSS (transWSS).

	low	Intermediate	High
TAWSS regions, n	193	996	1299
TAWSS magnitude [Pa]	0.78 (0.67 – 0.90)	1.65 (1.40 – 2.03)	3.69 (3.03 – 4.66)
OSI, RRT, CFI, transWSS regions, n	829	830	829
OSI·10^{-3} [-]	0.51 (0.25 – 0.85)	4.21 (2.61 – 6.91)	24.2 (16.4 – 42.4)
RRT [Pa^{-1}]	0.29 (0.23 – 0.37)	0.65 (0.56 – 0.74)	1.14 (0.95 – 1.60)
CFI [-]	0.03 (0.02 – 0.04)	0.08 (0.06 – 0.09)	0.16 (0.13 – 0.21)
transWSS [Pa]	0.06 (0.04 – 0.07)	0.11 (0.10 – 0.13)	0.18 (0.16 – 0.24)

4.3.3 Multidirectional shear stress

In general, we observed that multidirectional WSS was primarily involved in altering the plaque composition rather than the plaque size. No significant difference in total plaque area changes was found in low vs. high OSI regions (Figure 4.5A). An inverse relationship with OSI was found for FF tissue ($p<0.001$), implying the higher the OSI the more FF tissue regression. Significant higher progression was found for NC area ($p=0.001$) and DC area ($p<0.001$) in the high OSI regions compared to the intermediate and low OSI regions, but no differences were observed for FT regression in these regions. Evaluation of the changes in plaque exposed to low vs. high RRT revealed that plaques exposed to low RRT exhibited more regression of total plaque area ($p<0.001$) and FT ($p=0.003$) than plaques that were exposed to high RRT (Figure 4.5B). Similar to high OSI, high RRT regions showed more NC ($p=0.008$) and DC ($p<0.001$) progression and more regression of FF tissue ($p=0.0003$) than low RRT regions. A positive RRT relationship was found for DC ($p<0.001$) and FT ($p=0.01$), implying the higher the RRT the more DC progression and less FT tissue regression.

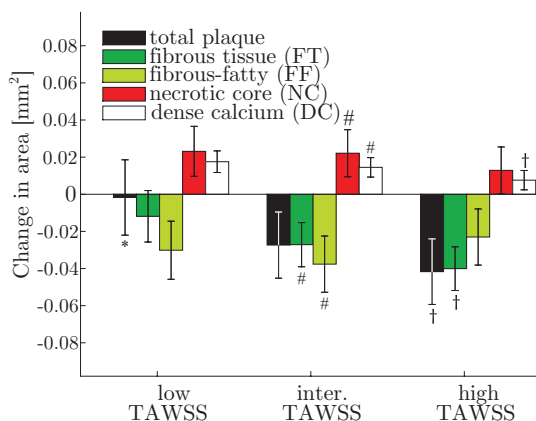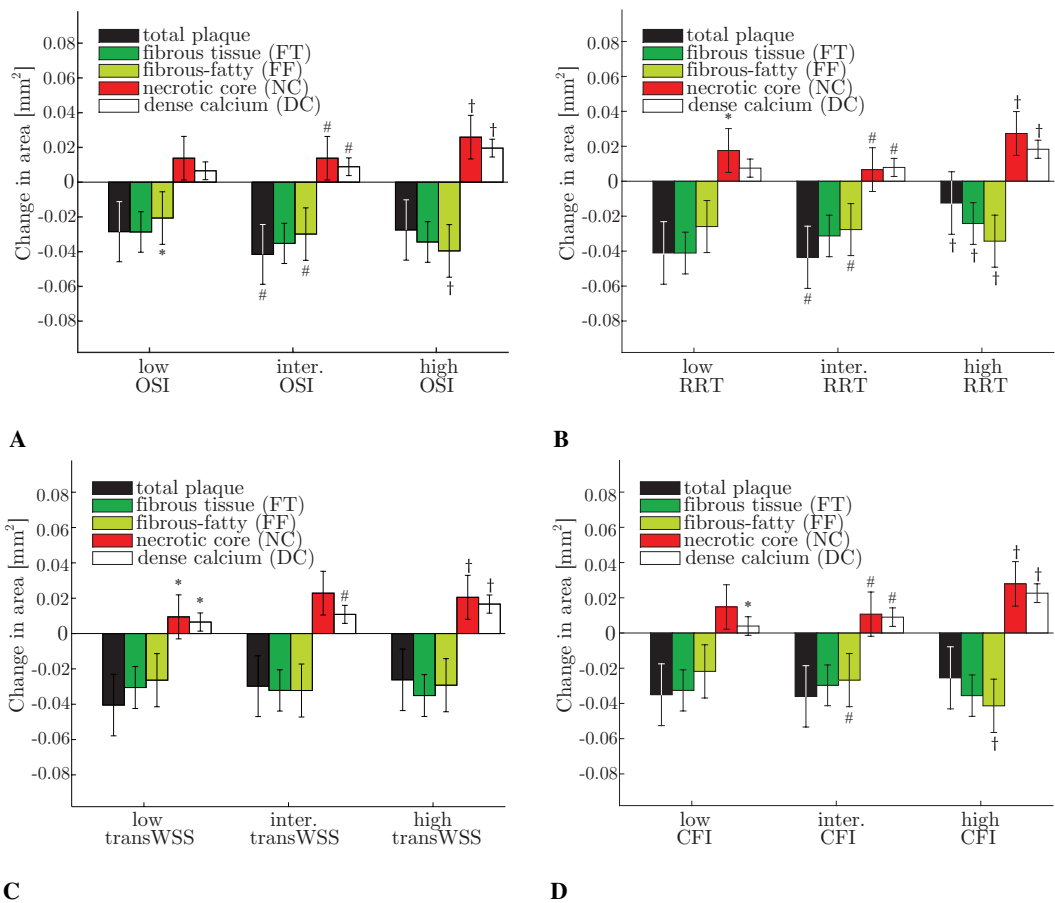**Figure 4.5:** *Plaque area and composition changes over a six-month period for plaques exposed to low, intermediate and high oscillatory shear index (OSI) (a), relative residence time (RRT) (b), cross-flow index (CFI) (c), and transverse wall shear stress (transWSS) (d) . Error bars are the standard error. p<0.05: low versus intermediate (*), intermediate versus high (#) and low versus high (†)*

Different levels of transWSS did not significantly influence the total plaque growth, FT, and FF (Figure 4.5C). Regions exposed to high transWSS showed more progression of NC area (p=0.01) and DC area (p<0.0001) than regions exposed to low transWSS. Similar patterns were seen for the cross-flow index (CFI) (Figure 4.5D). Changes in total plaque area and FT were unaffected by different levels of CFI. There was a positive relation between CFI and the NC (p<0.002) and DC groups (p<0.001), and a negative relation for the FF tissue (p<0.001).

4.3.4   Co-localization of TAWSS and multidirectional shear stress

To study whether plaque progression is influenced by multidirectional WSS additional to TAWSS, regions of low and high TAWSS were co-localized with low, intermediate, and high multidirectional WSS. The greatest progression of total plaque, FT and FF area was found in regions of low TAWSS co-localized with low and intermediate CFI (low CFI: 0.15 mm^2, intermediate CFI: 0.10 mm^2), which was much larger than the average plaque growth in low TAWSS (-0.001 mm^2) (Figure 4.4 and Figure 4.6A). Further, the change in area in these groups was significantly greater than the change in area in the low TAWSS regions co-localized with high CFI (total plaque, FT, FF: p<0.0001). High TAWSS regions co-localized with low or high CFI demonstrated the greatest NC progression, while in high CFI regions the greatest regression was found for total plaque area, FT, and FF tissue. In high TAWSS regions, plaque regression (p<0.001) was observed in all the CFI groups, which resulted from significant changes in plaque components FT (p<0.001), FF tissue (p<0.001), NC (p<0.001), and DC (p<0.001). A significant synergetic effect was found for all the components (p<0.001).

The co-localization of TAWSS with OSI showed a similar response as the co-localization of TAWSS with CFI (Figure 4.6B). However, the co-localization results with RRT showed similar results as TAWSS alone (Figure 4.4). Interestingly, in the co-localization of high TAWSS with high RRT plaque growth and plaque composition changes mimics more the high RRT response.

4.4   Discussion

For the first time, the effect of TAWSS together with multidirectional WSS on plaque progression and compositional changes was investigated in coronary arteries of patients with CAD. We showed that multidirectional WSS mainly contributes to changes in plaque composition, such that plaque vulnerability is increased, and less to changes in plaque size. Interestingly, regions with low TAWSS co-localized with low to intermediate CFI
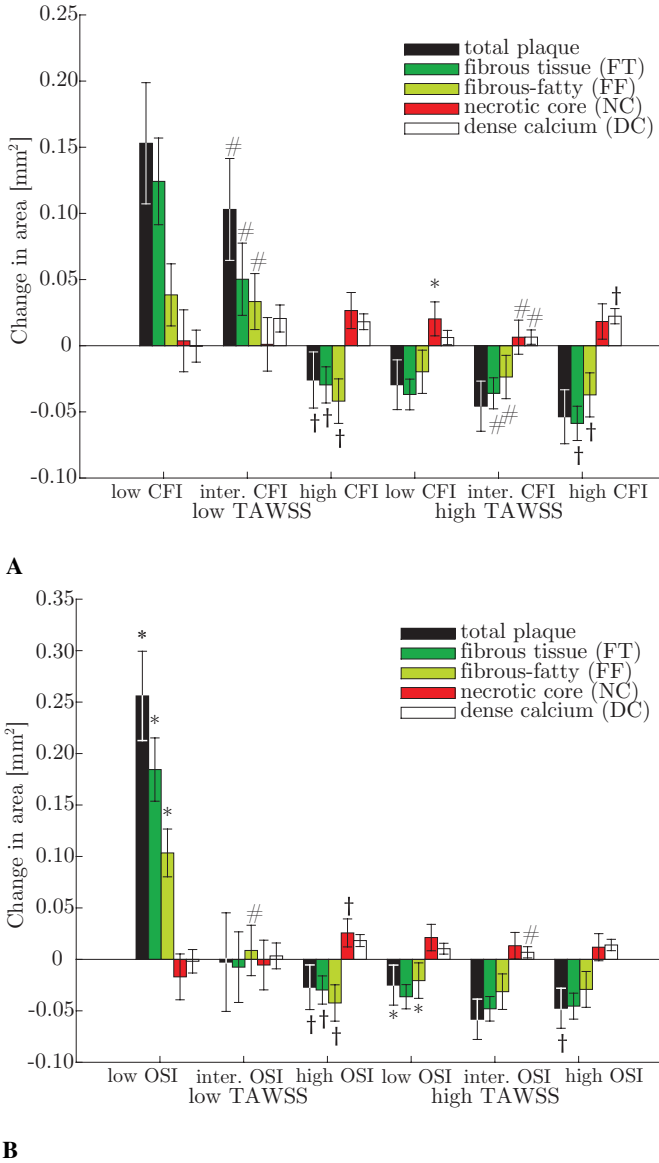
Figure 4.6: *Plaque area and composition changes over a six-month period for plaques exposed to low or, high time-averaged wall shear stress (TAWSS) co-localized with low, intermediate and high cross-flow index (CFI) in (a) and plaques exposed to low or, high time-averaged wall shear stress (TAWSS) co-localized with low, intermediate and high oscillatory shear index (OSI) in (b). Error bars are the standard error. p<0.05: low versus intermediate (*), intermediate versus high (#) and low versus high (†).*

resulted in the greatest plaque progression; interesting low TAWSS alone did not show significant plaque progression (see Figure 4.4). High TAWSS showed, regardless of the CFI magnitude, to influence characteristics of plaque vulnerability (i.e. total plaque area and FT regression, and NC progression).

4.4.1 Time-averaged wall shear stress

Our results on changes in plaque size and composition in regions with low and high TAWSS are in close agreement with previous studies (Samady et al., 2011). It is under debate whether high-risk plaque development is associated with either low or high TAWSS (Eshtehardi et al., 2017; Koskinas et al., 2010). We hypothesize that high TAWSS is atheroprotective in early atherosclerosis , but at later stages destabilizes the plaque.

4.4.2 Multidirectional shear stress

Only one study has investigated the influence of multidirectional WSS on plaque progression and compositional changes in human coronary arteries (Timmins et al., 2017). This study measured oscillatory WSS as the maximum angle deviation of WSS over the cardiac cycle. Plaques that were exposed to low TAWSS co-localized with a) low oscillatory WSS showed large plaque progression b) high oscillatory WSS showed transformation towards a vulnerable plaque phenotype. Both of these observations are in agreement with our study. However, that work did not address the individual effect of oscillatory WSS and the combined role of high TAWSS and multidirectional WSS in plaque progression and destabilization (Timmins et al., 2017).

The influence of OSI and RRT on plaque initiation was previously investigated. In murine aortas, plaque location was in better agreement with OSI and RRT than TAWSS (Hoi et al., 2011). A study in human coronary arteries showed that plaques are often located at low TAWSS regions (Rikhtegar et al., 2012), however both high OSI and RRT were more predictive for the presence of plaque. A caveat to this study was that, they virtually removed the plaque in order to represent the healthy state of the artery and assessed the TAWSS, OSI and RRT in this manipulated geometry. Therefore, this study cannot be regarded as a true natural history study and comparisons should be interpreted with caution. We found a more pronounced effect of RRT and OSI on changes in plaque composition than plaque growth. Specifically, regions with the largest progression of NC and DC and regression of FF tissue were associated with high OSI and RRT.

A recently introduced hemodynamic metric to characterize another feature of multidirectional flow is transverse WSS (transWSS) or normalized transWSS (CFI). The present

study shows that there is no effect of transWSS or CFI on plaque progression, however it appears to influence plaque composition. Indeed, a number of studies suggest that an increase in multidirectional flow or transverse WSS is atherogenic (Mohamied et al., 2015; Wang et al., 2013). In an in vitro study endothelial cells subjected to transverse flow resulted in an increase in inflammation (increase in expression of NF-κB) (Wang et al., 2013). In another study using rabbits, high transWSS was found at lesion sites, whereas this correlation was less apparent with either TAWSS or OSI (Mohamied et al., 2015). This relationship was less evident in more mature rabbits. However, they did not study plaque composition, which in our study proved to be most affected by the transWSS. It should be noted that these studies were performed using either cultured cells or atherosclerotic animal models and hence may not be fully representative of the human case.

4.4.3 Co-localization of time-averaged wall shear stress with multidirectional shear stress

We present for the first time data on low and high TAWSS regions co-localized with various multidirectional WSS parameters. In contrast to the low TAWSS, the plaque changes in the high TAWSS regions seem not so much influenced by the multi-directional WSS. Co-localization of TAWSS with CFI and OSI showed the same patterns in plaque progression, which was expected because of the high correlation between these parameters (r=0.83).

Our data on plaque progression potentially suffers from regression-to-the-mean effects. This was investigated in a separate analysis by incorporating baseline plaque area into the LME model and we observed that plaque progression was still significantly related to all multidirectional WSS parameters. However, although still significant, it was less pronounced in the low TAWSS co-localized with low CFI regions. Therefore, the conclusions are all valid.

4.4.4 Limitations

All patients were treated with high doses of statins. With this therapy often an overall plaque regression is observed. Therefore, the results that we obtained is a balance of pro-atherogenic hemodynamic conditions, e.g. low TAWSS, and the anti-atherogenic influence of statins. With current treatment strategy in CAD patients, these data reflect WSS-related plaque progression in this population.

Furthermore, our data on the relationship between plaque progression and (multidirec-

tional) WSS was obtained in LADs only. Although no data exist on possible differences in WSS-related plaque progression in the other coronary arteries, it cannot excluded that the multidirectional WSS in these arteries has a larger range and therefore show a different response.

VH-IVUS was used to assess the local plaque composition, but VH-IVUS is under debate for its applicability to identify local plaque composition. Although some studies showed a moderate correlation between VH-IVUS and histology especially for the FF and NC tissue (Granada et al., 2007) (Thim et al., 2010b), a number of studies showed >80% accuracy to identify FT, FF, NC, and DC compared to histology (Nasu et al., 2006). Therefore, in general, the found relationships between plaque components and multidirectional WSS reflect the actual changes in the tissue. But, conclusions with regard to FF and NC should be interpreted with caution.

The number of patients that was studied is limited. Therefore, multiple regions within a single coronary artery were analyzed. To obtain independent samples, the data was averaged over 3-mm and circumferentially over 45 degrees (Stone et al., 2012; Timmins et al., 2015). We opted for 45° sectors to ensure minimal loss in earlier observed details in the hemodynamic environment simultaneously with the highest possible accuracy in circumferential matching with follow-up data (Timmins et al., 2017, 2015). The circumferential registration algorithm showed a matching error of <10° in 78% of the cross-sections compared to manual image registration. This means that of these cross-sections 78%-100% of the sector is correctly matched. To further account for subject dependencies, for data analysis a sophisticated LME regression model was used. Using this approach we obtained statistical significance, despite the limited number of patients. Besides, this study is an exploratory study and therefore the conclusions should be confirmed in a larger patient database.

Because we defined low TAWSS as <1 Pa, in the co-localization analysis we ended up with a low number of regions exposed to both low TAWSS and low CFI (n=11) and low TAWSS and intermediate CFI (n=15), contrasting the other groups in which at least 167 data points were present. Splitting the TAWSS data in tertiles, would have resulted in a larger number of data points but does not allow to study the colocalization with true low TAWSS. Despite the fact that these sample sizes were low, the statistics revealed strong effects in these regions. Therefore, we are confident that our conclusions are valid.

4.4.5   Conclusions

In conclusion, this study shows that there are important associations between (multidirectional) WSS metrics and changes in plaque composition reflecting increased plaque destabilization. Further, multidirectional flow acts synergistically with TAWSS on plaque composition and plaque size. Therefore, the combination of (multidirectional) WSS profiling and plaque imaging in combination with systemic risk factors is imperative to identify plaques that potentially develop into a vulnerable plaque.

SYNERGY OF NIRS-DETECTED LIPID-RICH PLAQUE AND SHEAR STRESS ON HUMAN CORONARY PLAQUE GROWTH

5

Original chapter: ***Kok AM***, *Hartman EMJ, Hoogendoorn A, Chiastra C, Regar E, Zijlstra F, Gijsen FJH, van der Steen AFW, Daemen J, Wentzel JJ.*

ABSTRACT

The effect of lipids inside a plaque – using near-infrared spectroscopy intravascular ultrasound (NIRS-IVUS) catheter – in combination with detailed information of different local shear stress metrics has never been studied as a risk predictor for atherosclerotic lesion progression in human coronary arteries in vivo. In addition, the effect of systemic cholesterol levels in combination with the different shear stress metrics on plaque progression was investigated. 15 non-culprit arteries from acute coronary syndrome patients were imaged with coronary computed tomography angiography and NIRS-IVUS at baseline, and NIRS-IVUS imaging was repeated after one year follow-up. To assess the local shear stress, computational fluid dynamics was performed in 3D reconstructioned geometries of coronary arteries with Doppler velocity measurements as input. The arteries were divided into 2291 1.5mm-45° regions and in each region the wall thickness at baseline and follow-up was determined and indicated as NIRS positive or NIRS negative. Additionally, in each region the following shear stress metrics were computed: time-average wall shear stress (TAWSS), oscillatory shear index (OSI), relative residence time (RRT), cross-flow index (CFI), and transverse wall shear stress (transWSS). Finally, patients were classified as having low or high LDL levels based on a median split of all the participants. Plaque progression over a one year follow-up was not statistically different in patients with low versus high LDL levels (p=0.58) or in regions that were positive versus negative for NIRS based lipid assessment (p=0.2). However, compared to NIRS negative regions, NIRS positive regions show more plaque progression if they were additionally exposed to high RRT (p=0.01) or low transWSS (p=0.04), and more plaque regression in regions additionally exposed to high transWSS (p=0.02). Patients with high LDL levels showed a trend to more plaque growth in low TAWS and high RRT versus patients with low LDL levels, however this was not statistically significant. This is the first study to show that intravascular NIRS assessment is of additive value in combination with dif-

ferent shear stress metrics for the estimation of plaque progression in human coronary arteries. Therefore, these data suggest that future studies would benefit from assessment of NIRS in combination with different shear stress metrics for the estimation of regions at risk of plaque growth.

5.1   Introduction

Coronary artery disease (CAD) caused by atherosclerosis is one the major causes worldwide of myocardial infarction. Pathological studies showed that the most common cause of a myocardial infarction (MI) is rupture of a thin cap fibrous atheroma (TCFA), a plaque containing a lipid pool covered by a thin fibrous cap ((Naghavi et al., 2003; Virmani et al., 2006). Additional risk factors for major adverse cardiovascular events are minimal lumen area (MLA) (<=4 mm2) and plaque burden (PB) (>=70%) (Stone et al., 2011). However, taken together, these risk factors poorly predicted future events (Stone et al., 2018). Lesions that were imaged invasively only weeks or months prior to an MI showed rapid lumen narrowing and plaque progression (Ahmadi et al., 2015). Therefore, plaque progression might be an important added risk factor for a cardiac vascular event.

Plaque progression is associated with high cholesterol levels and with subclinical plaque rupture and healing of lesions (Burke et al., 2001; Cannon et al., 2004; Davies and Thomas, 1984; Nissen et al., 2004). Furthermore, it is well known that low shear stress, the frictional force of the blood at the vessel wall, plays an important role in plaque progression (Samady et al., 2011). Endothelial cells are very sensitive to shear stress (Kwak et al., 2014; Samady et al., 2011; Stone et al., 2012) and at regions of low shear stress they express pro-inflammatory genes, hereby creating a pro-atherogenic environment. The influence of cholesterol levels on shear stress related plaque progression was investigated in a pig study (Koskinas et al., 2013a). They showed that high systemic total cholesterol levels amplified the effect of low shear stress on plaque growth and on plaque vulnerability. Because, lipid accumulation also contributes to the activation of endothelial cells locally (Lusis, 2000); inflammation and thus plaque growth might be enhanced in the presence of lipids inside the plaque. Considering these observations, we hypothesized that low shear stress co-localized with local lipid rich plaques is perhaps a better predictor for local plaque progression than low shear stress alone or in combination with systemic cholesterol levels.

Recently, a new intravascular imaging catheter was introduced at the clinical market allowing simultaneous assessment of the plaque morphology using intravascular ultrasound (IVUS) as well as presence of lipids with near-infrared spectroscopy (NIRS). Data ob-

tained with this catheter already showed promising results that potentially contribute to the decision making in clinical practice (Danek et al., 2017; Madder et al., 2016; Oemrawsingh et al., 2014; Schuurman et al., 2017). Coronary artery disease patients with a high lipid core burden index (> 227), measured with NIRS catheter, demonstrated an increased risk of major adverse cardiovascular events (Schuurman et al., 2017). To the best of the author's knowledge, lipids inside a plaque (using this new NIRS-IVUS catheter) in combination with detailed information of local shear stress distribution has not been studied as a predictor for local atherosclerotic lesion progression in human coronary arteries in vivo.

5.2 Material and Methods

5.2.1 Subjects

Hemodynamically stable ACS patients admitted for percutaneous coronary intervention (PCI) were enrolled in the IMPACT study (imaging and modeling to investigate the mutual relationship of plaque growth and biomechanical parameters in human coronary arteries study). The most important exclusion criteria were: history of coronary bypass graft, three vessel disease, and renal insufficiency (creatinine clearing <50 ml/min). In the end, 14 patients were treated with PCI of the culprit vessel(s) according to the local treatment standards. At least one non-treated coronary segment was imaged according to the IMPACT acquisition protocol at index procedure and after one year of follow-up. At one month follow-up, a coronary computed tomography angiography (CCTA) was made in the outpatient clinic. Written informed consent was obtained from all patients. This study was approved by the local medical ethical committee of the Erasmus MC (MEC 2015-535, NL54519.078.15) and conducted in accordance with the World Medical Association Declaration of Helsinki (64th WMA General Assembly, Fortaleza, Brazil, October 2013) and Medical Research Involving Human Subjects Act (WMO).

5.2.2 Acquisition protocol

Before the start of the procedure, blood was collected in EDTA and clotting tubes and was send to the Clinical Chemistry lab for further analysis. A non-culprit coronary segment was imaged using angiography and NIRS-IVUS (TVC, insight coronary imaging catheter, InfraReDx (Burlington, Massachusetts, USA)) at index procedure and after one year of follow-up. The NIRS-IVUS pullback was at least 30 mm in length and contained at least two side branches. The side branches were used as matching points for registration of the various imaging modalities that were fused to obtain a 3D reconstruc-

tion. At multiple locations within the imaged region Doppler-derived blood velocity measurements were performed with a ComboWire (Volcano, Corporation, Rancho Cardova, USA). The location of the ComboWire was documented using angiography. One month after the index procedure, a CCTA scan was made using the SOMATOM Force (192 slice, 3rd generation, dual-source CT scanner (SOMATOM Force, Siemens AG, Germany)). In order to 3D reconstruct the coronary arteries we combined information from the IVUS images with CCTA as depicted in Figure 5.1.
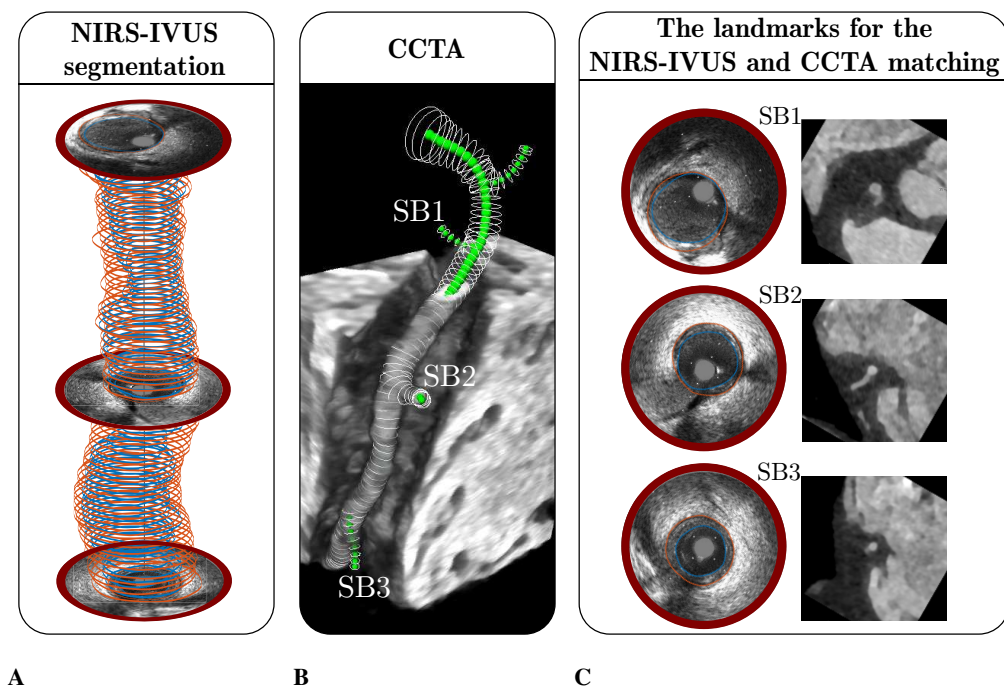
Figure 5.1: *An overview of the segmentation and matching methodology of the near-infrared spectroscopy intravascular ultrasound (NIRS-IVUS) and coronary computed tomography angiography (CCTA) imaging is shown. In A) three NIRS-IVUS images are shown on the vertically stacked manually-segmented lumen (blue) and external elastic membrane (orange) contours. In B) a partial CCTA view is shown with semi-automatically segmented CCTA contours (white) and their centerlines (green spheres). Also three sidebranches (SBs) are indicated which are also as landmarks to match the NIRS-IVUS images (left) with the 2D CCTA (right) images as shown in C).*

5.2.3   IVUS gating and segmentation

IVUS-images were acquired during a continuous motorized pullback, which results in variations in the lumen area due to the cardiac contraction. Since this is not related to true variations in local lumen area, this is problematic for the 3D reconstruction and therefore off-line ECG gating was performed using an in-house developed algorithm using MATLAB (v. 2015a, Mathworks Inc., Natick, MA, USA). The algorithm determines differences in grey values in consecutive IVUS images. The largest difference in overall grey values is typically found near the R-top in the ECG. Based on this algorithm, one IVUS frame per cardiac cycle was selected in the same diastolic phase (6 frames before the R-top). The IVUS-gating algorithm was validated using 42 IVUS pull-backs from a different study in pig coronary arteries. For that purpose, the ECG heart rate of the pig was documented during the IVUS pullback. Subsequently, the heart rate derived from the IVUS gating algorithm was compared to the ECG heart rate. Our IVUS-gating algorithm showed a median error in heart rate <0.5% only (0.38% (IQR 0.22 – 0.70%). The gated NIRS-IVUS images were segmented by one experienced reader (EH) using QCU-CMS software (Leiden, The Netherlands). In each NIRS-IVUS image the lumen and the external elastic membrane (EEM) were segmented, see Figure 5.1A. An interobserver variability analysis plaque segmentation was performed using 1192 NIRS-IVUS images (from 6 mildly diseased pig coronary arteries). The average intraclass correlation coefficient showed good results: 0.927 (0.805-0.976).

5.2.4   CCTA segmentation

Semi-automatic CCTA segmentation of the coronary arteries and all visible side branches was performed (by EH) using graph cuts and robust kernel regression as previously described (Schaap et al., 2009). The CCTA segmentation of the main vessel started at the ostium and ended 20 mm distal from the most distal side branch that was imaged using NIRS-IVUS. From these segmentations, the 3D-centerline of both the main branch and side branches was determined (Schaap et al., 2009), Figure 5.1B.

5.2.5   3D reconstruction

A 3D reconstruction of the coronary artery was obtained by fusing information from CCTA and IVUS using in-house developed software using Mevislab (Bremen, Germany). In general, the following steps were taken: 1) matching of the IVUS images with the CT images, 2) defining the region of interest (ROI), 3) correcting for the volume mismatch between IVUS and CT, 4) replace the ROI in the CCTA segmentation with IVUS contours, 5) 3D surface generation, and 6) smoothing.

First the IVUS images were matched with the CCTA images. In detail, the CCTA centerline from the main vessel was used to interpolate new CCTA images perpendicular to the centerline at the same locations as the NIRS-IVUS images. see Figure 5.1C. Then the CCTA and IVUS images were longitudinally and circumferentially matched using landmarks (see Figure 5.1C). Subsequently, the IVUS-lumen contours were stacked on the 3D CCTA centerline and rotated according to the IVUS-CT matching procedure as previously described (van der Giessen et al., 2010). The 3D-matched region containing the IVUS contours is hereafter referred to as the region of interest (ROI).

IVUS and the CCTA segmented lumen volumes differ due to blooming artifacts or contrast filling in CT (Bulant et al., 2017; Stolzmann et al., 2012). Therefore a correction factor was calculated by comparing the average lumen area in both the CCTA ROI as well as the IVUS ROI. Subsequently, this correction factor was converted to a 1-D correction factor and was applied to the radii of the CCTA contours (including the side branches). The next step was to replace the CCTA lumen contours in the ROI by the NIRS-IVUS lumen contours, see Figure 5.2A.

All the contours were 3D interpolated and transformed to a volume using a recurving marching-cubes algorithm. The longitudinal sampling of the IVUS contours was higher than the CCTA contours, therefore more smoothing was applied to the IVUS ROI surface region using a Gaussian filter. An additional smoothing step was applied to the full geometry with a Laplacian filter. Some of these smoothing steps induced volume changes, these volume changes were calculated and countered by scaling back to the original volume. Then, the volume was converted to a 3D STL surface, see Figure 5.2B. In some cases local smoothing of the surface was needed at the transition of the CCTA to NIRS-IVUS surface or near side branches. These artifacts created by the merging step were removed with the Laplacian smoothing filter using MeshLab (Visual Computing Lab, Pisa, Italy).

5.2.6   Computational fluid dynamics

Each 3D generated geometry was converted to a tetrahedral mesh in ICEM CFD (v.17.1, ANSYS Inc., Canonsburg, PA, USA) with a 5-prism layer at the boundary to resolve shear stress effects (Chiastra et al., 2016). The mesh size was determined by a mesh independence study (only errors within 1% of shear stress were allowed). A typical mesh consisted of six million elements. Unsteady computational fluid dynamics simulations were performed using the commercially available finite volume solver Fluent (v.17.1, ANSYS Inc.). The vessel lumen was considered as rigid and subjected to no-slip boundary condition. Blood was assumed to behave as shear-thinning fluid, which was modelled
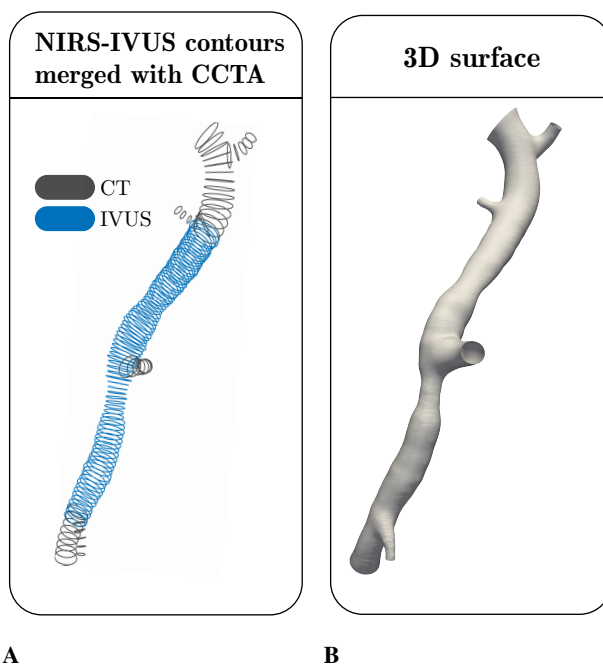
Figure 5.2: *Surface generation. In A) the region of interest intravascular ultrasound (IVUS) contours (blue) fused with the CCTA contours(grey). In B) the contours were 3D interpolated and transformed to a 3D surface.*

with the Carreau model:

$$\frac{\mu - \mu_\infty}{\mu_0 - \mu_\infty} = [1 + \lambda\dot{\gamma}^2]^{(n-1)/2} \tag{5.1}$$

with μ, the dynamic viscosity, approaching to μ_0 (0.25 Pa·s) at low shear rate ($\dot{\gamma}$) and to μ_∞ (0.0035 Pa·s) at high shear rate; the parameter n is the power law constant (0.25) and λ is a time constant (25 s) (Seo et al., 2005). The blood density was set to be 1060 kg/m3 (Cutnell and Johnson, 2007). Reynolds numbers did not exceed 500, therefore the flow was assumed to be laminar. The Fluent pressure-based solver with a coupled scheme for the velocity-pressure coupling was used to solve the Navier-Stokes equations of unsteady, incompressible fluid motion. The second order scheme was used for the pressure spatial discretization and a second order upwind scheme for the momentum spatial discretization. The second order implicit scheme was chosen for the unsteady formulation. The flow Courant number was set to 50 while the under relaxation factors to 0.3 for the pressure and the momentum, and to 1 for the density. As convergence criterion, continuity and velocity residuals were set to 10^{-5}. 1.5 patient-specific heart beat was simulated (only the last beat was used for analysis). Two types of boundary conditions were applied used for the 3D CFD simulation: 1) flow distribution through the side branches and 2) a time-dependent velocity profile at the inlet, see subsection 5.2.7. Each heartbeat consisted of 100 time steps. All settings regarding the time steps and convergence criteria were determined by a sensitivity analysis (only errors within 1% of wall shear stress were allowed). Wall shear stresses were exported on each node of the mesh for each time step. Further post-processing was done using VMTK (Orobix, Bergamo, Italy) and MATLAB (v. 2015a, Mathworks Inc., Natick, MA, USA).

5.2.7   Boundary conditions

As outlet boundary condition, the flow distribution through the side branches was pre-scribed. The flow distribution was derived from intravascular velocity measurements using a Doppler wire. Time-averaged flow can be calculated by multiplying the local area with the time averaged mean velocity. The local cross-sectional area was obtained from the 3D vessel reconstruction at the location of the Doppler wire documented by an-giography. As the device measures the local maximum velocity, the velocity values were first converted to the mean velocity by following a previously proposed method (Ponzini et al., 2006). An experienced consensus committee (AM, EH, AH, FG, JJW) classified all the velocity measurements as good, moderate, or bad since not all measurements were

optimal. The following criteria were used for the classification: signal intensity, repeating pattern, and similarity to the already established pattern by literature (Davies et al., 2006; Hadjiloizou et al., 2008). While bad measurements were discarded, good measurements were used to calculate the flow-rate in the vessel region (between two side branches). Moderate classified measurements were only used if they were in agreement (less than 20% error) with the other flows derived from flow-diameter scaling law based on flow measurements from diseased human coronary arteries (van der Giessen et al., 2011). This scaling law calculates the flow-rate (Q) distributed through two daughter branches (D1 and D2) with a certain diameter (d):

$$\frac{Q_{D1}}{Q_{D2}} = \left(\frac{d_{D1}}{d_{D2}}\right)^{2.27} \tag{5.2}$$

The scaling law was also used at regions were no measurements were available. In this way, the flow distribution through the entire coronary artery was established. As inlet boundary condition, a time-dependent velocity waveform was applied to enable unsteady flow simulations. The most proximal good classified velocity measurement was used for the shape of this waveform. The shape of the inflow velocity profile was assumed to be flat, since the most proximal part of the 3D reconstruction is at the ostium of the artery close to the aorta where the flow presumably has not been developed yet. In one coronary artery no good velocity measurement was available in the proximal region of the main vessel to determine the time-dependent velocity wave form. In this case a typical human velocity waveform was used (Davies et al., 2006). Furthermore, the amplitude of the velocity curve was scaled to obtain the mean flow-rate estimated with the following equation (van der Giessen et al., 2011):

$$Q = 1.43 \cdot d^{2.55} \tag{5.3}$$

where Q is the flow-rate and d the diameter of the vessel.

5.2.8 Analysis

The wall thickness was defined as the distance between the EEM and the lumen distance from the center point. All the parameters of interest (wall thickness at baseline, wall thickness at follow-up and baseline NIRS) were projected onto the 3D geometry at baseline using VMTK (Orobix, Bergamo, Italy) and MATLAB (v. 2015a, Mathworks Inc.,

Natick, MA, USA) to enable an one-to-one comparison with the shear stress. Although shear stresses were calculated for the full 3D geometry, only the ROI was retained for further analysis. In IVUS images, the presence of calcium causes a bright signal with a shadow in the image and therefore the EEM was difficult to segment. The regions in which the EEM could not be reliably segmented was removed from further analysis. Similar for the NIRS, the analysis is hampered by artifacts created by the presence of the guide wire, therefore the regions in which the guide wire was present were removed for further NIRS analysis. To minimize the influence of possible registration mismatch of the IVUS images at baseline and follow up on the final results, the data were averaged over 1.5 mm in the axial direction and over 45° in the circumferential direction. We chose 1.5 mm since the registration of baseline and follow up images can be performed with an accuracy of approximately one image frame (+0.5 mm and -0.5 mm), leading to at least 75% overlap in the worst case scenario. We chose to average the data within the cross-sections over 45° so that heterogeneity in shear stress due to curvature and tortuosity was still captured, but ensuring the highest possible overlap between baseline and follow-up registration (Timmins et al., 2017).

The shear stress was averaged over the cardiac cycle to obtain the time-averaged wall shear stress (TAWSS). Per vessel, the regions were divided into 3 groups based on the average TAWSS in the region (low, intermediate, and high). A similar procedure was performed for the multidirectional shear stress metrics. Furthermore, the regions were classified as NIRS positive if more than 50% of the region had a high probability (>60%) for the presence of lipids, otherwise they were classified as NIRS negative. In order to investigate the influence of systemic levels of LDL on shear stress-related plaque growth, the patients were split based on the median LDL level (at follow-up; into a low (<1.78 mmol/L) and high (>1.78 mmol/L) LDL group. Also, the synergistic effect of LDL and NIRS with shear stress on plaque growth was investigated. Plaque progression was present if the wall thickness increased more than 0.1 mm.

5.2.9   Statistical analysis

Normality of the data was tested with a Kolmogorov-Smirnov test. If the data was normally distributed mean and standard deviation were presented otherwise median and the interquartile range was reported. A Wilcoxon-signed rank test was performed to test the difference between baseline and follow up LDL levels. Linear mixed effect (LME) model was used to perform the statistical analysis of the shear stress metrics on plaque progression and we corrected for baseline wall thickness , using the LME4 package in R (version 3.3.2, Vienna, Austria). Also the interaction effect (to test for synergetic effects)

between NIRS and TAWSS was investigated with this model. P<0.05 was considered significant. Also the positive predictive value (PPV) of low TAWSS and the high levels of multidirectional shear stress for plaque progression was calculated. Similarly, PPVs were calculated for the combination of the shear stress metrics and positive NIRS signals.

5.3 Results

In total 15 coronary arteries from 14 patients were analyzed. The patient demographics and clinical characteristics are presented in Table 5.1.

The length of the ROIs in the coronary arteries was 49.5 mm (39.4 – 57.4 mm). In total 11% (5.8% – 22%) of the data was excluded (due to calcium, artefacts, and guide wire), resulting in 2291 regions (1.5mm-45°) included in the analysis (138 (101 – 190) regions per artery). 482 regions showed plaque progression (>0.1 mm) and 572 regions showed plaque regression (<-0.1 mm). The absolute TAWSS value for all the regions was 0.80 Pa (0.44 – 1.41 Pa), for the OSI $0.6 \cdot 10^{-3}$ ($0.1 \cdot 10^{-3}$ – $3.1 \cdot 10^{-3}$) for RRT 1.33 Pa^{-1} (0.76 – 2.41 Pa^{-1}), for CFI 0.04 (0.02 – 0.08), and transWSS 0.03 Pa (0.01 – 0.07 Pa). Plaque progression over a one year follow-up was not statistically different in patients with low versus high LDL levels (p=0.58) or in regions that were positive versus negative for NIRS based lipid assessment (p=0.2), see Figure 5.3.

5.3.1 Association of plaque progression with different shear stress parameters

The vessel-specific thresholds that were used to subdivide the five different shear stress metrics in low, intermediate, and high shear stress regions are presented in Table 5.2.

Plaque growth and its relationship with the five different shear stress parameters is presented in Figure 5.4.

Our data showed that plaque changes over time were associated with TAWSS, RRT, OSI and CFI, but not with transWSS. Plaque growth was inversely related to TAWSS, with plaque progression at regions exposed to low TAWSS (0.03 ± 0.01 mm) and plaque regression in regions exposed to high TAWSS (-0.04 ± 0.01 mm). An opposite trend was observed for RRT, with plaque regression in regions exposed to low RRT (-0.04 ± 0.01) and progression in regions exposed to high RRT (0.03 ± 0.01 mm). Regions exposed to low and intermediate OSI and CFI demonstrated plaque regression, whereas

Table 5.1: *Patient demographics and clinical characteristics of the study population at baseline.*

General	
Number of patients	14
Age, yrs, median (IQR)	62 (56 - 68)
Male/female ratio	13/14 (92,9%/7,1%)
Body mass index, BMI, median (IQR)	26 (25 – 30)
LDL [mmol/L]	2.52 (2.23 – 3.01)
Risk factors	
Diabetes mellitus [n(%)]	4 (28,6%)
Hypertension [n(%)]	4 (28,6%)
Hypercholesterolemia [n(%)]	9 (64,3%)
current smoking [n(%)]	4 (28,6%)
previous smoker [n(%)]	4 (28,6%)
positive family history [n(%)]	7 (50%)
Previous stable angina [n(%)]	6 (42,9%)
previous MI [n(%)]	3 (21,4%)
previous PCI [n(%)]	4 (28,6%)
previous statine use [n(%)]	9 (64,3%)
Indication for coronary angiography	
Unstable angina	7 (50%)
NSTEMI	6 (42,9%)
STEMI	1 (7,1%)
Non-culprit coronary artery	
Left anterior descending	6 (35,7%)
Left circumflex	4 (28,6%)
Right coronary artery	5 (35,7%)

Table 5.2: *Vessel specific thresholds, based on tertiles, the lower and upper thresholds are depicted for the following five shear stress metrics: time-averaged wall shear stress (TAWSS), oscillatory shear index (OSI), relative residence Time (RRT), crossflow index, and transverse wall shear stress (transWSS).*

	TAWSS [Pa]		OSI·10-3 [-]		RRT [Pa^{-1}]		CFI [-]		transWSS [Pa]	
Vessel	Low	High	Low	High	Low	High	Low	High	Low	High
1	1.34	2.29	0.38	5.59	0.50	0.96	0.03	0.10	0.05	0.10
2	0.79	1.12	0.14	0.69	0.91	1.31	0.02	0.05	0.02	0.04
3	0.27	0.40	0.19	1.44	2.53	3.97	0.02	0.07	0.01	0.02
4	0.31	0.43	0.14	0.68	2.35	3.30	0.02	0.04	0.01	0.02
5	1.30	2.40	0.40	7.96	0.43	1.36	0.03	0.11	0.05	0.10
6	0.51	1.06	1.20	30.82	1.03	2.34	0.05	0.18	0.05	0.10
7	0.84	1.36	0.42	4.56	0.74	1.35	0.04	0.11	0.04	0.10
8	0.38	0.56	0.31	1.10	1.81	2.75	0.03	0.05	0.01	0.02
9	0.37	0.53	0.44	13.23	1.98	3.18	0.03	0.12	0.02	0.04
10	0.69	0.86	0.06	0.23	1.18	1.46	0.01	0.02	0.01	0.02
11	1.31	1.98	0.31	1.25	0.52	0.80	0.03	0.06	0.05	0.08
12	0.33	0.43	0.02	0.17	2.35	3.09	0.01	0.02	0.00	0.01
13	0.55	0.88	0.06	0.57	1.17	1.82	0.01	0.04	0.01	0.02
14	0.55	1.49	1.93	37.55	0.73	2.43	0.06	0.19	0.05	0.08
15	0.99	1.58	0.54	1.89	0.65	1.06	0.04	0.07	0.05	0.08
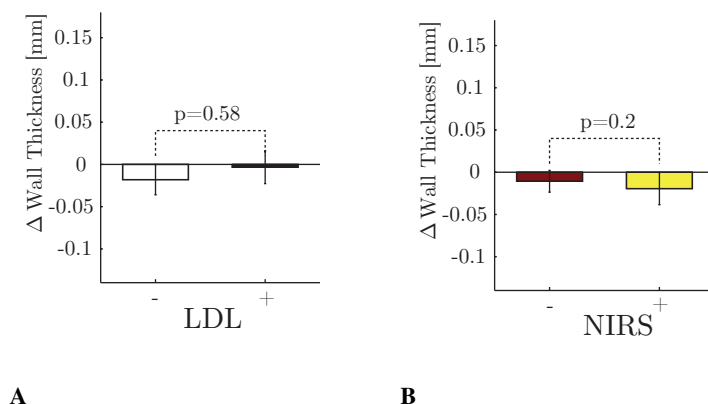
Figure 5.3: *Change in wall thickness (mm) after one year follow-up of A) patients with low LDL levels (white) and for patients with high LDL levels (black), and B) NIRS negative (red) and NIRS positive regions (yellow). Error bars are the standard error.*

no significant plaque progression was observed for the regions exposed to high OSI or CFI.

The highest positive predictive values for plaque progression were also observed for low TAWSS (43%) and high RRT (42%). Interestingly the PPV of the other shear stress metrics (OSI and CFI) was only slightly lower Table 5.3.

5.3.2 The influence of LDL concentration on shear stress related plaque progression

To assess a potential synergistic effect of shear stress and circulating LDL levels on change in plaque size, the relationship between plaque progression and TAWSS, RRT, and transWSS was shown in Figure 5.5 for patients with low and high LDL levels. For both LDL levels a step-wise relationship between plaque progression and all the shear stress metrics was observed, except for the transWSS. No significant difference on plaque progression was observed in regions exposed high TAWSS (p=0.62), low RRT (p=0.60), low transWSS (p=0.51), or high transWSS (p=0.80) for low versus high LDL levels. However, in regions exposed to high RRT (p=0.17) and low TAWSS (p=0.18) the higher LDL level tended to augment the plaque progression but this didn't reach statistical significance. The PPVs in the patients with high circulating LDL levels were slightly

Figure 5.4: *Change in wall thickness (mm) after one year follow-up for each low, intermediate, and high shear stress group for the five different parameters: A) Time-average wall shear stress (TAWSS), B) Oscillatory shear index (OSI), C) Relative residence time (RRT), D) Cross-flow index (CFI), and E) Transverse wall shear stress (transWSS). Error bars are the standard error. p<0.05: low versus intermediate (∗), intermediate versus high (#) and low versus high (†).*

Table 5.3: *Positive predictive value (PPV) for plaque progression (>0.1 mm) for each individual shear stress parameters low time-average wall shear stress (TAWSS), high oscillatory shear index (OSI), high relative residence time (RRT), high cross-flow index (CFI), and high transverse wall shear stress (transWSS). Furthermore, the PPV is the shear stress metrics are provided colocalized with NIRS positive regions and the PPV values are provided of the group of participants with high circulating LDL levels.*

	Positive predictive value (PPV) for plaque progression [%], >0.1 mm Δ wall thickness		
	Shear stress	Shear stress with high circulating LDL levels	Shear stress with positive NIRS signal
Low TAWSS	43%	47%	48%
High OSI	42%	39%	47%
High RRT	44%	47%	49%
High CFI	42%	39%	47%
High transWSS	36%	32%	41%

increased compared to the shear stress metrics alone (Table 5.3).

5.3.3 The influence of NIRS in the plaque on shear stress related plaque progression

In order to investigate the additive value of NIRS information, on top of shear stress, for plaque progression estimation, regions were selected that were NIRS positive or NIRS negative and were co-localized with low, intermediate, or high shear stress. The results on plaque progression for each shear stress metric for NIRS negative (red) and NIRS positive regions (yellow) is shown Figure 5.6

For both the NIRS negative and the NIRS positive regions a stepwise relationship was observed between plaque growth and TAWSS and RRT, similar to TAWSS and RRT alone. Interestingly, the presence of lipids (positive NIRS signal), amplified this stepwise decreasing pattern of plaque growth versus TAWSS; the positive NIRS regions tend to show more plaque progression (p=0.07) in the low TAWSS regions and more plaque regression (p=0.10) in the high TAWSS regions than the NIRS negative regions. The opposite is true for RRT with significant more plaque progression (p=0.012) in regions exposed to high RRT, and a trend towards more plaque regression in regions exposed to low RRT
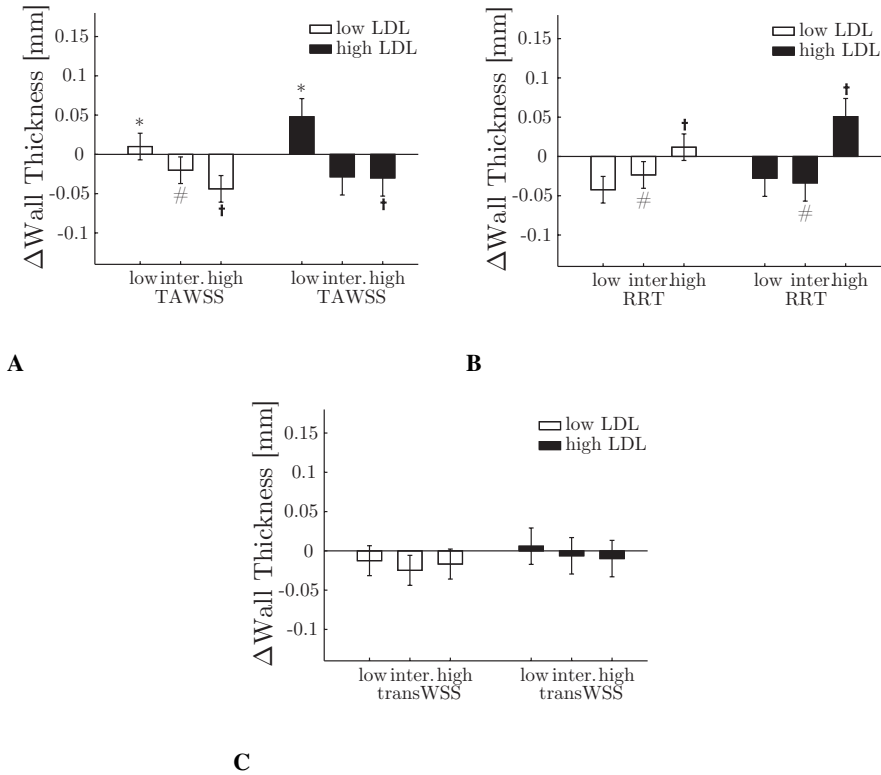
Figure 5.5: *Change in wall thickness (mm) after one year follow-up for each low, intermediate, and high shear stress group for: A) Time-average wall shear stress (TAWSS),B) Relative residence time (RRT), and C) transverse wall shear stress (transWSS) splitted for patients with low LDL levels (white) and for patients with high LDL levels (black). Error bars are the standard error. p<0.05: low versus intermediate (∗), intermediate versus high (#) and low versus high (†).*
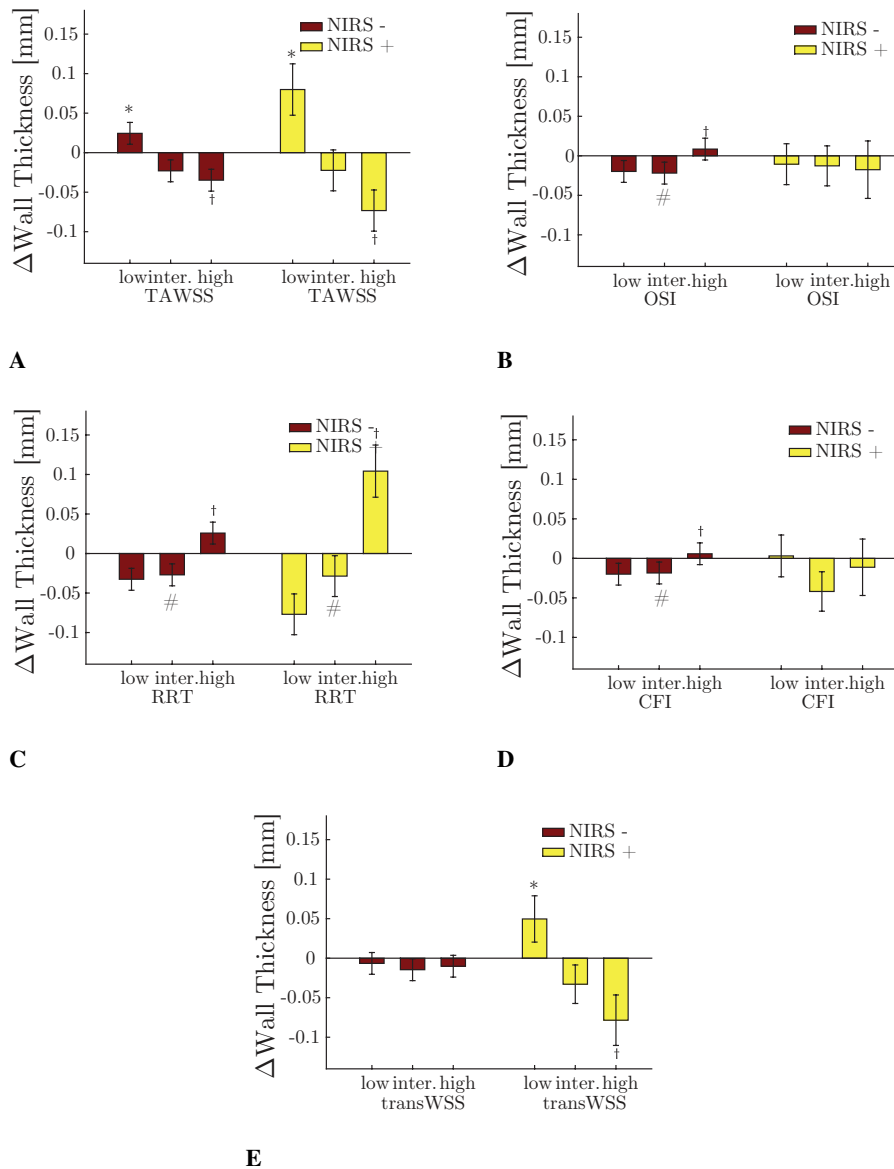
Figure 5.6: *Change in wall thickness (mm) after one year follow-up for each low,
intermediate, and high shear stress group for the five different parameters: A) Time-
average wall shear stress (TAWSS), B) Oscillatory shear index (OSI), C) Relative res-
idence time (RRT), D) Cross-flow index (CFI), and E) Transverse wall shear stress
(transWSS) co-localized with NIRS negative regions (red) or NIRS positive regions
(yellow). Error bars are the standard error. p<0.05: low versus intermediate (∗),
intermediate versus high (#) and low versus high (†).*

(p=0.06) in NIRS positive regions compared to NIRS negative regions. Interestingly, only in the NIRS positive regions, a significant inverse trend between plaque growth and transWSS was observed. Regions exposed to low transWSS showed significant plaque progression (p=0.04), and regions exposed to high transWSS showed significant plaque regression (p=0.02). Remarkably, no effect was observed of NIRS-detected local lipids on the relation between plaque growth and OSI and CFI. Despite the observed effect of NIRS on the relationship between the shear stress metrics and plaque size, the additive value of NIRS, on top of shear stress parameters, for the positive predictive value of plaque progression only slightly improved compared to the shear stress metrics alone (Table 5.3).

5.4   Discussion

In this natural history study, we investigated the influence of the presence of lipid-rich plaques at baseline, as assessed by NIRS invasive imaging, on shear stress related plaque progression in human coronary of ACS patients. Because the multi-directionality of shear stress is gaining attention for its involvement in plaque progression, we also investigated a number of multidirectional shear stress parameters. The main findings are that 1) plaque progression over a one year follow up is not statistically different in patients with either lower versus higher LDL levels nor in NIRS positive versus NIRS negative regions at baseline, 2) NIRS positive regions show more plaque progression if they are additionally exposed to high RRT or low transWSS, and more plaque regression in regions additionally exposed to high transWSS, 3) in patients with high LDL levels at follow-up the effect of low TAWSS and high RRT on plaque progression was amplified. However it did not reach statistically significance.

In this study, an optimized methodology was used to assess the local shear stress compared to many studies published before (Samady et al., 2011; Stone et al., 2012). In our study, we included side branches in the 3D reconstruction of the coronary arteries. Often, side branches are not included in the shear stress calculations (Bourantas et al., 2018) (Stone et al., 2012) (Vergallo et al., 2014), which is remarkable since plaques are usually formed near side branch regions and affect absolute shear stress values (Li et al., 2015). Therefore, it is not surprising that Sakellarios et al demonstrated that improving the 3D models with side branches to assess the local shear stress distribution contributes to a better prediction of the shear stress related plaque progression (Sakellarios et al., 2017). Our data also confirm this observation with a higher positive predictive value of TAWSS for plaque growth compared to previous studies (Stone et al., 2012). Since most of the studies discard the side branches, our shear stress values might be lower than reported

before. Interestingly, the absolute TAWSS in this study are in quite close agreement with
the previous reported values of TAWSS (Doriot et al., 2000; Pinho et al., 2018; Vergallo
et al., 2014), but lower than previously reported in the study described by Samady et al.
(Samady et al., 2011). However, in this study we found lower multidirectionality values
of all the four multidirectional shear stress metric compared to the study described in
chapter 4 and described by Pinho et al. (Pinho et al., 2018). However, these studies are
difficult to compare since different in flow boundary conditions were used.

Another optimization was to use Doppler-derived velocity measurements at multiple lo-
cations throughout the artery to obtain patient-specific boundary conditions. Interest-
ingly, in the porcine study of this thesis (chapter 6) a similar study protocol was used and
the boundary conditions were also based on Doppler derived velocity measurements in
between side branches, and compared to those data all the shear stress metrics were in
close agreement.

Plaque progression was confirmed in low TAWSS regions and plaque regression was
confirmed in high TAWSS regions (Samady et al., 2011). Moreover, similar as the data
described in Chapter 4 OSI, CFI, and transWSS could not significantly distinguish plaque
progression from regression. Different from chapter 4 a positive trend for RRT was ob-
served, with significant plaque progression at regions exposed to high RRT, which might
be explained by the usage of different boundary conditions. This latter observation is also
in agreement with earlier reports on the positive effect on plaque progression (Rikhtegar
et al., 2012).

At first, we studied the influence of LDL levels on shear stress related plaque growth.
Although, as expected, higher plaque progression was observed in low TAWSS regions
for patients with higher LDL levels compared to patients with lower LDL levels, this
analysis did not reach statistical significance. Indeed, in an atherosclerotic pig model
high cholesterol levels amplified the shear stress related plaque progression (Koskinas
et al., 2013a). This resulted in plaques with high-risk features, such as inflammation, lipid
accumulation and plaque progression especially in the regions exposed to low TAWSS.
However, these studies are difficult to compare: in the study by Koskinas et al. pigs
were used which showed an overall strong plaque growth; the patients described in this
study were treated with with statin therapy, which is standard care, which is known to
result in an overall plaque regression, counteracting the effect of systemic lipid on plaque
progression.

In contrast to systemic lipid levels, we demonstrated a significant synergistic effect of
colocalization of NIRS-detected lipid-rich plaque and (multidirectional) shear stress on

plaque progression. It is unclear why the presence of lipid-rich plaque, as assessed by NIRS, seemed to amplify the observed relationship between plaque progression and TAWSS, RRT and transWSS, but not in combination with the other shear stress metrics. In a case report from our group, we described that NIRS positive regions were most often exposed to high shear stress (Wentzel et al., 2010), but that study did not present plaque progression information. Another study that demonstrated that regions that increased in lipid content over a 12-18 months period (Shishikura et al., 2018), were located at high shear stress. However, the shear stresses from that study were assessed with Doppler measurement under the assumption of a parabolic velocity profile and thereby do not take local differences in shear stress because of the local geometry into account. We excluded regions in which visualization of the wall was not possible because of the presence of calcium in the vessel wall. Since regions of calcium were not included in our analysis, which in general are the regions with the most advanced plaques, this could lead to an overall underestimation bias of wall thickness in the final results. Therefore, the results on plaque growth are only valid for uncalcified regions. The number of patients in this sub study was limited. Therefore, multiple independent regions (n=2291) out of the 15 coronary arteries were analyzed. In the statistics we accounted for the clustering of the data per vessel. Using this approach we obtained statistical significance, despite the limited number of patients. Besides, this study is an exploratory study and therefore the conclusions should be confirmed in a larger patient database.

With the recently available NIRS-IVUS catheter on the clinical market, lipid-rich regions can be identified locally. This study demonstrated that the presence of local lipids acts in synergy with several shear stress metrics on plaque progression, whereas systemic cholesterol levels only showed a moderate effect. These conclusions indicate that NIRS can help to identify the high-risk plaque that will further progress, which has potential to aid in identification of regions that need to be treated to prevent future cardiac events.

5.5 Conclusions

This is the first study to show that intravascular NIRS assessment is of additive value with different shear stress parameters for the estimation of plaque progression in human coronary arteries. Specifically, high RRT and low transWSS are more predictive for plaque progression and high transWSS for plaque regression in NIRS positive regions than NIRS negative regions. Therefore, these data suggest that future studies would benefit from assessment of NIRS in combination with different shear stress parameters for the estimation of regions at risk of plaque growth.

5.6   Funding

5.7   Acknowledgements

The Effect of Multidirectional Wall Shear Stress on Coronary Plaque Development

6

Based on: *Hoogendoorn A, **Kok AM**, Hartman EMJ, Coenen A, Korteland S-A, Gijsen FJH, Duncker DJ, van der Steen AFW, Wentzel JJ. Multidirectional wall shear stress promotes development of advanced coronary plaques with vulnerable characteristics – a pre-clinical serial imaging study. (Submitted).*

ABSTRACT

The purpose of this study was to investigate the influence and predictive value of five (multidirectional) WSS parameters for coronary plaque progression and composition. Adult familial hypercholesterolemic pigs (n=10) were put on a high-fat diet for 12 months and underwent imaging of the three main coronary arteries at three time points (3, 9 and 12 months follow-up). A 3D-geometry of the arterial lumen, in combination with local flow velocity measurements, was used to calculate baseline WSS. For the analysis, arteries were divided into 3mm/45° sectors (n = 3627). Changes in wall thickness and plaque composition were assessed with near-infrared spectroscopy – intravascular ultrasound (NIRS-IVUS) and optical coherence tomography (OCT) imaging, and histology. Half of the pigs developed large, lumen intruding, lipid-rich plaques which were highly associated with low and multidirectional WSS at baseline (p<0.05). All multidirectional WSS metrics had a good predictive value for the development of plaque (43-50%) and this value was even higher for the prediction of advanced fibrous cap atheroma development: 49-61%. This study demonstrates that both low and multidirectional WSS promote the development of large and complex coronary atherosclerotic plaques. The high predictive values of the multidirectional WSS metrics indicate their potential as a clinical marker for vulnerable disease.

6.1   Introduction

Ischemic coronary artery disease (CAD), caused by destabilization and subsequent rupture of atherosclerotic plaques, is predicted to remain the leading cause of death (Mathers and Loncar, 2006). Although the complex process of plaque development is incompletely understood, wall shear stress (WSS) is known to play a key role. WSS is the biomechanical metric that describes the frictional force between blood flow and the endothelial cells covering the arterial wall. Both pre-clinical and clinical studies established the role of WSS in advanced (vulnerable) plaque development. However, this role is complex and sometimes appears contradictory since both low and high WSS have been associated with plaque growth and destabilization (Chatzizis et al., 2008; Corban et al., 2014; Koskinas et al., 2013a, 2009; Peiffer et al., 2013a; Samady et al., 2011; Stone et al., 2018, 2012).

To further elucidate the role of WSS in coronary atherosclerosis, longitudinal imaging studies are crucial. Moreover, since most studies only use time-averaged WSS as a descriptor of disturbed blood flow, the multidirectionality of blood flow, induced by its pulsatile nature in combination with the 3D geometry, is not taken into account. Therefore, in recent years, new WSS metrics have been developed to capture this multidirectional flow behaviour: the oscillatory shear index (OSI), relative residence time (RRT), transverse WSS (transWSS) and its normalized version: the cross-flow index (CFI) (Appendix A). The importance of some of these multidirectional WSS metrics was demonstrated in a few studies (Knight et al., 2010; Pedrigi et al., 2015; Peiffer et al., 2013a,b; Rikhtegar et al., 2012; Timmins et al., 2017). However, transWSS and CFI have never been investigated in a longitunidal imaging study with histopathology.

We now set out to perform a comprehensive study to assess the role of all these metrics in plaque initiation and progression to, for the first time, compare their predictive value. Since patient studies do not allow for multiple invasive imaging procedures and the collection of tissue, we employed a highly relevant porcine model of familial hypercholesterolemia (Thim et al., 2010a). By using adult, full grown pigs, we excluded the influence of growth-related changes in the geometry of the coronaries, important for serial assessment of WSS and plaque size. Serial multimodality invasive imaging, combined with a detailed histological analysis, enabled us to simultaneous assess the relation and predictive value of the five (multidirectional) WSS metrics for the changes in plaque size and composition over time.

6.2 Methods

6.2.1 Subjects

At the age of 34±3 months, familial-hypercholesterolemic Bretonchelles Meishan (FBM) pigs (Thim et al., 2010a) (n=10, castrated males) were put on a high-fat diet (10% lard and 0.75% cholesterol, the National Institute of Agronomic Research, France) that was given in restricted amounts to maintain a constant weight. The day before the imaging procedure, animals were fasted and received an oral loading dose of 300mg carbasalate calcium. On the day of the procedure, the pigs were sedated with an intramuscular injection of a mix of Xylazine (2.25mg/kg, 20 mg/ml) and Zoletil 100 (tiletamine/zolazepam) (6mg/kg, 100 mg/ml). Sodium thiopental (4mg/kg, 50mg/ml) was administered via the ear vein before intubation. For the CT-scan procedure, the pigs were kept under anaesthesia with Sufentanyl (10 μg/kg/h IV). All animals were placed in a supine position and an abdominal vein was cannulated to use for high-pressure contrast infusion during the CT angiography (CTA) scan (192 slice, 3rd generation, dual-source CT scanner (SOMATOM Force, Siemens AG, Germany)). The animal protocol was approved by the local animal ethics committee of the Erasmus MC (DEC EMC109-14-10) and the study was performed according to the National Institutes of Health guide for the care and use of Laboratory animals.

6.2.2 Imaging

At three months of high-fat diet (T1), the 3D geometry of the coronary arteries was assessed by CT angiography (CTA). Subsequently, an invasive imaging procedure was conducted in which near-infrared spectroscopy - intravascular ultrasound (NIRS-IVUS), and optical coherence tomography (OCT) imaging were used to assess the coronary plaque size and composition. For the invasive imaging procedure, anaesthesia was switched to isoflurane inhalation (1–2.5% v/v) after administration of Naloxon to antagonize the Sufentanyl. At the start of the procedure, a sheath was introduced into the carotid artery of the pig. Via this sheath, blood was collected in EDTA and clotting tubes for further analysis. Subsequently, 250mg acetylsalicylic acid and 10,000 units of heparin were administered intra-arterial. Heparin administration was repeated every hour with a dosage of 5,000 units. A guiding catheter (Mach 1, 8F, various types, Boston Scientific, Marlborough, MA, USA) was advanced through the carotid sheath into the ostium of either one of the coronary arteries under angiographic guidance. Before imaging, isosorbide mononitrate (0.04mg/kg, 1mg/ml) was administered via the guiding catheter to induce vasodilation. The position of all imaging catheters was documented by serial monoplane

angiography at different viewing angles. A NIRS-IVUS pullback (TVC Insight Coronary Imaging Catheter, InfraRedX, Burlington, MA, USA) (0.5mm/s) and a 75mm OCT pullback (Dragonfly Optis Imaging Catheter, St. Jude Medical, St. Paul, MN, USA) (36 mm/s) were made in the same coronary regions. During the IVUS pullback, the heart rate was closely monitored and registered for later use in IVUS triggering. A ComboWire (Volcano, Corporation, Rancho Cardova, USA) was used to measure the average peak velocity (APV) downstream of every large side branch in the region that was imaged by NIRS-IVUS. The location of the tip of the ComboWire at the time of the measurement was documented with angiography. APV measurements were obtained at multiple locations in the coronaries.

For all three main coronary arteries (i.e., left anterior descending (LAD), left circumflex (LCX) and right coronary artery (RCA)), the same imaging procedure was performed at T1 and repeated at 9 (T2) and 10 or 12 months (T3) for all pigs. At the last imaging time point, the animals were sacrificed, and the coronary arteries were collected and used for histological analysis.

6.2.3 OCT and IVUS analysis

OCT analysis was performed using QCU-CMS software (version 4.69, LKEB, Division of Image Processing, Leiden University Medical Centre, Leiden, The Netherlands) and plaque composition was assessed every millimetre (1 out of every 5 frames) according to the OCT analysis consensus standards (Tearney et al., 2012). Lumen contours were delineated semi-automatically. Fibrous tissue, lipid-rich tissue or lipid-pools were indicated manually by drawing angles from the lumen centre. Fibrous tissue was indicated when a plaque (WT>0.5mm), presenting as homogeneous and low-attenuation signal with the 3-layered structure still visible was present. A plaque region with an inhomogeneous, slowly attenuating signal and an invisible 3-layered wall structure was classified as lipid-rich. A lipid-pool angle was indicated as a region with a sudden drop in signal with a diffuse border and an overlying signal rich cap structure. Each frame was classified according to its most advanced component as fibrous, lipid-rich or fibrous cap atheroma (FCA). The latter classification was given when a lipid pool was present. Before analysis, the IVUS pullbacks were gated by selecting the frames that were located 6 frames before the R-peak in the ECG signal using in-house developed software. Hereby, changes in lumen size caused by movement of the catheter or by the contraction of the heart were removed. Analysis of the gated IVUS pullbacks was performed using QCU-CMS software. In every gated IVUS frame, vessel wall and lumen borders were delineated semi-automatically with manual correction. Total vessel area (VA), lumen area (LA) and

plaque area (PA=VA–LA) (mm^2) were quantified. Interobserver variability was assessed for the manual segmentation of the plaque area. For this analysis, two independent expert observers (AH and EH) both segmented a total of 1192 IVUS frames derived from multiple different pullbacks of different disease stages. The average intraclass correlation coefficient was high: 0.927 (0.805-0.976).

6.2.4 Histological tissue processing

After the last imaging procedure, the animals were sacrificed and the three main coronary arteries were collected to use for histological analysis. Each coronary artery was sliced into 3 mm blocks which were embedded in Tissue Tek (O.C.T. Compound, Sakura® Finetek, VWR) and were slowly frozen on dry-ice-cooled 2-propanol. The blocks were stored at -80 °C until further processing. Of the proximal side of each block, 20 5μm sections were sliced with a cryostat (Leica 3050s cryostat) and used for histological and immunohistochemical stainings. Haematoxylin and Eosin (HE), Resorcin-Fuchsin or Miller (collagen and elastin) and Oil-red-O (ORO) (lipids) stainings were used for the analyses. An immunohistochemical staining for CD68 (1st antibody (Ab): Bio-Rad, MCA2317GA, mouse anti-pig, 1:1600; 2nd antibody: ready-to-use EnVision™+ System/HRP, K4001, goat anti-mouse; antibody detection: liquid DAB+ Substrate kit (DAKO, K3468)) was used to detect the presence of macrophages. The histological sections taken every 3 mm were classified according to the revised AHA classification (Virmani et al., 2000): no plaque, intimal thickening (IT), intimal xanthoma (IX), pathological intimal thickening (PIT) and fibrous cap atheroma (FCA). For quantification of lipid and macrophage content, lumen, media, and outer wall were manually delineated on every histological image. Positive staining was determined by setting standardized HSB values for each artery. Necrotic core area was delineated manually and was characterised by an area of positive lipid staining and scarce in nuclei and fibrous tissue.

6.2.5 Geometry Reconstruction

The coronary arteries were 3D-reconstructed by fusion of IVUS-derived lumen and wall contours with the 3D CT-centreline, which resulted in a luminal surface and measurements of local wall thickness (WT) (Figure 6.1). The wall thickness (WT) was computed by calculating the distance between the vessel wall and lumen contours. The reconstructed lumen surface together with the local velocity measurements served as input to compute the (multidirectional) WSS metrics using computational fluid dynamics (CFD).
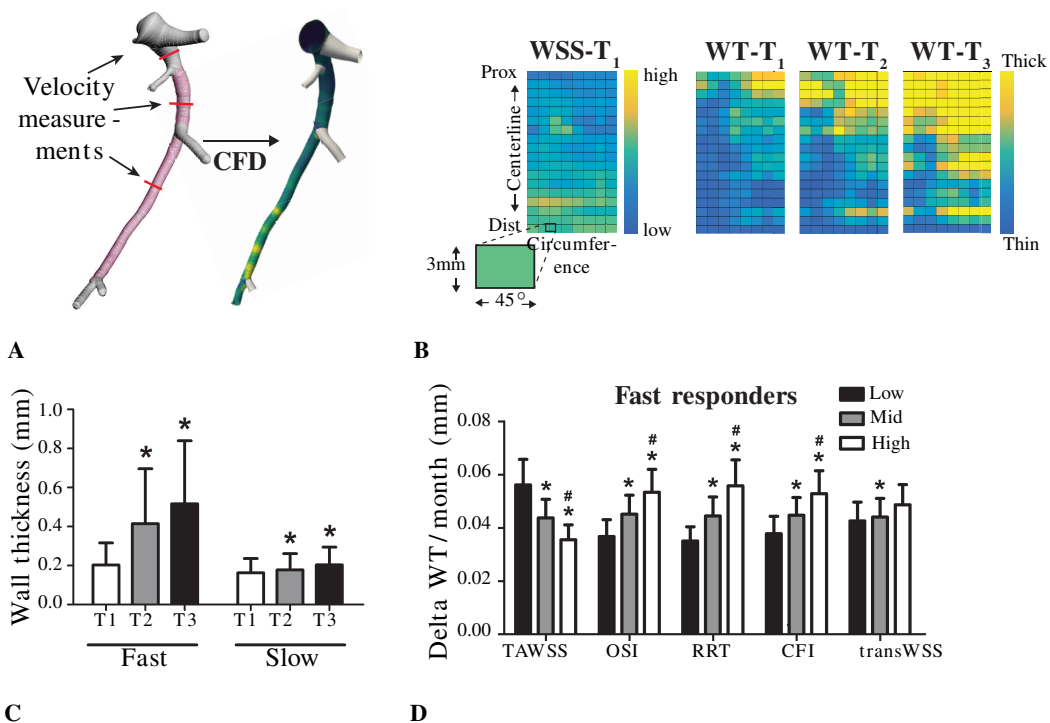
Figure 6.1: *The association between change in IVUS derived plaque size and T1 WSS levels. A) IVUS (pink) and CT (white) contours were fused to reconstruct the grey lumen surface which was used as input for CFD together with local flow measurements, resulting in local WSS values (yellow=high; blue=low). B) From the 3D reconstructions, a 2D map of the WSS levels at T1 and of the wall thickness (WT, T1-T3) was created. For the analysis, the artery was divided in 3mm/45° sectors. C) The mean (±SD) WT at T1-T3 in SR and FR pigs. ∗p <0.05 compared to one time point earlier. D) The relation between the five WSS metrics at T1 and the estimated ΔWT/month (mm) (mean±SEM) (T1-Tlast) in FR pigs. The WSS metrics were divided in low (black bars), mid (grey bars) and high (white bars) tertiles per artery. ∗p <0.05 compared to the low tertile, #p <0.05 compared to the mid tertile.*

In detail, for the 3D reconstruction of the coronary arteries, the CTA scan was reconstructed over a 300 ms time window at diastole to ensure maximal filling of the coronary arteries, including all side branches. Semi-automatic CTA segmentation (Schaap et al., 2009) was performed in Mevislab (Bremen, Germany) whereby the centreline of the coronary artery was determined. The IVUS images were longitudinally and circumferentially registered to the CTA using the location of side branches. Subsequently, the IVUS lumen and wall contours were placed at the corresponding location on the centreline. The side branches and the proximal and distal ends of the artery outside of the IVUS region were segmented on CTA. These CTA contours were scaled to match the IVUS lumen contours of the main artery to account for incomplete filling of the artery or for the blooming effect of the contrast. The IVUS contours (main artery and thus region-of-interest) and CTA contours (proximal and distal section outside the IVUS region and the side branches) were fused to reconstruct a 3D geometry of the luminal surface of the whole coronary artery.

6.2.6   Boundary conditions and computational fluid dynamics

For the computational fluid dynamics (CFD), flow distribution through the side branches was applied at the outlets of each vessel model. The flow distribution was derived from the intravascular Doppler-derived velocity measurements. Quality of these measurements was assessed by an experienced committee (AH, AK, EH, FG, JW) and only reliable measurements were used to determine the velocity rate in the corresponding arterial segment where the measurement was performed. For regions where no (reliable) flow measurements were available, the Huo-Kassab diameter-based scaling law (Huo and Kassab, 2012) was applied to determine the flow distribution between the main branch and the side branch. The most proximal good flow measurement was used for a time-dependent velocity waveform that was imposed on the inlet of the artery. Furthermore, the vessel lumen was considered as rigid and subjected to no-slip boundary condition. Blood was assumed to behave as shear-thinning fluid and was modelled according to the Carreau model (Seo et al., 2005). Each 3D geometry of the lumen at T1 was converted to a tetrahedral mesh in ICEM CFD (v.17.1, ANSYS Inc., Canonsburg, PA, USA) which was used for CFD simulations. The mesh size was determined by a mesh independence study (errors <1% of shear stress were allowed), resulting in a typical element size of 0.05 mm. Unsteady CFD simulations were performed using Fluent (v.17.1, ANSYS Inc.). The solution procedure was carried out following previously described methods in chapter 3 and chapter 5.

6.2.7   Analysis

To assess the association between baseline WSS levels and plaque composition, OCT
and NIRS-IVUS data at Tlast were matched to the T1 IVUS pullback to allow a direct
coupling to the 3D lumen geometry and thus the WSS data. The match was performed
both longitudinally and circumferentially based on the location of side branches. Analy-
sis of the OCT-WSS data and of the NIRS-WSS data at Tlast was performed in 3mm/45°
sectors (Figure 6.1B). For each individual artery, the WSS metrics at T1 were divided
into artery-specific tertiles (low, mid and high) (Table 6.1). Sectors regarded as 'positive'
on OCT (fibrous or lipid-rich) or on NIRS (a 'high probability' (>60%)) were selected.
The distribution of preceding WSS tertiles at T1 was assessed as a percentage of all OCT
or NIRS positive sectors.

To match the histology data with WSS, the 3mm-segments were matched on the IVUS
pullback taken at the Tlast. Matching was performed in longitudinal direction and was
based on the location of side branches and typical plaque components like calcifica-
tions. Between the matching points, the histology blocks were linearly divided. Since
the matching between histology and IVUS was not performed in circumferential direc-
tion, the WSS data of each matched 3mm segment was averaged circumferentially. All
data on plaque growth (ΔWT) were expressed as ΔWT per month on high-fat diet.

6.2.8   Statistics

IBM SPSS Statistics (version 24.0) software was used for statistical analysis. Normally
distributed data are shown as mean±standard deviation (SD) and statistical difference
was determined with an unpaired t-test, a paired t-test, or repeated measures ANOVA
with Bonferroni post-hoc testing, as appropriate. Statistical differences in frequency dis-
tributions were assessed using a Chi-square test. Non-normally distributed data are pre-
sented as median (inter-quartile range (IQR)) and statistical difference was determined
with a Mann-Whitney U test. Statistical analysis of the WSS data was performed us-
ing a generalized-estimators equation model, with WSS as fixed factor and the individ-
ual vessel as random factor, adjusting for cholesterol levels. The Bonferroni correction
was applied to adjust for multiple comparisons between the WSS tertiles. In all figures
that display the association between plaque size and the five WSS-metrics, the estimated
means and standard errors derived from this model are displayed. $p < 0.05$ was regarded
as significant.

Table 6.1: *WSS metric tertile cut-off values*

Pig ID & vessel	TAWSS [Pa] Low	High	OSI [-] Low	High	RRT [Pa^{-1}] Low	High	CFI [-] Low	High	TransWSS [Pa] Low	High
1 LAD	0.855	1.142	0.004	0.013	0.906	1.234	0.081	0.144	0.048	0.090
1 LCX	0.291	0.372	0.0003	0.001	2.824	3.570	0.029	0.049	0.009	0.015
1 RCA	0.629	0.848	0.008	0.023	1.217	1.707	0.127	0.193	0.050	0.090
2 LAD	0.920	1.288	0.002	0.009	0.823	1.211	0.063	0.134	0.059	0.094
2 LCX	0.559	0.592	0.0001	0.0003	1.697	1.794	0.020	0.030	0.010	0.017
2 RCA	0.723	1.030	0.001	0.010	0.983	1.467	0.054	0.115	0.039	0.067
3 LAD	1.057	1.347	0.0004	0.002	0.758	0.977	0.044	0.099	0.035	0.069
3 LCX	0.599	0.703	0.0001	0.0004	1.447	1.708	0.016	0.034	0.010	0.018
3 RCA	0.908	1.212	0.0006	0.003	0.838	1.129	0.042	0.097	0.035	0.064
4 LAD	0.841	1.003	0.0006	0.002	1.026	1.222	0.049	0.087	0.027	0.054
4 LCX	0.962	1.302	0.0002	0.001	0.775	1.095	0.026	0.056	0.025	0.053
4 RCA	0.851	1.029	0.0004	0.001	0.982	1.186	0.036	0.063	0.027	0.042
5 LAD	1.098	1.426	0.0004	0.001	0.712	0.935	0.036	0.069	0.037	0.068
5 LCX	0.678	0.804	0.002	0.004	1.251	1.490	0.059	0.094	0.040	0.060
5 RCA	0.460	0.507	0.001	0.001	1.991	2.196	0.039	0.064	0.015	0.024
6 LAD	0.644	0.744	0.002	0.004	1.374	1.629	0.068	0.112	0.031	0.053
6 LCX	0.980	1.394	0.0002	0.001	0.732	1.037	0.023	0.048	0.026	0.045
6 RCA	0.532	0.617	0.0005	0.002	1.640	1.890	0.037	0.072	0.019	0.034
7 LAD	0.703	0.935	0.0003	0.002	1.109	1.458	0.037	0.084	0.023	0.041
7 LCX	0.398	0.442	0.0004	0.001	2.281	2.536	0.036	0.065	0.015	0.025
7 RCA	0.565	0.722	0.0006	0.002	1.412	1.875	0.042	0.083	0.021	0.042
8 LAD	0.544	0.649	0.007	0.017	1.620	1.914	0.093	0.149	0.029	0.046
8 LCX	0.899	0.976	0.0001	0.0002	1.030	1.117	0.014	0.028	0.013	0.025
8 RCA	1.602	2.232	0.0008	0.003	0.457	0.644	0.059	0.101	0.078	0.147
9 LAD	1.259	1.629	0.004	0.022	0.648	0.896	0.123	0.208	0.097	0.162
9 LCX	0.952	1.261	0.003	0.007	0.837	1.076	0.074	0.133	0.053	0.084
9 RCA	0.572	0.717	0.0004	0.001	1.423	1.795	0.035	0.065	0.020	0.035
10 LAD	0.397	0.492	0.0007	0.006	2.113	2.601	0.043	0.092	0.012	0.023
10 LCX	0.536	0.633	0.0001	0.0003	1.596	1.876	0.018	0.034	0.011	0.017
10 RCA	0.522	0.561	0.0001	0.0003	1.789	1.923	0.014	0.031	0.008	0.018
Average	0.752	0.953	0.002	0.005	1.278	1.571	0.048	0.087	0.031	0.054

6.3 Results

Of the ten pigs, one pig died during feeding, a day after the invasive imaging procedure at T2 due to an unknown cause. One pig had to be sacrificed between T2 and T3 because of suffering from thrombosis in the leg. Data of these pigs have been included in the analysis, although imaging information at T3 is missing. Therefore T2 was considered as Tlast. For the the other pigs, T3 equalled Tlast. In total, 30 vessels relating to 3627 3mm/45° sectors were analysed.

6.3.1 Fast and slow responding pigs

Although all pigs had the same mutation and were fed the same diet, 5 of the 10 pigs developed large, lumen intruding coronary plaques (plaque burden (PB) >40%) (fast responders, FRs) within 9 months, while the other 5 pigs only developed limited atherosclerosis (PB<40%) within 12 months follow-up (slow responders, SR)). The two groups of pigs showed no difference in weight (SRs: 87 kg (85–92) vs. FRs 87 kg (77–93), p=ns) and in cholesterol, LDL, HDL levels (10.7±2.8 vs. 12.9±4.4; 8.7±2.8 vs. 12.2±5.7 and 3.1±0.9 vs. 3.0±0.8 mmol/L in SR versus FR respectively; all p=ns).

6.3.2 Increase in IVUS-measured plaque size was associated with low and multidirectional WSS

Overall, the FRs demonstrated a significant increase of the average WT over the three imaging time points (T1-T3) ($p < 0.001$), which was less pronounced, but also significant in the SRs ($p < 0.001$) (Figure 6.1C). In the FR pigs, coronary segments exposed to low baseline levels of TAWSS exhibited a significantly larger plaque growth per month between T1-Tlast compared to regions with either mid or high TAWSS ($p < 0.05$). Furthermore, in FRs, the multidirectional WSS metrics OSI, RRT and CFI positively correlated with plaque growth, with high multidirectionality resulting in the largest growth (Figure 6.1D). The positive predictive values (PPV) of the WSS metrics for plaque presence (WT>0.5mm) at Tlast were 50% (low TAWSS), 48% (high OSI), 49% (high RRT), 47% (high CFI) and 43% (high transWSS). In contrast, in the SR pigs, no relation was found between the plaque growth rate and all baseline WSS metrics (Figure 6.2) and a PPV analysis was not applied since only 10 segments (of the total of 1747 segments) presented with a WT>0.5 mm.
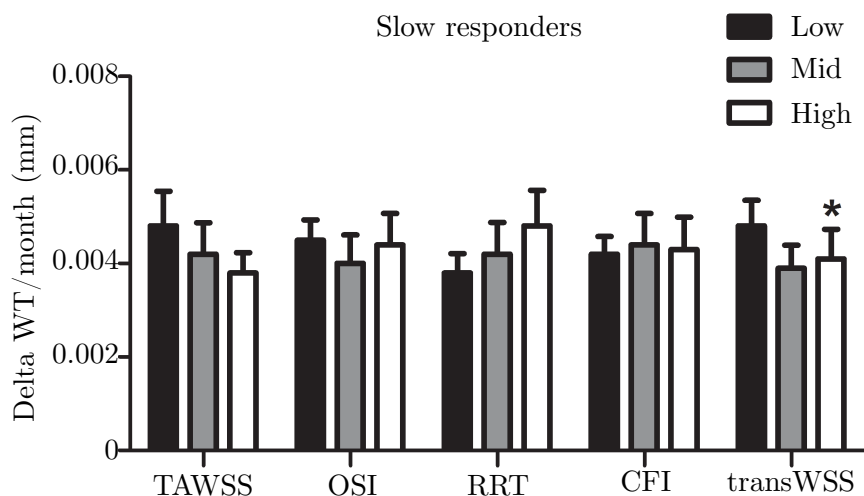
Figure 6.2: *Association between change in plaque size and WSS levels in the SR pigs.*
*p<0.05 compared to the low tertile.

6.3.3 OCT lipid-rich plaques and NIRS-positive plaques were most often preceded by low and multidirectional WSS

Analysis of the NIRS signal at Tlast (Figure 6.3A) showed that 33 sectors derived from 6 arteries of the FRs demonstrated a positive NIRS signal. These NIRS positive sectors were most frequently preceded by low TAWSS (p=0.10) or high OSI (p<0.05), RRT (p=0.08) or CFI (p<0.05) (Figure 6.3B). Only transWSS showed no relation with NIRS-positive plaque development. For the OCT analysis (Figure 6.3A), 2 pullbacks from Tlast had to be excluded due to bad image quality or technical problems. From the remaining pullbacks at Tlast, 668 sectors from 14 arteries of the FRs and 66 sectors from 10 arteries of the SRs showed plaque presence. In the FRs the plaque positive sectors could be characterised as either a fibrous (n=196), lipid-rich (n=469) or FCA (lipid pool) (n=3) plaque (Figure 6.3D). Since the FCAs (with lipid-pool) were scarce, no statistical analysis and thus no WSS analysis could be performed on this plaque type. The development of a fibrous plaque showed no relation with baseline WSS levels in both types of pigs. In contrast, OCT lipid-rich plaques were most frequently preceded by low and multidirectional WSS in the FRs (p<0.05) (Figure 6.3C), but not in the SRs (p=NS, data of the SRs not shown).

A

B

C

D
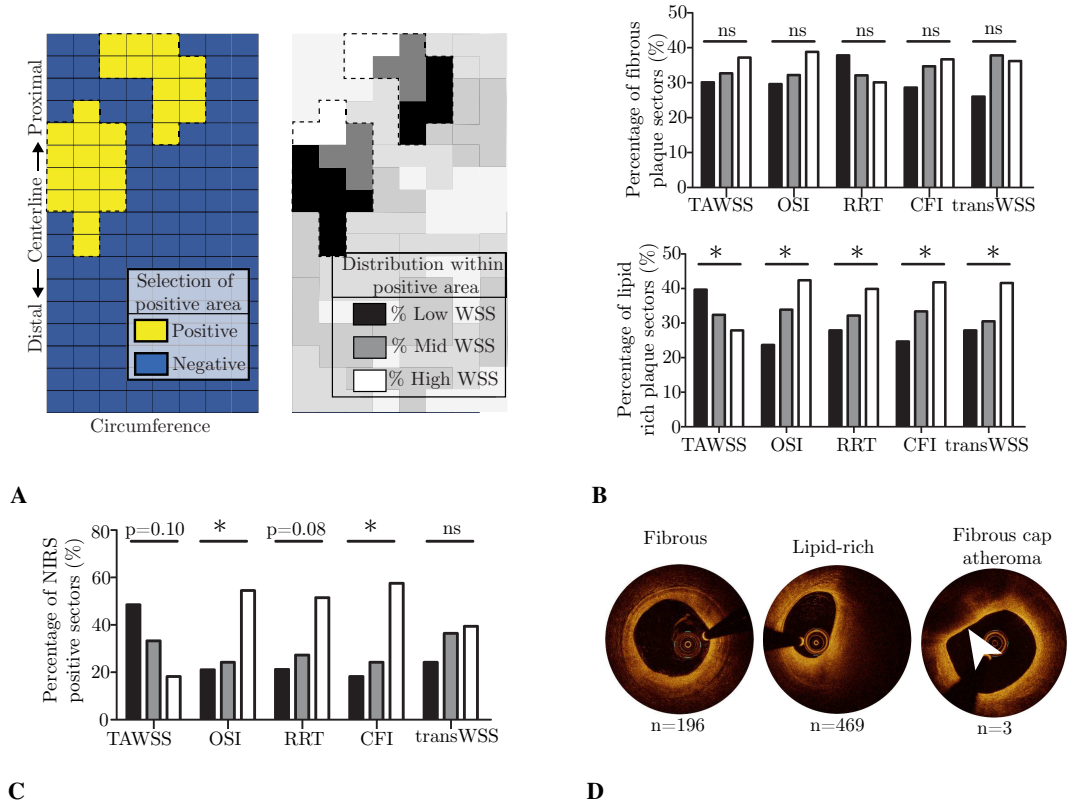
Figure 6.3: *Association between baseline WSS levels and plaque composition detected by OCT and NIRS in fast responders (FRs). A) OCT and NIRS analysis method: all positive 3mm/45° sectors were selected. Within these positive regions, the positive sectors (%) that was preceded by one of the WSS tertiles was quantified. B) The NIRS-positive sectors (%) that was preceded by low (black bars), mid (grey bars) or high (white bars) levels of the respective WSS tertiles. C) The sectors (%) presenting fibrous or lipid-rich plaque that was preceded by low (black bars), mid (grey bars) or high (white bars) levels of the respective WSS metrics. Fibrous plaques displayed no significant relation (p=ns). D) Examples of fibrous, lipid rich and FCA (arrowhead) plaques on OCT. n=number of sectors of FRs presenting with each respective plaque classification at Tlast.*p<0.05 for the overall relation.*

6.3.4 Low and multidirectional WSS promoted the development of advanced histological plaque classes

For a detailed analysis of the association between histological plaque classification, composition and WSS levels, 190 3mm-segments (15 arteries) from FRs and 145 3mm-segments (13 arteries) derived from SRs could be reliably matched. In the SRs, no association was observed between any WSS metrics and the plaque composition (Figure 6.4). In the FRs, the absolute levels of OSI, RRT and CFI were higher in regions where the most advanced plaque type (i.e., FCA) developed, compared to regions with no plaque or IT ($p<0.05$) (Figure 6.5A). The absolute levels of TAWSS and CFI did not differ between the plaque types in the FRs (p=ns, Figure 6.4). Upon division of the WSS metrics into tertiles, regions with either low TAWSS, high OSI or high RRT displayed the most advanced plaque phenotype ($p<0.05$) (Figure 6.5C), while this association was not observed for transWSS and CFI (data not shown). The PPVs for the presence of a FCA were 61% (low TAWSS), 58% (high OSI), 61% (high RRT), 59% (high CFI) and 49% (high transWSS).

These results were supported by a more detailed assessment of the plaque composition in the FRs, in which we observed that in regions with low and multidirectional WSS (OSI, RRT and CFI), plaques presented with the largest lipid, macrophage and necrotic core area ($p<0.05$) (Figure 6.6). Again, transWSS showed no relation with plaque composition (p=NS).

6.4 Discussion

In the present study, we performed an serial, multimodality imaging protocol in conjunction with histological analyses to assess the influence of (multidirectional) WSS on the natural development, progression and composition of coronary atherosclerotic plaques in adult familial hypercholesterolemia pigs. The results of the study demonstrated that: 1) plaque growth and an advanced plaque phenotype as seen on NIRS, OCT and histology, were strongly associated with low and multidirectional WSS at baseline in the fast responders; 2) multidirectional WSS metrics have a good positive predictive value for development of plaque, and an even better predictive value for advanced plaque composition, but only in the fast responders; 3) a large difference was observed between slow and fast responding pigs with regard to plaque development and response to WSS.
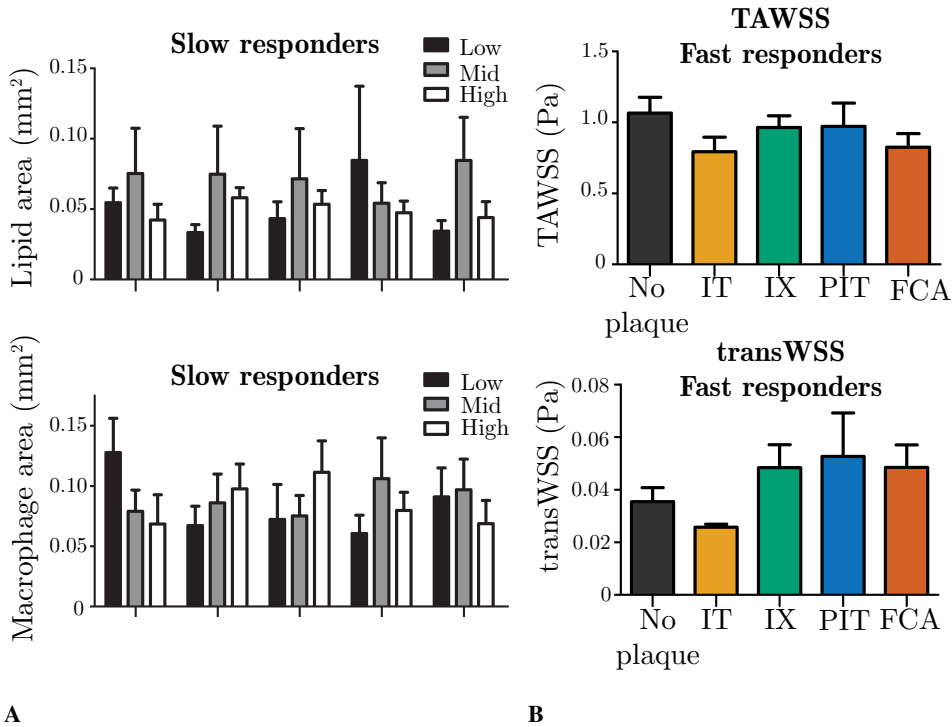
Figure 6.4: *Histological plaque composition and the relation with WSS metrics. A)
The relationship between absolute baseline TAWSS and transWSS levels and the ob-
served histological plaque classification upon Tlast in the FRs. B) The absolute lipid
or macrophage area observed in regions with either preceding low (black bars), mid
(grey bars) or high (white bars) levels of the respective WSS metrics in the SR pigs. No
significant relationships were observed (A+B).*

Figure 6.5: *Relationship between histological plaque classification and preceding baseline (multidirectional) WSS levels in the FRs. A) Histological examples of plaques according to the revised AHA plaque classification. B) Absolute levels of OSI, RRT and CFI at the location of one of the respective plaque types: no plaque, IT, IX, PIT or FCA. p<0.05 compared to no plaque, #p<0.05 compared to IT. C) Distribution of the plaque types over regions with preceding low, mid or high levels of TAWSS, OSI or RRT.*

A

B

C
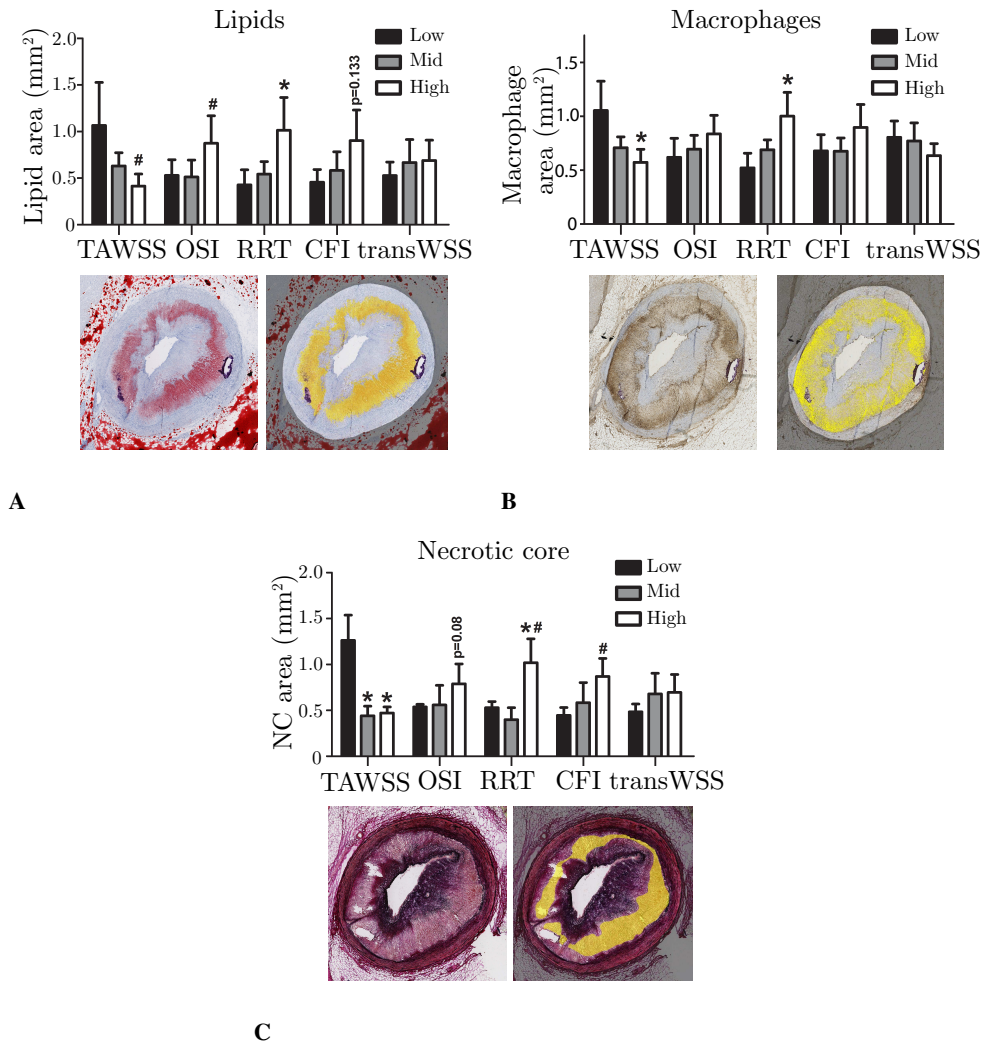
Figure 6.6: *Relationship between histological plaque classification and preceding baseline (multidirectional) WSS levels in the FRs. A) Histological examples of plaques according to the revised AHA plaque classification. B) Absolute levels of OSI, RRT and CFI at the location of one of the respective plaque types: no plaque, IT, IX, PIT or FCA. p<0.05 compared to no plaque, #p<0.05 compared to IT. C) Distribution of the plaque types over regions with preceding low, mid or high levels of TAWSS, OSI or RRT.*

6.4.1 Relation of low and multidirectional WSS with plaque growth and composition

It is vital to distinguish the role of WSS in the different stages of atherosclerosis when comparing results from WSS studies (Wentzel et al., 2012). In clinical studies, the presence of advanced disease and larger stenosis degrees lead to local elevation of the WSS which inevitably results in a stronger association between large, advanced plaques and high WSS. In these advanced disease stages, WSS serves as a marker for the localization of the largest and most vulnerable plaques, as very recently confirmed in a study of Kumar et al. (2018), or as a predictor for plaque destabilization (Slager et al., 2005). Furthermore, since patients with advanced disease are often put on statin treatment, known to induce plaque regression, studying the role of WSS in plaque progression in these studies cannot be seen independent from optimal medical therapy. Pre-clinical studies, or clinical studies that exclude narrowed arterial regions, are the only way to assess the causal role of WSS in plaque intitation and progression. In this discussion, considering the scope of our study design, we focussed on the role of (multidirectional) WSS in early disease development.

Previous studies on low TAWSS and high OSI or RRT tend to confirm the hypothesis that plaques develop and progress in regions with low and multidirectional WSS (Chatzizisis et al., 2008; Koskinas et al., 2010; Peiffer et al., 2013a). However, since absolute WSS levels are highly dependent on the used methodology, a reliable comparison of the effect of multidirectional WSS parameters is only possible within one study. With this study, we are the first to assess and compare the effect of five different (multidirectional) WSS metrics on plaque development and composition. With regard to the development of plaque, we showed that low TAWSS and high levels of OSI, RRT and CFI lead to the largest plaque growth. Only transWSS did not demonstrate a relation with plaque development, contrasting the results presented by Peiffer et al. (2013b) in rabbit aorta. However, since CFI, the normalized version of transWSS, did demonstrate a clear relation in our study, the magnitude of WSS perpendicular to the mean WSS vector does influence plaque growth.

Not only plaque size, but also plaque composition is important for risk-assessment of coronary events (Garcia-Garcia et al., 2014). We are the first pre-clinical study that applied invasive imaging, together with an extensive histological analysis to assess the effect of WSS on plaque composition. NIRS is the first in vivo imaging technique that can detect lipid core plaques and thereby also FCAs (Gardner et al., 2008). In two human studies with advanced disease, a correlation has been shown between (the development of) a positive NIRS signal and high TAWSS (Shishikura et al., 2018; Wentzel

et al., 2010). Such a relation has never been described for earlier disease stages. In this study, we demonstrated a trend between NIRS positive plaques and preceding low TAWSS. Furthermore, multidirectional WSS metrics even showed a stronger effect since NIRS-positive plaque development was significantly more often preceded by high OSI and CFI levels compared to low multidirectional WSS. However, since the number and size of NIRS-positive regions was limited, our results on the correlation between WSS and NIRS should be interpreted with care.

The relationship between (multidirectional) WSS and lipid-rich plaques derived from NIRS imaging was confirmed by OCT. Unfortunately, the number of OCT-detected FCAs was much lower compared to our histological findings. Reassessment of the accompanying histological data revealed that many lipid-rich necrotic cores are apparently invisible on OCT, hypothetically because they are 'shielded' by a layer of lipids in the cap structure.

Previous pre-clinical studies applied histology to determine the relation between plaque composition and WSS. These studies demonstrated that the development of advanced plaques with lipid and inflammatory cell infiltration was associated with low WSS (Chatzizisis et al., 2008; Koskinas et al., 2010; Millon et al., 2015; Pedrigi et al., 2015). Furthermore, Pedrigi et al. (2015), who used a perivascular cuff to induce atherosclerosis formation, concluded that besides low WSS, also a variant metric of the transWSS was associated with advanced plaques. Unfortunately, implantation of a perivascular device may inadvertently induce damage and stress to the outer vessel wall and thereby interfere with the process of plaque development, independent of WSS levels. In light of these considerations, we elected to use a porcine model of natural disease development. With this model, we demonstrated with histology that advanced plaques with a higher lipid and inflammatory cell content and larger necrotic cores developed in regions with low WSS, confirming the results from previous studies (Chatzizisis et al., 2008; Koskinas et al., 2010; Millon et al., 2015; Pedrigi et al., 2015). Furthermore, we demonstrated that the multidirectional metrics OSI, RRT and CFI, but not transWSS, were strongly associated with the development of plaques with an advanced and complex composition.

6.4.2   The predictive value of multidirectional WSS metrics

To apply WSS measurements in the clinic, establishing its positive predictive value for plaque progression is important, which has been assessed in several studies. The PREDICTION study (Stone et al., 2012) reported a positive predictive value of low TAWSS of 25% in comparison to 50% in our study, which could be explained, at least in part, by the fact that all patients were put on statin treatment. In stable ACS patients, Rikhtegar

et al. (Rikhtegar et al., 2012) reported that multidirectional WSS parameters might be a better predictor for plaque localization at one time point than low TAWSS (low TAWSS: 31%; high OSI: 35%; high RRT: 49%). In our study, where the effect of WSS metrics on plaque development over time was assessed, we show that low TAWSS and high RRT are the best predictors, partially contrasting the results of Rikhtegar et al. Finally, while most studies have evaluated the PPV of WSS for plaque size, we are the first to assess the predictive value of WSS for plaque composition. Interestingly, we observed that WSS might be an even better predictor for the development of FCA than for plaque size (PPV of 61% versus 50% for TAWSS and RRT).

6.4.3 Fast and slow responders: difference in plaque growth and response to WSS metrics

We observed clear differences in plaque size and growth, but also in the response to WSS between SR and FR animals. Although the absolute WT was much lower in the SRs compared to the FRs, the growth rate of the SRs resembles the growth rate seen in humans (Samady et al., 2011). So far, no biological reasons, including cholesterol levels and diet, could be identified for the difference between both groups. Interestingly, and in stark contrast to the plaque development in the FRs, the development of plaques in SRs was independent of WSS. Unfortunately, comparison of these results to other pre-clinical WSS literature is difficult, since animals that present with limited plaque growth are regarded as 'non-responders' and are often not taken into account for analysis. To make an honest assessment of the role of WSS in plaque development, we retained the SR pigs in the analysis. The large difference in response to WSS between FRs and SRs could provide a very interesting basis for the discovery of biological factors that potentially interact with the effect of WSS on coronary plaque development.

6.4.4 Limitations

The present study has a number of limitations. First, the number of pigs used in this study was small and the unexpected split into fast and slow responders further reduced the number of arteries that was available to investigate advanced plaque development. However, multiple segments within one coronary artery were analysed to capture the local WSS effect. A generalized estimated equations model was applied to correct for remaining dependencies. Using this approach, a statistically significant effect of multidirectional WSS on plaque development could be identified. Furthermore, since the absolute levels of OSI, CFI and transWSS were low, the division of the WSS tertiles could be considered as somewhat artificial. Still, we did find significant relations between these metrics and

both plaque size and composition.

6.4.5 Conclusion

The present study combined detailed invasive imaging and histopathology to demon-
strate that natural plaque development and advanced plaque composition were highly
associated with low and multidirectional WSS metrics (i.e. OSI, RRT and CFI). Only
transWSS could not be linked to advanced plaque growth. While the predictive values
of the individual multidirectional WSS metrics for plaque growth were high, advanced
plaque composition was even more reliably predicted by multidirectional WSS metrics.
This highlights the potential of multidirectional WSS as a predictive clinical marker for
vulnerable disease.

Part 2:
Wall stress

7

WALL STRESS IN CORONARY ATHEROSCLEROTIC PLAQUES WITH AN INCOMPLETE NECROTIC CORE GEOMETRY

ABSTRACT

In vivo plaque geometry and composition of coronary arteries can merely be obtained via intravascular imaging. Only optical driven imaging techniques have sufficient resolution to visualize the fibrous cap, but due to limited penetration depth deeper components such as the backside of the necrotic core (NC) are generally not visible. This study investigated whether peak cap stresses can be approximated by reconstructing the backside of the NC. Manual segmentations of coronary histological cross sections served as a geometrical ground truth and were obtained from seven patients resulting in 73 NCs. Next, the backside was removed and reconstructed according to an estimation of the relative necrotic core thickness (rNCt). The rNCt was estimated at three locations along the NC angle and based on either group averaged parameters or plaque specific parameters. Stress calculations were performed in both the ground truth geometry and the reconstructed geometries and compared. Good geometrical agreement was found between the ground truth NC and the reconstructed NCs, based on group averaged rNCt estimation and plaque specific rNCt estimation, measuring the NC area difference (25.1% IQR: 14.0 – 41.3% and 17.9% IQR: 9.81 – 32.7%) and similarity index (0.85 IQR: 0.77 – 0.90 and 0.88 IQR: 0.79 – 0.91). The peak cap stresses obtained with both reconstruction methods showed a high correlation with respect to the ground truth, $r^2 = 0.91$ and $r^2 = 0.95$, respectively. For high stress plaques, the peak cap stress difference with respect to the ground truth significantly improved for the NC reconstruction based plaque specific features (6%) compared to the reconstruction group averaged based (16%). In conclusion, this study showed that reconstruction of the backside of a NC can be performed using either group averaged NC data or plaque specific NC data.

7.1   Introduction

The main cause of myocardial infarction is coronary plaque rupture. Not all coronary
plaques will rupture; therefore it is of imminent importance to distinguish rupture prone
plaques from stable plaques. Pathological studies showed that rupture prone plaques con-
sists of a large necrotic core (NC), a thin fibrous cap and often are positively remodeled
(Schaar et al., 2004). However, geometric and compositional information appeared to be
insufficient to predict cardiovascular events, therefore new rupture risk parameters should
be investigated (Stone et al., 2011).

From a biomechanical point of view, plaque rupture occurs when the stresses in the cap
exceed the strength of the cap. Mechanical studies have shown that stress is an important
indicator for plaque vulnerability (Gijsen and Migliavacca, 2014; Tang et al., 2009; Wang
et al., 2015). Therefore, determining stresses in a cap can aid in predicting cap rupture. A
common technique to calculate stresses is by using finite element analysis (FEA). In order
to accurately calculate these stresses, blood pressure, material properties, and geometric
factors are required. The most important geometric factor influencing peak cap stress
(PCS) predictor is cap thickness, but also lumen size and shape and NC size and shape
(Akyildiz et al., 2016, 2011; Finet et al., 2004; Gao and Long, 2008; Loree et al., 1992;
Ohayon et al., 2008).

To capture plaque geometry and composition in vivo, intravascular imaging is required.
The only imaging techniques with sufficient resolution to accurately visualize the cap
thickness are optical driven, such as optical coherence tomography. However, necrotic
core tissue highly attenuates light, and thereby limits the penetration depth. Conse-
quently, the NC geometry can become obscured, and thus is often only the front side
of the NC visible. In order to allow FEA the complete geometry of the NC is essen-
tial.

The goal of this study was to investigate whether peak cap stresses can be approximated
by reconstructing the backside of the NC. Therefore, we used a three-step approach: 1) a
model was generated based on the histology data to estimate the NC thickness at several
locations along the NC angle, 2) the backside of the NC was artificially removed and re-
constructed based on characteristics of the NCs, 3) stresses and geometries of the plaque
containing the reconstructed NC geometries were compared with the plaque containing
the ground truth NC.

7.2   Material and methods

In order to reconstruct the backside of the NC, MATLAB (version 2014a, Mathworks Inc., Natick, MA, USA) was used. Six steps were taken: 1) manual segmentation of the coronary plaque geometry from histology ('ground truth'), 2) geometrical characterization was performed of all the plaques and NCs: to determine the group average (relative) NC thickness at the center (50%) of the NC angle (midcap) and ±25% of the NC angle (sidecaps) and corresponding plaque specific properties: cap thickness, NC angle, and intima-media thickness (IMT) were determined, 3) plaque specific relation between the relative NC thickness (rNCt) and plaque specific properties was determined with a Generalized Estimation Equation (GEE) model, 4) the backside of the NC geometry was removed and thereafter reconstructed based on group averaged rNCt estimation and a plaque specific rNCt estimation, 5) geometry assessment: the reconstructed NC geometries were compared with the ground truth geometry, and 6) the effect of the reconstruction on the PCS calculations was evaluated. All steps are explained in more detail below.

7.2.1   Histology

Histology was used to obtain the NC geometry in atherosclerotic plaques to serve as the geometrical ground truth. It is important to obtain representative plaque cross-sections. Therefore, we used coronary plaque data of seven patients who died from severe coronary artery disease. The specimens were obtained from CVpath (CVPath Institute, Inc., Gaithersburg, MD, USA). Only those cross-sections that contained at least one NC were included. The coronary arteries were perfusion fixed in formalin at 100 mmHg prior to the histological preparation. Each consecutive cross section had a distance of at least 200 µm to the next cross section in the longitudinal direction. In total, 54 cross sections (5 µm in thickness) were obtained from 13 different arteries of which 31 plaques included one necrotic core and 21 contained two NCs. When multiple NCs were present in a cross section, the NCs were treated separately; this resulted in 73 plaque geometries. A Modified Movat pentachrome staining was used to identify different plaque components. The lumen, NC, intima, media and adventitia layer were manually delineated. The ground truth contours were finalized during a consensus meeting.

7.2.2   Plaque and necrotic core characterization

Geometrical characterization of the atherosclerotic plaque was performed by determining the geometrical properties of the plaque and the NC, see Figure 7.1A. First, the minimum

cap thickness and the front side of the NC were determined from the perspective of the lumen center, see Figure 7.1B. Second, the NC angle was determined as the angle of the front side of the NC geometry, also with respect to the center of the lumen. Third, at three locations along the NC angle, the NC thickness was determined: at the center (50%) of the NC angle (midcap) and ±25% of the NC angle (±sidecap). Also, the cap thickness and IMT were determined at these corresponding positions, see Figure 7.1A.

7.2.3   Group averaged necrotic core thickness estimation

From the plaque and NC characterization we obtained group averaged the NC thicknesses at three different locations: midcap and both sidecap positions. To make it robust for all plaque sizes, these NC thicknesses were divided by their corresponding IMT, hereafter referred to as relative NC thickness (rNCt). The median of the whole plaque group was calculated for the midcap position and the median was calculated for both sidecap positions. These two rNCt were then used in the NC reconstruction, this method is hereafter referred to as the group averaged method.

7.2.4   Plaque specific necrotic core thickness estimation

Since, we assume that the NC thickness is depends on plaque characteristics, we developed a method that estimates the NC thickness on a plaque specific level. Generalized Estimation Equation (GEE) model was used to determine a relationship between NC thickness and plaque specific parameters. In order to determine if each parameter in the model significantly contributed, the covariance matrix of β was determined. This was done by a method previously described by Liang and Zeger et al. (Liang and Zeger, 1986). To also make the GEE model more robust, the rNCt was calculated. The plaque specific geometrical parameters used as input for the GEE model consist of NC angle, IMT, and cap thickness. We assume that the rNCt is symmetrical around the center of the NC angle, therefore two relationships were derived; one for the midcap and one for the combined sidecap positions. This relationship was defined as:

$$
\begin{aligned}
rNCt_i = {} & \beta_0 + \beta_{NCangle} * NCangle[rad]_i + \\
& \beta_{IMT} * IMT[\mu m]_i + \beta_{capT} * capT[\mu m]_i
\end{aligned}
\tag{7.1}
$$

with i indicating the relation at midcap or ±sidecap and β the constants determined by the GEE model. The GEE model was corrected for correlation amongst cross sections within an artery (Ratcliffe and Shults, 2008). Next, for each plaque the rNCt at the midcap and side cap positions was determined with the GEE model.
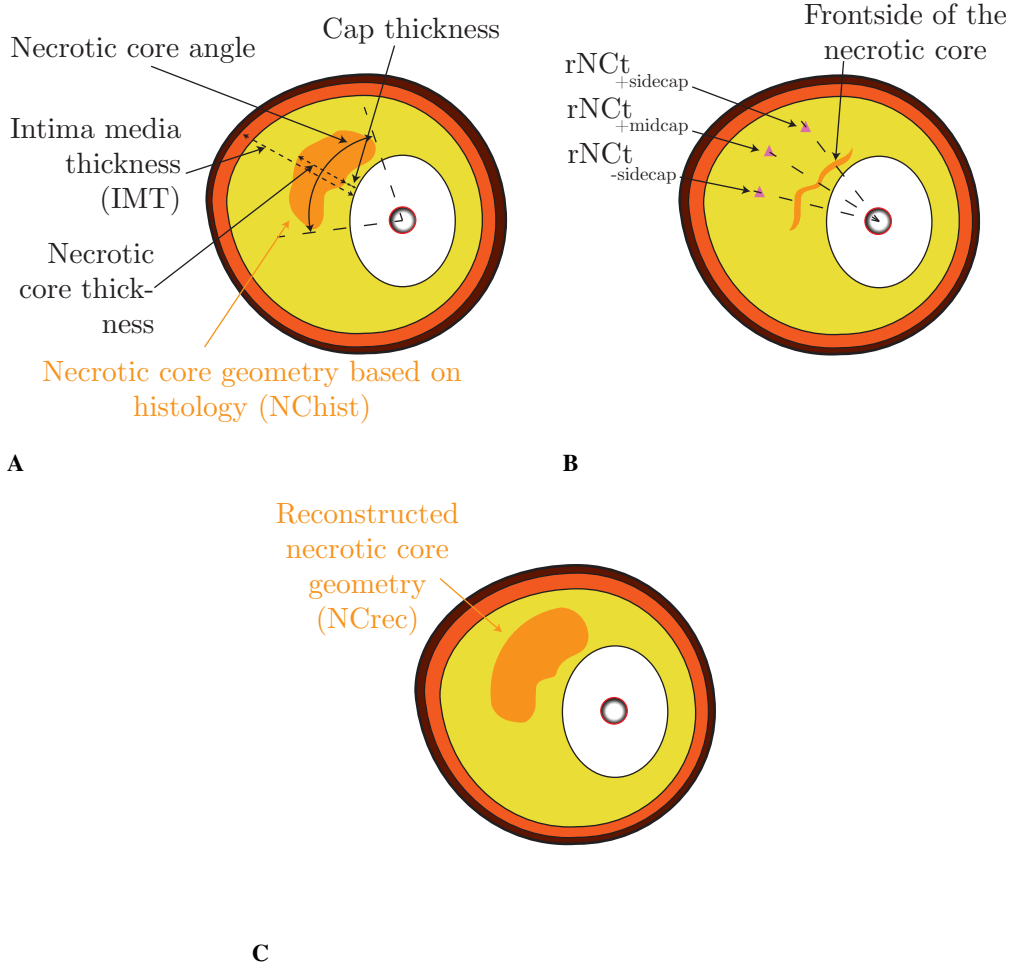
Figure 7.1: *A schematic overview of the coronary plaque (A) and the corresponding reconstruction methodology (B and C). The adventitia (brown), media (dark orange), intima (yellow) and the necrotic core (orange) were obtained by segmentations of the ground truth. A) overview of the plaque specifics properties, B) the backside is removed and the relative NC thicknesses (rNCt) (pink triangles) were calculated for the mid and sidecaps, and C) the reconstruction of the necrotic core.*

7.2.5 Reconstruction

Optical driven imaging techniques suffer from fatty tissues, since they highly scatter and absorb light, therefore limiting visualization beyond the NC. Thus, only the front side of the NC can be visualized reliably. To account for this only the front line of the NC was kept. This was done by drawing a line from the lumen center to each point in the NC. If the point was not the first intersection it was removed, in this way the backside of the NC was removed. The NC reconstruction was performed based on the group average rNCt estimations and the plaque specific rNCt estimation. The rNCt (at midcap and sidecaps) were converted to the absolute NC thickness and were placed at the corresponding positions. From histology we observed that NCs often have rounded features at the edges. Therefore, a part of a circle was attached to the edges of the NC, this also prevents geometric discontinuities in the reconstructed NC. The radius and angle of this part of the circle was empirically determined by optimizing the overlapping areas of all the reconstructed NCs with the ground truth areas. The optimized value for the angle was 30 [°] and the radius was dependent on the NC angle: $0.14[mm] * NCangle[rad]$, these values were used for all the NC reconstructions. A visualization and description of how the center point of this circle was obtained is given in Figure 7.2.
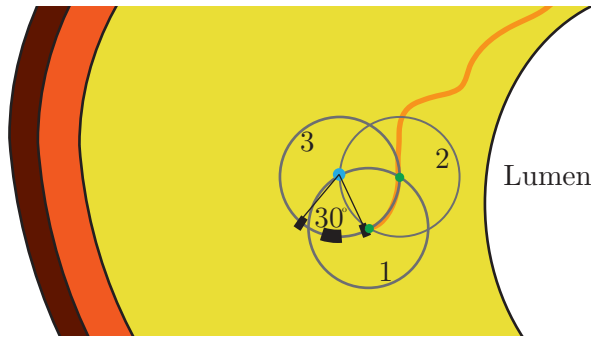
Figure 7.2: *Schematic illustration of the creation of the side of the NC using part of a circle. To calculate the center point of the circle used for creation of the side of the NC a combination of circles was used. The center of circle 1 was located at the edge of the necrotic core. One point in circle 1 intersects the cap, and this point is used as center point for circle 2. Then the two circles intersect at two locations, and the intersection most distant from the lumen was the center point of the final blue circle (3) for the side of the necrotic core (blue dot). Together with the empirically determined radius and angle the side can be reconstructed, see the black dotted line.*

Hereafter the backside is closed with the attached part of the circle by forcing the poly-

nominal function to go through the side of the attached part of the circles (Figure 7.1C). In case the polynomial function intersects the media layer (n=20 for the group average rNCt, n=8 for the plaque specific rNCt estimation), the NC area outside the intima is removed. Since it is not physiological that the NC is attached to the medial layer, a small layer was removed from the NC. In order not to alter the predicted geometry this layer was kept very small (10 µm).

7.2.6 Geometry analysis

To investigate to what extent the reconstructed NC geometry corresponds with the histology based NC geometry, two measures were used: 1) the similarity index (SI) and 2) the relative difference in NC area, $\Delta A(\%)$. The SI is a measure for overlap, defined as:

$$SI = \frac{2 * (A_{GT} \cap A_{rec})}{A_{GT} + A_{rec}} \tag{7.2}$$

with A_{GT} the area of the ground truth NC geometry and A_{rec} the area of the reconstructed NC geometry. To quantify mismatches in area the $\Delta A(\%)$:

$$\Delta A(\%) = \frac{|A_{rec} - A_{GT}|}{A_{GT}} * 100\% \tag{7.3}$$

was used, with A_{GT} the area of ground truth NC and A_{rec} the area of the reconstructed NC.

7.2.7 Wall stress calculation

Contours of the plaque with the ground truth NC and the reconstructed NC were imported and meshed in Abaqus for FEA (version 6.13, Dassault Systemes Simulia Corp., Providence, RI, USA). All material properties were assumed to be homogeneous and incompressible. Neo-Hookean material models for all components were used, as was done in similar parametric studies (Badel et al., 2014; Kelly-Arnold et al., 2013; Speelman

et al., 2011). The mechanical properties of the components are listed in Table 7.1.

Table 7.1: *Material properties of the buffer and different components in the plaque.*

Material	E-modulus (kPa)	Poisson ratio (-)	C_{10} (kPa)	D_1 (-)	Reference
Intima	1000	0.498	166.7	1e-5	Holzapfel et al. (2005)
Media + adventitia	1500	0.498	250	1e-5	Holzapfel et al. (2005)
Necrotic core	6	0.498	1	1e-5	Loree et al. (1994)
Buffer	60	0.45	10	0.02	Choi and Zheng (2005)

* C_{10} and D_1 are constants to describe the Neo-Hookean model as used by Abaqus, representing the shear and bulk modulus as: $G=2*C_{10}$ and $K=1/D_1$.

To restrain rigid body motion, a compressible soft buffer around the model was used and the outer contour of the buffer was fully constrained. The material properties of the buffer are also listed in Table 7.1. Plaque stresses were computed by solving the mass and momentum equations. Linear tetrahedral elements were used with at least 7 elements at the minimum thickness of the cap. One simulation of a 2D plaque took approximately 4 hours with typically $1*10^6$ elements on a standard desktop computer. Due to pressure fixation in the histology process, the histology based geometry was not stress free. Therefore, initial stresses up to 100 mmHg were calculated with the backward incremental method (Speelman et al., 2011). Subsequently, a systolic blood pressure of 140 mmHg was applied. PCS was defined as the maximum von Mises stress in the cap (defined as intima in front of the NC) and at the shoulders of the cap; defined as the area 15 degrees adjacent to the cap, see Figure 7.3 (Akyildiz et al., 2016). Peak cap stresses were calculated and analyzed for the intima of the geometry containing the ground truth NC from histology (PCS_{GT}), the reconstructed NC based on group average rNCt estimation (PCS_{GA}) and the NC based on plaque specific rNCt estimation (PCS_{PS}). The distance between the PCS location of the ground truth and the reconstructed plaque was determined. Hereafter co-localization was determined based on visual inspection.

If the PCS was delocalized, displacement was classified as 1) shift from one side to the other side of the NC 2) slight delocalization or 3) translocation from the lumen to the NC side or vice versa.
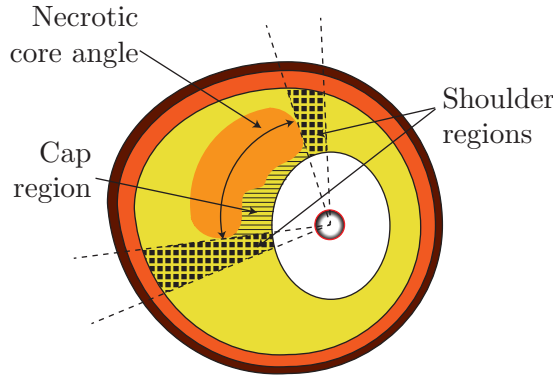
Figure 7.3: *A schematic illustration of the regions were the peak cap stress (PCS) is determined. The PCS was defined as the maximum von Mises stress located in either the cap region (striped area) or in the shoulder regions, 15° adjacent to the NC (blocked area).*

7.2.8 Statistics

The data was tested for normality with a Kolmogorov-Smirnov test. If the data was normally distributed, mean and standard deviation are given and differences between data were tested with a paired t-test. Otherwise, the median and interquartile range were given and a paired non-parametric test (Wilcoxon signed ranktest) was used to test for significant differences. Statistical significance was considered as $p < 0.05$. The SI and $\Delta A\%$ were analyzed for the geometry of the ground truth NC (NC_{GT}) vs. the reconstructed NC based on group averaged rNCt (NC_{GA}), and the reconstructed NC based on the plaque specific rNCt (NC_{PS}). Good similarity index was assumed to be at least SI > 0.8. Linear regression analysis was performed to compare peak wall stress of the different models.

7.3 Results

On average, the 73 plaques had a minimum cap thickness of 0.20 mm (0.09 – 0.40 mm) and NC angle of and 54° (35 – 75°). At the midcap location, the cap thickness, IMT, and

absolute NC thickness were 0.30 mm (0.13 – 0.53 mm), 1.05 mm (0.89 – 1.29 mm), and 0.46 mm (0.27 – 0.54 mm), respectively. For the sidecaps, the cap thickness, IMT, and absolute NC thickness were 0.31 mm (0.16 – 0.54 mm), 1.03 mm (0.84 – 1.24 mm), and 0.36 mm (0.21 – 0.51 mm). The median of the relative NC thicknesses at midcap and sidecap positions were 0.40 and 0.35, respectively.

The GEE model showed a significant correlation between the estimated rNCt and the ground truth rNCt: at midcap ($r^2 = 0.47$) and at sidecap ($r^2 = 0.44$), see Table 7.2. All parameters (cap thickness, IMT and NC angle) were found to have a significant contribution for predicting the rNCt at both positions.

Table 7.2: Generalized Estimation Equation (GEE) parameters with their standard errors. Predictive for the relative necrotic core thickness (rNCt), the r^2 and p value of the regression line between the actual rNCt value and the GEE model estimated value rNCt.

	β_0	$\beta_{NCangle}$	β_{IMT}	β_{capT}	r^2	P-value
rNCt$_{midcap}$	187 ± 55.4	63.3 ± 26.6	0.29 ± 0.07	-0.51 ± 0.08	0.47	< 0.05
rNCt$_{\pm sidecap}$	175 ± 46.4	130 ± 19.8	0.18 ± 0.05	-0.42 ± 0.06	0.44	< 0.05

[*] All parameters with corresponding standard deviations are *1000 fold.

Figure 7.4 A-C shows a typical example of the segmentation and reconstruction of the NC. The NC reconstruction based on group average (Figure 7.4 B underestimated (SI = 0.83) the NC area, whereas the plaque specific (Figure 7.4) NC reconstruction predicted (SI = 0.93) the NC area better. For all plaques, the NC$_{GA}$ matched the NC$_{GT}$ well with a SI and ΔA% of 0.85 (0.77 – 0.90) and 25.1% (14.0 – 41.3%), respectively. The NC$_{PS}$ matched the NC$_{GT}$ even better with a SI and ΔA% of 0.88 (0.79 – 0.91) and 17.9% (9.81 – 32.7%), respectively. The NC core geometries based on plaque specific rNCt had significantly better SI and ΔA% (p < 0.01) opposed to the NC geometry that were reconstructed solely based on group averaged rNCt.

For the typical example also the corresponding stress distribution in the fibrous cap of the ground truth geometry, and the reconstructed geometries are depicted in Figure 7.4 D-F. The PCS$_{GA}$ and PCS$_{PS}$ for this example showed 18% and 6% PCS difference with respect to the ground truth PCS. The absolute PCS values were 192 kPa (82.1 – 355 kPa) for the ground truth, 192 kPa (96.0 – 354 kPa) for the group average method and 196 kPa (95.6 – 369 kPa) for the plaque specific method. The overall difference in PCS
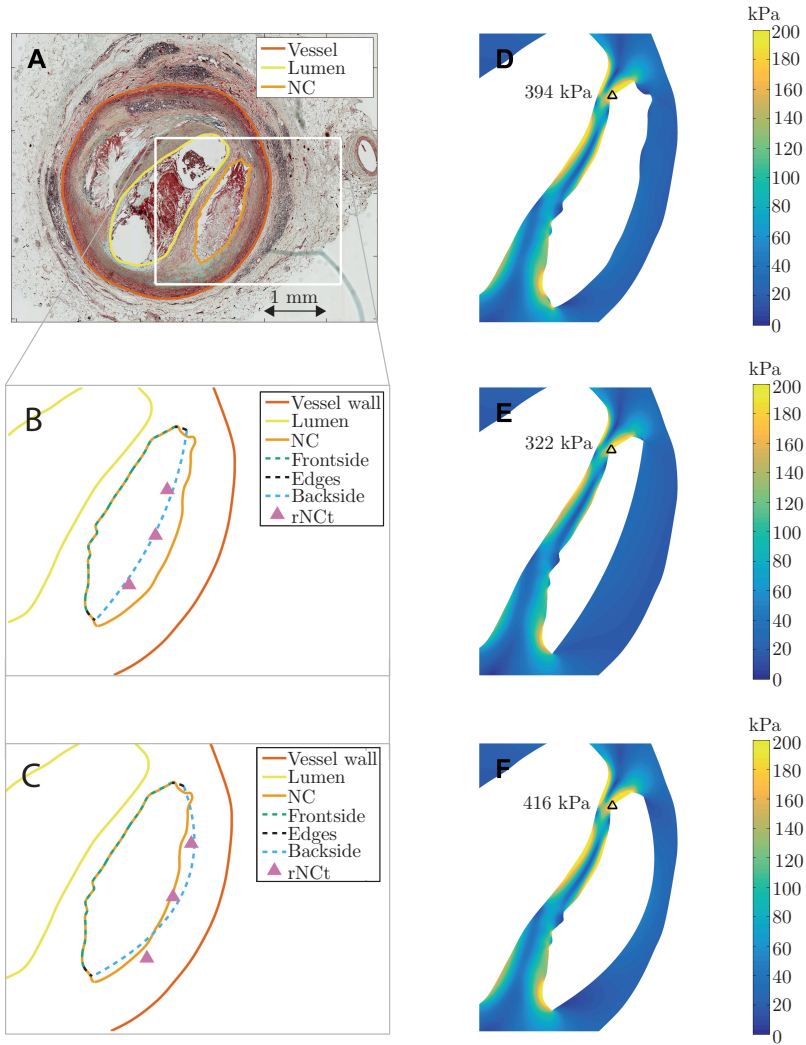
Figure 7.4: *From the histology image to stress calculations. A) Cross-sectional slice from histology with the vessel wall, lumen, and necrotic core already delineated. B-F are zoomed versions of (A) with necrotic core reconstruction based on the group averaged NC data (B) and with necrotic core reconstruction based on the plaque specific (C) rNCt estimation methods. D-F) are the wall stresses of the plaque containing the necrotic core geometry from the ground truth (D), reconstruction of the necrotic core based on group averaged data (E) and reconstruction of the necrotic core based on plaque specific (F) method and the black triangles indicate the location of the peak cap stress.*

between PCS_{GT} vs. PCS_{GA} was 15% (5 – 25%) and PCS_{GT} versus PCS_{PS} was 8% (5 – 23%). For all plaques, no significant difference was found in peak cap stresses between both reconstruction methods and the ground truth, only PCS_{GA} versus PCS_{PS} showed a significant difference ($p<0.05$). The correlation between the PCS of the ground truth and the PCS of the reconstructed geometries are shown in Figure 7.5. Both the PCS_{GA} and PCS_{PS} showed a high correlation with PCS_{GT}, $r^2 = 0.91$ and $r^2 = 0.95$, respectively. The PCS_{GT} vs. PCS_{GA} showed a higher offset and lower slope compared to the regression line obtained with the PCS_{GT} vs. PCS_{PS}.

A   **B**
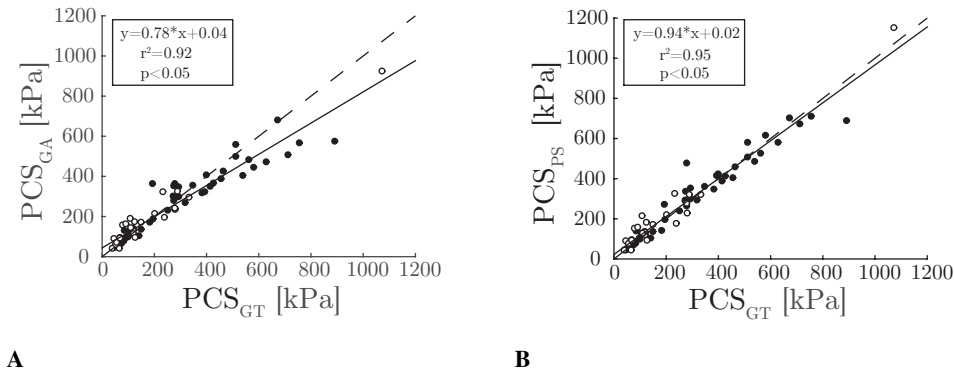
Figure 7.5: *The peak cap stress (PCS) of 73 plaque models from ground truth (histology) (x-axis) versus the peak cap stress of the reconstructed necrotic core geometry (y-axis) are depicted. In A) the PCS based on the NC reconstruction using group averaged rNCt estimation, PCS_{GA}, and B) PCS based on the NC reconstruction using the plaque specific rNCt estimation, PCS_{PS}. The closed circles indicate the cases for which the locations of the peak cap stresses was not shifted with respect to the ground truth, whereas the open circles did shift.*

In Figure 7.5A, there seems to be a visual cut-off value at 300 kPa were the group averaged method seems to underestimate the peak cap stresses. Coincidentally, this 300 kPa threshold is also mentioned in literature as a rupture risk threshold (Cheng et al., 1993). In order to investigate if the high PCS_{GT} were better estimated for the PCS_{PS} than the PCS_{GA}, the cross sections were divided based on the PCS in a low (<300 kPa) and high stress (>300 kPa) group. Next, for both groups the PCS differences with respect to the ground truth were calculated. For the plaques with PCS_{GT} below 300 kPa both reconstruction methods showed 15% difference in PCS ($p>0.05$) compared to the ground truth. Interestingly, for the plaques with relative high PCS_{GT} (>300 kPa), the PCS difference was 16% for the group averaged rNCt and only 6% for the plaque specific rNCt based

reconstruction (p<0.05).

The distance between the locations of the PCS in the ground truth compared to the reconstructed geometries were evaluated. Since the distance between the location of the PCS_{GT} and PCS_{GA} was not different from the distance between the location of PCS_{GT} and PCS_{PS} (p = 0.29), only the distances between PCS_{GT} and PCS_{PS} are hereafter listed. In 67% (n = 49), the location of the PCS_{PS} was similar as the location of the PCS_{GT}, with a distance of 4.13 μm (2.66 – 17.6 μm), indicated by the closed circles in Figure 7.5. For the remaining 33% of the data (n=24), the location of the PCS was not similar and is depicted in Figure 7.5 by the open circles. The shift in PCS was 1) from one side of the NC to the other side (n=9) with a distance of 0.99 mm (0.72 – 1.47 mm) or 2) at the same side (n=4) with a distance of 0.21 mm (0.07 – 0.66 mm) or 3) translocated from the lumen side towards the front side of the NC or vice versa (n=11) with a distance of 0.92 mm (0.24 – 1.32 mm). For plaques that showed a shift in the peak stress location, the difference in PCS compared to the ground truth was larger (35%) than for plaques with the same peak stress location (11%). The PCS_{PS} that were not at the same locations as the PCS_{GT} had stresses mostly below 300 kPa and represent the more stable plaque: 160 kPa (93.9 – 226 kPa), respectively. For the PCS_{PS} at the same location as the ground truth the stresses had a higher variation: 281 kPa (102 – 392 kPa).

7.4 Discussion

In this study, we analyzed the effect of the reconstruction of the missing NC backside with respect to geometry and stress calculations. The backside of the NC can be obscured due to limited penetration depth of in vivo light based imaging in coronary arteries. Histological cross-sections ('ground truth') were used to characterize the plaque and to reconstruct the NC geometry. Reconstruction was performed by determining the relative NC thickness (rNCt) at three locations along the NC angle. The rNCt was either based on a group average or plaque specific parameters. Subsequently, the reconstructed NC geometries and the corresponding plaques from both methods were compared with the ground truth regarding the geometry and PCS. The following are the two main findings of this study: 1) high agreement was found between the NC geometries and the corresponding peak cap stresses of the reconstructed NCs and the ground truth, 2) reconstructing the NC based on average NC data resulted in underestimated peak cap stresses for high stress plaques only, whereas including plaque specific data for the NC reconstruction improved the stress prediction for these high stress plaques.

In terms of PCS prediction in the low PCS group (<300 kPa), representing the more stable

plaques, both NC reconstruction methods performed equally well, resulting both in 15% difference in PCS. This is relative low compared to changes in PCS in idealized models due to cap material properties (55 – 200%) (Akyildiz et al., 2011). In patient specific plaque geometries, the PCS showed to have two independent predictors: cap thickness and lumen curvature (Akyildiz et al., 2016). In the current study, the cap thickness and lumen geometry were unchanged, which may explain the relative good prediction of the peak cap stresses with the NC reconstruction methods.

A significant improvement in PCS was found for high PCS group (>300 kPa) using the plaque specific NC reconstruction method. This could be explained by the fact that an increase in NC area affects the PCS more in thin compared to thick fibrous caps (Aky-ildiz et al., 2011). Thus, it is likely that for high stress plaques, which have in general thin caps, a more precise reconstruction of the NC results would result in more accurate PCS prediction. Indeed, our data showed that for the plaques with a thin cap (<0.20 mm), a) the corresponding SI and $\Delta A\%$ significantly improved using plaque specific NC reconstruction method (SI: 0.83 vs 0.87 and $\Delta A\%$: 25% vs. 14%) b) the PCS estimation improved with respect to PCS_{GT} when using plaque specific information (difference PCS_{GA}: 14% and PCS_{PS} : 7%) whereas plaques with a thick cap did not show a significant improvement (15% vs. 18%).

For in vivo PCS computations in (vulnerable) coronary plaques, visualization of the cap is needed. The only possibility to obtain the cap thickness is with optical driven imaging techniques (e.g. optical coherence tomography, OCT), but it has limited penetration depth. Therefore the deeper lying tissues will become obscured, causing incomplete geometries for stress calculations. In this study, on purpose we investigated the influence of the reconstruction of the NC only. Using histology as ground truth enabled us to isolate the effects of reconstruction of the NC from possible other factors that can influence the PCS calculation. Logically, if the NC is obscured also the deeper laying vessel wall is missing. In a recent study it was shown that the vessel area in coronary arteries can be approximated by interpolating the non-obscured vessel wall (Kubo et al., 2015). Thus when moving forward to a clinical application the latter technique should be combined with the reconstruction of the NC to enable **in vivo** PCS calculations in coronary arteries.

Another attractive feature of OCT is that it shows potential to image macrophages. Extensive research showed that macrophages are linked with plaque instability (Lendon et al., 1991; Moreno et al., 1994; van der Wal et al., 1994), therefore macrophages can be interpreted as a surrogate marker of cap strength. Co-localization of PCS and presence of macrophages might be instrumental in risk prediction. In that respect not only the PCS is of importance, but also the location. In this study a number of the PCS locations were

not co-localized with the PCS$_{GT}$ and thus might have consequences for risk prediction. However, most of the plaques with incorrect PCS locations showed low peak cap stresses, representing the more stable plaque.

Histological processing and variations in the manual segmentation might affect the ultimate geometry of the plaque and NC. We showed in an earlier study that histological processing hardly affects the geometry compared to the in vivo situation (Groen et al., 2010). However, since the model is tuned to this data-set, it is conceivable that variations because of the manual delineation and histological processing has some influence on the outcome of this model. We expect that the peak cap stress is minimally influenced, since we showed that the peak cap stress are hardly influenced by the exact geometry of the backside of the NC, and we are therefore confident that the minor impact of intra- and inter-observer variability on the model has also minor impact on the final stress. Therefore, it will not change the main conclusion of this study. Despite the relative large sample size of NCs (n = 73), the geometrical variation in the histology contours might not completely represent the whole population of NCs, due to the limited number of patients (n=7). Little data is available on the geometrical variation of NC dimensions (e.g. lipid angle and NC thickness at midcap and sidecaps of the lipid angle). In a study by Gardner et al. (2008), lipid cores were only assessed in plaques with a lipid core >60° in circumferential extent, >200 μm thick lipid core, and a mean fibrous cap thickness <450 μm. They found a median minimum cap thickness of 164 μm (IQR: 101 – 243 μm) μm, an median lipid angle 102° (IQR: 77 – 132°), and an median NC thickness of 448 μm (IQR: 315 – 565 μm) (Gardner et al., 2008). The NC thickness in our study showed a similar range (461 μm, IQR: 268 - 543 μm), however, our median lipid angle was lower and showed less variation: 54° (IQR: 35 – 75°). This might be not so accurate to the estimation of the NC thickness and wall stress calculations for larger angles. However, no significant differences were found in PCS between plaques with a NC angle below or above the median NC angle of 60.9° (20.6% and 22.6%).

In the stress calculations of this study relative simple material models were chosen for the plaque components. In diseased tissue there are usually extra collagen fibers present to absorb higher stresses. Ideally, tissue nonlinearity and anisotropy should be taken into account. However, to the knowledge of the authors, experimental data representing anisotropy in coronary arteries is not available. Although in carotid arteries this data is available, the dispersion range is so high that modeling with isotropic model could suffice (Chai et al., 2014). In addition to anisotropy and the geometric factors other factors will also influence the absolute values of PCS, such as, luminal pressure, initial stress, residual stress, 2D vs 3D assumptions, and material properties. The latter, might

be the most important one, since it was shown that in an idealized geometry the PCS
could change 200 %, just by changing the material properties of the intima. Since in this
study in all models, the ground truth and reconstructed, the same material properties were
used, no differences in absolute PCS based on the material properties may be expected.
Therefore, conclusions on the reconstruction methodology and resulting differences in
PCS still hold. However, when performing plaque specific risk analysis, nonlinearity and
anisotropy will definitely impact the stresses.

In this study, we only retain the front line of the NC such that it resembles the optical
driven imaging techniques. Another approach would be removing the NC behind a cer-
tain distance from the lumen. In this way, other features such as the edges of the NC and
NC area change. It would be interesting to investigate to what extent these edges and
area change affect the PCS calculation. However, it is arguable whether these methods
will affect our results, since we already observed that a significant area difference did
not result in a significant PCS change between the reconstruction methods. Another ap-
proach to refine our method in future work is to improve the GEE model by categorizing
NC cores based on, size, shape, and location in the vessel wall. This refinement will
probably improve the predictive value of the GEE model. However, we already showed
that the PCS estimation between the group averaged and plaque specific method does not
differ that much. Therefore, it is arguable whether this categorizing method will show an
improvement in cap stress.

7.5 Conclusions

In conclusion, this study showed that reconstruction of the backside of a NC can be
performed using either group averaged NC data or plaque specific NC data. A high cor-
relation was found between peak cap stresses as obtained with the ground truth geometry
and the peak cap stresses of both reconstruction methods. Although using group averaged
NC data for the reconstruction of the backside of the NC performs well for the stress cal-
culations, including plaque specific data in the NC reconstruction method improves the
stress prediction, especially for high stress plaques.

MODEL-BASED CAP THICKNESS AND PEAK CAP STRESS PREDICTION FOR CAROTID MRI.

ABSTRACT

A rupture-prone carotid plaque can potentially be identified by calculating the peak cap stress (PCS). For these calculations, plaque geometry from MRI is often used. Unfortunately, MRI is hampered by a low resolution, leading to an overestimation of cap thickness and an underestimation of PCS. We developed a model to reconstruct the cap based on plaque geometry to better predict cap thickness and PCS. We used histological stained plaques from 34 patients. These plaques were segmented and served as the ground truth. Sections of these plaques contained 93 necrotic cores with a cap thickness < 0.62 mm which were used to generate a geometry-based model. The histological data was used to simulate in vivo MRI images, which were manually delineated by three experienced MRI readers. Caps below the MRI resolution (n=31) were (digitally removed and) reconstructed according to the geometry-based model. Cap thickness and PCS were determined for the ground truth, readers, and reconstructed geometries. Cap thickness was 0.07 mm for the ground truth, 0.23 mm for the readers, and 0.12 mm for the reconstructed geometries. The model predicts cap thickness significantly better than the readers. PCS was 464 kPa for the ground truth, 262 kPa for the readers and 384 kPa for the reconstructed geometries. The model did not predict the PCS significantly better than the readers. The geometry-based model provided a significant improvement for cap thickness estimation and can potentially help in rupture-risk prediction, solely based on cap thickness. Estimation of PCS estimation did not improve, probably due to the complex shape of the plaques.

8.1   Introduction

Stroke is the second cause of death worldwide and the third leading cause of disability
in the western world (Johnson et al., 2016). One of the causes of an ischemic stroke is
atherosclerotic disease in the carotid artery. As a consequence of atherosclerotic plaque
rupture, a thrombus might form, which can deprive part of the brain of blood. Several
histological studies have provided important insights about plaques that are vulnerable to
rupture (Virmani et al., 2002). A vulnerable plaque is characterized by a large and soft
lipid rich necrotic core (NC), a thin fibrous cap, and infiltration of macrophages (Falk,
2006).

Plaque rupture occurs when the stresses in the cap exceed the strength of the cap. These
cap stresses can be calculated with finite element analysis (FEA). Apart from material
properties and boundary conditions, stress computations with FEA critically depend on
the geometry of the plaque. Some of the geometry parameters highly influence the cap
stresses, including the lumen and the NC curvature, but most importantly the cap thick-
ness (Akyildiz et al., 2016). Geometrical information of carotid plaques is often obtained
with magnetic resonance imaging (MRI) because of its ability to distinguish relevant
plaque components. However, the in-plane pixel resolution of a carotid MRI is low. The
minimum cap thickness, which is typically around 0.3 mm (Redgrave et al., 2008), is of-
ten smaller than the pixel size. Therefore, even experienced MRI readers have difficulties
in estimating the minimum cap thickness (CapT); they almost always overestimate the
CapT, especially when the caps are thin (Nieuwstadt et al., 2014a).

The overestimation of CapT with MRI will lead to an underestimation of the cap stress.
The error in cap stress computations are much higher in the thin caps than in the thick
caps (Nieuwstadt et al., 2014b). A more accurate CapT is needed to improve cap stress
calculations.

Previously, we showed that a geometric relation was found between the NC thickness and
geometric parameters in coronary arteries (Kok et al., 2016). Here, we apply a similar
approach in order to estimate the cap thickness. We hypothesize that the geometry-based
regression model will improve the CapT and thereby also the cap stresses compared to
the CapT estimated by the experienced MRI readers.

8.2   Methods

A graphical summary of the methods is presented in Figure 8.1, the steps are explained
in detail below.
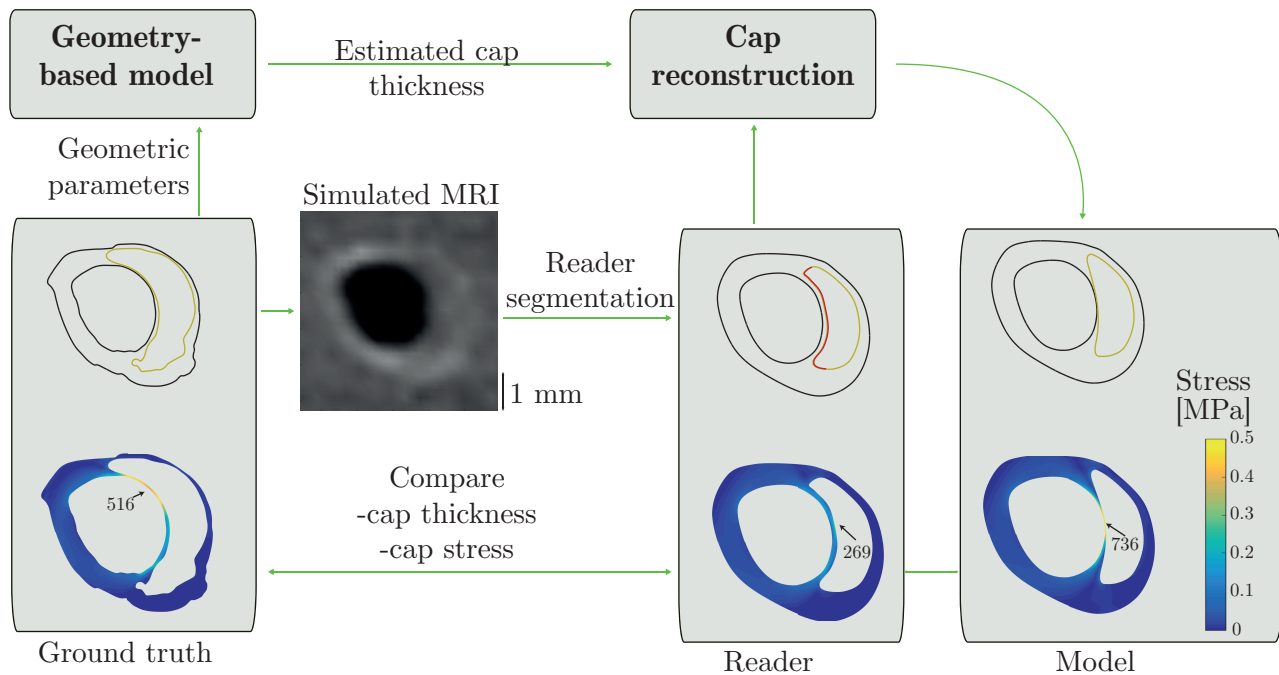
Figure 8.1: *A schematic overview of the methods section. From the middle left to the middle right: the ground truth (based on histology), reader and model contours with the corresponding stress calculations below. Based on the ground truth contours carotid MRI images were simulated using JEMRIS software. These simulated MRI images were segmented by experienced MRI readers. The cap smaller than 0.62 mm was highlighted in red and was removed for the cap reconstruction. At the right, the cap was reconstructed using cap thickness information from the geometry-based model resulting in new contours ('model') contours.*

8.2.1 Histology

From 34 symptomatic patients (> 70 % stenosis) who were scheduled for carotid en-
darterectomy 34 plaques were obtained. All plaques were decalcified and embedded in
paraffin and cut in 5 μm sections. The sections were stained with either Elastica van
Gieson or Resorcine Fuchine. In total 76 cross sections were selected for further anal-
ysis, all sections contained at least one NC. The lumen, the NC, and the vessel outer
wall were manually delineated. Since these histological plaque cross-sections were not
pressure fixated, the contours were computationally pressurized at mean arterial pres-
sure (100 mmHg) with finite element analysis (FEA). These pressurized contours were
considered to represent the ground truth geometry.

8.2.2 Geometry-based model

Since we were interested in the thin caps, all NCs that were located closer than 0.62 mm
– a representative value for the clinically used resolution of MRI – to the lumen in the
ground truth geometry were selected. Then, the CapT was estimated with a statistical
model which was constructed based on geometry features of the plaque. In a previous
study, it was shown that lumen area, vessel area and NC area could be quantified ac-
curately with MRI (Nieuwstadt et al., 2014a). Therefore, in the model the following
geometry features were used: 1) the NC angle, 2) the distance from the lumen border to
the NC center (Centroid Distance), and 3) the NC thickness, see Figure 8.2A. To make
the model robust for all plaques sizes, the geometry parameters as well as the output pa-
rameter (CapT), were normalized with respect to the corresponding vessel wall thickness,
except for the NC angle, which is expressed in radians. To reconstruct the new cap, the
model estimated the normalized CapT at three positions. The first position is at the center
(50%) of the NC angle and the other two are positioned at the sides (25% and 75%) of
the NC angle. One geometry-based model was used for the center and one for the side
positions, since these are assumed to be symmetric. The following relation was fitted to
the data:

$$
\begin{aligned}
CapT_i = &\beta_{NCangle,i} \times NCangle_i + \beta_{CentroidDistance,i} \times \\
&CentroidDistance_i + \beta_{NCthickenss,i} \times NCthickness_i + \beta_{0,i}
\end{aligned}
\tag{8.1}
$$

with $\beta's$ the parameters as determined with the geometry-based model and i the location
at the NC (center or side). All the geometry parameters, NC angle, Centroid Distance and
NC thickness, were determined along the line of the corresponding NC angle. The CapT

was determined as the minimum cap thickness per segment: in the center (37.5% < NC angle < 62.5%) or at the side positions (NC angle < 37.5° or NC angle > 62.5°). The NC area obtained with histology underestimates the NC area obtained via MRI images by 24% (Nieuwstadt et al., 2014a). To account for this underestimation of the NC area, the NC angle and NC thickness were scaled with $\sqrt{1.24}$. Since a negative CapT is physically not possible and extremely thin caps would lead to extreme and unrealistic stress value. Hence, a cut-off value of 0.069 mm was used for the CapT, which is the mean minimum cap thickness of a fibrous cap minus twice the standard deviation of the minimum cap thickness earlier reported (Cicha et al., 2011).

8.2.3 MRI segmentation

A subset of 33 cross-sections from 12 patients was used to simulate in vivo carotid MRI images. A clinical MRI protocol was simulated by solving the Bloch equations, with an in-plane resolution for the simulations was 0.62 mm. The protocol was described in more detail by Nieuwstadt et al. (Nieuwstadt et al., 2014a). Three independent experienced MRI readers manually delineated the lumen, vessel wall, and NCs in the MRI simulated images. In some cases multiple NCs were present in one cross-section. For example, if in a cross-section two NCs were present, the cross-section was analyzed twice; once with one NC and the other NC discarded and vice versa.

8.2.4 Reconstruction

Reconstruction of the fibrous cap was performed on the cross-sections that met the following criteria: 1) the reader correctly identified the NC, 2) the cap thickness was less than 0.62 mm and, 3) more than 50% of the NC angle of the cap was below 0.62 mm. First, the part of the cap that was thinner than 0.62 mm was removed, see Figure 8.2B. The geometry parameters (NC angle, Centroid Distance and NC thickness) obtained by the readers were used to estimate the normalized CapT at 25, 50 and 75% of the NC angle. Then, the absolute CapT values were calculated using these normalized CapT by multiplying with the corresponding vessel wall thickness, and placed at that distance from the lumen, see Figure 8.2C. Subsequently, a Non-Uniform Rational B-Spline (NURBS) was used to generate the reconstructed cap contour, see Figure 8.2D. The reconstruction with the NURBS can cause the CapT to become less than the previous reported cut-off (0.069 mm) value; if this was the case the cap was adjusted using this cut-off value. In order to remove and reconstruct the cap of the NC, MATLAB (version 2014a, Mathworks Inc., Natick, MA, USA) was used.
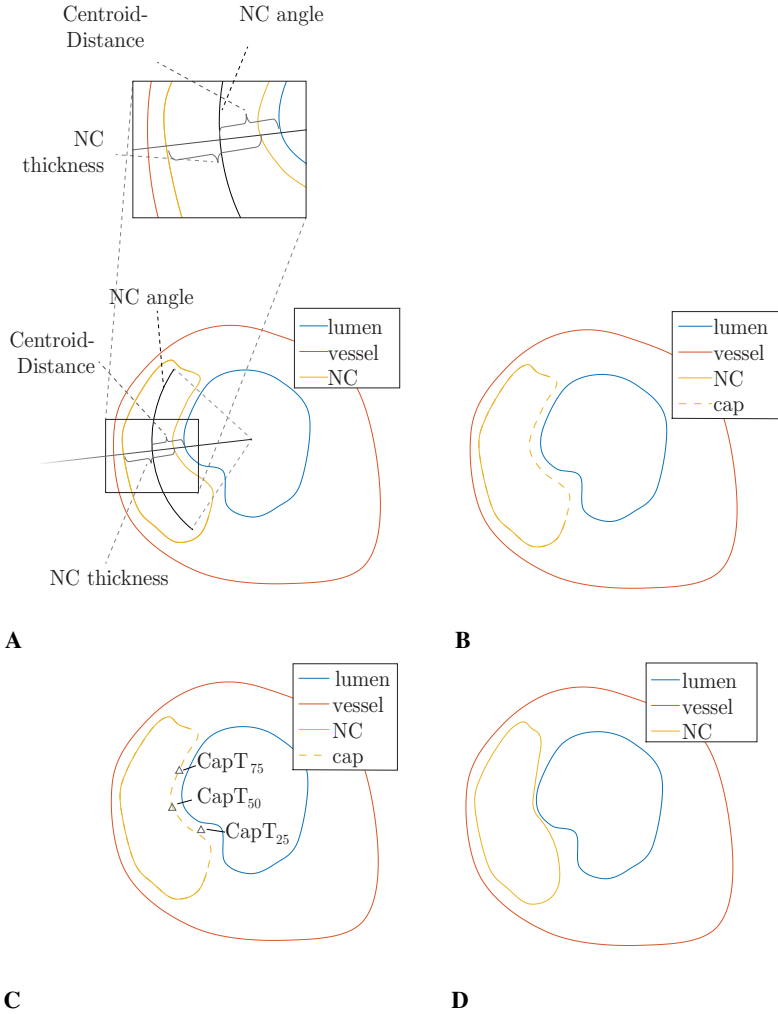
Figure 8.2: *A schematic overview of the cap reconstruction. A) the geometry param-
eters are determined for the geometry-based model visualized for 50% Necrotic core
(NC) angle (midcap), this was also done for 25% and 75% NC angle (sidecap), B) the
cap thinner than 0.62 mm was removed, C) the cap thicknesses estimated by the GEE
model are placed at the three locations along the NC angle D) the remainder of the
cap is reconstructed using a Non-Uniform Rational B-Spline.*

8.2.5 Finite Element Analysis

Wall stress calculations in the plaque geometries were performed with Abaqus (version 6.13, Dassault Systemes Simulia Corp., Providence, RI, USA). Incompressible, Neo-hookean material properties were used for all plaque components (Akyildiz et al., 2011; Badel et al., 2014; Kelly-Arnold et al., 2013). The Young's moduli for the components are 1000 kPa for the intima and 6 kPa for the NC. In order to restrain rigid body movement a soft compressible buffer (Poisson ratio: 0.45, Young's modulus: 60 kPa) was placed around the intima with the outer border fully constraint. Approximately, 100.000 tetrahedral elements were used to for the plaque (at least four elements were located across the cap). The initial stresses were calculated at 100 mmHg with the backward incremental method (de Putter et al., 2007; Speelman et al., 2009). The final pressure (125 mmHg) was applied at the lumen contour. Peak cap stress (PCS) was defined as the 99th percentile von Mises stress in front of the cap or in the shoulder region of the cap (15° adjacent to the cap) (Kok et al., 2016).

8.2.6 Analysis and statistics

For the geometry based model, a generalized estimating equations (GEE) method was used, which accounts for using multiple cross sections from one plaque. To quantify the correlation between the ground truth cap thickness and the model cap thickness the r^2 and the concordance correlation coefficient (CCC) were determined. Normal distribution was tested with a Kolmogorov-Smirnov test. Since the data were not normally distributed, the data were reported as median and interquartile range. An ANOVA (with a Bonferroni correction) was used to test absolute differences among groups. The error (with respect to the ground truth) of the cap thickness and PCS observations were pairedand tested with a non-parametric signed Wilcoxon rank test was used. Especially, the effect of the reconstruction in the thin caps is of interest. Therefore, all data were divided based on the ground truth minimal cap thickness ($CapT_{GT}$), in a thin (<0.1 mm) or a thick (>0.1 mm) cap group. The CapT of the geometry-based model ($CapT_{model}$) and the CapT of the reader ($CapT_{reader}$) were compared with respect to the $CapT_{GT}$. A similar approach was followed for PCS.

8.3   Results

8.3.1   Geometry-based model

In total, the 76 cross-sections contained 148 NCs which had the following characteristics:
the CapT was 0.23 mm (0.08 – 0.40 mm), the NC angle was 97.6° (49.7 – 147°) and the
NC thickness at the center of the NC was 0.83 mm (0.39 – 1.99 mm). Ninety-three NCs
had a CapT smaller than 0.62 mm which were used for the construction of the geometry-
based regression model. The geometry-based model estimated the normalized CapT, and
revealed for both the center and the side positions significant relations, see Table 8.1.
Each of the geometry parameters had a significant ($p < 0.05$) individual effect on the
CapT estimation. The parameters showed that the normalized $CapT_{GT}$ was positively
related with the normalized Centroid Distance and that it was negatively related with the
normalized NC thickness and the NC angle.

Table 8.1: *Generalized Estimation Equation (GEE) parameters with their standard er-
rors. The predictive values, β′s, of the GEE model for NC angle, Centroid Distance and
the NC thickness and a constant value. NC=Necrotic core.*

	$\beta_{NCangle}$	$\beta_{CentroidDistance}$	$\beta_{NCthickness}$	β_0
$CapT_{midcap}$	-0.028 ± 0.01	0.82 ± 0.04	-0.35 ± 0.03	0.01 ± 0.02*
$CapT_{\pm sidecap}$	-0.027 ± 0.01	0.54 ± 0.07	-0.28 ± 0.05	0.12 ± 0.04

* no significant contribution to the model.

The geometry-based model for the NC center estimated the normalized $CapT_{model}$ ($r^2 =$
0.89 and CCC = 0.95) compared very well to the normalized $CapT_{GT}$, see Figure 8.3A.
The normalized $CapT_{model}$ for the NC side position was moderately estimated ($r^2 = 0.46$
and CCC = 0.68), see Figure 8.3B.

8.3.2   Cap thickness reconstruction

Thirty-one NCs met the reconstruction criteria. The $CapT_{GT}$ was 0.07 mm (0.06 – 0.11
mm), $CapT_{reader}$ was 0.23 mm (0.18 – 0.29 mm) and the $CapT_{model}$ was 0.12 mm (0.03
– 0.22 mm), see Figure 8.4A. Figure 8.4B shows the absolute $CapT_{GT}$, $CapT_{reader}$, and
$CapT_{model}$ for the thin and the thick caps. For the thin cap group, the reader overestimates
cap thickness while the $CapT_{model}$ is significantly closer to the ground truth data. For the
thick cap group, a similar trend is observed, although not significant. Figure 8.4C shows
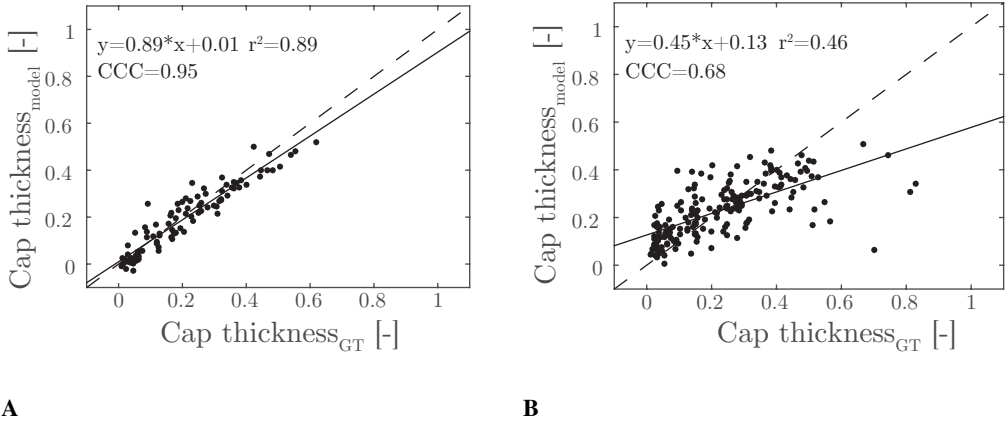
Figure 8.3: The normalized estimated cap thickness of the model (CapT$_{model}$) versus the normalized ground truth cap thickness (CapT$_{GT}$) A) for the midcap and B) for the sidecap. The dashed line is the line of equality, the solid line is a linear fit through the data.

the absolute errors of the CapT$_{model}$ is significantly smaller than those of CapT$_{reader}$ for both thin and thick caps. In 95% of the thin cap cases the CapT estimation improved using the geometry-based model. In contrast, in the thick caps the model improved only 58% of the cases. For the thin caps, the reconstructed geometries predicted the CapT significantly ($p < 0.01$) better than the reader. Also, the reconstructed CapT estimation in the thick caps improved ($p < 0.01$) compared to the reader CapT.

8.3.3 Wall stress

The PCS$_{reader}$, 262 kPa (132 – 356 kPa), almost always underestimated the PCS$_{GT}$, 464 kPa (311 – 554 kPa). The PCS$_{model}$, 384 kPa (228 – 632 kPa), showed a high variation compared to the PCS$_{reader}$ and the PCS$_{GT}$, see Figure 8.2A. For example the model improved the PCS in NC 16, the reader underestimated the PCS with 161 kPa, and the model made a small overestimation of 58 kPa, with respect to the PCS$_{GT}$. In contrast, in NC 14 the model does not improve the PCS, the reader underestimated the PCS by 264 kPa and the model overestimated it by 354 kPa with respect to the PCS$_{GT}$. There was no significant difference between the PCS$_{model}$ and the PCS$_{GT}$ ($p = 0.21$). Figure 8.5B shows the absolute PCS$_{GT}$, PCS$_{reader}$, and PCS$_{model}$ for the thin and the thick caps. For the thin caps, the PCS obtained by the reader geometries significantly underestimated the

A

B

C
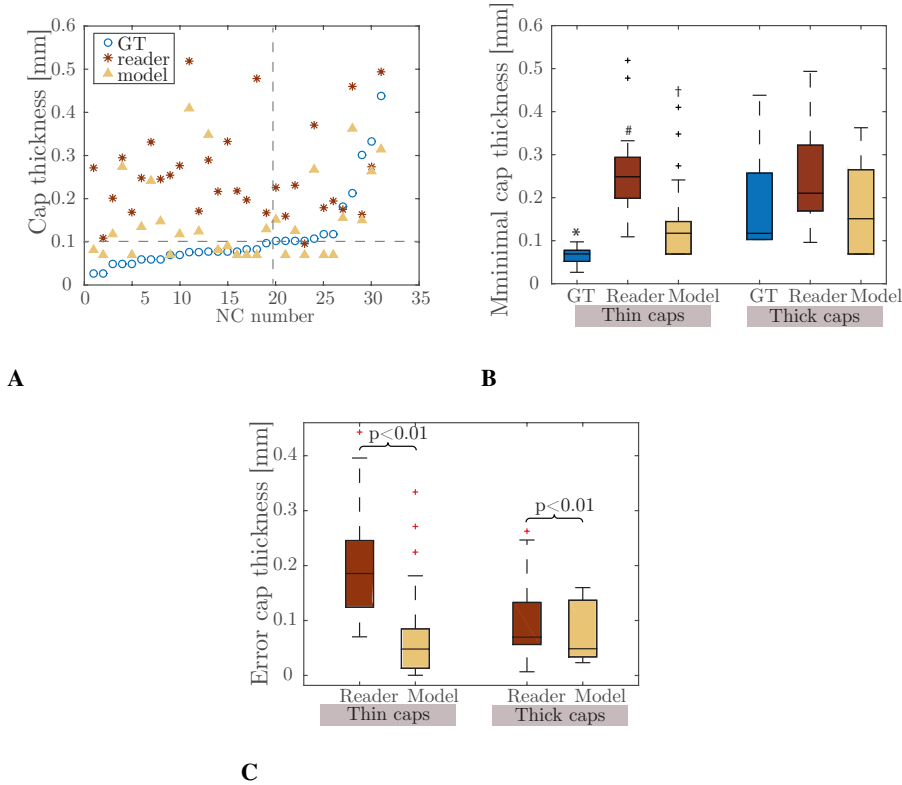
Figure 8.4: *In A) the absolute cap thickness values for the ground truth, reader and model geometries. The horizontal grey dotted line indicates 0.1 mm cap thickness, the vertical grey dotted line indicates the division line between thin (<0.1 mm) and thick (>0.1 mm) caps. B) the absolute cap thickness, on the left the results for the thin caps and on the right for the thick caps. In C) the absolute cap thickness error with respect to the ground truth, on the left the results for the thin caps and on the right for the thick caps. * = p<0.05 for ground truth vs. reader, # = p<0.05 for ground truth vs. model, † = p < 0.05 for reader vs. model.*

PCS of the ground truth and the model (p = 0.04). There was no difference between the PCS_{GT} and the PCS_{model} (p = 0.24). For the thick caps a similar trend was observed, however there are no significant differences.Figure 8.5C shows that for the thin caps, the absolute stress error of the model geometries was lower than the reader geometries, however not significant (p = 0.09). In this group two outliers were observed: one outlier showed an error in PCS_{reader} of 882 kPa and one outlier showed an error of PCS_{model} 651 kPa. These are caused because the ground truth CapT (0.05 mm) is highly overestimated by the reader (0.30 mm) and model (0.27 mm). For the thick caps, the absolute error in PCS did not improve with the model (p = 1). In 74% of the thin cap cases the PCS was improved by the model. In the thick caps, the model improved only 58% of the cases. In the thin caps, the absolute stress error reduced in the reconstructed geometries when comparing to the readers, however this was not significant (p = 0.09), see Figure 8.5C. In 74% of the thin cap cases the PCS was improved by the model. In the thick caps, the model improved only 58% of the cases. In case of the thin caps, one outlier showed an error in PCS_{reader} of 882 kPa and one outlier showed an error of PCS_{model} 651 kPa. These are caused because the ground truth CapT (0.05 mm) is highly overestimated by the reader (0.30 mm) and model (0.27 mm). For the thick caps, the absolute error in PCS did not improve with the model (p = 1).

8.4 Discussion

For peak cap stress assessment using FEA, a reliable estimate of the cap thickness is essential. MRI readers tend to overestimate the cap thickness and hereby also underestimate the PCS. In this study, we investigated if we can reconstruct the cap with a geometry-based regression model based on geometry features, and thereby improving the estimation of the PCS. The first main finding was that the estimation of the CapT on MR images can be improved using this model. The second main finding was that application of the model, despite the improved CapT estimation, did not lead to a better prediction of PCS.

8.4.1 Cap thickness

In an earlier study on coronary plaques, we showed an association among NC thickness, NC angle, intima-media thickness and cap thickness (Kok et al., 2016). Therefore, in carotid arteries a relationship between geometry parameters and the normalized CapT was expected. The association between CapT and the geometry features at the NC center was very strong (r^2 = 0.89), the model improves the CapT estimation in 81% of the cross-sections. However, the NC side relation was less pronounced, most probably because the
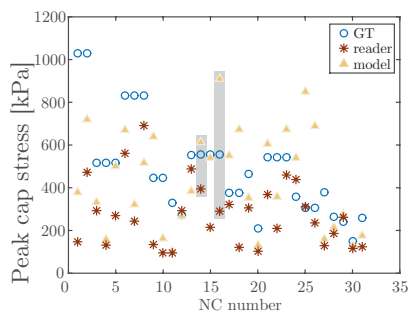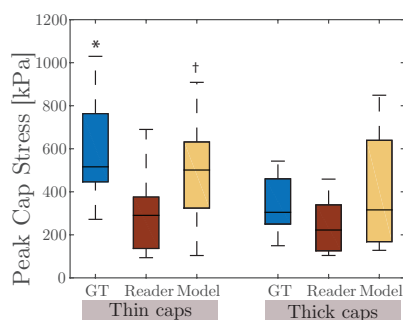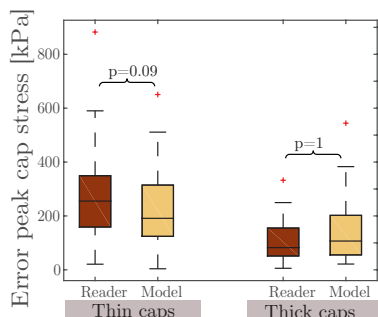
Figure 8.5: *In A) the absolute peak cap stress values for the ground truth, reader and model geometries. In grey are the Necrotic Core (NC) numbers 14 and 16 highlighted, which are referred to in the text. In B) the absolute peak cap stress, on the left the results for thin (<0.1 mm) caps and on the right for the thick (>0.1 mm) caps. In C) the absolute peak cap stress error with respect to the ground truth cap thickness, on the left the results for thin (<0.1 mm) caps and on the right for the thick (>0.1 mm) caps. * = p<0.05 for ground truth vs. reader, # = p<0.05 for ground truth vs. model, † = p < 0.05 for reader vs. model.*

fibrous cap was not as symmetric as was assumed.

Shindo et al. found that all carotid plaques with caps above 150 μm were stable (not ruptured) and that all caps lower than 76 μm were ruptured (Shindo et al., 2015). Similar results appeared in a larger histology-based study of symptomatic carotid stenosis patients, which showed that 81% of all plaques lower than 100 μm were ruptured (Redgrave et al., 2008). Therefore, the CapT could be instrumental in indicating the need for surgery. In this study, the sole input to estimate CapT are geometrical plaque features, which can be measured fast and accurately with MRI. Although the model improves CapT estimation in 81% of the cases, in 19% of the cases it does not. In these cases the error of the CapT is in the same range as the CapT associated with carotid rupture prone risk. More research is needed to improve the model before it can be used to predict the rupture risk of an individual plaque. The geometry-based model could also be used to estimate the CapT for plaque de-stabilization studies with respect to medications. For example, statin therapy has already been shown to decrease the NC area and increase CapT (Du et al., 2016; Takarada et al., 2009). If CapT is considered as a secondary endpoint in these studies, this model could be used to better estimate this value.

8.4.2 Peak cap stress

Peak cap stress is often used as surrogate marker for rupture risk (Cheng et al., 1993; Tang et al., 2005a). In this study we sought a solution for the MRI based overestimation of the CapT, and thereby we hoped to improve the PCS. Interestingly, while in the thin caps the geometry-based model aided in decreasing the CapT error, the PCS showed only a trend towards improvement ($p = 0.09$). Previous studies showed a strong relation between cap thickness and PCS (Akyildiz et al., 2016; Ohayon et al., 2008), but also pointed out the importance of lumen and NC curvature (Akyildiz et al., 2016). Edges of components are smoothed in the MRI model due to the limited spatial resolution which results in a severe underestimation of the curvature. This loss in curvature will lead to an underestimation of the PCS (Nieuwstadt et al., 2014b). To quantify this loss of detail, we determined the lumen and NC curvature of the ground truth and the reader. We found that the reader curvature was much lower than the ground truth curvature for the lumen: 0.61 mm^{-1} (0.54 – 0.70 mm^{-1}) vs. 0.98 mm^{-1} (0.78 – 1.13 mm^{-1}) and the NC curvature 0.86 mm^{-1} (0.73 – 1.02 mm^{-1}) vs. 1.61 mm^{-1} (1.47 – 2.02 mm^{-1}).

Altogether, it is not recommended to calculate PCS in these thin caps (< 0.1mm) with manually segmented MRI images for rupture risk prediction. Gijsen et al. showed that due to MRI resolution problem, it is better to look for the stable plaque with thick caps and low PCS (Gijsen et al., 2015). We cannot resolve the resolution issue in MRI with

a geometry-based model to improve the PCS estimation. Further research is necessary
to improve rupture risk assessment based on geometrical plaque features in carotid arter-
ies.

8.4.3   Limitations

One of the limitations of our study is the relative simple isotropic material model that
was used. In diseased tissue, collagen fibers are orientated in a certain direction in order
to absorb higher stresses. However, literature on fiber orientation in carotid arteries is
sparse. A recent study reported a high dispersion of fibers in carotid arteries (Chai et al.,
2014). Therefore, we assume that an isotropic model should be sufficient. Besides,
since this is comparison study, we do not expect another material model to change our
conclusions.

A relatively low number of caps was reconstructed (n = 31) because of several reasons.
From the subset of sections that were used for MRI simulation only half of the NCs were
identified by the readers. The smaller NCs were probably missed because of the size
and the limited resolution. Furthermore, not all NCs that were included had a ground
truth cap smaller than 0.62 mm. Although a low number of sections were included in our
study, we don't expect that increasing the number would have changed our conclusion on
the absence of improvement of PCS, because of the large error range of the PCS for the
reconstructed NCs.

The geometry-based model to estimate $CapT_{model}$ used all the cross-sections obtained
via histology. The same cross-sections were used in the MRI simulations, therefore there
might be dependency among the data. As a consequence, our results might be positively
influenced. An MR scan prior to endarterectomy combined with histology would be an
alternative approach for the MRI simulation. However, in this case 3D registration of
the histology with the MR images is needed which is not straight forward, due to several
problems including deformation due to histological post-processing, and the limited MRI
resolution (Groen et al., 2010), leading to registration errors of 0.6 mm. Thus, 3D regis-
tration with histology yields errors larger than the MRI simulations (Groen et al., 2010).
Furthermore, Nieuwstadt et al. have shown that the MRI simulation are very similar to
in vivo MR images with respect to image contrast, SNR, spatial resolution and intensity
gradients over plaque components. Therefore, we chose to simulate the MRI directly
from the ground truth histology contours.

8.4.4 Conclusion

In conclusion, our model that uses geometry-based features estimates the cap thickness better than experienced MRI readers, which could potentially contribute to risk stratification. The peak cap stress did not significantly improve, probably due to smoothing of other important geometry parameters, such as lumen and NC curvature.

Feasibility of Wall Stress Analysis of Abdominal Aortic Aneurysms using three-dimensional Ultrasound

ABSTRACT

Abdominal aortic aneurysms (AAAs) are local dilations that can lead to a fatal hemorrhage when ruptured. Wall stress analysis of AAAs is a novel tool that has proven high potential to improve risk stratification. Currently, wall stress analysis of AAAs is based on computed tomography (CT) and magnetic resonance imaging; however, three-dimensional (3D) ultrasound (US) has great advantages over CT and magnetic resonance imaging in terms of costs, speed, and lack of radiation. In this study, the feasibility of 3D US as input for wall stress analysis is investigated. Second, 3D US-based wall stress analysis was compared with CT-based results. The 3D US and CT data were acquired in 12 patients (diameter, 35–90 mm). US data were segmented manually and compared with automatically acquired CT geometries by calculating the similarity index and Hausdorff distance. Wall stresses were simulated at P = 140 mm Hg and compared between both modalities. The similarity index of US vs CT was 0.75 to 0.91 (n = 12), with a median Hausdorff distance ranging from 4.8 to 13.9 mm, with the higher values found at the proximal and distal sides of the AAA. Wall stresses were in accordance with literature, and a good agreement was found between US- and CT-based median stresses and interquartile stresses, which was confirmed by Bland-Altman and regression analysis (n = 8). Wall stresses based on US were typically higher (+ 23%), caused by geometric irregularities due to the registration of several 3D volumes and manual segmentation. In future work, an automated US registration and segmentation approach is the essential point of improvement before pursuing large-scale patient studies. This study is a first step toward US-based wall stress analysis, which would be the modality of choice to monitor wall stress development over time because no ionizing radiation and contrast material are involved.

9.1 Introduction

Abdominal aortic aneurysms (AAA) are currently monitored using (mostly) ultrasound based measurements of the maximum anterior-posterior diameter of the aneurysmal wall. Large clinical trials have set the cut-off point for surgical intervention of AAAs at a diameter of 5.5 cm or an expansion rate of 0.5 cm in the last six months (Brewster et al., 2003; Greenhalgh et al., 1998; Singh et al., 2001). However, the associated morbidity and mortality risk (Rose et al., 2014; Scv et al., 2014) of endovascular repair and open surgical repair must be weighed against the risk of rupture. Unfortunately, some AAAs rupture before reaching a maximal diameter of 5.5 cm and some will remain stable up to a diameter of 8.0 to 9.0 cm (Conway et al., 2001; Darling et al., 1977; Kurvers et al., 2004). Hence, a more adequate criterion for patient stratification is sought.

From a biomechanical point of view, rupture will occur when local wall stress exceeds the wall strength. Mechanical analysis of a vessel can be performed by performing a measurement of mechanical properties and/or deformation of the vessel wall, or building a numerical model of the AAA to simulate stresses and deformation. This study will focus on wall stress analysis. In general, wall stress analysis is performed using finite element analysis (FEA), a numerical method that solves a set of linear partial differential equations representing mechanical equilibrium using a patient-specific geometry, material properties and boundary conditions. The three-dimensional (3-D) AAA geometry generally is determined from computed tomography data (CT) or Magnetic Resonance Imaging (MRI). The geometry is converted into a volume mesh of the wall and subjected to a physiological load, i.e., blood pressure. The mechanical behavior of the wall is usually described using either a linear or non-linear material model (Holzapfel et al., 2000; Raghavan et al., 2000).

Numerous studies have shown that wall stress analysis is a potential tool to further indicate the AAA rupture risk (de Putter et al., 2007; Fillinger et al., 2002; Merkx et al., 2009; Raghavan et al., 2000; Speelman et al., 2008; Truijers et al., 2007; Venkatasubramaniam et al., 2004). In these studies, it was found that 99th percentile wall stresses increased with diameter (Speelman et al., 2008) and that peak wall stresses were higher in groups with ruptured AAAs (de Putter et al., 2007; Truijers et al., 2007; Venkatasubramaniam et al., 2004). This technique has led to the introduction of the Rupture Potential Index (RPI), which now is a parameter used in clinical studies (Vande Geest et al., 2006). Besides for global statistical analysis, wall stress computations can also be used for regional analysis. In a study by Li et al. (2010), higher wall stress at the proximal shoulder of the AAA were associated with rapid expansion and possibly rupture (Li et al., 2010).

Most studies are limited to the use of a single set of pre-operative CT-data. However, it would be of great interest to investigate the prediction of aneurysm growth requiring follow-up data. Only a few studies are found on the association between wall stress and aneurysm growth (Li et al., 2010; Speelman et al., 2010), which can be explained by the fact that the use of CT is limited due to the ionizing radiation and contrast agents involved. Magnetic resonance would be a good alternative (de Putter et al., 2007; Merkx et al., 2009), but requires long scanning times, is relatively expensive, and is not applicable to all patients because of e.g. claustrophobia, and the presence of metal implants. Another alternative, as used in this study, is ultrasound (US) imaging.

Nowadays, two-dimensional (2-D) Doppler US is globally used as a screening tool for AAAs, to assess maximum AAA diameter and to investigate the presence of endoleaks after endovascular aneurysm repair (Brewster et al., 2003; Hirsch et al., 2006). US has a relatively high temporal and spatial resolution compared to CT and magnetic resonance and no ionizing radiation involved. Furthermore, US is a patient-friendly, cheap, fast, and easy to use imaging modality. The challenges in US are the low contrast, small field-of-view (FOV) and its operator dependency. In addition, a small percentage of patients is difficult to image due to the aorta's deep position, US attenuation by fatty tissue, or by shadowing caused by bowel gas (Silverstein et al., 2005).

More recently, three-dimensional (3-D) ultrasound has become commercially available. Wittek et al. (2013) showed that combined FEA with 4-D ultrasound data can be used to determine material properties in healthy and diseased aortas (Wittek et al., 2013). In a study by the same group, finite element models have been successfully applied to regularize 3-D strain data obtained with 3-D speckle tracking (Karatolios et al., 2013). In these studies, ultrasound based 3-D wall stress analysis was not the focus and a comparison with established techniques, such as CT, was not made.

The aim of this study was to investigate the feasibility of 3D US-based wall stress analysis of AAAs. Additionally, US-based wall stress analysis was compared with the golden standard, i.e., CT-based wall stress analysis.

9.2 Methods

9.2.1 Population and data acquisition

3-D ultrasound acquisitions were obtained in 15 patients (13 males and 2 females), 0 to 12 weeks prior to or after a contrast enhanced computed tomography angiography (CTA) scan. The CTA scan was performed for pre-operative planning and is part of normal

clinical practice, with the exception of one patient who received a CTA scan for other medical reasons. The age of the subjects ranged from 55 to 83 years, with diameters varying from 35 to 90 mm. The study was approved by the local ethics committee of the Maastricht University Medical Center and all patients gave written informed consent prior to inclusion.

Ultrasound acquisitions were performed by the same experienced physician with 3 years of experience in performing AAA US examinations using a MyLab 70 US system (ESAOTE, Maastricht, The Netherlands) equipped with a BC431 probe with a center frequency of 3.5 MHz. The BC-431 is a mechanical 3-D array, consisting of a 2-D curved array which is rotated over a total elevational angle of 73 degrees. Raw radio-frequency (RF) data were acquired and sampled at 50 MHz with a depth of 10 to 15 cm and an opening angle of 55 degrees in the lateral direction.

As a consequence of the limited field-of-view of the 3-D US data, the complete geometry of the AAAs could not always be captured in a single 3-D sweep. In this case, multiple acquisitions were needed, typically two (n = 4) or three (n = 6).

All CT scans were performed with a Somatom Definition Flash C (Siemens, Erlangen, Germany). Images consisted of 512 x 512 pixels, with a pixel distance ranging from 0.65 to 0.79 mm. Slice thickness varied between 0.7 to 0.8 mm with the exception of one dataset that was obtained in the patient that did not receive a pre-operative CTA scan (4 mm). All data were anonymized and exported for further processing.

Arterial brachial blood pressure was measured in all patients using a conventional arm cuff in a supine position approximately ten minutes after the US exam. No blood pressure measurements were performed during the CT acquisitions.

9.2.2   US-based geometry assessment

The pipeline of the image processing and mesh generation is summarized in Figure 9.1, revealing the longitudinal and cross-sectional US images (Figure 9.1A-D), the resulting segmentation results (Figure 9.1E) and corresponding mesh (Figure 9.1F). The 3-D US data were loaded into Matlab (2012b, Mathworks Inc., Natick, MA, USA) for scan conversion, filtering and segmentation. First the RF-data were converted from the semi-spherical coordinate system into a Cartesian coordinate system using standard 3-D bi-cubic interpolation. The resulting images were aligned in such a fashion, that the y-direction resembles depth, the x-direction equals the width of the aneurysm and the z-direction its length (Figure 9.1). Each cross-sectional image (x,y) was 208 mm by 208 mm with a resulting pixel size of 0.6–0.70 mm by 0.65–0.70 mm. These images were

available for every 2 mm in the longitudinal direction (z). A 3-D cylindrical Gaussian filter of 5 by 5 by 7 pixels ($\sigma = 1$) was used to improve contrast.
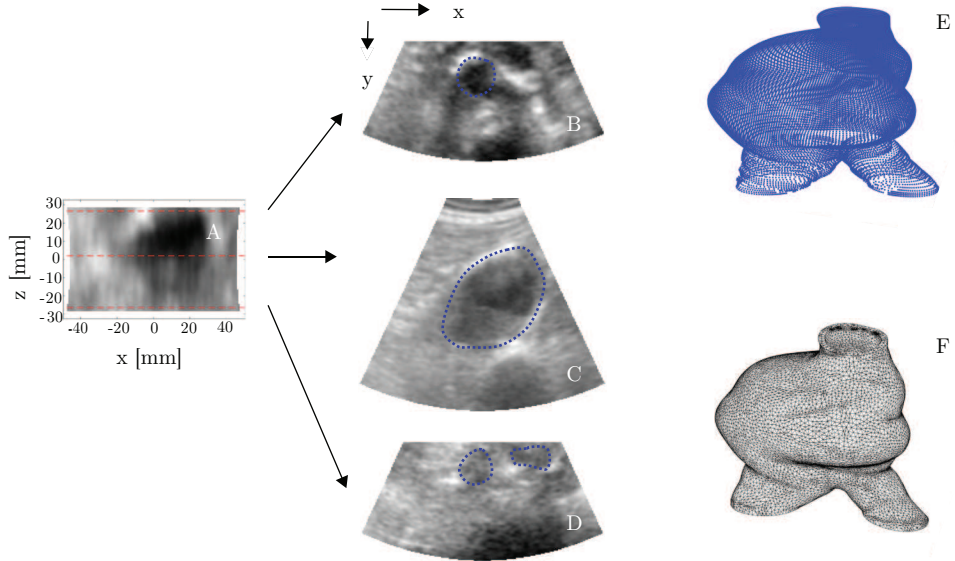
Figure 9.1: *Example of ultrasound (US) based geometry and finite element mesh of an abdominal aortic aneurysm. A longitudinal cross-section of the 3D US dataset is shown (A) with three different transverse cross-sections (dashed red lines) corresponding to the images shown in B, C and D. The manual segmentation of the lumen is shown (blue dashed lines). All contours after regularization (E) and the resulting finite element volume mesh (F) are shown.*

The data were manually segmented by delineating the lumen – wall interface in the transverse cross-sectional image data from the proximal neck up to the bifurcation by a trained observer. Subsequently, all segmentations were checked and corrected by a second reader with 3 years of experience in US and AAA vessel wall segmentation. Finally, the user-defined contours were up-sampled to 181 data points (incremental angle of 2°) by transforming the coordinates to the Fourier domain. By only maintaining the Fourier coefficients of the first two harmonics for the inverse transformation, the reconstructed data were also regularized.

A Graphic User Interface (GUI) was created in Matlab to merge the resulting 3-D point clouds obtained from multiple US acquisitions. The GUI enabled rigid rotation and trans-

lation in all three directions, amounting to a total of six degrees of freedom.

Irregularities in the resulting AAA vessel wall contours may result in (false) high wall
stress regions in the FEA models. Therefore, a second regularization step was applied to
ensure smoother gradients in all directions. All Cartesian coordinates (Figure 9.2A) were
transformed to a radial grid with radius r as a function of (θ, z), see Figure 9.2B. This
surface is smoothed by fitting a surface to the scattered radius data using a modified ridge
estimator (Figure 9.2C) and transformed back to Cartesian coordinates. An example of
the resulting contours is found in Figure 9.2D.
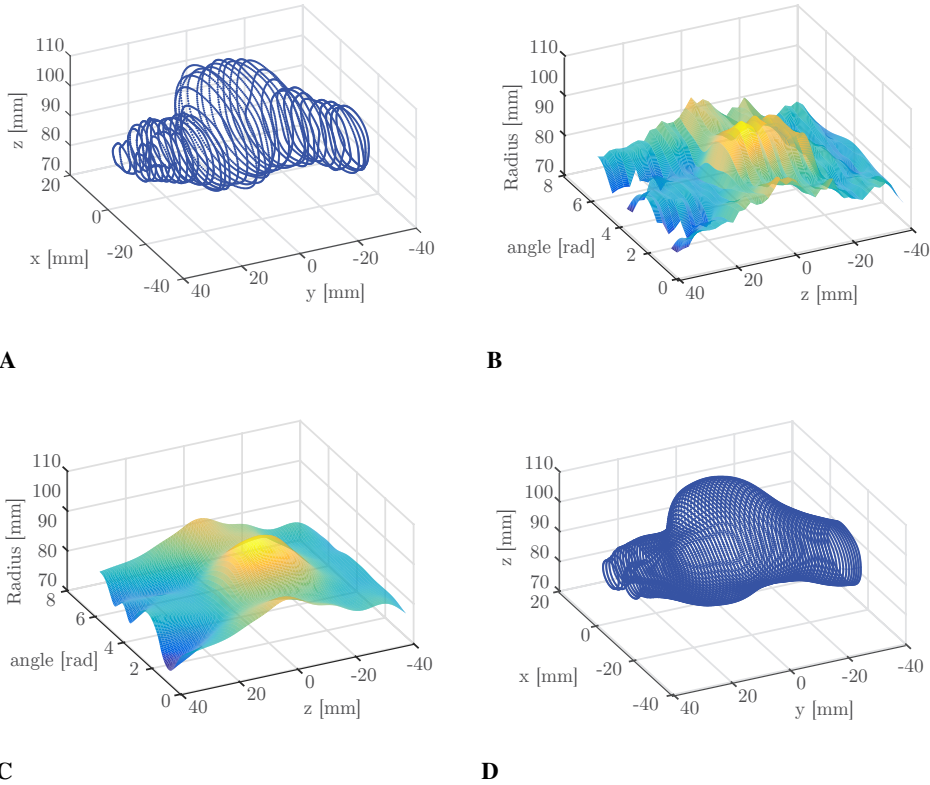
Figure 9.2: *The manual, up-sampled lumen segmentation obtained in three-dimensional ultrasound data in Cartesian coordinates (A) and polar coordinates (B), respectively. The contours were regularized (C) and were converted back to the Cartesian domain (D).*

9.2.3 CT-based geometry assessment

An example of CT data is found in (Figure 9.3A-D). Commercial software (Mimics 5.0, Materialise, Belgium) was used for semi-automatic segmentation of the border between the outer AAA vessel wall and the surrounding tissue (Figure 9.3E) to generate a volume mesh (Figure 9.3F). An initial segmentation was performed using a region growing method, after which surrounding structures were detached from the AAA manually. The final segmentation was exported to Matlab for further processing.
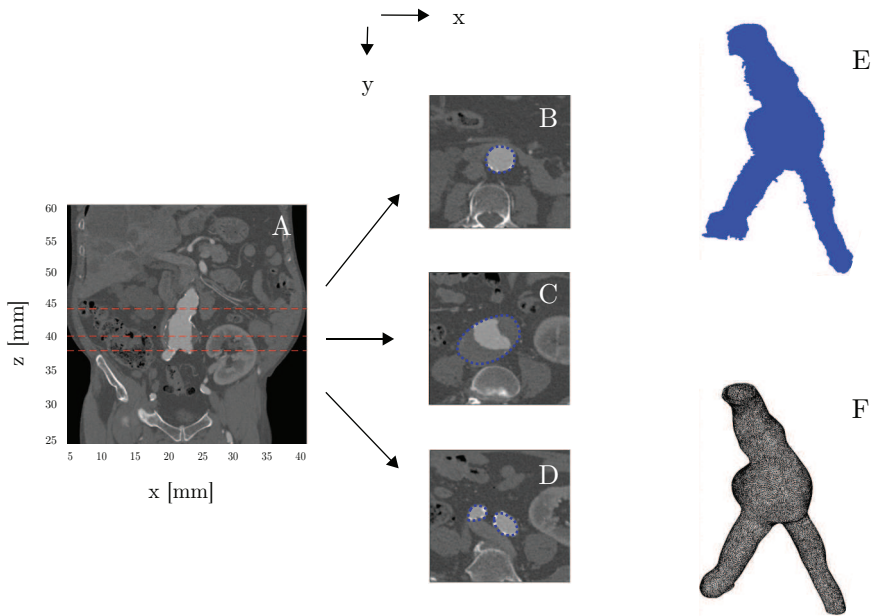
Figure 9.3: *Example of computed tomography (CT) based geometry and finite element mesh of an abdominal aortic aneurysm. A longitudinal cross-section of the 3D CT dataset is shown (A) with three different transverse cross-sections (dashed red lines) corresponding to the images shown in B, C and D. The automatic segmentation of the lumen after processing in 3-Matic is indicated (blue dashed lines). All contours after processing in 3-Matic (E) and the resulting finite element volume mesh (F) are shown.*

9.2.4 Comparison of US and CT-based geometries

To compare US and CT geometries, the GUI was used to manually register US with
CT data. The US contour data were resampled to match the CT based contours for
comparison. The top and bottom sections were trimmed to ensure that the region of
comparison was present in both the CT and US geometries. The mean curvature was
calculated for the surface mesh to assess local smoothness.

To quantify the similarity between the US and CT based segmentation, the similarity
index (SI) was calculated, also known as the Dice coefficient (Bartko, 1991). The SI is a
measure for volume overlap and is defined as:

$$SI = \frac{2 \cdot \{P_{US} \cap P_{CT}\}}{P_{US} + P_{CT}} \tag{9.1}$$

with P_{US} the number of pixels of the US contour, and P_{CT} the number of pixels within
the CT contour.

In addition, to quantify the (maximum) distance between the US and CT segmentations,
the Hausdorff distance(HD) was used. The HD is the maximum of the minimal distances
between points on the US and CT contours, respectively. The calculated distances are
used to quantify the local similarity within the two volumes by measuring the extent to
which each point of the US shape lies near a point on the CT contour set (Huttenlocher
et al., 1993). For a more regional analysis, the HD was calculated per transverse slice.
The SI was calculated for the total overlapping geometry of both US and CT data and for
the same geometry without the bifurcation. The Hausdorff distance, however, was only
calculated for the geometry without the bifurcation.

9.2.5 Wall stress analysis

The common iliac arteries and the proximal part of the US based AAA geometry were
imported in 3-Matic, version 8.0 (Materialise, Leuven, Belgium). The bifurcation was
manually connected to the proximal part and rough edges were smoothed using 3-Matic.
The outer wall was generated by expanding the surface in the normal direction assuming
a uniform wall thickness of 2 mm, creating a volume mesh of the wall.

The CT geometries were also processed in 3-Matic. The point cloud was converted
into a surface, which was also smoothed to remove sharp edges. Opposed to the US

contours, the inner wall was created by expanding the CT-based surface 2 mm inwards in the normal direction.

In 3-Matic, a wall mesh was generated using 10-node quadratic tetrahedral elements (100000 – 170000 elements). It was ensured that at least two layers of elements were present in the radial direction. The resulting mesh was exported to ABAQUS v6.11 (Dassault Systèmes, Paris, France), see also Figure 9.1F and Figure 9.3F.

The top and lower planes were constricted entirely. The AAA wall was assumed to behave as an incompressible, isotropic, hyperelastic solid (Raghavan et al., 2000) with parameters reported by Raghavan and Vorp (2000). They found values for the material properties, α=17.4 MPa and β=188.1 MPa, by performing tensile tests on 69 human specimens of AAAs (Raghavan et al., 2000).

Because the US and CT acquisition were not ECG triggered, the measured geometries were assumed to resemble the geometry obtained at mean arterial blood pressure (MAP). Therefore, the initial meshes are not stress-free. To obtain the stresses in the geometry at MAP, the backward incremental (BI) method was implemented in ABAQUS and applied to each geometry using the MAP measured in each patient(de Putter et al., 2007). The aortic MAP was estimated from the brachial MAP as described by Van 't Veer et al (van 't Veer et al., 2008), by assuming that the aortic systolic pressure is 5% higher than the brachial pressure and the aortic diastolic pressure is 15% lower than the brachial pressure.

Next, the vessel was pressurized to a peak systolic pressure of 140 mmHg. The resulting solution of the FEA was used to calculate Von Mises stresses (σ_{VM}), which enables comparison with previous studies (Fillinger et al., 2002; Speelman et al., 2008; van 't Veer et al., 2008). The Von Mises stress at a systolic blood pressure at 140 mmHg is hereinafter referred to as wall stress.

9.2.6 Analysis and statistics

The SIs for the total geometry, and both SIs and HDs for the geometry without bifurcation, were tested for normality using a Kolmogorov-Smirnov test. In all tests a significance level of $p < 0.05$ was considered to be significant. The Hausdorff distances per AAA for all slices were not normally distributed; therefore, the median and percentiles are reported.

The registered CT and US geometries were divided in regions, slices of 1 cm thickness from the distal to proximal side. The wall stresses were tested not normally distributed

(Kolmogorov-Smirnov test, p<0.05), so the median stresses were calculated. The median
CT and US stresses were compared for all regions and all AAAs using regression analysis
and Bland-Altman analysis. The 25th, 50th, 75th, and 95th percentile wall stresses were
calculated for each aorta and modality and regression analysis was performed. Finally,
regions of high stress (> 350 kPa) were identified, and the curvature of these regions was
compared.

9.3   Results

CT and US data from twelve patients (11 males and 1 female; age 69 ± 8 years; maximum
diameter AAA 62 ± 14 mm) were included for analysis. One patient of the original fifteen
was excluded due to bad image quality, and two for a severely limited FOV. Figure 9.4
shows one example where the registered CT and US geometries show good similarity
Figure 9.4A, SI of total geometry = 0.89) and one case were this was less successful
(Figure 9.4B, SI of total geometry = 0.74) and a large region of the US geometry (red)
lies outside the CT based one (blue).

A   **B**
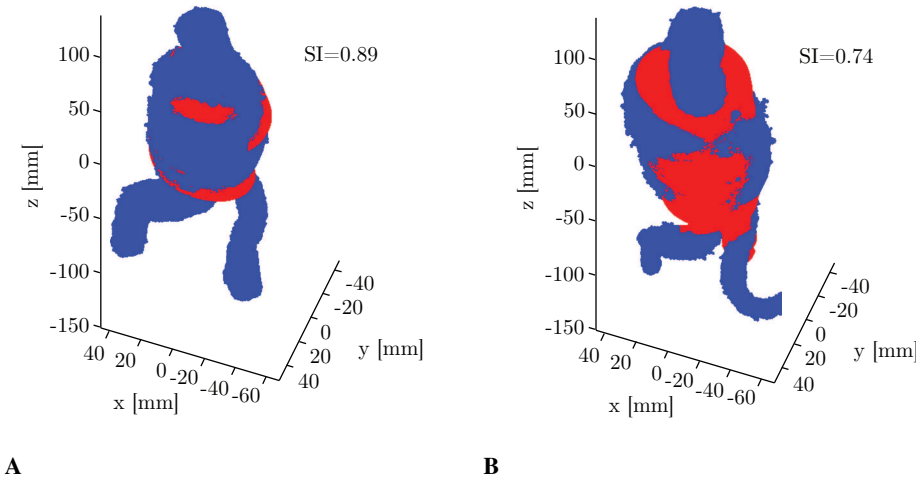
Figure 9.4: *Segmentation obtained from computed tomography (CT) data (blue) and
ultrasound data (red) after registration, revealing a good similarity (A) and a lower
level of similarity (B).*

The quantitative results of the geometry and wall stress analysis are listed in Table 9.1.
The SI values of the total geometry and the geometry without the bifurcation range be-

tween 0.74 - 0.89 (median = 0.81) and 0.76 - 0.91 (median = 0.85), respectively (see Table 9.1). The median Hausdorff distance per patient ranges from 4.8 – 13.9 mm, with a median of 7.3 (IQR: 6.5 – 10.1). For all contours of all patients combined, the median Hausdorff and interquartile range are 8.1 (6.0 – 11.1) mm. Higher HDs are found at both the proximal and distal ends of the geometry (Figure 9.5), whereas the median and interquartile range of the HD for the middle half of the AAA are lower, 7.4 (6.0 – 9.5) mm. The results are not significantly different for the eight patients that were included in the wall stress analysis.

Table 9.1: *The similarity index (SI) for the computed tomography (CT) and ultrasound (US) geometries with and without the bifurcation and the Hausdorff distance (HD) for the geometry without bifurcation.*

Patient	SI total geometry	SI, no bifurcation	HD in mm, median (IQR)	Von Mises Stress (kPa)						Maximum diameter (mm)
				CT median (IQR)	US median (IQR)	CT 95%	US 95%	CT 99%	US 99%	
1	0.85	0.86	4.8 (3.8-6.9)	68 (54-90)	75 (57-98)	147	153	252	212	35
2	0.78	0.80	11.3 (7.5-15.6)							64
3	0.85	0.88	6.1 (5.4-6.6)	129 (96-168)	167 (122-215)	236	351	310	521	52
4	0.77	0.86	7.0 (5.6-9.0)							60
5	0.89	0.91	5.5 (4.1-6.2)	136 (108-168)	144 (110-190)	215	276	276	363	65
6	0.83	0.86	8.4 (7.4-10.0)							72
7	0.75	0.76	9.6 (7.8-13.4)	131 (95-165)	148 (105-210)	240	338	336	485	61
8	0.74	0.79	13.9 (9.7-18.6)	222 (178-270)	231 (165-299)	365	419	467	534	54
9	0.81	0.85	7.2 (5.1-9.3)	111 (85-144)	133 (100-189)	223	336	300	659	95
10	0.83	0.85	10.6 (9.3-12.6)	211 (172-254)	190 (140-262)	361	431	573	589	74
11	0.80	0.84	7.4 (6.2-9.5)	125 (98-158)	166 (125-218)	235	364	315	572	55
12	0.81	0.83	7.3 (6.0-8.6)							90

[*] IQR, Interquartile range. The median and IQR Von Mises stresses and the 95th and 99th percentile wall stresses are given for both US and CT as well as the maximum diameter (clinical measurement).
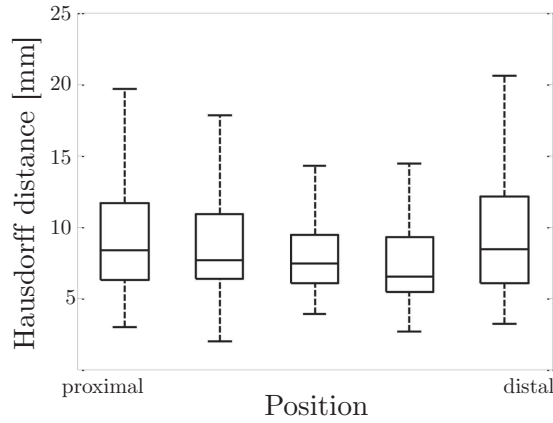
Figure 9.5: *Box-and-whiskers plots of the Hausdorff distance for all abdominal aortic aneurysms (AAA, n = 12). Each AAA was divided in five equidistant areas in longitudinal direction from the proximal to distal side of the AAA.*

The wall stresses of the CT and US geometries are shown in Figure 9.6. Good similarity in geometry can also be appreciated. Patients 1 and 5 are clear examples where the geometries show a high similarity (Figure 9.6A,C, respectively), whereas the agreement is much poorer for patients 8 and 10 (Figure 9.6D,E, respectively). The stress images reveal similarities as well, but high-stress spots are found in the US-based results. In two cases, the US geometries shows significant irregularities in the geometry whilst the CT geometries have a much smoother appearance. This leads to large high stress bands in the US-based wall stress images. This was corroborated by the curvature analysis. Regions with high stresses revealed curvatures in the US data that were 1.5 to 75 times higher as compared to the CT based results. Wall stresses are reported for 8 of 12 cases because of converge issues of the FEA computations in the other four. The total computation time for US based and CT based wall stress analysis was 0.5 – 9 hours (3.5 hours on average).
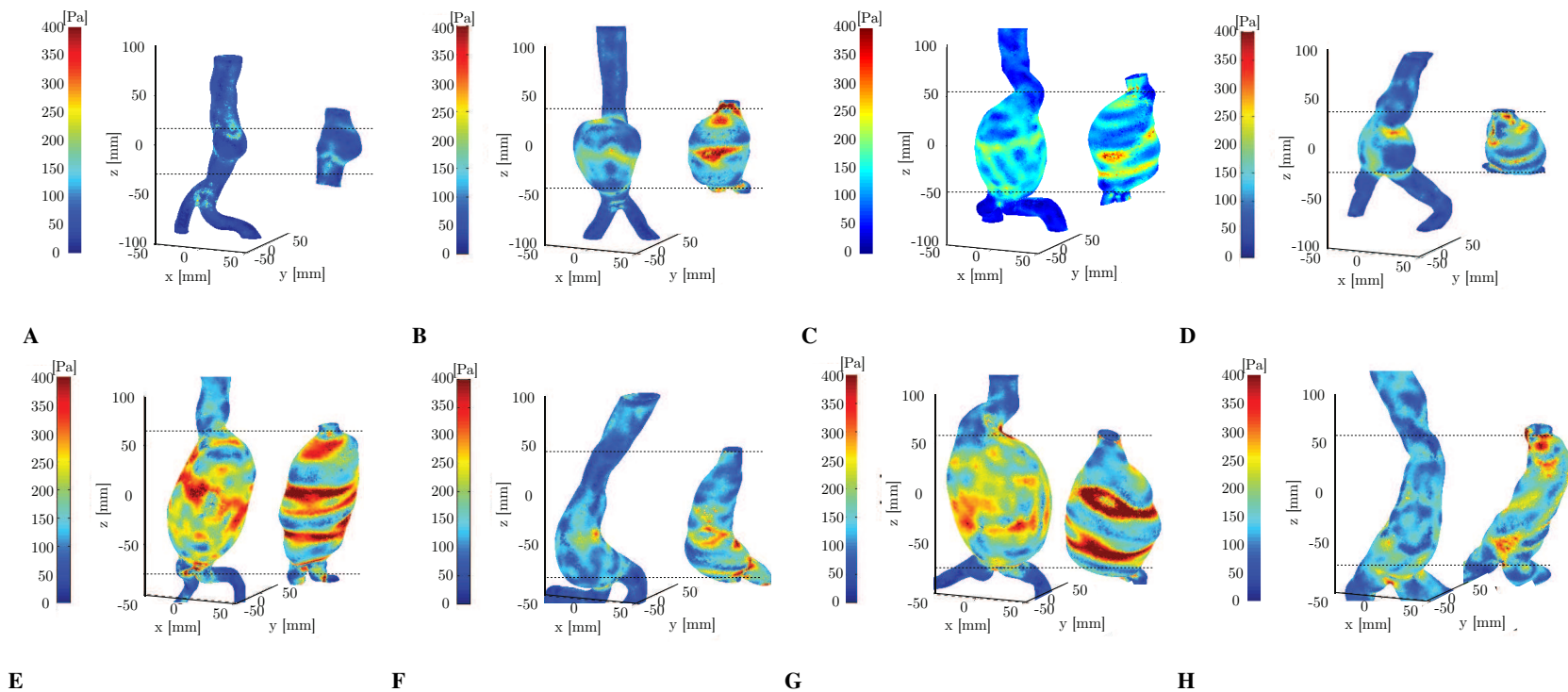
Figure 9.6: *Wall stress images of abdominal aortic aneurysms (AAA) for the resulting eight patients (A-H). For each AAA, the computed tomography (CT) based wall stress (left) and ultrasound (US) based wall stress are shown (right). The black dashed lines are added to indicate the region in the CT results that corresponds to the US based wall stress data.*

The median stresses of the US-based analysis per slice were slightly higher compared to the CT-based results (Figure 9.7A). However, regression analysis revealed no consistent overestimation in terms of slope ($\approx$1). A fixed bias of 15 kPa was found between US and CT stress measurements and was corroborated by Bland-Altman analysis (Figure 9.7B).

A

B
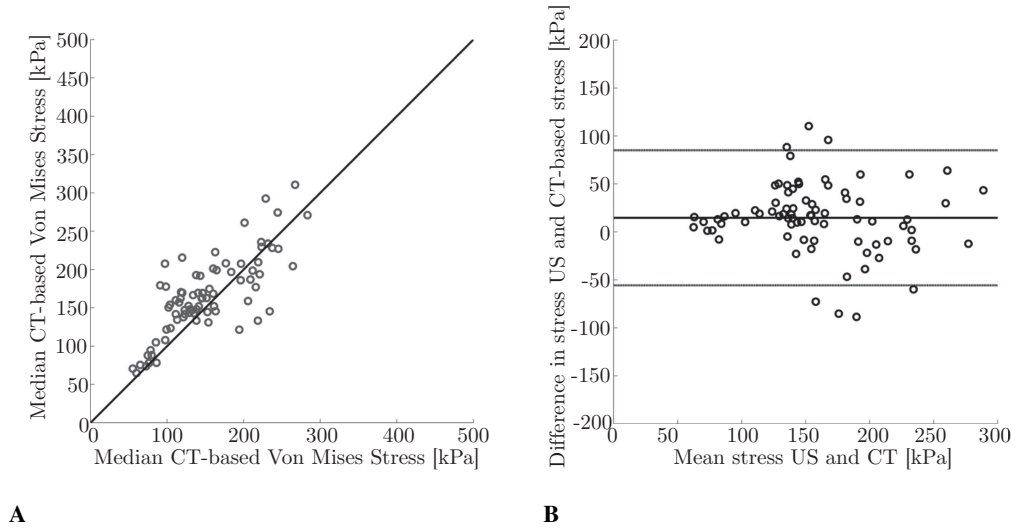
Figure 9.7: *Median wall stress based on 3D ultrasound data (US) vs. computed tomography (CT) data for all patients. The median wall stress was calculated for corresponding, registered slices with a thickness of 1 cm (circles). The line of equality is added for visualization purposes (black solid line); B) Bland-Altman plot, comparing the differences in median wall stress between US and CT. The bias (15 kPa) and the limits of agreement are indicated (black solid lines)*

Figure 9.8 and Table 9.1 show all percentile stresses obtained with CT and US-based wall stress analysis. Overall agreement is good, but the higher US-based stresses exceed those of the CT data. Regression analysis over the percentiles calculated reveals that US stresses are 23% higher (6 – 39%) than those calculated from CT data, indicating that larger differences are found between the two modalities when considering higher stresses in the comparison as well. The 99th percentile stress is significantly larger for the US data, which is in agreement with the high-stress bands found in the US-based results in Figure 9.6, especially for in Figure 9.6D and in Figure 9.6H.
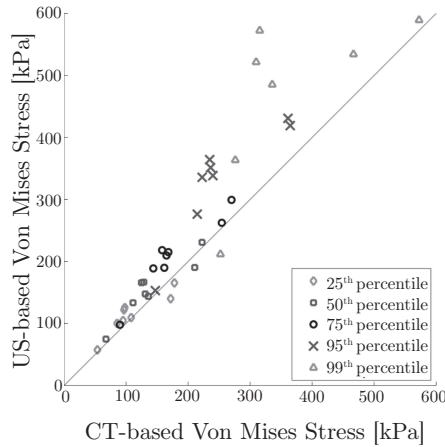
Figure 9.8: *Comparison of the 25th, 50th, 75th, 95th and 99th percentile wall stresses calculated for the entire geometry, as obtained with computed tomography and three-dimensional ultrasound. The line of equality was added as a visual aid (black solid line).*

9.4   Discussion

In this study, the feasibility of 3D ultrasound based wall stress analysis was investigated and compared to the golden standard, i.e., CT-based wall stress analysis. The two main findings of this study are: 3-D geometry can be successfully obtained using 3D US. In case of a limited field-of-view, multiple acquisitions can be used and registered. A good correspondence was found between the two modalities in terms of geometry. Wall stresses are in correspondence with previous studies and on average the overall agreement was good. However, the 3D US overestimates CT-based wall stresses in the higher stress regions.

The main difference between the CT and US data is the manual handling of the probe, the limited field-of-view and relatively low contrast. To circumvent the FOV limitations, multiple datasets were acquired in several patients. The resulting geometries are in good correspondence with the CT geometry (Table 9.1). One of the major limitations was imaging of the neck and bifurcation of the aneurysm. It was hypothesized that the bifurcation would reveal poor resemblance to the CT data. However, exclusion of the bifurcation, only led to a minor increase in SI.

In general, similarity indexes of 70% and higher are indicated as 'good agreement' between two geometries (Bartko, 1991). Comparison between CT and 3D US geometries of these twelve AAA patients revealed similarities of at least 0.74, indicating a good to excellent (0.91) level of geometry overlap. The Hausdorff distances are a measure for the largest mismatches between contours. Per patient the median Hausdorff distance revealed considerable range. However, a clear trend was observed of higher HDs at both the proximal and distal ends of the geometry (Figure 9.5). This can be explained by possible erroneous registration of the multiple contours and low echogenicity at the proximal end the distal sides of the AAA. However, there is no clear relation between lower SIs or higher HDs and the presence of the high stress regions (Table 9.1). Hence, overall geometry is assessed to an appropriate level, but local irregularities result in artifacts in the stress data.

These local irregularities can be explained by the other major limitation of this study: manual segmentation and registration. The volumes with the most predominant high stress regions are in fact the result of registration of three separate sub-volumes (Figure 9.6E,G. The fusion of the different geometries needs to be improved to result in smoother transitions. More acquisitions can be used to increase the overlapping area, but this would increase the examination time. Automated segmentation and registration of 3D US data of AAAs is not straightforward and only few scientific studies are found (Rouet et al., 2010). The availability of automated processing would also decrease the labor intensity and reproducibility.

It was assumed that the blood pressure of the patients was equal during US and CT acquisition. However, it is possible that the mean arterial blood pressure was higher during the US examination, which could also explain the higher stresses, or higher during the CTA scan due to anxiety of the patient. In future studies, the blood pressure should be assessed before and after each US and CTA exam.

The median stresses of the US and CT data were in good correspondence. No obvious reason for the fixed bias present between the median stresses of US and CT (15kPa) was found. The 99th percentile stresses of the CT data (250 kPa – 570 kPa) were in correspondence with previous studies (Fillinger et al., 2002; Raghavan et al., 2005; Speelman et al., 2010) However, an overestimation of stresses was found when comparing the 99th percentile stresses of US to CT due to the aforementioned reasons (Table 9.1). The 95th percentile wall stress is for this study more appropriate for comparison.

The same boundary conditions were chosen as in the study by Speelman et al. (Speelman et al., 2008). Because the FOV of US is smaller than that of CT, this may explain why

higher stresses were found in the US data. To enable comparison with previous studies, the material model by Raghavan and Vorp was chosen (Raghavan et al., 2000). However, if 4-D ultrasound would be available, the actual material properties of the model could be estimated from these data by measuring displacements and strains, yielding a patient-specific model of the aneurysm, and thus more accurate stresses in the wall. Moreover, local material properties (calcifications) and the influence of thrombus and vessel tortuosity should be considered. Finally, an anisotropic, fiber-reinforced model could be employed for a more realistic description of the AAA's material behavior (Holzapfel et al., 2000). In future research, there is a need for further optimization of the US acquisition, and an automated segmentation and registration method. When these issues are addressed, a larger sample size can be included and, ultimately, a longitudinal study to investigate growth.

9.5   Conclusion

In conclusion, this study is a first step towards wall stress analysis using 3D US. Good similarities in geometry and median stresses were found, but the registration of multiple volumes caused high stress bands, thereby prohibiting comparison of the 99th percentile and peak stresses. With the appropriate algorithms in place, 3D US is a good and economical image modality for AAA monitoring and wall stress analysis and a promising tool for longitudinal studies on growth.

10

DISCUSSION

In this thesis, studies were described in which computational modelling was applied to investigate the relationship between blood flow-induced shear stress, wall stress, and the vascular diseases (atherosclerosis and AAA).

10.0.1 Summary

Shear stress

Atherosclerosis is a complex, multifactorial arterial disease that arises from the interplay of haemodynamic, systemic, and biological factors. Because of geometry's major influence on local haemodynamics, geometrical factors, rather than haemodynamic factors, were proposed as alternative risk predictors for atherosclerosis. In **Chapter 2**, the influence of geometry on haemodynamic parameters in both carotid and coronary arteries was described: for both carotid and coronary arteries, multiple geometric features were associated with low and oscillatory shear stress. Carotid artery bifurcations (in which the internal carotid artery was much smaller than the common carotid artery) and tortuous carotid arteries were more often exposed to low and oscillatory shear stress. Coronary bifurcations with higher tortuosity and wider bifurcation angles were associated with lower shear stress.

Helical flow, which was observed in various arteries throughout the cardiovascular system, was proposed to be atheroprotective. In **Chapter 3**, computational modelling was used to investigate the presence of helical flow structures in porcine coronary arteries. This study illustrated the counter-rotating bi-helical flow being present in coronary arteries, as expressed by several helicity indexes. High helicity was associated with favorable high WSS conditions, which indeed suggests that helical flow is atheroprotective in coronary arteries.

In the cardiovascular system, blood flow pulsates over the cardiac cycle, resulting in temporal and spatial fluctuations in the magnitude and direction of shear stress. New metrics that capture the multidirectionality of shear stress were used to assess its influence on plaque growth and compositional changes in twenty human coronary arteries (**Chapter 4**). We provided evidence that multidirectional shear stress influences changes in plaque composition but less involved in changes in plaque size over a six-month follow-up period. TAWSS and cross-flow index (CFI), a multidirectional shear stress metric, proved to

synergistically affect plaque growth and changes in plaque composition. Taken together, an image-based assessment of multidirectional shear stress and plaque composition is imperative to understand the process of coronary atherosclerotic plaque progression and destabilization.

In **Chapter 5**, a study is described in which a new imaging NIRS-IVUS catheter is used that allows simultaneous assessment on plaque size and the probability that lipids are present inside the plaque in ACS patients. Shear stress was assessed at baseline, and imaging was repeated after one year to study plaque progression. We hypothesized that shear stress in the presence of lipid-rich plaques is a more accurate predictor for plaque progression than high patient-based systemic LDL levels. We found that neither NIRS positive regions nor high LDL levels alone predicted plaque growth. However, synergy was observed between NIRS positive regions and multidirectional shear stress; specifically, high relative residence time (RRT) and low transWSS were more predictive for plaque progression. High systemic LDL levels in combination with shear stress did not predict plaque progression. These data suggest that future studies estimating regions at risk of plaque growth would benefit from NIRS-based lipid assessment in combination with different shear stress parameters.

Chapter 6 describes a study on the relationship between atherosclerotic plaque progression, composition changes, and multidirectional shear stress in a new porcine model for atherosclerosis. The adult pigs were hypercholesteraemic because of a mutation in the LDL receptor, and they received a high-fat diet for 9-12 months to promote the development of atherosclerosis. This model resulted in two distinct groups of animals in terms of plaque growth speed. Plaque growth and more advanced plaque phenotypes were strongly associated with low TAWSS and high multidirectional shear stress. Interestingly, in the slow responders, no relationship between plaque growth and multidirectional shear stress was observed.

Wall stress

A subgroup of atherosclerotic plaques that develop in the cardiovascular system are at high risk of rupture, potentially leading to cardiovascular events such as a myocardial infarction or stroke. These high-risk plaques typically contain a large NC, are highly inflamed, and present with a thin fibrous cap. Comprehensive approaches, such as computational modelling, are employed to assess the local stress distribution inside the plaque and predict the risk of rupture. To enable computational modelling of such a risk, a model of the plaque's NC, cap thickness and outer wall is required. Invasive imaging technology does not allow for visualization of all important individual components si-

multaneously. In case of plaque imaging with both IVUS and OCT, two clinical invasive imaging techniques, the back side of the NC is not fully captured. A new methodology was developed (using histology as ground truth geometry) to reconstruct the backside of the NC by determining the empirical relation between a number of geometric features and the NC thickness (**Chapter 7**). The NC thickness was found to be related to NC angle, intima-media thickness, and cap thickness. The peak cap stress values obtained in the ground truth geometries were highly correlated with the stress values calculated in the reconstructed geometries. The methodology developed in this study enables IVUS and OCT data to be fused in future wall stress studies.

MRI of carotid plaques suffers from low in-plane resolution: the fibrous cap cannot be accurately visualized. In **Chapter 8**, a new methodology to complete the front side of the NC using a geometric model was developed. The ground truth geometry was based on histology, thereby preserving detailed features such as lumen and NC curvature. However, neither the human readers nor the geometry models were able to identify these small features due to the limited resolution of the MRI. Consequently, these features were artificially smoothed out in the model. The geometric model's estimation of cap thickness was more accurate than those of experienced MRI readers. However, this improvement did not translate into improvements in the peak cap stresses. The detailed features captured by histology but not by MRI were probably dominant over the cap thickness improvement.

Chapter 9 reveals the first models of peak wall stresses in AAA geometries derived from 3D-US. The results were compared with the ground truth geometries obtained via CT. Good geometric similarity was found between both imaging modalities. In some AAAs, the full AAA geometry could not be captured in one 3D US view. Therefore multiple views were fused, but caused irregularities in geometry which caused high-stress bands. These high stress bands hindered the analysis of the 99 percentile and peak stresses. However, the median stresses were congruent. If 3D reconstruction based on 3D-US improves, it has the potential to be a useful imaging modality for both medical and research purposes.

10.1   Methodology and Analysis

10.1.1   Shear stress

In this thesis, the 3D-reconstruction of the coronary arteries, the boundary conditions, and the post-processing were carefully established to allow accurate determined of shear

stresses and optimal data interpretation.

First, we reconstructed the geometry of the coronary artery all the way up to the aorta to include the full curvature of the artery. In this way, we assumed a flat pulsatile velocity profile at the inlet; which is realistic since the inlet is close to the aorta where a flat profile is present, we therefore believe that this approach mimics in vivo inflow conditions as closely as possible. In this way, the inlet velocity profile in the region of interest is well developed, and the entire region of interest can be analysed.

Second, side branches were included in the 3D reconstruction because these regions are of particular interest for the development of atherosclerosis. Previous studies often neglect to include these side branches (Bourantas et al., 2018; Stone et al., 2012; Vergallo et al., 2014), even though plaques are usually formed therein (VanderLaan et al., 2004). Furthermore, side branches are needed to determine the flow that leaves the artery. Therefore, side branches affect absolute shear stress values (Li et al., 2015), especially distal from side branches in the more downstream regions of the artery. Sakellarios et al. demonstrated that including side branches in computational models allows shear stress-related plaque progression to be more accurately predicted (Sakellarios et al., 2017). The data found in chapter 5 and chapter 6 confirm this observation with higher positive predictive values (PPVs) of TAWSS for plaque growth compared to previous studies (Stone et al., 2012).

Third, patient-specific invasive Doppler measurements have been used to determine in- and outflow boundary conditions. Although our analysis benefits from patient-specific flow measurements which allow the assessment of absolute shear stress values, it is rather difficult to position the catheter in the centre of the lumen. Because of this challenge, the measurements can be inaccurate and since erroneous boundary conditions directly affect shear stresses, a consensus meeting was held to judge the reliability of the measurements. The data described in chapters 5 and 6 were obtained using this strategy. As an alternative to invasive velocity measurements, a resistance-compliance element, lumped parameter Windkessel model could estimate vascular impedance. This model could potentially replace invasive velocity measurements (Duanmu et al., 2018).

In this thesis, fluid-structure interaction (FSI) simulations, which model the fluid (blood) simultaneously with the solid (vessel wall), were not performed. In simulations using rigid walls, FSI's effect on shear stress is small (5%–7.2%) (Bahrami and Norouzi, 2018; Lee and Xu, 2002). Bahrami et al. found similar results for oscillatory shear index (OSI). However, Pinho et al. found larger differences for OSI (37%) and RRT (49%) (Pinho et al., 2018). FSI might be important in regions where severe stenosis influences

pressure and velocity fields, leading to large gradients in radial wall displacement (Nejad et al., 2018) and further leading to high velocity, high shear stress, and recirculation zones. Therefore, it would be wise to use our workflow to investigate the degree to which FSI influences the analysis of different multidirectional shear stress parameters and helical flow. It would be especially important to investigate FSI's influence especially on geometries without stenosis and in the presence of severe stenosis. Note that FSI will dramatically increase the computational simulation time, which makes it impractical for clinical use.

We did not account for the motion of the heart, which contracts and twists over the cardiac cycle, potentially affecting shear stress in the coronary arteries. Several methods can determine cardiac motion (Somphone et al., 2013; Xavier et al., 2012). Zeng et al. found that cardiac deformation has minimal effect on TAWSS in RCAs (Zeng et al., 2003). However, in RCAs, it affected temporal shear stress variations due to the large variation in curvature and torsion during the cardiac cycle (Zeng et al., 2003). Moreover, cardiac deformation affects the secondary flow patterns, especially the size, strength, and location of secondary vortices in RCAs. The OSI was also affected in RCAs (Torii et al., 2010). The effect of heart movement will most likely be less significant in LAD and LCX, since the displacement caused by cardiac contraction is largest in the RCA (Shechter et al., 2006). Future studies should explore the effect of heart movement on the relationship between multidirectional shear stress, plaque progression, and plaque composition changes.

After a successful CFD simulation, the local shear stress vector over time can be derived from the local velocity field. Different metrics describe different aspects of the time varying shear stress vector at a certain location, see chapter 3, 4, 5, and 6. Alternative methods can be used to summarize velocity patterns inside the coronary artery with, for example, using helicity indices. Chapter 3 shows that these helicity indices are related to shear stress. The studies described in chapters 4, 5, and 6 investigated the relationship between multidirectional shear stress metrics and plaque growth (and changes in composition).

To further analyse the influence of shear stress on plaque progression, studies described in literature employed a variety of post-processing analysis strategies (Bourantas et al., 2018; Samady et al., 2011; Stone et al., 2012; Vergallo et al., 2014). To summarize, researchers subdivide the vessel into multiple longitudinal and circumferential regions and average the shear stress and wall parameters in these regions. By doing so, researchers obtain independent samples from multiple locations within the vessels, which allows them to study the local response of the artery. In this thesis, we based our circumferential

and longitudinal subdivision on the potential mismatch error of baseline and follow-up frames and on the presence of circumferential heterogeneity (Timmins et al., 2017) of the haemodynamic environment (chapter 4); we therefore used 1.5 or 3 mm by 45° regions. Others used 3 mm segments without circumferential subdivision of the segments, but checked for the lowest 90° of TAWSS (Stone et al., 2012). Because different studies employed various post-processing approaches (Koskinas et al., 2010; Samady et al., 2011; Stone et al., 2012), study comparisons are difficult. Therefore, it would be beneficial for the research community that investigates shear stress-related coronary atherosclerosis to reach a consensus on post-processing techniques.

Furthermore, to study shear stress-related plaque progression or composition changes, regions are typically divided into two (low, high) or three (low, mid, high) shear stress groups based on the absolute average shear stress in that region. Many absolute thresholds for these groups can be found in literature, see Table 10.1.

Table 10.1: *A literature overview of different absolute thresholds used for the time-average wall shear stress (TAWSS). For each study, the thresholds for low, intermediate, and high TAWSS and the characteristics of the studied subjects are presented. Some studies divided the TAWSS in two groups (indicated with*).*

	Low [Pa]	Intermediate [Pa]	High [Pa]	Subjects
Koskinas et al. (2013a,b)*	<1.2	-	>1.2	Swine
Stone et al. (2012)	<1	1–1.7	>1.7	Human
Samady et al. (2011)	<1	1–2.5	>2.5	Human
Davies et al. (1984)*	<0.3	-	>1.3	Human cells
Koskinas et al. (2010)	<1	1–1.5	>1.5	Swine
Stone et al. (2018)	<1.3	-	>1.3	Human

In chapters 5 and 6, we use vessel-specific shear stress thresholds. Liu et al. also used vessel-specific thresholds; however, the applied values were not reported (Liu et al., 2017).

The threshold (absolute or vessel-specific) that best predicts plaque growth or changes in plaque composition is unknown. Endothelial cells respond to shear stress; regions of low and oscillatory shear stress are especially atheroprone (Davies et al., 1986; Malek et al., 1999). However, it is unknown whether all endothelial cells—independent of vessel where they reside—react at the same (absolute) thresholds. Alternatively, endothelial

cell response may be dependent on overall shear stresses per individual vessel, and cells may react to relative shear stress changes. If endothelial cell response is relative and if the overall shear stress in a vessel is low, then atheroprone shear stress might be much lower than if absolute values would be used. However, if overall shear stress is high, then atheroprone behaviour might be expected at absolute high shear stress. From this thesis, we cannot conclude whether cells respond to absolute or relative shear stress values and thus which threshold is appropriate.

The TAWSS and multidirectional shear stress metrics reported in the patient study in chapter 4 are significantly higher than the values in the patient and pig study described in chapter 5 and 6, see Table 10.2. Note that the shear stress in an artery is dependent on the flow through the artery, which in all studies was assessed using Doppler-derived velocity measurements multiplied by the cross sectional area of the artery. The question arises whether the significant differences in shear stress could be explained by differences in flow. Indeed, the inlet flows (216 mL/min IQR: 126 -– 324 mL/min) of the analysed LADs in chapter 4 were significantly two-three times higher than the inlet flows measured in the LADs analysed in 5 (60 mL/min IQR 48 -– 108 mL/min) and 6 (90 mL/min IQR: 66 – 120 mL/min). Another reason for the higher shear stress values obtained in the study in chapter 4 is perhaps the bias in the shear stress data because of the exclusive study of the LAD coronary artery. Interestingly, the flow data from the studies described in chapter 5 and 6 revealed that the flows in LADs are similar to LCXs, but significantly higher than RCAs. The higher flow through LADs therefore could lead to higher shear stress for that study, which however, in part is probably counteracted by the larger size of the LADs compared to the RCAs. Additionally, in the LAD study (chapter 4), we employed different boundary conditions at the outlets, which most likely also contributed to the observed differences in TAWSS. The boundary conditions for side branches applied in the studies in chapter 5 and 6 followed a similar strategy, which resulted in comparable TAWSS (0.80 Pa (0.44 - 1.41 Pa), chapter 5 vs. 0.80 Pa (0.58 - 1.14 Pa), chapter 6). These values agree with previously reported data on TAWSS (mean 0.68 Pa, SEM, 0.027 Pa) using in vivo Doppler measurements (Doriot et al., 2000). For OSI and RRT, CFI, and transWSS, no absolute reference values for the coronary arteries were described in literature. Alternatively, the flow in the coronary arteries can be obtained using angiography. This methodology uses the visualization of flowing contrast through the artery. Using this method, Stone et al reported TAWSS values (median: (1.3 – 1.9 Pa)) which were slightly lower than those reported in the studies described in chapter 5 and 6 (Stone et al., 2003).

Table 10.2: *The shear stress distributions fort the different shear stress metrics: time-average wall shear stress (TAWSS), oscillatory shear index (OSI), relative residence time (RRT), cross-flow index (CFI) and transverse wall shear stress (transWSS) for chapters 4, 5, and 6. The values are listed as median and interquartile range.*

Chapter		Shear stress metrics				
		TAWSS [Pa]	OSI e-3 [-]	RRT [Pa^{-1}]	CFI [-]	transWSS [Pa]
4		2.59 (1.60 - 3.77)	4.21 (0.95 - 16.4)	0.65 (0.37 - 0.95)	0.08 (0.04 - 0.13)	0.11 (0.07 - 0.16)
5		0.80 (0.44 - 1.41)	0.64 (0.15 - 3.13)	1.33 (0.75 - 2.41)	0.04 (0.02 - 0.08)	0.03 (0.01 -0.07)
6	All	0.80 (0.58 - 1.14)	1.30 (3.55 - 4.36)	1.29 (0.91 - 1.79)	0.06 (0.03 - 0.11)	0.04 (0.02 - 0.07)
	SR	0.83 (0.58 - 1.22)	1.29 (3.65 – 4.26)	1.25 (0.84 - 1.78)	0.06 (0.03 - 0.11)	0.04 (0.02 - 0.07)
	FR	0.79 (0.57 - 1.07)	1.32 (3.52 – 4.43)	1.32 (0.98 - 1.80)	0.06 (0.03 - 0.11)	0.04 (0.02 - 0.06)

[*] SR=slow responders, FR=fast responders.

10.1.2 Wall stress

The solid mechanics studies' findings on wall stresses largely depended on the material properties of the components. The arterial wall consists of heterogeneous layers, which are even more complex in a diseased artery. All these components (e.g. micro calcification, fibres, thin caps) influence wall strength and thus the level of stress at which a plaque ruptures (Akyildiz et al., 2016; Hutcheson et al., 2014; Nieuwstadt et al., 2014b) . Peak stresses are especially sensitive to small errors in geometry (Speelman et al., 2008). It is difficult to accurately determine geometry and material properties in vivo, but they significantly influence the wall stresses and therefore must be accurately assessed (see chapter 7 and 8). Thus, Gijsen et al. suggested that if the resolution is not sufficient to capture the essential detailed structures, then it might be more feasible, at least for now, to detect stable plaques, that consist of thicker fibrous caps that can be assessed more accurately (Gijsen et al., 2015). Identifying stable plaques may reduce needless interventions. Furthermore, it is difficult to determine residual stresses in the arteries in an unloaded state (Fung, 1991). In this thesis, we used the backward incremental method to address this problem.

10.2 Differences between animal and human modelling

In this thesis, both animal and human data were used to study atherosclerotic plaque progression. Studies using animal models have several advantages and limitations compared to studies in human studies. A first advantage is that laboratory animals typically have a uniform genetic background with respect to important disease-related genes. Thus, variation in the investigated responses (e.g. to an atherogenic stimulus) are not related to variation in genetic expression. In contrast, patients usually do not have an uniform genetic background, which potentially hampers the interpretation of the data. Furthermore, despite strict guidelines, studies in animal models allow repeated vessel imaging at multiple time points, which is less straightforward in patients. Moreover, animals can be sacrificed in order to analyse their tissue with histology. In this way, detailed analysis of the cellular composition of an atherosclerotic plaque can be assessed, which is not generally possible using the imaging techniques available to patients.

A limitation of animal models is that plaque development in animals—specifically, final plaque size and composition—is not identical to that in patients. For example, in human data, we observed plaques with the potential to rupture; these are eccentric, heterogeneous plaques with a thin cap covering a large lipid pool. Mice and rabbits have been explored as an atherosclerotic animal model, but they do not naturally develop plaques as

a response to a high-fat diet, and plaque composition did not demonstrate important features as observed in human rupture prone plaques (van der Heiden et al., 2015). In pigs, atherosclerosis develops naturally; however, this process takes place over decades, as it does in humans, and pigs are therefore generally not feasible for research purposes. Alternative methods have been used to accelerate atherosclerotic development in pigs, such as the creation of a pro-atherogenic haemodynamic environment by ligation of arteries, cast placement, genetic modification, and inducing diabetes (Al-Mashhadi et al., 2013; Granada et al., 2009; Hamamdzic and Wilensky, 2013; Ogita et al., 2016; Shim et al., 2017; Thim et al., 2010a; van der Heiden et al., 2015). However, plaques that develop in a short time frame often do not resemble advanced human plaques in terms of location, size, and composition.

We used a relatively new porcine model in our studies on shear stress-related plaque progression (chapter 3 and 6). The animals were adult mini-pigs with familial hypercholesterolemia (LDL$^{-/-}$), and atherosclerotic plaque development was accelerated by feeding a high-fat diet. Plaque growth in our animals demonstrated a clear split in response to the high-fat diet. The slow-responding animals had a final wall thickness of 0.19 mm (0.13 – 0.26 mm), and the plaques of fast-responding animals were much larger in size (0.39 mm (0.23 – 0.67 mm)) at follow-up. The plaques observed in the fast-responding animals were comparable in size to human plaques (chapter 4 0.43 mm (IQR: 0.11 – 0.87 mm) and chapter 5: 0.48 mm (IQR: 0.30 – 0.64 mm)). Furthermore, the plaques of the fast responders had a high plaque burden (PB > 40%); plaques above this threshold become lumen-intruding and impede blood flow (Glagov et al., 1987). Furthermore, we confirmed previous findings (Thim et al., 2010a) in terms of plaque composition; the plaques of the fast responders resembled a human vulnerable plaque phenotype. The porcine plaques contained large necrotic core covered by a thin and inflamed fibrous cap, neovascularisation, intraplaque haemorrhage, and expansive remodelling.

The plaque development process that takes decades in humans is accelerated in pigs, such that similar plaques develop within a year. In chapter 6, plaque growth per year was 0.07 mm (IQR: 0.02 – 0.20 mm). The fast responders had a plaque growth per year of 0.20 mm (IQR: 0.06 – 0.44 mm) whereas the slow responders had a plaque growth per year of 0.03 mm (IQR: 0.003 – 0.07 mm). In the two patient studies described in this thesis, we found overall plaque regression: in chapter 4, plaque growth over six months was -0.019 mm2 (IQR: -0.08 – 0.02 mm2), and in chapter 5, plaque growth over a year was -0.01 mm (IQR: -0.10 – 0.08 mm). That we find plaque regression in patient studies is unsurprising given that these patients are often treated with statins that reduce or reverse plaque growth (Hartmann et al., 2011). Similar plaque regression was found by Stone et

al. (Stone et al., 2012).

Shear stresses in the pigs (chapter 6) were more associated to overall plaque progression than plaque regression, whereas the opposite was observed in patients (chapter 4 and 5). These differences are explained by the different stages of atherosclerotic disease in pigs versus humans and statin treatment of patients with atherosclerosis. Despite these obvious differences, low TAWSS and high RRT were still the most predictive for plaque growth. Furthermore, in both studies, high OSI and high CFI predicted plaque growth slightly less accurately than TAWSS and RRT. TransWSS did not exert a direct effect on plaque growth. The pig model described in this thesis exhibited plaque features and associations with haemodynamics that we also observed in the patient studies. Therefore, it is reasonable to translate the results obtained in this animal model to a clinical setting.

10.3 Clinical perspective

It is important for clinical decision-making to know which plaque is vulnerable to acute rupture, which plaque will become vulnerable in the future, and which AAA will cause a life-threatening event.

10.3.1 Shear stress

Shear stress may help identify a region at risk: plaque progression is associated with low shear stress (Bourantas et al., 2018; Samady et al., 2011; Yamamoto et al., 2017) and rapid plaque progression is observed just prior to a myocardial infarction (Ahmadi et al., 2015). Taken together, these results indicate that regions with low shear stress are at risk for future cardiovascular events. Using data from the PREDICTION study, Stone et al. investigated the predictive value of low shear stress combined with geometric parameters (i.e. small MLA and plaque burden) already proven to be predictive of plaque progression (Stone et al., 2012). Low shear stress, when, combined with these parameters had a PPV of 41% to predict the progression of a significant obstruction that needed treatment with a percutaneous coronary intervention. In this thesis, we observed that low TAWSS alone had a PPV of 43% for plaque growth, which is higher than in previous studies. At NIRS positive regions, an even higher PPV (48%) of TAWSS for plaque growth was observed. 6, describing the pig study, illustrated that TAWSS was more predictive for plaque composition (PPV = 61%) than plaque size (PPV = 50%).

In contrast, high shear stress was also proposed to predict future events because of its involvement in plaque destabilization (Eshtehardi et al., 2017). At later stages of the

disease, when plaques encroach into the lumen, high shear stress acts on the lumen-intruding plaque. In high shear stress regions, there is an increase in lipids (Samady et al., 2011; Wentzel et al., 2013). Furthermore, high shear stress regions were co-localized with plaque rupture sites (Fukumoto et al., 2008; Groen et al., 2007), and plaques with high shear stress upstream are associated with more MIs (Kumar et al., 2018). Taken together, these studies support the hypothesis that coronary segments exposed to high shear stress are more prone to evolve a high-risk plaque (Eshtehardi et al., 2017).

Although these PPVs seem high, it is clinically more relevant to investigate the proportion of high-risk plaques that result in severe adverse events or MACEs. In a recent study by Stone et al., MACEs were investigated in the PROSPECT dataset (Stone et al., 2018), and no events were reported in the presence of high SS. However, the predictive value for MACE of a high-risk plaque (with at least two high-risk features such as MLA < 4.0 mm2, PB > 70%, and TCFA morphology) colocalized with low shear stress is only 0.52%. Shear stress contributes to a better understanding in plaque growth and destabilization; however, further research is necessary to identify exactly which high-risk plaques require treatment.

Plaque development is a highly dynamic process, which may explain the low predictive value of shear stress with or without the use of geometric features. Stable plaques can become unstable, and vice versa (Koskinas et al., 2010). This dynamic process can be overlooked despite the plentiful information provided by analysis at baseline and follow-up. This thesis presents the effects of multidirectional shear stress metrics on plaque growth and changes in composition in human studies over time. Chapter 5 illustrated significant plaque progression in regions exposed to RRT and TAWSS. The fast responders described in 6 experienced significant associations between plaque progression and multidirectional shear stress, except for transWSS. By contrast, the study in LADs described in chapter 4 did not find any significant effect of low TAWSS on plaque growth. Chapter 4 used absolute thresholds for TAWSS (<1, 1–2.5 Pa, and >2.5 Pa), and in chapter 5 and 6 population-based thresholds were used for the TAWSS, which may explain this disparity. The response of plaque progression is an interplay of different factors, such as genetics factors, which also affect whether the endothelium responds to oscillatory flow (Krause et al., 2018).

Chapter 4 also presented the additive effect of multidirectional flow when combining TAWSS with another multidirectional shear stress metric. Timmins et al. investigated the influence of multidirectional WSS on plaque progression and compositional changes in human coronary arteries (Timmins et al., 2017). However, he used a different shear stress metric for oscillatory WSS: the maximum angle deviation of WSS over the cardiac cycle.

Plaques that were exposed to low TAWSS co-localized with this maximal angle deviation exhibited substantial plaque progression and transformation towards a vulnerable plaque phenotype. The observations in chapter 4 agree with the aforementioned study. Chapter 5 also investigated the synergistic effect of lipids on shear stress related-plaque growth at follow-up. Systemic LDL levels or NIRS positive regions alone were not associated with plaque growth. However, when these parameters were combined with several shear stress metrics, TAWSS, transWSS and RRT exhibited an effect on plaque growth regions. Further studies should elucidate which shear stress metric, perhaps in combination with geometric features, is the best predictor for changes in plaque composition and plaque growth.

It is currently very labour intensive to prepare a mesh suitable for the shear stress calculations on site; this process requires manual segmentation, registration, and analysis of the boundary conditions and takes multiple days. In addition, for unsteady CFD, computational times on a computer cluster will vary from 1-2 days. For shear stress to be used clinically, it should be computed on site with minimal user input required and a user-friendly software interface. Commercial software often meets these requirements; however, at this moment, no commercially available software packages achieve the same level of accuracy obtained in this thesis. If the added value of shear stress in clinical settings is fully clarified, then companies will be more inclined to invest in new technology and make shear stress computations clinically viable. In order to reduce computational times, the models could be simplified if the accuracy is preserved. For example, we could perform shear stress calculations based on angiographic input alone. Although some differences in shear stress values were found, Bourantas et al. already proved that shear stress calculation based on angiographic input alone is predictive for plaque progression (Bourantas et al., 2018; Schrauwen et al., 2015).

10.3.2 Wall stress

In this thesis, wall stress studies (chapter 7, 8, 9) have been performed in three different arteries: the carotid artery, coronary artery, and the abdominal aorta. Wall stress can be a surrogate marker for immediate rupture risk when wall stress exceeds wall strength; however, wall stress analysis is not currently used in a clinical setting. Absolute thresholds for maximum wall stress have been reported to evaluate rupture risk for both atherosclerotic plaques and aneurysms; however, the incidence of plaque rupture depends on both wall stress and an accurate definition of the wall's material properties and thus their strength.

Costopoulos et al. studied 32 ruptured atherosclerotic plaques and 32 non-ruptured

atherosclerotic plaques as determined by OCT (Costopoulos et al., 2017). The maximum principal stresses in these plaques were determined using IVUS-VH images. They found significant differences in stress between the ruptured and the non-ruptured plaques, and they proposed a rupture risk threshold of > 135 kPa. Another study performed mechanical testing on ruptured aortic plaques vs. non-ruptured aortic plaques and proposed a threshold of 300 kPa (Lendon et al., 1991). The same threshold was found in the maximum circumferential stress of coronary plaques that caused an MI compared to stable plaques (Cheng et al., 1993). For carotid plaques, ruptures were observed above Cauchy stresses of 131 kPa and 770 kPa (Lawlor et al., 2011). At this moment, these thresholds are not sufficiently accurate.

For AAAs, analysing wall stress might be instrumental for the physician's decision-making process, for example when determining whether the rupture risk is greater than the surgery risk; such analysis might replace the sometimes inadequate diameter criteria (Vande Geest et al., 2006). Nine studies have examined peak wall stress as a surrogate marker for rupture risk in AAA, of which seven were significant (Groeneveld et al., 2018). All studies indicated elevated wall stresses in ruptured (or symptomatic) compared to non-ruptured aneurysm. No clear rupture threshold can be extrapolated from these studies: they reported a wide range in values, and overlap was observed for the aneurysms with and without rupture (Fillinger et al., 2002, 2003; Gasser et al., 2014; Heng et al., 2008). These discrepancies are likely due to the differences in boundary conditions and the difficulty of determining the material properties.

10.3.3 Shear stress and wall stress

Where wall stress is a marker for immediate rupture risk, shear stress might be a marker for future rupture risk; combining these two markers could provide additional information on rupture (Balocco et al., 2012; Fan et al., 2014). Guo et al. demonstrated that fusion of OCT with IVUS combination provides a more accurate cap thickness than IVUS-VH (Guo et al., 2018). Cap thickness greatly affected wall stress; however, its effect on strain and wall shear stress was modest (Guo et al., 2018). In the studies described in chapter 5 and 6, both OCT and IVUS imaging was performed. Combining the imaging information using the methods described in chapter 7 can enable wall stress analysis or FSI. We hypothesize that combining shear stress with wall stress will increase the PPVs to detect vulnerable plaques that lead to cardiovascular events.

The potential of computational modelling has only recently been recognized. The Food and Drug Administration (FDA) recognizes modelling and simulation as a potential tool for rupture risk assessment and has launched its Modelling and Simulation Working

Group (U.S. FOOD AND DRUG ADMINISTRATION, 2011). In addition, commercial companies such as VASCOPS (Graz, Austria) have begun to offer services assessing rupture risk for AAAs. No software to determine plaque risk or vulnerability based on shear stresses is clinically available yet.

10.4 Conclusions

Computational modelling is a powerful tool to identify stresses in diseased arteries to predict which artery or plaque is at immediate or future risk of a cardiovascular event. In this thesis, new methodologies have been developed to further improve computational modelling of biomechanical stresses in diseased arteries. These new methodologies enabled wall stress analysis in AAA geometries obtained via 3D-US and in plaque geometries obtained via combined OCT and IVUS imaging. Further, multidirectional shear stress parameters proved to be importantly affecting plaque composition. Moreover, shear stress in combination with NIRS positive regions produced promising results for predicting plaque progression and composition changes. Therefore, multidirectional shear stress, perhaps in combination with NIRS, might potentially serve as a risk factor for plaque progression and changes in plaque composition in the clinic. Before these factors can be clinically employed, future research should further elucidate the clinical value of shear stress and wall stress as a predictor of changes in disease stage and cardiovascular events.

LIST OF REFERENCES

Ahmadi, A., Leipsic, J., Blankstein, R., Taylor, C., Hecht, H., Stone, G. W., and Narula, J. Do Plaques Rapidly Progress Prior to Myocardial Infarction?: The Interplay between Plaque Vulnerability and Progression. *Circulation Research*, **117**(1):99–104, 2015.

Akyildiz, A. C., Speelman, L., van Brummelen, H., Gutiérrez, M. a., Virmani, R., van der Lugt, A., van der Steen, A. F., Wentzel, J. J., and Gijsen, F. J. Effects of intima stiffness and plaque morphology on peak cap stress. *Biomedical engineering online*, **10**(1):25, jan 2011.

Akyildiz, A. C., Speelman, L., and Gijsen, F. J. H. Mechanical properties of human atherosclerotic intima tissue. *Journal of Biomechanics*, **47**(4):773–783, 2014.

Akyildiz, A. C., Speelman, L., Nieuwstadt, H. A., van Brummelen, H., Virmani, R., van der Lugt, A., van der Steen, A. F., Wentzel, J. J., and Gijsen, F. J. The effects of plaque morphology and material properties on peak cap stress in human coronary arteries. *Computer Methods in Biomechanics and Biomedical Engineering*, **19**(7):771–779, may 2016.

Al-Mashhadi, R. H., Sorensen, C. B., Kragh, P. M., Christoffersen, C., Mortensen, M. B., Tolbod, L. P., Thim, T., Du, Y., Li, J., Liu, Y., Moldt, B., Schmidt, M., Vajta, G., Larsen, T., Purup, S., Bolund, L., Nielsen, L. B., Callesen, H., Falk, E., Mikkelsen, J. G., and Bentzon, J. F. Familial Hypercholesterolemia and Atherosclerosis in Cloned Minipigs Created by DNA Transposition of a Human PCSK9 Gain-of-Function Mutant. *Science Translational Medicine*, **5**(166):166ra1–166ra1, jan 2013.

Al-saadi, A., Hassanpour, A., and Mahmud, T. Simulation of Aerodynamic Behaviour of a Super Utility Vehicle in Turbulent Flow. In *Proceedings of the 25th UKACM Conference on Computational Mechanics*, number 6, pages 6–7, 2017.

Alastruey, J., Siggers, J. H., Peiffer, V., Doorly, D. J., and Sherwin, S. J. Reducing the data: Analysis of the role of vascular geometry on blood flow patterns in curved vessels. *Physics of Fluids*, **24**(3):031902, mar 2012.

Ando, J. and Yamamoto, K. Flow detection and calcium signalling in vascular endothelial cells. *Cardiovascular Research*, **99**(2):260–268, 2013.

Aristokleous, N., Seimenis, I., Georgiou, G. C., Nicolaides, A., and Anayiotos, A. S. The effect of head rotation on the geometry and hemodynamics of healthy vertebral arteries. *Annals of biomedical engineering*, **43**(6):1287–97, jun 2015.

Arnold, R., Neu, M., Hirtler, D., Gimpel, C., Markl, M., and Geiger, J. Magnetic resonance imaging 4-D flow-based analysis of aortic hemodynamics in Turner syndrome. *Pediatric Radiology*, **47**(4):382–390, apr 2017.

Asakura, T. and Karino, T. Flow patterns and spatial distribution of atherosclerotic lesions in human coronary arteries. *Circulation research*, **66**(4):1045–1066, 1990.

Bächler, P., Pinochet, N., Sotelo, J., Crelier, G., Irarrazaval, P., Tejos, C., and Uribe, S. Assessment of normal flow patterns in the pulmonary circulation by using 4D magnetic resonance velocity mapping. *Magnetic resonance imaging*, **31**(2):178–88, feb 2013.

Badak, O., Schoenhagen, P., Tsunoda, T., Magyar, W. a., Coughlin, J., Kapadia, S., Nissen, S. E., and Tuzcu, E. M. Characteristics of atherosclerotic plaque distribution in coronary artery bifurcations: an intravascular ultrasound analysis. *Coronary artery disease*, **14**(4):309–316, 2003.

Badel, P., Avril, S., Sutton, M. a., and Lessner, S. M. Numerical simulation of arterial dissection during balloon angioplasty of atherosclerotic coronary arteries. *Journal of biomechanics*, **47**(4):878–89, mar 2014.

Baeyens, N., Mulligan-Kehoe, M. J., Corti, F., Simon, D. D., Ross, T. D., Rhodes, J. M., Wang, T. Z., Mejean, C. O., Simons, M., Humphrey, J., and Schwartz, M. a. Syndecan 4 is required for endothelial alignment in flow and atheroprotective signaling. *Proceedings of the National Academy of Sciences of the United States of America*, **111**(48):17308–13, 2014.

Bahrami, S. and Norouzi, M. A numerical study on hemodynamics in the left coronary bifurcation with normal and hypertension conditions. *Biomechanics and Modeling in Mechanobiology*, **17**(6):1785–1796, 2018.

Balocco, S., Gatta, C., Alberti, M., Carrillo, X., Rigla, J., and Radeva, P. Relation between plaque type, plaque thickness, blood shear stress, and plaque stress in coronary arteries assessed by X-ray Angiography and Intravascular Ultrasound. *Medical Physics*, **39**(12):7430–7445, 2012.

Bammer, R., Hope, T. A., Aksoy, M., and Alley, M. T. Time-resolved 3D quantitative flow MRI of the major intracranial vessels: Initial experience and comparative evaluation at 1.5T and 3.0T in combination with parallel imaging. *Magnetic Resonance in Medicine*, **57**(1):127–140, jan 2007.

Bartko, J. J. Measurement and reliability: statistical thinking considerations. *Schizophrenia bulletin*, **17**(3):483–9, jan 1991.

Baxter, B. T., Davis, V. A., Minion, D. J., Wang, Y. P., Lynch, T. G., and McManus, B. M. Abdominal aortic aneurysms are associated with altered matrix proteins of the nonaneurysmal aortic segments. *Journal of vascular surgery*, **19**(5):797–802; discussion 803, may 1994.

Belytschko, T. On computational methods for crashworthiness. *Computers and Structures*, **42**(2):271–279, 1992.

Bengtsson, H. and Bergqvist, D. Ruptured abdominal aortic aneurysm: A population-based study. *Journal of Vascular Surgery*, **18**(1):74–80, jul 1993.

LIST OF REFERENCES

Bijari, P. B., Antiga, L., Gallo, D., Wasserman, B. A., and Steinman, D. A. Improved prediction of disturbed flow via hemodynamically-inspired geometric variables. *Journal of biomechanics*, **45**(9):1632–7, jun 2012.

Bijari, P. B., Wasserman, B. A., and Steinman, D. A. Carotid bifurcation geometry is an independent predictor of early wall thickening at the carotid bulb. *Stroke; a journal of cerebral circulation*, **45**(2):473–8, feb 2014.

Bogren, H. G. and Buonocore, M. H. Blood flow measurements in the aorta and major arteries with MR velocity mapping. *Journal of magnetic resonance imaging : JMRI*, **4**(2):119–30, 1994.

Bogren, H. G., Mohiaddin, R. H., Kilner, P. J., Jimenez-Borreguero, L. J., Yang, G. Z., and Firmin, D. N. Blood flow patterns in the thoracic aorta studied with three-directional MR velocity mapping: the effects of age and coronary artery disease. *Journal of magnetic resonance imaging : JMRI*, **7**(5):784–93, 1997.

Bogren, H. G., Buonocore, M. H., and Valente, R. J. Four-dimensional magnetic resonance velocity mapping of blood flow patterns in the aorta in patients with atherosclerotic coronary artery disease compared to age-matched normal subjects. *Journal of magnetic resonance imaging : JMRI*, **19**(4):417–27, apr 2004.

Boon, R. A. and Horrevoets, A. J. G. Key transcriptional regulators of the vasoprotective effects of shear stress. *Hämostaseologie*, **29**(1):39–43, feb 2009.

Boucek, R. J., Romanelli, R., Willis, W. H., and Mitchell, W. A. Clinical and pathologic features of obstructive disease in the predominant right and left coronary circulations in man. *Circulation*, **62**(3):485–90, sep 1980.

Bourantas, C. V., Ramasamy, A., Karagiannis, A., Sakellarios, A., Zanchin, T., Yamaji, K., Ueki, Y., Shen, X., Fotiadis, D. I., Michalis, L. K., Mathur, A., Serruys, P. W., Garcia-Garcia, H. M., Koskinas, K., Torii, R., Windecker, S., and Räber, L. Angiographic derived endothelial shear stress: a new predictor of atherosclerotic disease progression. *European Heart Journal - Cardiovascular Imaging*, **44**(0):1–9, 2018.

Bressloff, N. W. Parametric geometry exploration of the human carotid artery bifurcation. *Journal of Biomechanics*, **40**(0):2483–2491, 2007.

Brewster, D. C., Cronenwett, J. L., Hallett, J. W., Johnston, K. W., Krupski, W. C., and Matsumura, J. S. Guidelines for the treatment of abdominal aortic aneurysms. Report of a subcommittee of the Joint Council of the American Association for Vascular Surgery and Society for Vascular Surgery. *Journal of vascular surgery*, **37**(5):1106–17, may 2003.

Brophy, C. M., Reilly, J. M., Smith, G. J., and Tilson, M. D. The role of inflammation in nonspecific abdominal aortic aneurysm disease. *Annals of vascular surgery*, **5**(3):229–33, may 1991.

Bulant, C. A., Blanco, P. J., Maso Talou, G. D., Bezerra, C. G., Lemos, P. A., and Feijóo, R. A. A head-to-head comparison between CT- and IVUS-derived coronary blood flow models. *Journal of biomechanics*, **51**(0):65–76, jan 2017.

Bürk, J., Blanke, P., Stankovic, Z., Barker, A., Russe, M., Geiger, J., Frydrychowicz, A., Langer, M., and Markl, M. Evaluation of 3D blood flow patterns and wall shear stress in the normal and dilated thoracic aorta using flow-sensitive 4D CMR. *Journal of cardiovascular magnetic resonance : official journal of the Society for Cardiovascular Magnetic Resonance*, **14**(1):84, dec 2012.

Burke, A. P., Kolodgie, F. D., Farb, A., Weber, D. K., Malcom, G. T., Smialek, J., and Virmani, R. Healed plaque ruptures and sudden coronary death: evidence that subclinical rupture has a role in plaque progression. *Circulation*, **103**(7):934–40, feb 2001.

Campa, J. S., Greenhalgh, R. M., and Powell, J. T. Elastin degradation in abdominal aortic aneurysms. *Atherosclerosis*, **65**(1-2):13–21, 1987.

Cannon, C. P., Braunwald, E., McCabe, C. H., Rader, D. J., Rouleau, J. L., Belder, R., Joyal, S. V., Hill, K. A., Pfeffer, M. A., Skene, A. M., and Pravastatin or Atorvastatin Evaluation and Infection Therapy-Thrombolysis in Myocardial Infarction 22 Investigators. Intensive versus Moderate Lipid Lowering with Statins after Acute Coronary Syndromes. *New England Journal of Medicine*, **350**(15):1495–1504, apr 2004.

Caro, C. G., Doorly, D. J., Tarnawski, M., Scott, K. T., Long, Q., and Dumoulin, C. L. Non-Planar Curvature and Branching of Arteries and Non-Planar-Type Flow. *Proceedings of the Royal Society A: Mathematical, Physical and Engineering Sciences*, **452**(1944):185–197, jan 1996.

Chai, C. K., Akyildiz, A. C., Speelman, L., Gijsen, F. J. H., Oomens, C. W. J., van Sambeek, M. R. H. M., van der Lugt, A., and Baaijens, F. P. T. Local axial compressive mechanical properties of human carotid atherosclerotic plaques-characterisation by indentation test and inverse finite element analysis. *Journal of Biomechanics*, **46**(10):1759–1766, 2013.

Chai, C.-K., Speelman, L., Oomens, C. W. J., and Baaijens, F. P. T. Compressive mechanical properties of atherosclerotic plaques–indentation test to characterise the local anisotropic behaviour. *Journal of biomechanics*, **47**(4):784–92, 2014.

Chaichana, T., Sun, Z., and Jewkes, J. Computation of hemodynamics in the left coronary artery with variable angulations. *Journal of Biomechanics*, **44**(10):1869–1878, 2011.

Chatzizisis, Y. S., Jonas, M., Coskun, A. U., Beigel, R., Stone, B. V., Maynard, C., Gerrity, R. G., Daley, W., Rogers, C., Edelman, E. R., Feldman, C. L., and Stone, P. H. Prediction of the Localization of High-Risk Coronary Atherosclerotic Plaques on the Basis of Low Endothelial Shear Stress: An Intravascular Ultrasound and Histopathology Natural History Study. *Circulation*, **117**(8):993–1002, feb 2008.

LIST OF REFERENCES

Chatzizisis, Y. S., Baker, A. B., Sukhova, G. K., Koskinas, K. C., Papafaklis, M. I., Beigel, R., Jonas, M., Coskun, A. U., Stone, B. V., Maynard, C., Shi, G. P., Libby, P., Feldman, C. L., Edelman, E. R., and Stone, P. H. Augmented expression and activity of extracellular matrix-degrading enzymes in regions of low endothelial shear stress colocalize with coronary athero-mata with thin fibrous caps in pigs. *Circulation*, **123**(6):621–630, 2011.

Cheng, C., Tempel, D., Van Haperen, R., Van Der Baan, A., Grosveld, F., Daemen, M. J. a. P., Krams, R., and De Crom, R. Atherosclerotic lesion size and vulnerability are determined by patterns of fluid shear stress. *Circulation*, **113**(23):2744–2753, 2006.

Cheng, G. C., Loree, H. M., Kamm, R. D., Fishbein, M. C., and Lee, R. T. Distribution of circumferential stress in ruptured and stable atherosclerotic lesions. A structural analysis with histopathological correlation. *Circulation*, **87**(4):1179–1187, apr 1993.

Chiastra, C., Iannaccone, F., Grundeken, M. J., Gijsen, F. J. H., Segers, P., De Beule, M., Serruys, P. W., Wykrzykowska, J. J., van der Steen, A. F. W., and Wentzel, J. J. Coronary fractional flow reserve measurements of a stenosed side branch: a computational study investigating the influence of the bifurcation angle. *Biomedical engineering online*, **15**(1):91, aug 2016.

Chiastra, C., Gallo, D., Tasso, P., Iannaccone, F., Migliavacca, F., Wentzel, J. J., and Morbiducci, U. Healthy and diseased coronary bifurcation geometries influence near-wall and intravascular flow: A computational exploration of the hemodynamic risk. *Journal of biomechanics*, **58**(0):79–88, jun 2017.

Choi, A. and Zheng, Y. Estimation of Young' s modulus and Poisson' s ratio of soft tissue from indentation using two different-sized indentors: finite element analysis of the finite deformation effect. *Medical & Biological Engineering*, **43**(0):258–264, 2005.

Choksy, S. a., Wilmink, a. B., and Quick, C. R. Ruptured abdominal aortic aneurysm in the Huntingdon district: a 10-year experience. *Annals of the Royal College of Surgeons of England*, **81**(1):27–31, jan 1999.

Cibis, M., Potters, W. V., Gijsen, F. J. H., Marquering, H., VanBavel, E., van der Steen, A. F. W., Nederveen, A. J., and Wentzel, J. J. Wall shear stress calculations based on 3D cine phase contrast MRI and computational fluid dynamics: a comparison study in healthy carotid arteries. *NMR in biomedicine*, **27**(7):826–34, jul 2014.

Cibis, M., Bustamante, M., Eriksson, J., Carlhäll, C. J., and Ebbers, T. Creating hemodynamic atlases of cardiac 4D flow MRI. *Journal of Magnetic Resonance Imaging*, **46**(5):1389–1399, 2017.

Cicha, I., Wörner, A., Urschel, K., Beronov, K., Goppelt-Struebe, M., Verhoeven, E., Daniel, W. G., and Garlichs, C. D. Carotid plaque vulnerability: A positive feedback between hemodynamic and biochemical mechanisms. *Stroke*, **42**(12):3502–3510, dec 2011.

Condemi, F., Campisi, S., Viallon, M., Troalen, T., Xuexin, G., Barker, A. J., Markl, M., Croisille, P., Trabelsi, O., Cavinato, C., Duprey, A., and Avril, S. Fluid- and Biomechanical Analysis of Ascending Thoracic Aorta Aneurysm with Concomitant Aortic Insufficiency. *Annals of Biomedical Engineering*, **45**(12):2921–2932, dec 2017.

Conway, K. P., Byrne, J., Townsend, M., and Lane, I. F. Prognosis of patients turned down for conventional abdominal aortic aneurysm repair in the endovascular and sonographic era: Szilagyi revisited? *Journal of vascular surgery*, **33**(4):752–7, apr 2001.

Coppola, G. and Caro, C. Oxygen mass transfer in a model three-dimensional artery. *Journal of the Royal Society Interface*, **5**(26):1067–1075, 2008.

Corban, M. T. T., Eshtehardi, P., Suo, J., McDaniel, M. C. C., Timmins, L. H. H., Rassoul-Arzrumly, E., Maynard, C., Mekonnen, G., King, S., Quyyumi, A. A. a., Giddens, D. P. P., and Samady, H. Combination of plaque burden, wall shear stress, and plaque phenotype has incremental value for prediction of coronary atherosclerotic plaque progression and vulnerability. *Atherosclerosis*, **232**(2):271–276, feb 2014.

Costopoulos, C., Huang, Y., Brown, A. J., Calvert, P. A., Hoole, S. P., West, N. E., Gillard, J. H., Teng, Z., and Bennett, M. R. Plaque Rupture in Coronary Atherosclerosis Is Associated With Increased Plaque Structural Stress. *JACC: Cardiovascular Imaging*, **10**(12):1472–1483, 2017.

Craig Kent, K. Abdominal Aortic Aneurysms. *New England Journal of Medicine*, **371**(22): 2101–2108, 2014.

Cutnell, J. D. and Johnson, K. W. *Physics*. John Wiley & Sons Inc, 4th edition, 2007.

Danek, B. A., Karatasakis, A., Karacsonyi, J., Alame, A., Resendes, E., Kalsaria, P., Nguyen-Trong, P.-K. J., Rangan, B. V., Roesle, M., Abdullah, S., Banerjee, S., and Brilakis, E. S. Long-term follow-up after near-infrared spectroscopy coronary imaging: Insights from the lipid cORe plaque association with CLinical events (ORACLE-NIRS) registry. *Cardiovascular revascularization medicine : including molecular interventions*, **18**(3):177–181, apr 2017.

Darling, R. C., Messina, C. R., Brewster, D. C., and Ottinger, L. W. Autopsy study of unoperated abdominal aortic aneurysms. The case for early resection. *Circulation*, **56**(3 Suppl):II161–4, sep 1977.

Davies, J. E., Whinnett, Z. I., Francis, D. P., Manisty, C. H., Aguado-Sierra, J., Willson, K., Foale, R. a., Malik, I. S., Hughes, A. D., Parker, K. H., and Mayet, J. Evidence of a dominant backward-propagating "suction" wave responsible for diastolic coronary filling in humans, attenuated in left ventricular hypertrophy. *Circulation*, **113**(14):1768–1778, 2006.

Davies, M. J. and Thomas, A. Thrombosis and Acute Coronary-Artery Lesions in Sudden Cardiac Ischemic Death. *New England Journal of Medicine*, **310**(18):1137–1140, may 1984.

LIST OF REFERENCES

Davies, P. F., Dewey, C. F., Bussolari, S. R., Gordon, E. J., and Gimbrone, M. a. Influence of Hemodynamic Forces Vascular Endothelial Function Pinocytosis. *J. Clin. Invest*, **73**(0):1121–1129, 1984.

Davies, P. F., Remuzzi, A., Gordon, E. J., Dewey, C. F., and Gimbrone, M. A. Turbulent fluid shear stress induces vascular endothelial cell turnover in vitro. *Proceedings of the National Academy of Sciences of the United States of America*, **83**(7):2114–7, 1986.

Davies, P. F., Civelek, M., Fang, Y., and Fleming, I. The atherosusceptible endothelium: Endothelial phenotypes in complex haemodynamic shear stress regions in vivo. *Cardiovascular Research*, **99**(2):315–327, 2013.

de Putter, S., Wolters, B. J. B. M., Rutten, M. C. M., Breeuwer, M., Gerritsen, F. a., and van de Vosse, F. N. Patient-specific initial wall stress in abdominal aortic aneurysms with a backward incremental method. *Journal of biomechanics*, **40**(5):1081–90, jan 2007.

de Weert, T. T., Cretier, S., Groen, H. C., Homburg, P., Cakir, H., Wentzel, J. J., Dippel, D. W. J., and van der Lugt, A. Atherosclerotic plaque surface morphology in the carotid bifurcation assessed with multidetector computed tomography angiography. *Stroke; a journal of cerebral circulation*, **40**(4):1334–40, apr 2009.

Death, A. K., Nakhla, S., McGrath, K. C., Martell, S., Yue, D. K., Jessup, W., and Celermajer, D. S. Nitroglycerin upregulates matrix metalloproteinase expression by human macrophages. *Journal of the American College of Cardiology*, **39**(12):1943–1950, 2002.

Demirbag, R. and Yilmaz, R. Effects of the shape of coronary arteries on the presence, extent, and severity of their disease. *Heart and Vessels*, **20**(5):224–229, sep 2005.

Di Martino, E., Mantero, S., Inzoli, F., Melissano, G., Astore, D., Chiesa, R., and Fumero, R. Biomechanics of abdominal aortic aneurysm in the! presence of endoluminal thrombus: Experimental characterisation and structural static computational analysis. *European Journal of Vascular and Endovascular Surgery*, **15**(4):290–299, 1998.

Diletti, R., Garcia-Garcia, H. M., Gomez-Lara, J., Brugaletta, S., Wykrzykowska, J. J., Van Ditzhuijzen, N., Van Geuns, R. J., Regar, E., Ambrosio, G., and Serruys, P. W. Assessment of coronary atherosclerosis progression and regression at bifurcations using combined IVUS and OCT. *JACC: Cardiovascular Imaging*, **4**(7):774–780, 2011.

Ding, Z., Biggs, T., Seed, W. A., and Friedman, M. H. Influence of the geometry of the left main coronary artery bifurcation on the distribution of sudanophilia in the daughter vessels. *Arteriosclerosis, thrombosis, and vascular biology*, **17**(7):1356–60, jul 1997.

Dirksen, M. T., van der Wal, a. C., van den Berg, F. M., van der Loos, C. M., and Becker, a. E. Distribution of inflammatory cells in atherosclerotic plaques relates to the direction of flow. *Circulation*, **98**(19):2000–2003, nov 1998.

Dobrin, P. B., Baker, W. H., and Gley, W. C. Elastolytic and Collagenolytic Studies of Arteries: Implications for the Mechanical Properties of Aneurysms. *Archives of Surgery*, **119**(4):405–409, 1984.

Dong, J., Sun, Z., Inthavong, K., and Tu, J. Fluid-structure interaction analysis of the left coronary artery with variable angulation. *Computer methods in biomechanics and biomedical engineering*, **18**(14):1500–1508, 2015.

Doriot, P., Dorsaz, P., Dorsaz, L., De Benedetti, E., Chatelain, P., and Delafontaine, P. In-vivo measurements of wall shear stress in human coronary arteries. *Coronary artery disease*, **11**(6): 495–502, 2000.

Doucette, J. W., Corl, P. D., Payne, H. M., Flynn, A. E., Goto, M., Nassi, M., and Segal, J. Validation of a Doppler guide wire for intravascular measurement of coronary artery flow velocity. *Circulation*, **85**(5):1899–911, may 1992.

Du, R., Zhao, X.-Q., Cai, J., Cui, B., Wu, H.-M., and Ye, P. Changes in carotid plaque tissue composition in subjects who continued and discontinued statin therapy. *Journal of Clinical Lipidology*, **10**(3):587–593, 2016.

Duanmu, Z., Yin, M., Fan, X., Yang, X., and Luo, X. A patient-specific lumped-parameter model of coronary circulation. *Scientific Reports*, **8**(1):1–10, 2018.

Dull, R. O. and Davies, P. F. Flow modulation of agonist (ATP)-response (Ca2+) coupling in vascular endothelial cells. *The American journal of physiology*, **261**(1 Pt 2):H149–54, jul 1991.

Dvir, D., Kornowski, R., Gurevich, J., Orlov, B., and Aravot, D. Degrees of severe stenoses in sigma-shaped versus C-shaped right coronary arteries. *The American Journal of Cardiology*, **92**(3):294–298, aug 2003.

Eshtehardi, P., McDaniel, M. C., Suo, J., Dhawan, S. S., Timmins, L. H., Binongo, J. N. G., Golub, L. J., Corban, M. T., Finn, A. V., Oshinski, J. N., Quyyumi, A. a., Giddens, D. P., and Samady, H. Association of coronary wall shear stress with atherosclerotic plaque burden, composition, and distribution in patients with coronary artery disease. *Journal of the American Heart Association*, **1**(4):e002543, 2012.

Eshtehardi, P., Brown, A. J., Bhargava, A., Costopoulos, C., Hung, O. Y., Corban, M. T., Hosseini, H., Gogas, B. D., Giddens, D. P., and Samady, H. High wall shear stress and high-risk plaque: an emerging concept. *The International Journal of Cardiovascular Imaging*, **33**(7): 1089–1099, 2017.

Falk, E. Pathogenesis of Atherosclerosis. *Journal of the American College of Cardiology*, **47**(8 SUPPL.):0–5, 2006.

LIST OF REFERENCES

Fan, R., Tang, D., Yang, C., Zheng, J., Bach, R., Wang, L., Muccigrosso, D., Billiar, K., Zhu, J., Ma, G., Maehara, A., and Mintz, G. S. Human coronary plaque wall thickness correlated positively with flow shear stress and negatively with plaque wall stress: an IVUS-based fluid-structure interaction multi-patient study. *Biomedical engineering online*, **13**(1):32, jan 2014.

Félétou, M., Köhler, R., and Vanhoutte, P. M. Nitric oxide: Orchestrator of endothelium-dependent responses. *Annals of Medicine*, **44**(7):694–716, 2012.

Fillinger, M. F., Raghavan, M., Marra, S. P., Cronenwett, J. L., and Kennedy, F. E. In vivo analysis of mechanical wall stress and abdominal aortic aneurysm rupture risk. *Journal of Vascular Surgery*, **36**(3):589–597, sep 2002.

Fillinger, M. F., Marra, S. P., Raghavan, M. L., and Kennedy, F. E. Prediction of rupture risk in abdominal aortic aneurysm during observation: wall stress versus diameter. *Journal of vascular surgery*, **37**(4):724–32, apr 2003.

Finet, G., Ohayon, J., and Rioufol, G. Biomechanical interaction between cap thickness, lipid core composition and blood pressure in vulnerable coronary plaque: impact on stability or instability. *Coronary artery disease*, **15**(1):13–20, feb 2004.

Fisher, M. and Fieman, S. Geometric factors of the bifurcation in carotid atherogenesis. *Stroke; a journal of cerebral circulation*, **21**(2):267–71, feb 1990.

Fox, B. and Seed, W. A. Location of early atheroma in the human coronary arteries. *Journal of biomechanical engineering*, **103**(3):208–12, aug 1981.

Fox, B., James, K., Morgan, B., and Seed, a. Distribution of fatty and fibrous plaques in young human coronary arteries. *Atherosclerosis*, **41**(2-3):337–347, 1982.

François, C. J., Srinivasan, S., Schiebler, M. L., Reeder, S. B., Niespodzany, E., Landgraf, B. R., Wieben, O., and Frydrychowicz, A. 4D cardiovascular magnetic resonance velocity mapping of alterations of right heart flow patterns and main pulmonary artery hemodynamics in tetralogy of Fallot. *Journal of cardiovascular magnetic resonance : official journal of the Society for Cardiovascular Magnetic Resonance*, **14**(1):16, feb 2012.

Frattolin, J., Zarandi, M. M., Pagiatakis, C., Bertrand, O. F., and Mongrain, R. Numerical study of stenotic side branch hemodynamics in true bifurcation lesions. *Computers in Biology and Medicine*, **57**(0):130–138, 2015.

Frazin, L. J., Lanza, G., Vonesh, M., Khasho, F., Spitzzeri, C., McGee, S., Mehlman, D., Chandran, K. B., Talano, J., and McPherson, D. Functional chiral asymmetry in descending thoracic aorta. *Circulation*, **82**(6):1985–1994, 1990.

Friedman, M. H., Deters, O. J., Mark, F. F., Bargeron, C. B., and Hutchins, G. M. Arterial geometry affects hemodynamics. A potential risk factor for athersoclerosis. *Atherosclerosis*, **46**(2):225–31, feb 1983.

Frydrychowicz, A., Winterer, J. T., Zaitsev, M., Jung, B., Hennig, J., Langer, M., and Markl, M. Visualization of iliac and proximal femoral artery hemodynamics using time-resolved 3D phase contrast MRI at 3T. *Journal of magnetic resonance imaging : JMRI*, **25**(5):1085–92, may 2007.

Frydrychowicz, A., Berger, A., Munoz del Rio, A., Russe, M. F., Bock, J., Harloff, A., and Markl, M. Interdependencies of aortic arch secondary flow patterns, geometry, and age analysed by 4-dimensional phase contrast magnetic resonance imaging at 3 Tesla. *European radiology*, **22**(5):1122–30, may 2012.

Fukumoto, Y., Hiro, T., Fujii, T., Hashimoto, G., Fujimura, T., Yamada, J., Okamura, T., and Matsuzaki, M. Localized elevation of shear stress is related to coronary plaque rupture: a 3-dimensional intravascular ultrasound study with in-vivo color mapping of shear stress distribution. *Journal of the American College of Cardiology*, **51**(6):645–50, feb 2008.

Fung, Y. C. What Are the Residual-Stresses Doing in Our Blood-Vessels. *Annals of Biomedical Engineering*, **19**(3):237–249, 1991.

Gallo, D., Steinman, D. A., Bijari, P. B., and Morbiducci, U. Helical flow in carotid bifurcation as surrogate marker of exposure to disturbed shear. *Journal of biomechanics*, **45**(14):2398–404, sep 2012.

Gallo, D., Steinman, D. A., and Morbiducci, U. An insight into the mechanistic role of the common carotid artery on the hemodynamics at the carotid bifurcation. *Annals of biomedical engineering*, **43**(1):68–81, jan 2015.

Gallo, D., Steinman, D. A., and Morbiducci, U. Insights into the co-localization of magnitude-based versus direction-based indicators of disturbed shear at the carotid bifurcation. *Journal of biomechanics*, **49**(12):2413–9, aug 2016.

Gao, H. and Long, Q. Effects of varied lipid core volume and fibrous cap thickness on stress distribution in carotid arterial plaques. *Journal of biomechanics*, **41**(14):3053–9, oct 2008.

Garcia, J., Barker, A. J., Collins, J. D., Carr, J. C., and Markl, M. Volumetric quantification of absolute local normalized helicity in patients with bicuspid aortic valve and aortic dilatation. *Magnetic resonance in medicine*, **78**(2):689–701, aug 2017.

García-García, H. M., Gomez-Lara, J., Gonzalo, N., Garg, S., Shin, E. S., Goedhart, D., and Serruys, P. W. A comparison of the distribution of necrotic core in bifurcation and non-bifurcation coronary lesions: An in vivo assessment using intravascular ultrasound radiofrequency data analysis. *EuroIntervention*, **6**(3):321–327, 2010.

Garcia-Garcia, H. M., Jang, I.-K., Serruys, P. W., Kovacic, J. C., Narula, J., and Fayad, Z. A. Imaging plaques to predict and better manage patients with acute coronary events. *Circulation research*, **114**(12):1904–17, jun 2014.

LIST OF REFERENCES

Gardner, C. M., Tan, H., Hull, E. L., Lisauskas, J. B., Sum, S. T., Meese, T. M., Jiang, C., Madden, S. P., Caplan, J. D., Burke, A. P., Virmani, R., Goldstein, J., and Muller, J. E. Detection of Lipid Core Coronary Plaques in Autopsy Specimens With a Novel Catheter-Based Near-Infrared Spectroscopy System. *JACC: Cardiovascular Imaging*, **1**(5):638–648, sep 2008.

Garg, S., Serruys, P. W., van der Ent, M., Schultz, C., Mastik, F., van Soest, G., van der Steen, A. F. W., Wilder, M. A., Muller, J. E., and Regar, E. First use in patients of a combined near infra-red spectroscopy and intra-vascular ultrasound catheter to identify composition and structure of coronary plaque. *EuroIntervention : journal of EuroPCR in collaboration with the Working Group on Interventional Cardiology of the European Society of Cardiology*, **5**(6):755–6, jan 2010.

Gasser, T., Nchimi, A., Swedenborg, J., Roy, J., Sakalihasan, N., Böckler, D., and Hyhlik-Dürr, A. A Novel Strategy to Translate the Biomechanical Rupture Risk of Abdominal Aortic Aneurysms to their Equivalent Diameter Risk: Method and Retrospective Validation. *European Journal of Vascular and Endovascular Surgery*, **47**(3):288–295, mar 2014.

Gasser, T. C., Ogden, R. W., and Holzapfel, G. a. Hyperelastic modelling of arterial layers with distributed collagen fibre orientations. *Journal of The Royal Society Interface*, **3**(6):15–35, feb 2006.

Geiger, J., Markl, M., Herzer, L., Hirtler, D., Loeffelbein, F., Stiller, B., Langer, M., and Arnold, R. Aortic flow patterns in patients with Marfan syndrome assessed by flow-sensitive four-dimensional MRI. *Journal of magnetic resonance imaging : JMRI*, **35**(3):594–600, mar 2012.

Gijsen, F., van der Giessen, A., van der Steen, A., and Wentzel, J. Shear stress and advanced atherosclerosis in human coronary arteries. *Journal of Biomechanics*, **46**(2):240–247, 2013.

Gijsen, F. J. H. and Migliavacca, F. Plaque mechanics. *Journal of Biomechanics*, **47**(4):763–764, 2014.

Gijsen, F. J. H., Wentzel, J. J., Thury, A., Mastik, F., Schaar, J. a., Schuurbiers, J. C. H., Slager, C. J., van der Giessen, W. J., de Feyter, P. J., van der Steen, A. F. W., and Serruys, P. W. Strain distribution over plaques in human coronary arteries relates to shear stress. *American journal of physiology. Heart and circulatory physiology*, **295**(4):H1608–14, oct 2008.

Gijsen, F. J. H., Schuurbiers, J. C. H., van de Giessen, A. G., Schaap, M., van der Steen, A. F. W., and Wentzel, J. J. 3D reconstruction techniques of human coronary bifurcations for shear stress computations. *Journal of biomechanics*, **47**(1):39–43, jan 2014.

Gijsen, F. J. H., Nieuwstadt, H. a., Wentzel, J. J., Verhagen, H. J. M., van der Lugt, A., and van der Steen, A. F. W. Carotid Plaque Morphological Classification Compared With Biomechanical Cap Stress: Implications for a Magnetic Resonance Imaging-Based Assessment. *Stroke; a journal of cerebral circulation*, **46**(8):2124–2128, 2015.

Glagov, S., Weisenberg, E., Zarins, C. K., Stankunavicius, R., and Kolettis, G. J. Compensatory enlargement of human atherosclerotic coronary arteries. *The New England journal of medicine*, **316**(22):1371–5, may 1987.

Glagov, S., Zarins, C., Giddens, D. P., and Ku, D. N. Hemodynamics and atherosclerosis. Insights and perspectives gained from studies of human arteries. *Archives of pathology & laboratory medicine*, **112**(10):1018–31, oct 1988.

Gokaldas, R., Singh, M., Lal, S., Benenstein, R. J., and Sahni, R. Carotid Stenosis: From Diagnosis to Management, Where Do We Stand? *Current Atherosclerosis Reports*, **17**(2):3–10, 2015.

Goldstein, J. and Brown, M. A Century of Cholesterol and Coronaries: From Plaques to Genes to Statins. *Cell*, **161**(1):161–172, mar 2015.

Gonzalo, N., Garcia-Garcia, H. M., Regar, E., Barlis, P., Wentzel, J., Onuma, Y., Ligthart, J., and Serruys, P. W. In Vivo Assessment of High-Risk Coronary Plaques at Bifurcations With Combined Intravascular Ultrasound and Optical Coherence Tomography. *JACC: Cardiovascular Imaging*, **2**(4):473–482, 2009.

Goubergrits, L., Affeld, K., Fernandez-Britto, J., and Falcon, L. Atherosclerosis and flow in carotid arteries with authentic geometries. *Biorheology*, **39**(3-4):519–24, jan 2002.

Granada, J. F., Wallace-Bradley, D., Win, H. K., Alviar, C. L., Builes, A., Lev, E. I., Barrios, R., Schulz, D. G., Raizner, A. E., and Kaluza, G. L. In vivo plaque characterization using intravascular ultrasound-virtual histology in a porcine model of complex coronary lesions. *Arteriosclerosis, Thrombosis, and Vascular Biology*, **27**(2):387–393, 2007.

Granada, J. F., Kaluza, G. L., Wilensky, R. L., Biedermann, B. C., Schwartz, R. S., and Falk, E. Porcine models of coronary atherosclerosis and vulnerable plaque for imaging and interventional research. *EuroIntervention : journal of EuroPCR in collaboration with the Working Group on Interventional Cardiology of the European Society of Cardiology*, **5**(1):140–8, may 2009.

Greenhalgh, R. M., Forbes, J. F., Fowkes, F. G., Powel, J. T., Ruckley, C. V., Brady, a. R., Brown, L. C., and Thompson, S. G. Early elective open surgical repair of small abdominal aortic aneurysms is not recommended: results of the UK Small Aneurysm Trial. Steering Committee. *European journal of vascular and endovascular surgery : the official journal of the European Society for Vascular Surgery*, **16**(6):462–4, dec 1998.

Groen, H. C., Gijsen, F. J. H., van der Lugt, A., Ferguson, M. S., Hatsukami, T. S., van der Steen, A. F. W., Yuan, C., and Wentzel, J. J. Plaque rupture in the carotid artery is localized at the high shear stress region: a case report. *Stroke; a journal of cerebral circulation*, **38**(8): 2379–81, aug 2007.

LIST OF REFERENCES

Groen, H. C., van Walsum, T., Rozie, S., Klein, S., van Gaalen, K., Gijsen, F. J. H., Wielopolski, P. A., van Beusekom, H. M. M., de Crom, R., Verhagen, H. J. M., van der Steen, A. F. W., van der Lugt, A., Wentzel, J. J., and Niessen, W. J. Three-dimensional registration of histology of human atherosclerotic carotid plaques to in-vivo imaging. *Journal of biomechanics*, **43**(11): 2087–92, aug 2010.

Groeneveld, M. E., Meekel, J. P., Rubinstein, S. M., Merkestein, L. R., Tangelder, G. J., Wisselink, W., Truijers, M., and Yeung, K. K. Systematic review of circulating, biomechanical, and genetic markers for the prediction of abdominal aortic aneurysm growth and rupture. *Journal of the American Heart Association*, **7**(13):1–16, 2018.

Gullu, A. U., Kizilay, M., Ates, M., and Akcar, M. The comparison of angiographic lesions and clinical outcomes in identical twins. *Interactive cardiovascular and thoracic surgery*, **6**(4): 575–6, aug 2007.

Guo, X., Giddens, D. P., Molony, D., Yang, C., Samady, H., Zheng, J., Mintz, G. S., Maehara, A., Wang, L., Pei, X., Li, Z.-Y., and Tang, D. Combining IVUS and Optical Coherence Tomography for More Accurate Coronary Cap Thickness Quantification and Stress/Strain Calculations: A Patient-Specific Three-Dimensional Fluid-Structure Interaction Modeling Approach. *Journal of Biomechanical Engineering*, **140**(4):041005, jan 2018.

Hadjiloizou, N., Davies, J. E., Malik, I. S., Aguado-Sierra, J., Willson, K., Foale, R. a., Parker, K. H., Hughes, a. D., Francis, D. P., and Mayet, J. Differences in cardiac microcirculatory wave patterns between the proximal left mainstem and proximal right coronary artery. *AJP: Heart and Circulatory Physiology*, **295**(3):H1198–H1205, 2008.

Hamamdzic, D. and Wilensky, R. L. Porcine models of accelerated coronary atherosclerosis: role of diabetes mellitus and hypercholesterolemia. *Journal of diabetes research*, **2013**(761415): 1–7, jun 2013.

Hamilton, W. J. *Textbook of human anatomy*. Macmillan, 1976.

Hansen, K. L., Møller-Sørensen, H., Kjaergaard, J., Jensen, M. B., Lund, J. T., Pedersen, M. M., Lange, T., Jensen, J. A., and Nielsen, M. B. Analysis of Systolic Backflow and Secondary Helical Blood Flow in the Ascending Aorta Using Vector Flow Imaging. *Ultrasound in medicine & biology*, **42**(4):899–908, apr 2016.

Harrison, M. and Marshall, J. Does the geometry of the carotid bifurcation affect its predisposition to atheroma? *Stroke; a journal of cerebral circulation*, **14**(1):117–8, jan 1983.

Hartmann, M., Huisman, J., Bse, D., Jensen, L. O., Schoenhagen, P., Mintz, G. S., Erbel, R., and Von Birgelen, C. Serial intravascular ultrasound assessment of changes in coronary atherosclerotic plaque dimensions and composition: An update. *European Journal of Echocardiography*, **12**(0):313–321, 2011.

Heng, M. S., Fagan, M. J., Collier, J. W., Desai, G., McCollum, P. T., and Chetter, I. C. Peak wall stress measurement in elective and acute abdominal aortic aneurysms. *Journal of vascular surgery*, **47**(1):17–22; discussion 22, jan 2008.

Himburg, H. a., Grzybowski, D. M., Hazel, A. L., Lamack, J. A., Li, X.-m., Friedman, M. H., Heather, A., Grzybowski, D. M., Andrew, L., Lamack, J. A., Li, X.-m., and Friedman, M. H. Spatial comparison between wall shear stress measures and porcine arterial endothelial permeability. *American journal of physiology. Heart and circulatory physiology*, **286**(5):H1916–H1922, 2004.

Hirsch, A. T., Haskal, Z. J., Hertzer, N. R., Bakal, C. W., Creager, M. a., Halperin, J. L., Hiratzka, L. F., Murphy, W. R. C., Olin, J. W., Puschett, J. B., Rosenfield, K. a., Sacks, D., Stanley, J. C., Taylor, L. M., White, C. J., White, J., White, R. a., Antman, E. M., Smith, S. C., Adams, C. D., Anderson, J. L., Faxon, D. P., Fuster, V., Gibbons, R. J., Hunt, S. a., Jacobs, A. K., Nishimura, R., Ornato, J. P., Page, R. L., and Riegel, B. ACC/AHA 2005 Practice Guidelines for the management of patients with peripheral arterial disease (lower extremity, renal, mesenteric, and abdominal aortic): a collaborative report from the American Association for Vascular Surgery/Society for Vascular Sur. *Journal of the American College of Cardiology*, **47**(6):1239–312, mar 2006.

Hoi, Y., Zhou, Y.-Q., Zhang, X., Henkelman, R. M., and Steinman, D. A. Correlation between local hemodynamics and lesion distribution in a novel aortic regurgitation murine model of atherosclerosis. *Annals of biomedical engineering*, **39**(5):1414–22, may 2011.

Holzapfel, G. A., Gasser, T. C., and Ogden, R. A. Y. W. A New Constitutive Framework for Arterial Wall Mechanics and a Comparative Study of Material Models. *Journal of elasticity and the physical science of solids*, **61**(1-3):1–48, 2000.

Holzapfel, G. a., Sommer, G., Gasser, C. T., and Regitnig, P. Determination of layer-specific mechanical properties of human coronary arteries with nonatherosclerotic intimal thickening and related constitutive modeling. *American journal of physiology. Heart and circulatory physiology*, **289**(5):H2048–58, nov 2005.

Hope, M. D., Hope, T. A., Crook, S. E. S., Ordovas, K. G., Urbania, T. H., Alley, M. T., and Higgins, C. B. 4D flow CMR in assessment of valve-related ascending aortic disease. *JACC. Cardiovascular imaging*, **4**(7):781–7, jul 2011.

Hope, T. A. and Herfkens, R. J. Imaging of the Thoracic Aorta with Time-Resolved Three-Dimensional Phase-Contrast MRI: A Review. *Seminars in Thoracic and Cardiovascular Surgery*, **20**(4):358–364, dec 2008.

Houston, J. G., Gandy, S. J., Sheppard, D. G., Dick, J. B., Belch, J. J. F., and Stonebridge, P. A. Two-dimensional flow quantitative MRI of aortic arch blood flow patterns: Effect of age, sex, and presence of carotid atheromatous disease on prevalence of spiral blood flow. *Journal of magnetic resonance imaging : JMRI*, **18**(2):169–74, aug 2003.

216

LIST OF REFERENCES

Houston, J. G., Gandy, S. J., Milne, W., Dick, J. B. C., Belch, J. J. F., and Stonebridge, P. A. Spiral laminar flow in the abdominal aorta: a predictor of renal impairment deterioration in patients with renal artery stenosis? *Nephrology, dialysis, transplantation : official publication of the European Dialysis and Transplant Association - European Renal Association*, **19**(7):1786–91, jul 2004.

Huang, X., Teng, Z., Canton, G., Ferguson, M., Yuan, C., and Tang, D. Intraplaque hemorrhage is associated with higher structural stresses in human atherosclerotic plaques: An in vivo MRI-based 3d fluid-structure interaction study. *BioMedical Engineering Online*, **9**(1):86, 2010.

Huberts, W., Bode, A. S., Kroon, W., Planken, R. N., Tordoir, J. H., van de Vosse, F. N., and Bosboom, E. M. A pulse wave propagation model to support decision-making in vascular access planning in the clinic. *Medical Engineering and Physics*, **34**(2):233–248, 2012.

Huo, Y. and Kassab, G. S. Intraspecific scaling laws of vascular trees. *Journal of the Royal Society, Interface*, **9**(66):190–200, 2012.

Hutcheson, J. D., Maldonado, N., and Aikawa, E. Small entities with large impact: Microcalcifications and atherosclerotic plaque vulnerability. *Current Opinion in Lipidology*, **25**(5): 327–332, 2014.

Huttenlocher, D. P., Klanderman, G. A., and Rucklidge, W. J. Comparing Images Using the Hausdorff Distance. *IEEE transactions on pattern analysis and machine intelligence*, **15**(9): 850–863, 1993.

Ihara, M., Urata, H., Kinoshita, A., Suzumiya, J., Sasaguri, M., Kikuchi, M., Ideishi, M., and Arakawa, K. Human Atherosclerotic Aorta. *Hypertension*, **33**(0):1399–1405, 1999.

Jia, H., Hu, S., Uemura, S., Park, S.-J., Jang, Y., Prasad, A., Lee, S., Soeda, T., Abtahian, F., Vergallo, R., Tian, J., Lee, H., Stone, P. H., Yu, B., and Jang, I.-K. Insights into the spatial distribution of lipid-rich plaques in relation to coronary artery bifurcations. *Coronary Artery Disease*, **26**(2):133–141, 2015.

Johnson, W., Onuma, O., Owolabi, M., and Sachdev, S. Stroke: a global response is needed, 2016.

Kaijima, S., Bouffanais, R., Willcox, K., and Naidu, S. Computational fluid dynamics for architectural design. *Architectural Design*, **83**(2):118–123, 2013.

Karatolios, K., Wittek, A., Nwe, T. H., Bihari, P., Shelke, A., Josef, D., Schmitz-Rixen, T., Geks, J., Maisch, B., Blase, C., Moosdorf, R., and Vogt, S. Method for aortic wall strain measurement with three-dimensional ultrasound speckle tracking and fitted finite element analysis. *The Annals of thoracic surgery*, **96**(5):1664–71, nov 2013.

Karino, T. Microscopic structure of disturbed flows in the arterial and venous systems, and its implication in the localization of vascular diseases. *International angiology : a journal of the International Union of Angiology*, **5**(4):297–313, 1986.

Kelly-Arnold, A., Maldonado, N., Laudier, D., Aikawa, E., Cardoso, L., and Weinbaum, S. Revised microcalcification hypothesis for fibrous cap rupture in human coronary arteries. *Proceedings of the National Academy of Sciences of the United States of America*, **110**(26):10741–6, jun 2013.

Kenagy, R. D., Fischer, J. W., Davies, M. G., Berceli, S. A., Hawkins, S. M., Wight, T. N., and Clowes, A. W. Increased plasmin and serine proteinase activity during flow-induced intimal atrophy in baboon PTFE grafts. *Arteriosclerosis, thrombosis, and vascular biology*, **22**(3): 400–4, mar 2002.

Kilner, P. J., Yang, G. Z., Mohiaddin, R. H., Firmin, D. N., and Longmore, D. B. Helical and retrograde secondary flow patterns in the aortic arch studied by three-directional magnetic resonance velocity mapping. *Circulation*, **88**(5 Pt 1):2235–47, nov 1993.

Kimura, B. J., Russo, R. J., Bhargava, V., McDaniel, M. B., Peterson, K. L., and DeMaria, A. N. Atheroma morphology and distribution in proximal left anterior descending coronary artery: In vivo observations. *Journal of the American College of Cardiology*, **27**(4):825–831, 1996.

Knight, J., Olgac, U., Saur, S. C. C., Poulikakos, D., Marshall, W., Cattin, P. C. C., Alkadhi, H., and Kurtcuoglu, V. Choosing the optimal wall shear parameter for the prediction of plaque location - A patient-specific computational study in human right coronary arteries. *Atherosclerosis*, **211**(2):445–450, aug 2010.

Knobloch, V., Boesiger, P., and Kozerke, S. Sparsity transform k-t principal component analysis for accelerating cine three-dimensional flow measurements. *Magnetic Resonance in Medicine*, **70**(1):53–63, jul 2013.

Kok, A. A. M., Speelman, L., Virmani, R., Steen, A., Gijsen, F. J. H. F., Wentzel, J. J. J., van der Steen, A. F. W., Gijsen, F. J. H. F., and Wentzel, J. J. J. Peak cap stress calculations in coronary atherosclerotic plaques with an incomplete necrotic core geometry. *BioMedical Engineering OnLine*, **15**(1):48, 2016.

Koskinas, K. C., Chatzizisis, Y. S., Baker, A. B., Edelman, E. R., Stone, P. H., and Feldman, C. L. The role of low endothelial shear stress in the conversion of atherosclerotic lesions from stable to unstable plaque. *Current opinion in cardiology*, **24**(6):580–590, nov 2009.

Koskinas, K. C., Feldman, C. L., Chatzizisis, Y. S., Coskun, A. U., Jonas, M., Maynard, C., Baker, A. B., Papafaklis, M. I., Edelman, E. R., and Stone, P. H. Natural history of experimental coronary atherosclerosis and vascular remodeling in relation to endothelial shear stress: A serial, in vivo intravascular ultrasound study. *Circulation*, **121**(19):2092–2101, 2010.

LIST OF REFERENCES

Koskinas, K. C., Chatzizisis, Y. S., Papafaklis, M. I., Coskun, A. U., Baker, A. B., Jarolim, P., Antoniadis, A., Edelman, E. R., Stone, P. H., and Feldman, C. L. Synergistic effect of local endothelial shear stress and systemic hypercholesterolemia on coronary atherosclerotic plaque progression and composition in pigs. *International Journal of Cardiology*, **169**(6):394–401, 2013a.

Koskinas, K. C., Sukhova, G. K., Baker, A. B., Papafaklis, M. I., Chatzizisis, Y. S., Coskun, A. U., Quillard, T., Jonas, M., Maynard, C., Antoniadis, A. P., Shi, G. P., Libby, P., Edelman, E. R., Feldman, C. L., and Stone, P. H. Thin-capped atheromata with reduced collagen content in pigs develop in coronary arterial regions exposed to persistently low endothelial shear stress. *Arteriosclerosis, Thrombosis, and Vascular Biology*, **33**(7):1494–1504, 2013b.

Krause, M. D., Huang, R.-T., Wu, D., Shentu, T.-P., Harrison, D. L., Whalen, M. B., Stolze, L. K., Di Rienzo, A., Moskowitz, I. P., Civelek, M., Romanoski, C. E., and Fang, Y. Genetic variant at coronary artery disease and ischemic stroke locus 1p32.2 regulates endothelial responses to hemodynamics. *Proceedings of the National Academy of Sciences*, **115**(48):E11349–E11358, 2018.

Ku, D. N. and Giddens, D. P. Pulsatile flow in a model carotid bifurcation. *Arteriosclerosis (Dallas, Tex.)*, **3**(1):31–9, jan 1983.

Ku, D. N. and Giddens, D. P. Laser Doppler anemometer measurements of pulsatile flow in a model carotid bifurcation. *Journal of biomechanics*, **20**(4):407–21, 1987.

Ku, D. N., Giddens, D. P., Zarins, C. K., and Glagov, S. Pulsatile flow and atherosclerosis in the human carotid bifurcation. Positive correlation between plaque location and low oscillating shear stress. *Arteriosclerosis (Dallas, Tex.)*, **5**(3):293–302, jan 1985.

Kubo, T., Yamano, T., Liu, Y., Ino, Y., Shiono, Y., Orii, M., Taruya, A., Nishiguchi, T., Shimokado, A., Teraguchi, I., Tanimoto, T., Kitabata, H., Yamaguchi, T., Hirata, K., Tanaka, A., and Akasaka, T. Feasibility of Optical Coronary Tomography in Quantitative Measurement of Coronary Arteries With Lipid-Rich Plaque. *Circulation Journal*, **79**(3):600–606, 2015.

Kuivaniemi, H., Ryer, E. J., and Elmore, J. R. Understanding the pathogenesis of abdominal aortic aneurysms. *Curr Atheroscler Rep*, **13**(9):975–987, 2016.

Kumar, A., Thompson, E. W., Lefieux, A., Molony, D. S., Davis, E. L., Chand, N., Fournier, S., Lee, H. S., Suh, J., Sato, K., Ko, Y.-A. A., Molloy, D., Chandran, K., Hosseini, H., Gupta, S., Milkas, A., Gogas, B., Chang, H.-J. J., Min, J. K., Fearon, W. F., Veneziani, A., Giddens, D. P., King, S. B., De Bruyne, B., and Samady, H. High Coronary Shear Stress in Patients With Coronary Artery Disease Predicts Myocardial Infarction. *Journal of the American College of Cardiology*, **72**(16):1926–1935, oct 2018.

Kurvers, H., Veith, F. J., Lipsitz, E. C., Ohki, T., Gargiulo, N. J., Cayne, N. S., Suggs, W. D., Timaran, C. H., Kwon, G. Y., Rhee, S. J., and Santiago, C. Discontinuous, staccato growth of abdominal aortic aneurysms. *Journal of the American College of Surgeons*, **199**(5):709–15, nov 2004.

Kwak, B. R., Back, M., Bochaton-Piallat, M.-L., Caligiuri, G., Daemen, M. J. a. P., Davies, P. F., Hoefer, I. E., Holvoet, P., Jo, H., Krams, R., Lehoux, S., Monaco, C., Steffens, S., Virmani, R., Weber, C., Wentzel, J. J., and Evans, P. C. Biomechanical factors in atherosclerosis: mechanisms and clinical implications. *European Heart Journal*, **35**(43):3013–3020, 2014.

Lawlor, M. G., O'Donnell, M. R., O'Connell, B. M., and Walsh, M. T. Experimental determination of circumferential properties of fresh carotid artery plaques. *Journal of Biomechanics*, **44**(9):1709–1715, 2011.

Lee, K. W. and Xu, X. Y. Modelling of flow and wall behaviour in a mildly stenosed tube. *Medical Engineering and Physics*, **24**(9):575–586, 2002.

Lee, S.-W., Antiga, L., Spence, J. D., and Steinman, D. A. Geometry of the carotid bifurcation predicts its exposure to disturbed flow. *Stroke; a journal of cerebral circulation*, **39**(8):2341–7, aug 2008.

Lendon, C. L., Davies, M. J., Born, G. V., and Richardson, P. D. Atherosclerotic plaque caps are locally weakened when macrophages density is increased. *Atherosclerosis*, **87**(1):87–90, mar 1991.

Li, Y., Gutiérrez-Chico, J. L., Holm, N. R., Yang, W., Hebsgaard, L., Christiansen, E. H., Mæng, M., Lassen, J. F., Yan, F., Reiber, J. H., and Tu, S. Impact of Side Branch Modeling on Computation of Endothelial Shear Stress in Coronary Artery Disease. *Journal of the American College of Cardiology*, **66**(2):125–135, jul 2015.

Li, Z.-y., Tang, T., U-king im, J., Graves, M., Sutcliffe, M., and Gillard, J. H. Assessment of Carotid Plaque Vulnerability Using Structural and Geometrical Determinants. *Circulation Journal*, **72**(72):1092–1099, 2008.

Li, Z.-Y., Sadat, U., U-King-Im, J., Tang, T. Y., Bowden, D. J., Hayes, P. D., and Gillard, J. H. Association between aneurysm shoulder stress and abdominal aortic aneurysm expansion: a longitudinal follow-up study. *Circulation*, **122**(18):1815–22, nov 2010.

Liang, K.-Y. and Zeger, S. L. Longitudinal data analysis using generalized linear models. *Biometrika Trust*, **73**(1):13–22, 1986.

Libby, P., Ridker, P. M., and Hansson, G. K. Progress and challenges in translating the biology of atherosclerosis. *Nature*, **473**(7347):317–25, may 2011.

Libby, P., Lichtman, A. H., and Hansson, G. K. Immune effector mechanisms implicated in atherosclerosis: from mice to humans. *Immunity*, **38**(6):1092–104, jun 2013.

LIST OF REFERENCES

Lijnen, H. R. Plasmin and matrix metalloproteinases in vascular remodeling. *Thrombosis and haemostasis*, **86**(1):324–33, jul 2001.

Liu, X., Pu, F., Fan, Y., Deng, X., Li, D., and Li, S. A numerical study on the flow of blood and the transport of LDL in the human aorta: the physiological significance of the helical flow in the aortic arch. *American journal of physiology. Heart and circulatory physiology*, **297**(1): H163–70, jul 2009.

Liu, X., Fan, Y., and Deng, X. Effect of spiral flow on the transport of oxygen in the aorta: a numerical study. *Annals of biomedical engineering*, **38**(3):917–26, mar 2010.

Liu, X., Sun, A., Fan, Y., and Deng, X. Physiological Significance of Helical Flow in the Arterial System and its Potential Clinical Applications. *Annals of Biomedical Engineering*, **43**(1):3–15, jan 2015.

Liu, X., Wu, G., Xu, C., He, Y., Shu, L., Liu, Y., Zhang, N., and Lin, C. Prediction of coronary plaque progression using biomechanical factors and vascular characteristics based on computed tomography angiography. *Computer Assisted Surgery*, **22**(s1):286–294, 2017.

Loree, H. M., Kamm, R. D., Stringfellow, R. G., and Lee, R. T. Effects of Fibrous Cap Thickness on Peak Circumferential Stress in Model Atherosclerotic Vessels. *Circulation research*, **71**(0): 850–858, 1992.

Loree, H. M., Tobias, B. J., Gibson, L. J., Kamm, R. D., Small, D. M., and Lee, R. T. Mechanical Properties of Model Atherosclerotic Lesion Lipid Pools. *Arterios*, **14**(2):230–4, 1994.

Lovett, J. K. and Rothwell, P. M. Site of carotid plaque ulceration in relation to direction of blood flow: an angiographic and pathological study. *Cerebrovascular diseases (Basel, Switzerland)*, **16**(4):369–75, jan 2003.

Lusis, A. J. Atherosclerosis. *Nature*, **407**(6801):233–41, 2000.

Lynch, P. The origins of computer weather prediction and climate modeling. *Journal of Computational Physics*, **227**(7):3431–3444, 2008.

Madder, R. D., Husaini, M., Davis, A. T., VanOosterhout, S., Khan, M., Wohns, D., McNamara, R. F., Wolschleger, K., Gribar, J., Collins, J. S., Jacoby, M., Decker, J. M., Hendricks, M., Sum, S. T., Madden, S., Ware, J. H., and Muller, J. E. Large lipid-rich coronary plaques detected by near-infrared spectroscopy at non-stented sites in the target artery identify patients likely to experience future major adverse cardiovascular events. *European heart journal cardiovascular Imaging*, **17**(4):393–9, apr 2016.

Malek, A. M., Alper, S. L., and Izumo, S. Hemodynamic shear stress and its role in atherosclerosis. *JAMA*, **282**(21):2035–42, dec 1999.

221

Malvè, M., García, A., Ohayon, J., and Martínez, M. Unsteady blood flow and mass transfer of a human left coronary artery bifurcation: FSI vs. CFD. *International Communications in Heat and Mass Transfer*, **39**(6):745–751, jul 2012.

Malvè, M., Gharib, a. M., Yazdani, S. K., Finet, G., Martínez, M. a., Pettigrew, R., and Ohayon, J. Tortuosity of Coronary Bifurcation as a Potential Local Risk Factor for Atherosclerosis: CFD Steady State Study Based on In Vivo Dynamic CT Measurements. *Annals of Biomedical Engineering*, **43**(1):82–93, 2015.

Markl, M., Draney, M. T., Hope, M. D., Levin, J. M., Chan, F. P., Alley, M. T., Pelc, N. J., and Herfkens, R. J. Time-resolved 3-dimensional velocity mapping in the thoracic aorta: visualization of 3-directional blood flow patterns in healthy volunteers and patients. *Journal of computer assisted tomography*, **28**(4):459–68, 2004.

Markl, M., Wegent, F., Zech, T., Bauer, S., Strecker, C., Schumacher, M., Weiller, C., Hennig, J., and Harloff, A. In vivo wall shear stress distribution in the carotid artery: effect of bifurcation geometry, internal carotid artery stenosis, and recanalization therapy. *Circulation. Cardiovascular imaging*, **3**(6):647–55, nov 2010.

Mathers, C. D. and Loncar, D. Projections of Global Mortality and Burden of Disease from 2002 to 2030. 2006.

Meckel, S., Leitner, L., Bonati, L. H., Santini, F., Schubert, T., Stalder, A. F., Lyrer, P., Markl, M., and Wetzel, S. G. Intracranial artery velocity measurement using 4D PC MRI at 3 T: comparison with transcranial ultrasound techniques and 2D PC MRI. *Neuroradiology*, **55**(4):389–98, mar 2013.

Melnik, R. *Mathematical and computational modeling: with applications in natural and social sciences, engineering, and the arts*. John Wiley & Sons Inc, 2015.

Menees, D. S., Peterson, E. D., Wang, Y., Curtis, J. P., Messenger, J. C., Rumsfeld, J. S., and Gurm, H. S. Door-to-Balloon Time and Mortality among Patients Undergoing Primary PCI. *New England Journal of Medicine*, **369**(10):901–909, 2013.

Merkx, M. a. G., van 't Veer, M., Speelman, L., Breeuwer, M., Buth, J., and van de Vosse, F. N. Importance of initial stress for abdominal aortic aneurysm wall motion: dynamic MRI validated finite element analysis. *Journal of biomechanics*, **42**(14):2369–73, oct 2009.

Millon, A., Sigovan, M., Boussel, L., Mathevet, J.-L., Louzier, V., Paquet, C., Geloen, A., Provost, N., Majd, Z., Patsouris, D., Serusclat, A., and Canet-Soulas, E. Low WSS Induces Intimal Thickening, while Large WSS Variation and Inflammation Induce Medial Thinning, in an Animal Model of Atherosclerosis. *PLOS ONE*, **10**(11):e0141880, nov 2015.

Misra, S., Ramesh, K. T., and Okamura, A. M. Modeling of tool-tissue interactions for computer-based surgical simulation: A literature review. *Presence: Teleoperators and Virtual Environments*, **17**(5):463–491, oct 2008.

LIST OF REFERENCES

Moffatt, H. K. and Tsinober, A. Helicity in laminar and turbulent flow. *Annual Review of Fluid Mechanics*, **24**(0):281–312, 1992.

Mohamied, Y., Rowland, E. M., Bailey, E. L., Sherwin, S. J., Schwartz, M. a., and Weinberg, P. D. Change of Direction in the Biomechanics of Atherosclerosis. *Annals of Biomedical Engineering*, **43**(1):16–25, 2015.

Mohamied, Y., Sherwin, S. J., and Weinberg, P. D. Understanding the Fluid Mechanics Behind Transverse Wall Shear Stress. *Journal of Biomechanics*, **50**(0):102–109, 2017.

Molony, D. S., Timmins, L. H., Hung, O. Y., Rasoul-Arzrumly, E., Samady, H., and Giddens, D. P. An assessment of intra-patient variability on observed relationships between wall shear stress and plaque progression in coronary arteries. *BioMedical Engineering OnLine*, **14**(Suppl 1):S2, 2015.

Morbiducci, U., Ponzini, R., Grigioni, M., and Redaelli, A. Helical flow as fluid dynamic signature for atherogenesis risk in aortocoronary bypass. A numeric study. *Journal of biomechanics*, **40**(3):519–34, jan 2007.

Morbiducci, U., Ponzini, R., Rizzo, G., Cadioli, M., Esposito, A., De Cobelli, F., Del Maschio, A., Montevecchi, F. M., and Redaelli, A. In vivo quantification of helical blood flow in human aorta by time-resolved three-dimensional cine phase contrast magnetic resonance imaging. *Annals of biomedical engineering*, **37**(3):516–31, mar 2009.

Morbiducci, U., Ponzini, R., Rizzo, G., Cadioli, M., Esposito, A., Montevecchi, F. M., and Redaelli, A. Mechanistic insight into the physiological relevance of helical blood flow in the human aorta: an in vivo study. *Biomechanics and modeling in mechanobiology*, **10**(3):339–55, jul 2011.

Morbiducci, U., Ponzini, R., Gallo, D., Bignardi, C., and Rizzo, G. Inflow boundary conditions for image-based computational hemodynamics: impact of idealized versus measured velocity profiles in the human aorta. *Journal of biomechanics*, **46**(1):102–9, jan 2013.

Morbiducci, U., Gallo, D., Cristofanelli, S., Ponzini, R., Deriu, M. A., Rizzo, G., and Steinman, D. A. A rational approach to defining principal axes of multidirectional wall shear stress in realistic vascular geometries, with application to the study of the influence of helical flow on wall shear stress directionality in aorta. *Journal of Biomechanics*, **48**(6):899–906, 2015.

Morbiducci, U., Kok, A., Kwak, B., Stone, P., Steinman, D., and Wentzel, J. Atherosclerosis at arterial bifurcations: Evidence for the role of haemodynamics and geometry. *Thrombosis and Haemostasis*, **115**(3):484–92, 2016.

Moreno, P. R., Falk, E., Palacios, I. F., Newell, J. B., Fuster, V., and Fallon, J. T. Macrophage infiltration in acute coronary syndromes. Implications for plaque rupture. *Circulation*, **90**(2): 775–8, aug 1994.

Mower, W. R., Quiñones, W. J., and Gambhir, S. S. Effect of intraluminal thrombus on abdominal aortic aneurysm wall stress. *Journal of vascular surgery*, **26**(4):602–8, oct 1997.

Naghavi, M., Libby, P., Falk, E., Casscells, S. W., Litovsky, S., Rumberger, J., Badimon, J. J., Stefanadis, C., Moreno, P., Pasterkamp, G., Fayad, Z., Stone, P. H., Waxman, S., Raggi, P., Madjid, M., Zarrabi, A., Burke, A., Yuan, C., Fitzgerald, P. J., Siscovick, D. S., de Korte, C. L., Aikawa, M., Juhani Airaksinen, K. E., Assmann, G., Becker, C. R., Chesebro, J. H., Farb, A., Galis, Z. S., Jackson, C., Jang, I.-K., Koenig, W., Lodder, R. A., March, K., Demirovic, J., Navab, M., Priori, S. G., Rekhter, M. D., Bahr, R., Grundy, S. M., Mehran, R., Colombo, A., Boerwinkle, E., Ballantyne, C., Insull, W., Schwartz, R. S., Vogel, R., Serruys, P. W., Hansson, G. K., Faxon, D. P., Kaul, S., Drexler, H., Greenland, P., Muller, J. E., Virmani, R., Ridker, P. M., Zipes, D. P., Shah, P. K., and Willerson, J. T. From Vulnerable Plaque to Vulnerable Patient: A Call for New Definitions and Risk Assessment Strategies: Part I. *Circulation*, **108** (14):1664–1672, oct 2003.

Nair, A., Kuban, B. D., Tuzcu, E. M., Schoenhagen, P., Nissen, S. E., and Vince, D. G. Coronary plaque classification with intravascular ultrasound radiofrequency data analysis. *Circulation*, **106**(17):2200–2206, oct 2002.

Nakashima, T. and Tashiro, T. Early morphologic stage of human coronary atherosclerosis. *The Kurume medical journal*, **15**(4):235–42, 1968.

Nakashima, T., Iwanaga, Y., and Nakaura, Y. Pathologic study of hypertensive heart. *Acta pathologica japonica*, **14**(0):129–41, jan 1964.

Nasu, K., Tsuchikane, E., Katoh, O., Vince, D. G., Virmani, R., Surmely, J.-F. F., Murata, A., Takeda, Y., Ito, T., Ehara, M., Matsubara, T., Terashima, M., and Suzuki, T. Accuracy of in vivo coronary plaque morphology assessment: a validation study of in vivo virtual histology compared with in vitro histopathology. *Journal of the American College of Cardiology*, **47** (12):2405–2412, jun 2006.

Nathoe, H. M. W., Stella, P. R., Eefting, F. D., and de Jaegere, P. P. T. Angiographic findings in monozygotic twins with coronary artery disease. *The American journal of cardiology*, **89**(8): 1006–9, apr 2002.

Nejad, A. A., Talebi, Z., Cheraghali, D., Shahbani-Zahiri, A., and Norouzi, M. Pulsatile flow of non-Newtonian blood fluid inside stenosed arteries: Investigating the effects of viscoelastic and elastic walls, arteriosclerosis, and polycythemia diseases. *Computer Methods and Programs in Biomedicine*, **154**(0):109–122, 2018.

Nieuwstadt, H. A., Geraedts, T. R., Truijman, M. T. B., Kooi, M. E., van der Lugt, A., van der Steen, A. F. W., Wentzel, J. J., Breeuwer, M., and Gijsen, F. J. H. Numerical simulations of carotid MRI quantify the accuracy in measuring atherosclerotic plaque components in vivo. *Magnetic resonance in medicine : official journal of the Society of Magnetic Resonance in Medicine / Society of Magnetic Resonance in Medicine*, **72**(1):188–201, 2014a.

LIST OF REFERENCES

Nieuwstadt, H. A., Speelman, L., Breeuwer, M., van der Lugt, A., van der Steen, A. F. W., Wentzel, J. J., and Gijsen, F. J. H. The influence of inaccuracies in carotid MRI segmentation on atherosclerotic plaque stress computations. *Journal of biomechanical engineering*, **136** (2):21015, feb 2014b.

Nissen, S. E., Tuzcu, E. M., Schoenhagen, P., Brown, B. G., Ganz, P., Vogel, R. A., Crowe, T., Howard, G., Cooper, C. J., Brodie, B., Grines, C. L., DeMaria, A. N., and for the REVERSAL Investigators. Effect of Intensive Compared With Moderate Lipid-Lowering Therapy on Progression of Coronary Atherosclerosis. *JAMA*, **291**(9):1071, mar 2004.

Oemrawsingh, R. M., Cheng, J. M., García-García, H. M., Van Geuns, R. J., De Boer, S. P., Simsek, C., Kardys, I., Lenzen, M. J., Van Domburg, R. T., Regar, E., Serruys, P. W., Akkerhuis, K. M., and Boersma, E. Near-infrared spectroscopy predicts cardiovascular outcome in patients with coronary artery disease. *Journal of the American College of Cardiology*, **64**(23): 2510–2518, 2014.

Ogita, M., Miyauchi, K., Onishi, A., Tsuboi, S., Wada, H., Konishi, H., Naito, R., Dohi, T., Kasai, T., Kojima, Y., Schwartz, R. S., and Daida, H. Development of Accelerated Coronary Atherosclerosis Model Using Low Density Lipoprotein Receptor Knock-Out Swine with Balloon Injury. *PLOS ONE*, **11**(9):e0163055, sep 2016.

Ohayon, J., Finet, G., Gharib, A. M., Herzka, D. a., Tracqui, P., Heroux, J., Rioufol, G., Kotys, M. S., Elagha, A., and Pettigrew, R. I. Necrotic core thickness and positive arterial remodeling index: emergent biomechanical factors for evaluating the risk of plaque rupture. *American journal of physiology. Heart and circulatory physiology*, **295**(2):H717–27, aug 2008.

Papadopoulou, S. L., Brugaletta, S., Garcia-Garcia, H. M., Rossi, A., Girasis, C., Dharampal, A. S., Neefjes, L. a., Ligthart, J., Nieman, K., Krestin, G. P., Serruys, P. W., and De Feyter, P. J. Assessment of atherosclerotic plaques at coronary bifurcations with multidetector computed tomography angiography and intravascular ultrasound-virtual histology. *European Heart Journal Cardiovascular Imaging*, **13**(8):635–642, 2012.

Pedersen, E., Oyre, S., Agerbæk, M., Kristensen, I., Ringgaard, S., Boesiger, P., and Paaske, W. Distribution of early atherosclerotic lesions in the human abdominal aorta correlates with wall shear stresses measured in vivo. *European Journal of Vascular and Endovascular Surgery*, **18** (4):328–333, 1999.

Pedrigi, R. M., Poulsen, C. B., Mehta, V. V., Ramsing Holm, N., Pareek, N., Post, A. L., Kilic, I. D., Banya, W. A. S., Dall'Ara, G., Mattesini, A., Bjørklund, M. M., Andersen, N. P., Grøndal, A. K., Petretto, E., Foin, N., Davies, J. E., Di Mario, C., Fog Bentzon, J., Erik Bøtker, H., Falk, E., Krams, R., and de Silva, R. Inducing Persistent Flow Disturbances Accelerates Atherogenesis and Promotes Thin Cap Fibroatheroma Development in D374Y-PCSK9 Hypercholesterolemic Minipigs. *Circulation*, **132**(11):1003–12, sep 2015.

Peiffer, V., Sherwin, S. J., and Weinberg, P. D. Does low and oscillatory wall shear stress correlate spatially with early atherosclerosis ? A systematic review. *Cardiovascular Research*, **99**(0): 242–250, 2013a.

Peiffer, V., Sherwin, S. J., and Weinberg, P. D. Computation in the rabbit aorta of a new metric - the transverse wall shear stress - to quantify the multidirectional character of disturbed blood flow. *Journal of Biomechanics*, **46**(15):2651–2658, 2013b.

Perktold, K. and Peter, R. Numerical 3D-simulation of pulsatile wall shear stress in an arterial T-bifurcation model. *Journal of Biomedical Engineering*, **12**(0):2–12, 1990.

Perktold, K., Peter, R. O., Resch, M., and Langs, G. Pulsatile non-Newtonian blood flow in three-dimensional carotid bifurcation models: a numerical study of flow phenomena under different bifurcation angles. *Journal of biomedical engineering*, **13**(6):507–15, nov 1991.

Phan, T. G., Beare, R. J., Jolley, D., Das, G., Ren, M., Wong, K., Chong, W., Sinnott, M. D., Hilton, J. E., and Srikanth, V. Carotid artery anatomy and geometry as risk factors for carotid atherosclerotic disease. *Stroke; a journal of cerebral circulation*, **43**(6):1596–601, jun 2012.

Piechota-Polanczyk, A., Jozkowicz, A., Nowak, W., Eilenberg, W., Neumayer, C., Malinski, T., Huk, I., Brostjan, C., Vilahur, G., Francois, A., Stewart, R., Brostjan, C., Piechota-Polanczyk, A., Jozkowicz, A., Nowak, W., Eilenberg, W., Neumayer, C., Malinski, T., and Huk, I. The Abdominal Aortic Aneurysm and Intraluminal Thrombus: Current Concepts of Development and Treatment. *Frontiers in Cardiovascular Medicine*, **2**(May):1–14, 2015.

Pinho, N., Castro, C. F., António, C. C., Bettencourt, N., Sousa, L. C., and Pinto, S. I. S. Correlation between geometric parameters of the left coronary artery and hemodynamic descriptors of atherosclerosis: FSI and statistical study. *Medical & Biological Engineering & Computing*, **0**(0):6–9, 2018.

Pirola, S., Jarral, O. A., O'Regan, D. P., Asimakopoulos, G., Anderson, J. R., Pepper, J. R., Athanasiou, T., and Xu, X. Y. Computational study of aortic hemodynamics for patients with an abnormal aortic valve: The importance of secondary flow at the ascending aorta inlet. *APL Bioengineering*, **2**(2):026101, jun 2018.

Polak, J. F., Person, S. D., Wei, G. S., Godreau, A., Jacobs, D. R., Harrington, A., Sidney, S., and O'Leary, D. H. Segment-specific associations of carotid intima-media thickness with cardiovascular risk factors: the Coronary Artery Risk Development in Young Adults (CARDIA) study. *Stroke; a journal of cerebral circulation*, **41**(1):9–15, jan 2010.

Ponzini, R., Vergara, C., Redaelli, A., and Veneziani, A. Reliable CFD-based estimation of flow rate in haemodynamics measures. *Ultrasound in Medicine & Biology*, **32**(10):1545–1555, oct 2006.

Rader, D. J. and Puré, E. Lipoproteins, macrophage function, and atherosclerosis: Beyond the foam cell? *Cell Metabolism*, **1**(4):223–230, apr 2005.

LIST OF REFERENCES

Rafieian-Kopaei, M., Setorki, M., Doudi, M., Baradaran, A., and Nasri, H. Atherosclerosis: process, indicators, risk factors and new hopes. *International journal of preventive medicine*, **5**(8):927–46, aug 2014.

Raghavan, M. L., Vorp, D. a., Federle, M. P., Makaroun, M. S., and Webster, M. W. Wall stress distribution on three-dimensionally reconstructed models of human abdominal aortic aneurysm. *Journal of vascular surgery*, **31**(4):760–9, apr 2000.

Raghavan, M. L., Fillinger, M. F., Marra, S. P., Naegelein, B. P., and Kennedy, F. E. Automated Methodology for Determination of Stress Distribution in Human Abdominal Aortic Aneurysm. *Journal of Biomechanical Engineering*, **127**(5):868, 2005.

Raso, A. M., Levis, P., and Sottimano, C. Geometry of aortoiliac bifurcation in healthy men and women as possible atherogenic risk factor. *Panminerva medica*, **23**(1):33–7, jan 1981.

Ratcliffe, S. J. and Shults, J. GEEQBOX : A MATLAB Toolbox for Generalized Estimating Equations and Quasi-Least Squares. *Journal of statistical software*, **25**(14):1–14, 2008.

Ravensbergen, J., Ravensbergen, J. W., Krijger, J. K., Hillen, B., and Hoogstraten, H. W. Localizing role of hemodynamics in atherosclerosis in several human vertebrobasilar junction geometries. *Arteriosclerosis, thrombosis, and vascular biology*, **18**(5):708–16, may 1998.

Redgrave, J. N., Gallagher, P., Lovett, J. K., and Rothwell, P. M. Critical Cap Thickness and Rupture in Symptomatic Carotid Plaques: The Oxford Plaque Study. *Stroke*, **39**(6):1722–1729, 2008.

Rikhtegar, F., Knight, J. A. a., Olgac, U., Saur, S. C. C., Poulikakos, D., Marshall, W., Cattin, P. C. C., Alkadhi, H., and Kurtcuoglu, V. Choosing the optimal wall shear parameter for the prediction of plaque location—A patient-specific computational study in human left coronary arteries. *Atherosclerosis*, **221**(2):432–437, apr 2012.

Rose, J., Evans, C., Barleben, A., Bandyk, D., Wilson, S. E., Chang, D. C., and Lane, J. Comparative safety of endovascular aortic aneurysm repair over open repair using patient safety indicators during adoption. *JAMA surgery*, **149**(9):926–32, sep 2014.

Rouet, L., Ardon, R., Rouet, J.-M., Mory, B., Dufour, C., and Long, A. Semi-automatic abdominal aortic aneurysms geometry assessment based on 3D ultrasound. In *2010 IEEE International Ultrasonics Symposium*, pages 201–204. Ieee, oct 2010.

Sabbah, H. N., Walburn, F. J., and Stein, P. D. Patterns of flow in the left coronary artery. *Journal of biomechanical engineering*, **106**(3):272–9, aug 1984.

Sakellarios, A., Bourantas, C. V., Papadopoulou, S.-L., Kitslaar, P. H., Girasis, C., Stone, G. W., Reiber, J. H. C., Michalis, L. K., Serruys, P. W., de Feyter, P. J., Garcia-Garcia, H. M., and Fotiadis, D. I. The effect of coronary bifurcation and blood flow modelling in prediction of atherosclerotic plaque development: a Serial Computed Tomographic Coronary Angiographic

study. *EuroIntervention : journal of EuroPCR in collaboration with the Working Group on Interventional Cardiology of the European Society of Cardiology*, **13**(0):1084–1091, 2017.

Samady, H., Eshtehardi, P., McDaniel, M. C., Suo, J., Dhawan, S. S., Maynard, C., Timmins, L. H., Quyyumi, A. a., and Giddens, D. P. Coronary artery wall shear stress is associated with progression and transformation of atherosclerotic plaque and arterial remodeling in patients with coronary artery disease. *Circulation*, **124**(7):779–88, aug 2011.

Sangalli, L. M., Secchi, P., Vantini, S., and Veneziani, A. Efficient estimation of three-dimensional curves and their derivatives by free-knot regression splines, applied to the analysis of inner carotid artery centrelines. *Journal of the Royal Statistical Society: Series C (Applied Statistics)*, **58**(3):285–306, jul 2009.

Schaap, M., Neefjes, L., Metz, C., van der Giessen, A., Weustink, A., Mollet, N., Wentzel, J., van Walsum, T. W., and Niessen, W. Coronary lumen segmentation using graph cuts and robust kernel regression. In *Information processing in medical imaging : proceedings of the ... conference*, volume 21, pages 528–39, 2009.

Schaar, J. a., Muller, J. E., Falk, E., Virmani, R., Fuster, V., Serruys, P. W., Colombo, A., Stefanadis, C., Ward Casscells, S., Moreno, P. R., Maseri, A., and van der Steen, A. F. W. Terminology for high-risk and vulnerable coronary artery plaques. Report of a meeting on the vulnerable plaque, June 17 and 18, 2003, Santorini, Greece. *European heart journal*, **25**(12): 1077–82, jun 2004.

Schäfer, M., Barker, A. J., Kheyfets, V., Stenmark, K. R., Crapo, J., Yeager, M. E., Truong, U., Buckner, J. K., Fenster, B. E., and Hunter, K. S. Helicity and Vorticity of Pulmonary Arterial Flow in Patients With Pulmonary Hypertension: Quantitative Analysis of Flow Formations. *Journal of the American Heart Association*, **6**(12), dec 2017.

Schober, A., Nazari-Jahantigh, M., and Weber, C. MicroRNA-mediated mechanisms of the cellular stress response in atherosclerosis. *Nature Reviews Cardiology*, **12**(0):361–374, apr 2015.

Schrauwen, J. T., Karanasos, A., Van Ditzhuijzen, N. S., Aben, J. P., Van Der Steen, A. F., Wentzel, J. J., and Gijsen, F. J. Influence of the Accuracy of Angiography-Based Reconstructions on Velocity and Wall Shear Stress Computations in Coronary Bifurcations: A Phantom Study. *PLoS ONE*, **10**(12):1–19, 2015.

Schulz, U. G. and Rothwell, P. M. Major variation in carotid bifurcation anatomy: a possible risk factor for plaque development? *Stroke; a journal of cerebral circulation*, **32**(11):2522–9, nov 2001.

Schulz, U. G. R. and Rothwell, P. M. Association between arterial bifurcation anatomy and angiographic plaque ulceration among 4,627 carotid stenoses. *Cerebrovascular diseases (Basel, Switzerland)*, **15**(4):244–51, jan 2003.

LIST OF REFERENCES

Schuurman, A.-S., Vroegindewey, M., Kardys, I., Oemrawsingh, R. M., Cheng, J. M., de Boer, S., Garcia-Garcia, H. M., van Geuns, R.-J., Regar, E. S., Daemen, J., van Mieghem, N. M., Serruys, P. W., Boersma, E., and Akkerhuis, K. M. Near-infrared spectroscopy-derived lipid core burden index predicts adverse cardiovascular outcome in patients with coronary artery disease during long-term follow-up. *European Heart Journal*, **39**(4):295–302, 2017.

Scv, P., Jayarajasingam, R., Cottam, R., Sj, P., Ja, M., and Sm, T. Endovascular repair of abdominal aortic aneurysm (Review). *Cochrane Database Syst Rev.*, **23**(1), 2014.

Seo, T., Schachter, L. G., and Barakat, A. I. Computational Study of Fluid Mechanical Disturbance Induced by Endovascular Stents. *Annals of Biomedical Engineering*, **33**(4):444–456, 2005.

Seyyedabbasi, A., Candan, F., and Kiani, F. A Method for Forecasting Weather condition by Using Artificial Neural Network Algorithm. *ICTACT Journal on Soft Computing*, **8**(3), 2018.

Shechter, G., Resar, J. R., and McVeigh, E. R. Displacement and velocity of the coronary arteries: cardiac and respiratory motion. *IEEE transactions on medical imaging*, **25**(3):369–75, mar 2006.

Shim, J., Poulsen, C. B., Hagensen, M. K., Larsen, T., Heegaard, P. M., Christoffersen, C., Bolund, L., Schmidt, M., Liu, Y., Li, J., Li, R., Callesen, H., Bentzon, J. F., and Sørensen, C. B. Apolipoprotein E Deficiency Increases Remnant Lipoproteins and Accelerates Progressive Atherosclerosis, But Not Xanthoma Formation, in Gene-Modified Minipigs. *JACC: Basic to Translational Science*, **2**(5):591–600, oct 2017.

Shindo, S., Fujii, K., Shirakawa, M., Uchida, K., Enomoto, Y., Iwama, T., Kawasaki, M., Ando, Y., and Yoshimura, S. Morphologic Features of Carotid Plaque Rupture Assessed by Optical Coherence Tomography. *AJNR Am J Neuroradiol*, **36**(11):2140–2146, 2015.

Shishikura, D., Sidharta, S. L. L., Honda, S., Takata, K., Kim, S. W. W., Andrews, J., Montarello, N., Delacroix, S., Baillie, T., Worthley, M. I. I., Psaltis, P. J. J., and Nicholls, S. J. J. The relationship between segmental wall shear stress and lipid core plaque derived from near-infrared spectroscopy. *Atherosclerosis*, **275**(0):68–73, aug 2018.

Siasos, G., Sara, J. D., Zaromytidou, M., Park, K. H., Coskun, A. U., Lerman, L. O., Oikonomou, E., Maynard, C. C., Fotiadis, D., Stefanou, K., Papafaklis, M., Michalis, L., Feldman, C., Lerman, A., and Stone, P. H. Local Low Shear Stress and Endothelial Dysfunction in Patients With Nonobstructive Coronary Atherosclerosis. *Journal of the American College of Cardiology*, **71**(19):2092–2102, may 2018.

Siebes, M., Verhoeff, B.-J., Meuwissen, M., de Winter, R. J., Spaan, J. A. E., and Piek, J. J. Single-wire pressure and flow velocity measurement to quantify coronary stenosis hemodynamics and effects of percutaneous interventions. *Circulation*, **109**(6):756–62, feb 2004.

Sigfridsson, A., Petersson, S., Carlhäll, C.-J., and Ebbers, T. Four-dimensional flow MRI using spiral acquisition. *Magnetic Resonance in Medicine*, **68**(4):1065–1073, oct 2012.

Silverstein, M. D., Pitts, S. R., Chaikof, E. L., and Ballard, D. J. Abdominal aortic aneurysm (AAA): cost-effectiveness of screening, surveillance of intermediate-sized AAA, and management of symptomatic AAA. *Proceedings (Baylor University. Medical Center)*, **18**(4):345–67, oct 2005.

Singh, K., Bønaa, K. H., Jacobsen, B. K., Bjørk, L., and Solberg, S. Prevalence of and risk factors for abdominal aortic aneurysms in a population-based study : The Tromsø Study. *American journal of epidemiology*, **154**(3):236–44, aug 2001.

Sitzer, M., Puac, D., Buehler, A., Steckel, D. A., Von Kegler, S., Markus, H. S., and Steinmetz, H. Internal carotid artery angle of origin: A novel risk factor for early carotid atherosclerosis. *Stroke*, **34**(4):950–955, 2003.

Slager, C. J., Wentzel, J. J., Gijsen, F. J. H., Thury, A., van der Wal, A. C., Schaar, J. A., and Serruys, P. W. The role of shear stress in the destabilization of vulnerable plaques and related therapeutic implications. *Nature clinical practice. Cardiovascular medicine*, **2**(9):456–64, sep 2005.

Smedby, O. Geometric risk factors for atherosclerosis in the aortic bifurcation: a digitized angiography study. *Annals of biomedical engineering*, **24**(4):481–8, jan 1996.

Smedby, O. Geometrical risk factors for atherosclerosis in the femoral artery: a longitudinal angiographic study. *Annals of biomedical engineering*, **26**(3):391–7, jan 1998.

Smedby, O., Högman, N., Nilsson, S., Erikson, U., Olsson, A. G., and Walldius, G. Two-dimensional tortuosity of the superficial femoral artery in early atherosclerosis. *Journal of vascular research*, **30**(4):181–91, jan 1993.

Somphone, O., De Craene, M., Ardon, R., Mory, B., Allain, P., Gao, H., D'Hooge, J., Marchesseau, S., Sermesant, M., Delingette, H., and Saloux, E. Fast myocardial motion and strain estimation in 3D cardiac ultrasound with Sparse Demons. In *Proceedings - International Symposium on Biomedical Imaging*, number May 2014, pages 1182–1185, 2013.

Speelman, L., Bosboom, E. M. H., Schurink, G. W. H., Hellenthal, F. a. M. V. I., Buth, J., Breeuwer, M., Jacobs, M. J., and van de Vosse, F. N. Patient-specific AAA wall stress analysis: 99-percentile versus peak stress. *European journal of vascular and endovascular surgery : the official journal of the European Society for Vascular Surgery*, **36**(6):668–76, dec 2008.

Speelman, L., Bosboom, E. M. H., Schurink, G. W. H., Buth, J., Breeuwer, M., Jacobs, M. J., and van de Vosse, F. N. Initial stress and nonlinear material behavior in patient-specific AAA wall stress analysis. *Journal of biomechanics*, **42**(11):1713–9, aug 2009.

LIST OF REFERENCES

Speelman, L., Hellenthal, F. a., Pulinx, B., Bosboom, E. M. H., Breeuwer, M., van Sambeek, M. R., van de Vosse, F. N., Jacobs, M. J., Wodzig, W. K. W. H., and Schurink, G. W. H. The influence of wall stress on AAA growth and biomarkers. *European journal of vascular and endovascular surgery : the official journal of the European Society for Vascular Surgery*, **39**(4):410–6, apr 2010.

Speelman, L., Akyildiz, a. C., den Adel, B., Wentzel, J. J., van der Steen, a. F. W., Virmani, R., van der Weerd, L., Jukema, J. W., Poelmann, R. E., van Brummelen, E. H., and Gijsen, F. J. H. Initial stress in biomechanical models of atherosclerotic plaques. *Journal of biomechanics*, **44**(13):2376–82, sep 2011.

Spelde, A. G., de Vos, R. A., Hoogendam, I. J., and Heethaar, R. M. Pathological-anatomical study concerning the geometry and atherosclerosis of the carotid bifurcation. *European journal of vascular surgery*, **4**(4):345–8, aug 1990.

Stolzmann, P., Schlett, C. L., Maurovich-Horvat, P., Maehara, A., Ma, S., Scheffel, H., Engel, L. C., Károlyi, M., Mintz, G. S., and Hoffmann, U. Variability and accuracy of coronary CT angiography including use of iterative reconstruction algorithms for plaque burden assessment as compared with intravascular ultrasound-an ex vivo study. *European Radiology*, **22**(10):2067–2075, 2012.

Stone, G. W., Maehara, A., Lansky, A. J., de Bruyne, B., Cristea, E., Mintz, G. S., Mehran, R., McPherson, J., Farhat, N., Marso, S. P., Parise, H., Templin, B., White, R., Zhang, Z., and Serruys, P. W. A prospective natural-history study of coronary atherosclerosis. *The New England journal of medicine*, **364**(3):226–235, jan 2011.

Stone, P. H., Coskun, A. U., Kinlay, S., Clark, M. E., Sonka, M., Wahle, A., Ilegbusi, O. J., Yeghiazarians, Y., Popma, J. J., Orav, J., Kuntz, R. E., and Feldman, C. L. Effect of endothelial shear stress on the progression of coronary artery disease, vascular remodeling, and in-stent restenosis in humans: in vivo 6-month follow-up study. *Circulation*, **108**(4):438–44, jul 2003.

Stone, P. H., Saito, S., Takahashi, S., Makita, Y., Nakamura, S. S., Kawasaki, T., Takahashi, A., Katsuki, T., Nakamura, S. S., Namiki, A., Hirohata, A., Matsumura, T., Yamazaki, S., Yokoi, H., Tanaka, S., Otsuji, S., Yoshimachi, F., Honye, J., Harwood, D., Reitman, M., Coskun, A. U., Papafaklis, M. I., and Feldman, C. L. Prediction of progression of coronary artery disease and clinical outcomes using vascular profiling of endothelial shear stress and arterial plaque characteristics: The PREDICTION study. *Circulation*, **126**(2):172–181, jul 2012.

Stone, P. H., Maehara, A., Coskun, A. U., Maynard, C. C., Zaromytidou, M., Siasos, G., Andreou, I., Fotiadis, D., Stefanou, K., Papafaklis, M., Michalis, L., Lansky, A. J., Mintz, G. S., Serruys, P. W., Feldman, C. L., and Stone, G. W. Role of Low Endothelial Shear Stress and Plaque Characteristics in the Prediction of Nonculprit Major Adverse Cardiac Events: The PROSPECT Study. *JACC: Cardiovascular Imaging*, **11**(3):462–471, mar 2018.

Stonebridge, P. A., Hoskins, P. R., Allan, P. L., and Belch, J. F. Spiral laminar flow in vivo. *Clinical science (London)*, **91**(1):17–21, jul 1996.

Stonebridge, P. A., Suttie, S. A., Ross, R., and Dick, J. Spiral Laminar Flow: a Survey of a Three-Dimensional Arterial Flow Pattern in a Group of Volunteers. *European Journal of Vascular & Endovascular Surgery*, **52**(5):674–680, 2016.

Svindland, a. The localization of sudanophilic and fibrous plaques in the main left coronary bifurcation. *Atherosclerosis*, **48**(2):139–145, 1983.

Tabas, I., Williams, K. J., and Borén, J. Subendothelial lipoprotein retention as the initiating process in atherosclerosis: Update and therapeutic implications. *Circulation*, **116**(16):1832–1844, 2007.

Takarada, S., Imanishi, T., Kubo, T., Tanimoto, T., Kitabata, H., Nakamura, N., Tanaka, A., Mizukoshi, M., and Akasaka, T. Effect of statin therapy on coronary fibrous-cap thickness in patients with acute coronary syndrome: Assessment by optical coherence tomography study. *Atherosclerosis*, **202**(2):491–497, 2009.

Tang, D., Yang, C., Zheng, J., Woodard, P. K., Saffitz, J. E., Petruccelli, J. D., Sicard, G. A., and Yuan, C. Local maximal stress hypothesis and computational plaque vulnerability index for atherosclerotic plaque assessment. *Annals of biomedical engineering*, **33**(12):1789–801, dec 2005a.

Tang, D., Yang, C., Zheng, J., Woodard, P. K., Saffitz, J. E., Sicard, G. A., Pilgram, T. K., and Yuan, C. Quantifying effects of plaque structure and material properties on stress distributions in human atherosclerotic plaques using 3D FSI models. *Journal of biomechanical engineering*, **127**(7):1185–94, dec 2005b.

Tang, D., Yang, C., Mondal, S., Liu, F., Canton, G., Hatsukami, T. S., and Yuan, C. A negative correlation between human carotid atherosclerotic plaque progression and plaque wall stress: in vivo MRI-based 2D/3D FSI models. *Journal of biomechanics*, **41**(4):727–36, jan 2008.

Tang, D., Teng, Z., Canton, G., Hatsukami, T. S., Dong, L., Huang, X., and Yuan, C. Local critical stress correlates better than global maximum stress with plaque morphological features linked to atherosclerotic plaque vulnerability: an in vivo multi-patient study. *Biomedical engineering online*, **8**(0):15, jan 2009.

Tang, D., Kamm, R. D., Yang, C., Zheng, J., Canton, G., Bach, R., Huang, X., Hatsukami, T. S., Zhu, J., Ma, G., Maehara, A., Mintz, G. S., and Yuan, C. Image-based modeling for better understanding and assessment of atherosclerotic plaque progression and vulnerability: data, modeling, validation, uncertainty and predictions. *Journal of biomechanics*, **47**(4):834–46, mar 2014.

Tarbell, J. M. Mass Transport in Arteries and the Localization of Atherosclerosis. *Annual Review of Biomedical Engineering*, **5**(1):79–118, aug 2003.

LIST OF REFERENCES

Taylor, C. A. and Steinman, D. A. Image-based modeling of blood flow and vessel wall dynamics: applications, methods and future directions: Sixth International Bio-Fluid Mechanics Symposium and Workshop, March 28-30, 2008 Pasadena, California. *Annals of biomedical engineering*, **38**(3):1188–203, mar 2010.

Tearney, G. J., Regar, E., Akasaka, T., Adriaenssens, T., Barlis, P., Bezerra, H. G., Bouma, B., Bruining, N., Cho, J. M., Chowdhary, S., Costa, M. a., De Silva, R., Dijkstra, J., Di Mario, C., Dudeck, D., Falk, E., Feldman, M. D., Fitzgerald, P., Garcia, H., Gonzalo, N., Granada, J. F., Guagliumi, G., Holm, N. R., Honda, Y., Ikeno, F., Kawasaki, M., Kochman, J., Koltowski, L., Kubo, T., Kume, T., Kyono, H., Lam, C. C. S., Lamouche, G., Lee, D. P., Leon, M. B., Maehara, A., Manfrini, O., Mintz, G. S., Mizuno, K., Morel, M. A., Nadkarni, S., Okura, H., Otake, H., Pietrasik, A., Prati, F., Rber, L., Radu, M. D., Rieber, J., Riga, M., Rollins, A., Rosenberg, M., Sirbu, V., Serruys, P. W. J. C., Shimada, K., Shinke, T., Shite, J., Siegel, E., Sonada, S., Suter, M., Takarada, S., Tanaka, A., Terashima, M., Troels, T., Uemura, S., Ughi, G. J., Van Beusekom, H. M. M., Van Der Steen, A. F. W., Van Es, G. A., Van Soest, G., Virmani, R., Waxman, S., Weissman, N. J., and Weisz, G. Consensus standards for acquisition, measurement, and reporting of intravascular optical coherence tomography studies: A report from the International Working Group for Intravascular Optical Coherence Tomography Standardization and Validation. *Journal of the American College of Cardiology*, **59**(12):1058–1072, 2012.

Theodorakakos, A., Gavaises, M., Andriotis, A., Zifan, A., Liatsis, P., Pantos, I., Efstathopoulos, E. P., and Katritsis, D. Simulation of cardiac motion on non-Newtonian, pulsating flow development in the human left anterior descending coronary artery. *Physics in Medicine and Biology*, **53**(18):4875–4892, sep 2008.

Thim, T., Hagensen, M. K., Drouet, L., Bal Dit Sollier, C., Bonneau, M., Granada, J. F., Nielsen, L. B., Paaske, W. P., Bøtker, H. E., and Falk, E. Familial hypercholesterolaemic downsized pig with human-like coronary atherosclerosis: a model for preclinical studies. *EuroIntervention : journal of EuroPCR in collaboration with the Working Group on Interventional Cardiology of the European Society of Cardiology*, **6**(2):261–8, jun 2010a.

Thim, T., Hagensen, M. K., Wallace-Bradley, D., Granada, J. F., Kaluza, G. L., Drouet, L., Paaske, W. P., Bøtker, H. E., and Falk, E. Unreliable assessment of necrotic core by virtual histology intravascular ultrasound in porcine coronary artery disease. *Circulation: Cardiovascular Imaging*, **3**(4):384–391, 2010b.

Thomas, J. B., Milner, J. S., and Steinman, D. A. On the influence of vessel planarity on local hemodynamics at the human carotid bifurcation. *Biorheology*, **39**(3-4):443–8, jan 2002.

Thomas, J. B., Antiga, L., Che, S. L., Milner, J. S., Steinman, D. A. H., Spence, J. D., Rutt, B. K., and Steinman, D. A. Variation in the carotid bifurcation geometry of young versus older adults: implications for geometric risk of atherosclerosis. *Stroke; a journal of cerebral circulation*, **36**(11):2450–6, nov 2005.

Tilson, M. D. Histochemistry of Aortic Elastin in Patients With Nonspecific Abdominal Aortic Aneurysmal Disease. *Archives of Surgery*, **123**(4):503–505, 1988.

Timmins, L. H., Suever, J. D., Eshtehardi, P., McDaniel, M. C., Oshinski, J. N., Samady, H., and Giddens, D. P. Framework to co-register longitudinal virtual histology-intravascular ultrasound data in the circumferential direction. *IEEE transactions on medical imaging*, **32**(11):1989–96, nov 2013.

Timmins, L. H., Molony, D. S., Eshtehardi, P., McDaniel, M. C., Oshinski, J. N., Samady, H., and Giddens, D. P. Focal Association Between Wall Shear Stress and Clinical Coronary Artery Disease Progression. *Annals of Biomedical Engineering*, **43**(1):94–106, 2015.

Timmins, L. H., Molony, D. S., Eshtehardi, P., Mcdaniel, C., Oshinski, J. N., Giddens, D. P., and Samady, H. Oscillatory wall shear stress is a dominant flow characteristic affecting lesion progression patterns and plaque vulnerability in patients with coronary artery disease. *Journal of the Royal Society, Interface*, **14**(127):1–12, 2017.

Torii, R., Keegan, J., Wood, N. B., Dowsey, A. W., Hughes, A. D., Yang, G.-Z., Firmin, D. N., Thom, S. A. M., and Xu, X. Y. MR Image-Based Geometric and Hemodynamic Investigation of the Right Coronary Artery with Dynamic Vessel Motion. *Annals of Biomedical Engineering*, **38**(8):2606–2620, aug 2010.

Tromp, G., Kuivaniemi, H., Hinterseher, I., and Carey, D. J. Novel genetic mechanisms for aortic aneurysms. *Current Atherosclerosis Reports*, **12**(4):259–266, 2010.

Truijers, M., Pol, J. a., Schultzekool, L. J., van Sterkenburg, S. M., Fillinger, M. F., and Blanken-steijn, J. D. Wall stress analysis in small asymptomatic, symptomatic and ruptured abdominal aortic aneurysms. *European journal of vascular and endovascular surgery : the official journal of the European Society for Vascular Surgery*, **33**(4):401–7, apr 2007.

van der Giessen, A. G., Wentzel, J. J., Meijboom, W. B., Mollet, N. R., van der Steen, A. F. W., van de Vosse, F. N., de Feyter, P. J., and Gijsen, F. J. H. Plaque and shear stress distribution in human coronary bifurcations: a multislice computed tomography study. *EuroIntervention : journal of EuroPCR in collaboration with the Working Group on Interventional Cardiology of the European Society of Cardiology*, **4**(5):654–661, 2009.

van der Giessen, A. G., Schaap, M., Gijsen, F. J. H., Groen, H. C., van Walsum, T., Mollet, N. R., Dijkstra, J., van de Vosse, F. N., Niessen, W. J., de Feyter, P. J., van der Steen, A. F. W., and Wentzel, J. J. 3D fusion of intravascular ultrasound and coronary computed tomography for in-vivo wall shear stress analysis: a feasibility study. *The international journal of cardiovascular imaging*, **26**(7):781–96, oct 2010.

van der Giessen, A. G., Groen, H. C., Doriot, P.-A., de Feyter, P. J., van der Steen, A. F., van de Vosse, F. N., Wentzel, J. J., and Gijsen, F. J. The influence of boundary conditions on wall shear stress distribution in patients specific coronary trees. *Journal of Biomechanics*, **44**(6): 1089–1095, apr 2011.

LIST OF REFERENCES

van der Heiden, K., Hoogendoorn, A., Daemen, M. J., and Gijsen, F. J. H. Animal models for plaque rupture: a biomechanical assessment. *Thrombosis and Haemostasis*, **115**(3):501–508, 2015.

van der Wal, A. C., Becker, A. E., van der Loos, C. M., and Das, P. K. Site of intimal rupture or erosion of thrombosed coronary atherosclerotic plaques is characterized by an inflammatory process irrespective of the dominant plaque morphology. *Circulation*, **89**(1):36–44, jan 1994.

van 't Veer, M., Buth, J., Merkx, M., Tonino, P., van den Bosch, H., Pijls, N., and van de Vosse, F. Biomechanical properties of abdominal aortic aneurysms assessed by simultaneously measured pressure and volume changes in humans. *Journal of vascular surgery*, **48**(6):1401–7, dec 2008.

Van Vre, E. A., Ait-Oufella, H., Tedgui, A., Mallat, Z., Van Vré, E. a., Ait-Oufella, H., Tedgui, A., and Mallat, Z. Apoptotic cell death and efferocytosis in atherosclerosis. *Arteriosclerosis, Thrombosis, and Vascular Biology*, **32**(4):887–893, jun 2012.

Vande Geest, J. P., Di Martino, E. S., BOHRA, A., Makaroun, M. S., and VORP, D. a. A biomechanics-based rupture potential index for abdominal aortic aneurysm risk assessment: demonstrative application. *Annals of the New York Academy of Sciences*, **1085**(1):11–21, nov 2006.

VanderLaan, P. A., Reardon, C. A., and Getz, G. S. Site Specificity of Atherosclerosis: Site-Selective Responses to Atherosclerotic Modulators. *Arteriosclerosis, Thrombosis, and Vascular Biology*, **24**(1):12–22, jan 2004.

Venkatasubramaniam, a. K., Fagan, M. J., Mehta, T., Mylankal, K. J., Ray, B., Kuhan, G., Chetter, I. C., and McCollum, P. T. A comparative study of aortic wall stress using finite element analysis for ruptured and non-ruptured abdominal aortic aneurysms. *European journal of vascular and endovascular surgery : the official journal of the European Society for Vascular Surgery*, **28**(2):168–76, aug 2004.

Vergallo, R., Papafaklis, M. I., Yonetsu, T., Bourantas, C. V., Andreou, I., Wang, Z., Fujimoto, J. G., McNulty, I., Lee, H., Biasucci, L. M., Crea, F., Feldman, C. L., Michalis, L. K., Stone, P. H., and Jang, I. K. Endothelial shear stress and coronary plaque characteristics in humans combined frequency-domain optical coherence tomography and computational fluid dynamics study. *Circulation: Cardiovascular Imaging*, **7**(6):905–911, 2014.

Virmani, R., Kolodgie, F. D., Burke, a. P., Farb, A., and Schwartz, S. M. Lessons From Sudden Coronary Death : A Comprehensive Morphological Classification Scheme for Atherosclerotic Lesions. *Arteriosclerosis, Thrombosis, and Vascular Biology*, **20**(5):1262–1275, may 2000.

Virmani, R., Burke, A. P., Farb, A., and Kolodgie, F. D. Pathology of the unstable plaque. *Progress in cardiovascular diseases*, **44**(5):349–56, 2002.

Virmani, R., Burke, A. P., Farb, A., and Kolodgie, F. D. Pathology of the vulnerable plaque. *Journal of the American College of Cardiology*, **47**(8 Suppl):C13–8, apr 2006.

Vorobtsova, N., Chiastra, C., Stremler, M. A., Sane, D. C., Migliavacca, F., and Vlachos, P. Effects of Vessel Tortuosity on Coronary Hemodynamics: An Idealized and Patient-Specific Computational Study. *Annals of Biomedical Engineering*, **44**(7):2228–2239, jul 2016.

Wang, C., Baker, B. M., Chen, C. S., and Schwartz, M. A. Endothelial cell sensing of flow direction. *Arteriosclerosis, Thrombosis, and Vascular Biology*, **33**(9):2130–2136, 2013.

Wang, L., Zheng, J., Maehara, A., Yang, C., Billiar, K. L., Wu, Z., Bach, R., Muccigrosso, D., Mintz, G. S., and Tang, D. Morphological and Stress Vulnerability Indices for Human Coronary Plaques and Their Correlations with Cap Thickness and Lipid Percent: An IVUS-Based Fluid-Structure Interaction Multi-patient Study. *PLoS Computational Biology*, **11**(12):1–15, 2015.

Weber, C., Fraemohs, L., and Dejana, E. The role of junctional adhesion molecules in vascular inflammation. *Nature reviews. Immunology*, **7**(6):467–77, jun 2007.

Wentzel, J. J., Janssen, E., Vos, J., Schuurbiers, J. C. H., Krams, R., Serruys, P. W., de Feyter, P. J., and Slager, C. J. Extension of increased atherosclerotic wall thickness into high shear stress regions is associated with loss of compensatory remodeling. *Circulation*, **108**(1):17–23, jul 2003.

Wentzel, J. J., Van Der Giessen, A. G., Garg, S., Schultz, C., Mastik, F., Gijsen, F. J. H., Serruys, P. W., Van Der Steen, A. F. W., and Regar, E. In vivo 3D distribution of lipid-core plaque in human coronary artery as assessed by fusion of near infrared spectroscopy-intravascular ultrasound and multislice computed tomography scan. *Circulation: Cardiovascular Imaging*, **3** (6), 2010.

Wentzel, J. J., Chatzizisis, Y. S., Gijsen, F. J. H., Giannoglou, G. D., Feldman, C. L., and Stone, P. H. Endothelial shear stress in the evolution of coronary atherosclerotic plaque and vascular remodelling: current understanding and remaining questions. *Cardiovascular research*, **96**(2):234–43, nov 2012.

Wentzel, J. J., Schuurbiers, J. C., Lopez, N. G., Gijsen, F. J., van der Giessen, a. G., Groen, H. C., Dijkstra, J., Garcia-Garcia, H. M., and Serruys, P. W. In vivo assessment of the relationship between shear stress and necrotic core in early and advanced coronary artery disease. *EuroIntervention : journal of EuroPCR in collaboration with the Working Group on Interventional Cardiology of the European Society of Cardiology*, **9**(0):989–995, 2013.

Wetzel, S., Meckel, S., Frydrychowicz, A., Bonati, L., Radue, E.-W., Scheffler, K., Hennig, J., and Markl, M. In vivo assessment and visualization of intracranial arterial hemodynamics with flow-sensitized 4D MR imaging at 3T. *AJNR. American journal of neuroradiology*, **28** (3):433–8, mar 2007.

White, J. V., Haas, K., Phillips, S., and Comerota, A. J. Adventitial elastolysis is a primary event in aneurysm formation. *Journal of Vascular Surgery*, **17**(2):371–381, 1993.

236

LIST OF REFERENCES

Winkel, L. C., Hoogendoorn, A., Xing, R., Wentzel, J. J., and Van der Heiden, K. Animal models of surgically manipulated flow velocities to study shear stress-induced atherosclerosis. *Atherosclerosis*, **241**(1):100–110, jul 2015.

Wittek, A., Karatolios, K., Bihari, P., Schmitz-Rixen, T., Moosdorf, R., Vogt, S., and Blase, C. In vivo determination of elastic properties of the human aorta based on 4D ultrasound data. *Journal of the mechanical behavior of biomedical materials*, **27**(0):167–83, nov 2013.

Xavier, M., Lalande, A., Walker, P. M., Brunotte, F., and Legrand, L. An adapted optical flow algorithm for robust quantification of cardiac wall motion from standard cine-MR examinations. *IEEE Transactions on Information Technology in Biomedicine*, **16**(5):859–868, 2012.

Yamamoto, E., Siasos, G., Zaromytidou, M., Coskun, A. U., Xing, L., Bryniarski, K., Zanchin, T., Sugiyama, T., Lee, H., Stone, P. H., and Jang, I. K. Low Endothelial Shear Stress Predicts Evolution to High-Risk Coronary Plaque Phenotype in the Future: A Serial Optical Coherence Tomography and Computational Fluid Dynamics Study. *Circulation. Cardiovascular interventions*, **10**(8):1–8, 2017.

Ylä-Herttuala, S., Bentzon, J., Daemen, M., Falk, E., Garcia-Garcia, H., Herrmann, J., Hoefer, I., Jukema, J., Krams, R., Kwak, B., Marx, N., Naruszewicz, M., Newby, A., Pasterkamp, G., Serruys, P., Waltenberger, J., Weber, C., and Tokgözoglu, L. Stabilisation of atherosclerotic plaques. Position paper of the European Society of Cardiology (ESC) Working Group on atherosclerosis and vascular biology. *Thrombosis and Haemostasis*, **101**(6):1–19, 2011.

Ylä-Herttuala, S., Bentzon, J. F., Daemen, M., Falk, E., Garcia-Garcia, H. M., Herrmann, J., Hoefer, I., Jauhiainen, S., Jukema, J. W., Krams, R., Kwak, B. R., Marx, N., Naruszewicz, M., Newby, A., Pasterkamp, G., Serruys, P. W. J. C., Waltenberger, J., Weber, C., and Tokgözoglu, L. Stabilization of atherosclerotic plaques: an update. *European heart journal*, **34**(42):3251–8, nov 2013.

Zarbock, A. and Ley, K. Mechanisms and consequences of neutrophil interaction with the endothelium. *The American journal of pathology*, **172**(1):1–7, jan 2008.

Zarins, C. K., Giddens, D. P., Bharadvaj, B. K., Sottiurai, V. S., Mabon, R. F., Glasgov, S., and Glagov, S. Carotid Bifurcation Atherosclerosis: Quantitative Correlation of Plaque Localization with Flow Velocity Profiles and Wall Shear Stress. *Circ. Res.,*, **53**(4):502–514, oct 1983.

Zeng, D., Ding, Z., Friedman, M. H., and Ethier, C. R. Effects of cardiac motion on right coronary artery hemodynamics. *Annals of biomedical engineering*, **31**(4):420–9, apr 2003.

Zhang, Q., Steinman, D. A., and Friedman, M. H. Use of factor analysis to characterize arterial geometry and predict hemodynamic risk: application to the human carotid bifurcation. *Journal of biomechanical engineering*, **132**(11):114505, nov 2010.

Zhou, J., Li, Y.-S., and Chien, S. Shear stress-initiated signaling and its regulation of endothelial function. *Arteriosclerosis, thrombosis, and vascular biology*, **34**(10):2191–8, oct 2014.

Zonnebeld, N., Huberts, W., van Loon, M. M., Delhaas, T., and Tordoir, J. H. Preoperative computer simulation for planning of vascular access surgery in hemodialysis patients. *The Journal of Vascular Access*, **18**(1_suppl):S118–S124, mar 2017.

Mathematical descriptors of the shear stress metrics.

Shear stress metric	Formula
Time-averaged wall shear stress (TAWSS) [Pa]	$\text{TAWSS} = \dfrac{1}{T} \int_0^T \|\tau_w(x, t)\| dt$
Oscillatory shear index (OSI) [-]	$\text{OSI} \approx 0.5 * \left(1 - \dfrac{\left\| \int_0^T \tau_w(x, t) dt \right\|}{\int_0^T \|\tau_w(x, t)\| dt} \right)$
Relative residence time (RRT) [Pa^{-1}]	$\text{RRT} \approx \dfrac{1}{TAWSS(x) * (1 - 2 * OSI(x))}$
Transverse wall shear stress (transWSS) [Pa]	$\text{transWSS} = \dfrac{1}{T} \int_0^T \|\tau_w(x, t) \cdot p(x)\| dt$ with $p(x) = n(x) \times \dfrac{\frac{1}{T} \int_0^T \tau_w(x, t) dt}{\left\| \frac{1}{T} \int_0^T \tau_w(x, t) dt \right\|}$
Cross flow index (CFI) [-]	$\text{CFI} = \dfrac{1}{T} \int_0^T \left\| \dfrac{\tau_w(x, t)}{\|\tau_w(x, t)\|} \cdot p(x) \right\| dt$

* τ_w (x,t) is the instantaneous shear stress vector for each node x and time t. The cardiac cycle time is T. p(x) is the vector perpendicular to the surface normal n(x) and the mean wall shear stress vector.

DANKWOORD

Ruim 4 jaar lang heb ik me voor 100% ingezet om vasculaire ziekten te onderzoeken met behulp van biomechanica. Dit werk had ik alleen zeker niet kunnen doen, daarom wil ik een aantal mensen hier graag bedanken.

Allereerst mijn promotor, Ton van de Steen, dankzij zijn daadkracht en directe input is het gelukt om mijn thesis goed te stroomlijnen. De wijze waarop hij onze onderzoeksgroep als geheel zodanig weet te promoten dat hij internationaal een hoog aanzien heeft, is bewonderenswaardig.

Dan mijn copromotor, Jolanda, ik wil haar bedanken voor de 4 jaar die ik heb mogen doorbrengen in het biomechanica lab. Zij heeft het mogelijk gemaakt dat ik veel verschillende onderzoeken heb kunnen uitvoeren. Met haar snelle interpretatie van de data heeft zij een enorme bijdrage geleverd. Daarnaast heeft zij mij de ruimte gegeven om mijzelf verder te ontwikkelen en een externe stageperiode in Atlanta te volgen. Hierdoor hebben wij mooie papers kunnen publiceren, en heb ik mijn promotiewerk kunnen presenteren op vele (inter-)nationale congressen.

Mijn promotie onderzoek ben ik begonnen met het opzetten van de IMPACT patiënten studie en de daarbij behorende METC aanvraag. De input van Evelyn Regar en Joost Daemen was hier onmisbaar. Onze gezamenlijke inzet zal er toe leiden dat er in de toekomst nog vele mooie publicaties bij zullen komen. Verder wil ik alle overige interventie cardiologen, fellows, laboranten en verpleegkundigen van de afdeling interventie cardiologie bedanken voor hun betrokkenheid bij de IMPACT-studie. Zij hebben mij enorm veel geleerd op de katheterisatiekamer, daarnaast was de sfeer altijd top!

Jurgen, Karin en Mattie, woorden schieten mij tekort, bedankt voor jullie hulp bij de invasieve beeldvormingsprocedures, en het opzetten van OpenClinica en de IMPACT-onderzoeksprotocollen. Fijn dat ik altijd kon rekenen op jullie expertise! Ook ben ik enorm dankbaar voor de hulp van Elisabeth, Nico en Arno van het trialbureau. Jullie hielpen mij daar waar mijn eigen expertise ophield, ik kon altijd bij jullie terecht met vragen. Jullie betrokkenheid bij de studie en het includeren van de patiënten was onmisbaar.

Koen, Adriaan, Fay en Marcel: met jullie hulp hebben wij mooie CT's kunnen maken voor de 3D reconstructie die de schuifspanningsberekeningen mogelijk hebben gemaakt, bedankt! Eric Boersma bedankt voor de hulp bij de statistiek! Ook wil ik graag Theo

van Walsum bedanken voor de hulp bij Mevislab met betrekking tot de co-registraties algoritmen.

Frank en Lambert, ik wil jullie graag bedanken voor jullie betrokkenheid bij mijn promotieproject. Ik heb veel van jullie geleerd met betrekking tot schrijven, modelleren en presenteren. Verder heb ik altijd genoten van jullie aanwezigheid bij de congressen. Claudio, I am grateful that I had the chance to work with you on the CFD project. Both your expertise and educational skills greatly contributed to, not only my personal development, but also in the work described in chapters 3, 5 and 6. Not only the help from Milano was greatly appreciated but also from Turin, Giuseppe and Umberto. Thank you for the collaboration and nice talks and all the conferences.

Dan eeuwige roem voor Ayla en Eline! Zonder jullie inzet in het BioCCora project hadden we nooit zo'n mooi resultaat neer kunnen zetten. Ayla, jouw sterk inzichtelijke vermogen en grote biomedische kennis hebben veel bijgedragen! Eline, ik heb ontzettend veel geleerd van jouw gedrevenheid en medische kennis.

Daarnaast wil ik al mijn collega's (Kristina, Jelle, Harm, Leah, Merih, Ali, Hilary, Eric, Erik, Hans, Kim, Kim, Annelies, Ruoyu, Astrid, Imane, Jaela, Sophinese, Sally, Gayle) en alle overige Biomedical Engineering collega's bedanken voor alle steun en gezelligheid! Een speciaal bedankje voor alle cool-room collega's! And Ruoyu I am really grateful to have you as my friend, you are one of the most loving people I have ever met, and I am honoured to defend my thesis at the same day as you!

Giuliana, Fabiola, and Diede, I am really glad you decided to join our lab to work on the BioCCora project. Thank you for your 'gezelligheid' and for being great students. Your work greatly contributed to my PhD work!

During my PhD, I did an external internship in Atlanta, GA, USA. Thank you David, Luc, and Habib for this opportunity. During this internship I spend a lot of time discovering Atlanta as well, where I met some amazing people. Thank you guys, you really inspired me and showed me the American Culture (Hee Su, David, Emily, Beth, Jiu, Kelly, Ruby, Sophia, Michelle and Brian).

Het afronden van een PhD loopt bijna altijd trager dan gehoopt, zoals ook bij mij het geval was. Gelukkig heb ik bij Seats2Meet de rust gevonden om rustig mijn boekje af te schrijven. Daarom wil ik iedereen bij Seats2Meet bedanken voor hun onvoorwaardelijke interesse, die mij heeft gemotiveerd om dit werk tot een succesvol einde te brengen. En William; bedankt voor het helpen met cover design.

Lieve familie en vrienden, jullie hebben mij de energie gegeven die ik nodig had om

dit proefschrift tot een succesvol einde te brengen, daarom wil ik jullie hier bedanken. Laura, ik ben enorm dankbaar jou als vriendin te mogen hebben, ik hoop dat we nog vaak alpaca's mogen knuffelen. Ik ga er overigens nog steeds vanuit dat wij samen oud en grijs mogen worden op onze alpaca-boerderij. Vanuit BMT wil ik voornamelijk Tommy, Robbin, Thomas, Lenny, Berly, Jaap, Nicole, Ashley, Midas, Arjan bedanken maar natuurlijk ook alle overige BMT-vrienden! Oud-huisgenoten (Matijs, Martijn, Sandra, Kevin, Merlijn) bedankt voor alles. Ik hoop dat we samen nog vele mooie avonturen mogen beleven! En als laatste natuurlijk mijn Alyssa en Frank, waar ik veruit het langst mee bevriend ben en ook vele mooie avonturen mee heb beleefd. Hopelijk gaan er nog veel meer volgen (maar ook bordspellen spelen, BBQ-en, terrasjes pikken etc.).

Aan mijn ouders en mijn broertje, een PhD heeft zijn vallen en opstaan, maar ik kon altijd rekenen op jullie onvoorwaardelijke steun. Jullie hebben me geïnspireerd, zonder jullie was dit werk niet gelukt! Daarnaast wil ik ook mijn familie bedanken voor de steun die ze mij hebben gegeven tijdens het afronden van mijn promotie. En ook al leef je niet meer opa, bedankt dat jij me heel mijn leven lang hebt geïnspireerd hebt en altijd geïnteresseerd was! Ik hou van jullie allemaal, bedankt!

Marius, samen werken aan de laatste lootjes van onze proefschriften was fantastisch, alhoewel misschien niet altijd even productief. Ik ben ontzettend blij dat onze werelden zo goed samengaan als dat ze nu doen. Jij bent de meest unieke persoon die ik ooit heb ontmoet en met een hart van goud. Bedankt dat jij mijn leven kleurrijker maakt dan dat hij al was, en dat je mij op alle vlakken blijft uitdagen, ik hou van je!

SAMENVATTING

Door de opkomst van het digitale tijdperk worden computermodellen in de gezondheidszorg steeds meer gebruikt om ziekten bij de mens beter te begrijpen, te assisteren in de gezondheidzorg of bij te dragen aan de verbetering van gezondheidszorg. Met computermodellen kunnen fysische fenomenen worden gesimuleerd. In dit proefschrift zullen we computermodellen toepassen om spanningen uit te rekenen in aneurysmata in de abdominale aorta, en in slagaderen (kransslagaders en in de halsslagaders) met atherosclerose. Hierbij kan zowel gedacht worden aan schuifspanningen als gevolg van de wrijvingskracht van de arteriële bloedstroom tegen de slagaderwand, maar ook aan spanningen in de vaatwand veroorzaakt door de bloeddruk. Computermodellering is een krachtig hulpmiddel voor het identificeren van spanningen, die mogelijk kunnen dienen als een surrogaat risicomarker in door ziekte aangetaste slagaders.

Schuifspanningen

Atherosclerose is een complexe multifactoriële arteriële aandoening die ontstaat door een combinatie van hemodynamische, systemische en biologische factoren. De geometrie heeft een grote invloed heeft op de lokale stroming, daarom zijn geometrische parameters onderzocht op hun geschiktheid als alternatieve risicofactor voor atherosclerose. In **Hoofdstuk 2** is de invloed van de geometrie op hemodynamische parameters in zowel de halsslagaders als de kransslagaders beschreven. Voor zowel halsslagaders als kransslagaders werden meerdere geometrische kenmerken geïdentificeerd die samenhangen met de aanwezigheid van lage en oscillerende schuifspanning. Als de interne halsslagader, die distaal aftakt van de halsslagader, veel kleiner was dan de halsslagader zelf, dan was de halsslagader vaker blootgesteld aan lage en oscillerende schuifspanningen. Voor de kransslagaders was een grote hoek tussen het moedervat en de zijtakken ook geassocieerd met de aanwezigheid van lage schuifspanningen.

Verschillende slagaders in het lichaam vertonen helix-achtige stroming en deze zou beschermend zijn tegen atherosclerose. In **Hoofdstuk 3** werden computermodellen gebruikt om de aanwezigheid van helix-achtige stroming in (varkens) kransslagaders te onderzoeken. Deze studie toonde aan dat de stroming in kransslagaders bestaat uit twee tegengesteld draaiende helix stromen, deze werden beschreven in een aantal heliciteit-indexen. Hoge heliciteit-intensiteit was inderdaad geassocieerd met gunstige hoge WSS-condities, wat inderdaad suggereert dat de helix-achtige stroming beschermt tegen atherosclerose is in kransslagaders.

In het cardiovasculaire systeem pulseert de bloedstroom, resulterend in temporele en spatiele fluctuaties in schuifspanning in zowel de grootte als de richting. Nieuwe metrieken die de multi-directionaliteit van schuifspanning beschrijven werden bestudeerd in twintig humane kransslagaders met betrekking tot de invloed op de groei van plaques en veranderingen in de samenstelling van de plaque (**Hoofdstuk 4**). We toonden aan dat multidirectionele schuifspanningsveranderingen over een periode van 6 maanden de samenstelling van de plaque beïnvloedt, maar in mindere mate de veranderingen in de plaquegrootte beïnvloedt. Interessant genoeg bleken TAWSS en CFI (een van de multidirectionele schuifspanning metrieken) een synergetisch effect te hebben op de groei van plaques en veranderingen in de samenstelling van de plaque. Samengevat, beeld gebaseerde beoordeling van (multidirectionele) schuifspanning en plaquesamenstelling in kransslagaders is noodzakelijk om het proces van atherosclerotische plaqueprogressie en destabilisatie beter te begrijpen.

In **Hoofdstuk 5** werd een nieuwe beeldvormende NIRS-IVUS-katheter gebruikt om simultaan informatie te verkrijgen over de plaquegrootte en de aanwezigheid van lipiden in de plaque bij patiënten met acuut coronair syndroom. Schuifspanning werd berekend bij inclusie in de studie en de beeldvorming werd na een jaar herhaald om de progressie van de plaque te bestuderen. We observeerden dat schuifspanning gecolokaliseerd met lokale lipide-rijke plaques zelfs een betere voorspeller is voor plaqueprogressie dan schuifspanning alleen. We vonden geen verschil in plaquegroei van lipide-rijke plaques ten opzichte van lipide-arme plaques. Wel werd er een synergistisch en significant effect van NIRS-positieve gebieden met multidirectionele schuifspanning op plaquegroei waargenomen. In het bijzonder waren hoge RRT en lage transWSS meer voorspellend voor plaqueprogressie en hoge transWSS voor plaqueregressie in NIRS-positieve regio's vergeleken met NIRS-negatieve regio's. We vonden geen significant effect van hoge systemische LDL-spiegels in combinatie met schuifspanning om plaqueprogressie te voorspellen. Daarom suggereren deze gegevens dat toekomstige studies baat zouden hebben bij NIRS-gebaseerde lipidebepaling in combinatie met verschillende schuifspanningsparameters voor de schatting van regio's met een verhoogd risico op plaquegroei.

Hoofdstuk 6 beschrijft de relatie tussen atherosclerotische plaque-progressie en veranderingen in samenstelling en (multidirectionele) shear stress in een nieuw varkensmodel voor atherosclerose. De volwassen varkens waren hypercholesteremisch vanwege een mutatie in de LDL-receptor. Verder hebben deze varkens gedurende 9-12 maanden een vetrijk dieet gekregen om de ontwikkeling van atherosclerose te versnellen. Dit model liet een duidelijke verdeling zien in twee groepen met betrekking tot plaque groeisnelheid; in een groep ontstond er snel plaque verdikking en in de andere langzaam. Plaquegroei

en meer gevorderde plaquefenotypes waren sterk geassocieerd met lage TAWSS en hoge multidirectionele schuifspanning in de varkens met snelle plaque groei. Interessant is dat in de groep varkens die langzaam plaque groei vertoonde geen verband werd gevonden tussen plaquegroei en (multidirectionele) schuifspanning.

Wandspanningen

Een subgroep van atherosclerotische plaques die zich in het cardiovasculaire systeem ontwikkelen, loopt een hoog risico om te scheuren, wat mogelijk kan leiden tot een hartinfarct of een beroerte. Deze subgroep van plaques met een hoog risico op ruptuur bevatten meestal een grote necrotische kern, zijn zeer ontstoken en hebben een dunne kap die over de necrotische kern ligt. Computermodellen worden momenteel gebruikt om de lokale spanningsverdeling in de plaque te berekenen. De spanningsverdeling kan vervolgens gebruikt worden om het risico op kap ruptuur te voorspellen. Om computermodellering mogelijk te maken, is een geometrische beschrijving nodig van de plaque. Specifiek, de geometrie van de necrotische kern, de kap en de wand zijn nodig. In het geval intravasculaire ultrageluid (IVUS) en/of optische coherentietomografie (OCT) - twee klinische invasieve beeldvormingstechnieken – worden gebruikt om de plaque af te beelden. Met deze combinatie van beeldvormende technieken kan de necrotische kern niet volledig worden gevisualiseerd, dat wil zeggen de achterkant van de necrotische kern niet zichtbaar is op de beelden. Daarom werd een nieuwe methodologie ontwikkeld om de grootte van de necrotische kern te schatten (**Hoofdstuk 7**). Om dit mogelijk te maken werd een empirische relatie afgeleid tussen een aantal geometrische kenmerken van de plaque en de dikte van de necrotische kern (NC) met behulp van histologie als gouden standaard. De necrotische kerndikte bleek gerelateerd te zijn aan de volgende geometrische kenmerken: necrotische kern (NC) hoek, intima-mediadikte en kapdikte. Vervolgens werd deze kennis gebruikt om de achterkant van de necrotische kern te reconstrueren. De waarden van de piek spanning in de kap op basis van de histologie waren sterk gecorreleerd met de piek spanningen die werden berekend in de geometrieën waarin de NC's waren gesloten. De methodologie die in dit onderzoek is ontwikkeld, maakt toekomstige wandspanningsstudies mogelijk waarbij fusie van IVUS- en OCT-beeldvorming wordt toegepast.

Magnetische resonantie (MRI) wordt vaak gebruikt om plaques in de halsslagader af te beelden, maar heeft helaas een te lage resolutie om de kap nauwkeurig af te beelden. In **Hoofdstuk 8** werd een nieuwe methode ontwikkeld om de voorkant van de NC te schatten met behulp van een geometrisch model. De geometrie van de gouden standaard was gebaseerd op histologie en daardoor waren gedetailleerde kenmerken zoals lokale kromming in het lumen en de necrotische kern te zien. Echter een MRI-expert die dezelfde geometrieën segmenteerden in gesimuleerde MRI beelden van de histologische coupe

was niet in staat om deze kleine kenmerken te identificeren op deze MRI, vermoedelijk vanwege de beperkte resolutie. De resultaten van deze studie toonden aan dat met de dikte van de kap met behulp van het model beter werd beter dan de dikte die ervaren MRI-experts afleidde uit de MRI beelden. Deze verbetering vertaalde zich echter niet terug in een verbetering in de piek spanningen in de kap. Waarschijnlijk hebben de MRI simulaties belangrijke geometrische kenmerken glad gestreken, die belangrijker waren voor de wandspanningsberekeningen dan de minimale kapdikte.

Hoofdstuk 9 toont de eerste resultaten van piekwandspanningen in AAA-geometrieën afgeleid van 3D-US. De resultaten werden vergeleken met de geometrie van de gouden standaard verkregen met computer tomografie (CT). De 3D geometrie op basis van 3D US kwam goed overeen met de 3D geometrie verkregen met CT. Echter, in sommige AAA's kon de volledige AAA-geometrie niet in één 3D US-opname worden vastgelegd. Daarom werden in deze gevallen meerdere US opnames samengevoegd. Helaas leverde dit onregelmatigheden op in de geometrie, wat tot hoge lokale pieken in de wand spanning leidde. Hierdoor was het niet mogelijk om de 99ste percentiel te gebruiken als resultaat van de wandspanningsberekeningen. De gemiddelde CT vs. US wandspanningen van alle geometrieën waren echter in overeenstemming. Als de 3D-reconstructie op basis van 3D-US verbetert, is het mogelijk een goede beeldvormingsmodaliteit voor zowel medische als onderzoeksdoeleinden.

In dit proefschrift zijn nieuwe methodologieën ontwikkeld om computersimulaties in zieke slagaders verder te verbeteren. Deze nieuwe methodologieën maakten wandspanningsanalyse mogelijk in AAA-geometrieën verkregen via 3D-US en in plaque-geometrieën verkregen via zowel IVUS- als OCT-beeldvorming. Verder vertoonden (multidirectionele) schuifspanning in combinatie met NIRS-positieve gebieden veelbelovende resultaten voor voorspelling van plaque-progressie en veranderingen in samenstelling van de plaque. Daarom zou (multidirectionele) schuifspanning, misschien in combinatie met NIRS, kunnen worden gebruikt als een potentiële risicofactor voor plaque progressie en veranderingen in de samenstelling van de plaque. Toekomstig onderzoek moet de klinische waarde van (multidirectionele) schuifspanning en wandspanning aantonen op de voorspelling van plaque progressie en destabilizatie. Alleen dan zijn grote klinische studies nuttig om de effectiviteit van behandelingen op basis van deze risicofactoren te onderzoeken ten opzichte van de conventionele behandelmethoden.

SCIENTIFIC OUTPUT

Journal papers

Kok AM, Nguyen VL, Speelman L, Schurink GWH, van de Vosse FN, Lopata RGP. Wall stress analysis of abdominal aortic aneurysms using 3D ultrasound. J Vasc Surg. 2015 61(5):1175–84

Morbiducci U, **Kok AM**, Kwak BR, Stone PH, Steinman DA., Wentzel JJ. Atherosclerosis at arterial bifurcations: Evidence for the role of haemodynamics and geometry. Thromb Haemost. 2016;115(3):484–492.

Kok AM, Speelman L, Virmani R, van der Steen AFW, Gijsen FJH, Wentzel JJ. Peak cap stress calculations in coronary atherosclerotic plaques with an incomplete necrotic core geometry. Biomed Eng Online. 2016;15(1).

Kok AM, van der Lugt A, Verhagen HJM, van der Steen AFW, Wentzel JJ, Gijsen FJH. Model-based cap thickness and peak cap stress prediction for carotid MRI. J Biomech. 2017;60:175-180.

De Nisco G, **Kok AM**, Chiastra C, Gallo D, Hoogendoorn A, Migliavacca F, Wentzel JJ, Morbiducci U. The Atheroprotective Nature of Helical Flow in Coronary Arteries. Ann Biomed Eng. 2019;47(2)

Kok AM, Molony DS, Timmins LH, Ko Y-A, Boersma H, Eshtehardi P, Wentzel JJ[1], Samady H.[1] The Influence of Multidirectional Shear Stress on Plaque Progression and Composition Changes in Human Coronary Arteries. Eurointervention (Accepted 2019).

Hoogendoorn A, **Kok AM**, Hartman EMJ, Coenen A, Korteland S-A, Gijsen FJH, Duncker DJ, van der Steen AFW, Wentzel JJ. Multidirectional wall shear stress promotes development of advanced coronary plaques with vulnerable characteristics – a pre-clinical serial imaging study. (Submitted).

---

[1]Authors contributed equally

Conference abstracts

Kok AM, Nguyen VL, Speelman L, Schurink GWH, van de Vosse FN, Lopata RGP. 3D Ultrasound-based Finite Element Models of AAAs: First In Vivo Experience. Amsterdam: Computer Methods in Biomechanics and Biomedical Engineering; 2014.

Kok AM, Nguyen VL, Speelman L, Schurink GWH, van de Vosse FN, Lopata RGP. Wall stress analysis of abdominal aortic aneurysms using 3D ultrasound. Chicago, IL, USA: IEEE International Ultrasonics Symposium; 2014.

Kok AM, Speelman L, Gijsen FJH, Wentzel JJ. Reconstruction of Incomplete Lipid Pool Geometry for Stress Calculations in Atherosclerotic arteries. Rotterdam: Shear Stress Symposium; 2015.

Kok AM, Speelman L, Gijsen FJH, Wentzel JJ. Reconstruction of Incomplete Lipid Pool Geometry for Stress Calculations in Atherosclerotic arteries. Salt Lake City, UT, USA: SB3C: Summer Biomechanics, Bioengineering, and Biotransport Conference; 2015.

Kok AM, van der Lugt A, van der Steen AFW, Wentzel JJ, Gijsen FJH. Can a Model Predict the Cap Thickness and the Cap Stress better than an Experienced MRI Reader? Atlanta, GA, USA: Shear Stress Symposium; 2016.

Kok AM, van der Lugt A, van der Steen AFW, Wentzel JJ, Gijsen FJH. MRI Based Cap Thickness and Peak Cap Stress Prediction: Man versus Machine. National Harbor, MD, USA: SB3C: Summer Biomechanics, Bioengineering, and Biotransport Conference; 2016.

Kok AM, van der Lugt A, van der Steen AFW, Wentzel JJ, Gijsen FJH. MRI Based Cap Thickness and Peak Cap Stress Prediction: Man versus Machine. Amsterdam: Virtual Physiological Human Conference;

Kok AM, Molony DS, Timmins LH, Ko Y, Eshtehardi P, Samady H, Wentzel JJ. The Predictive Value of Transverse Shear Stress on Plaque Progression and Destabilisation in Human Coronary Arteries. Rotterdam: Shear Stress Symposium; 2017.

Hoogendoorn A, **Kok AM**, Hartman EMJ, Casadonte L, Peters I, Visser - te Lintel Hekkert M, Gijsen FJH, Duncker DJ, van der Steen AFW, Wentzel JJ. A pig model for advanced atherosclerosis: serial (non)invasive imaging, biomechanics and histology. Rotterdam: Shear Stress Symposium; 2017.

Hoogendoorn A, **Kok AM**, Hartman EMJ, Casadonte L, Peters I, Visser - te Lintel Hekkert M, Gijsen FJH, Duncker DJ, van der Steen AFW, Wentzel JJ. A pig model

for advanced atherosclerosis: serial (non)invasive imaging, biomechanics and histology. Rotterdam: Optics in Cardiology; 2017.

Kok AM, Molony DS, Timmins LH, Ko Y-A, Boersma H, Eshtehardi P, Wentzel JJ, Samady H. The Predictive Value of Transverse Shear Stress on Plaque Progression in Human Coronary Arteries. Tucson, AZ, USA: SB3C: Summer Biomechanics, Bioengineering, and Biotransport Conference; 2017.

Hoogendoorn A, **Kok AM**, Hartman EMJ, Casadonte L, Peters I, Visser - te Lintel Hekkert M, van Gaalen K, van der Heiden K, Gijsen FJH, Duncker DJ, van der Steen AFW, Wentzel JJ. The role of shear stress in localization and progression of atherosclerosis in porcine coronary arteries. Monterey, CA, USA: North American Vascular Biology Organization; 2017.

Hoogendoorn A[1], **Kok AM**[1], Hartman EMJ, Casadonte L, Peters I, Witberg KT, Visser - te Lintel Hekkert M, van Gaalen K, Ligthart J, Drouet L, van der Heiden K, Gijsen FJH, Duncker DJ, van der Steen AFW, Wentzel JJ. The influence of shear stress metrics on plaque progression in an adult hypercholesterolemic pig model: multimodality imaging, biomechanics and histology. Atlanta, GA, USA: Shear Stress Symposium; 2018.

De Nisco G, **Kok AM**, Chiastra C, Gallo D, Migliavacca F, Morbiducci U, Wentzel JJ. Physiological significance of helical flow in coronary arteries. Atlanta, GA, USA: Shear Stress Symposium; 2018.

Hoogendoorn A[1], **Kok AM**[1], Hartman EMJ, Casadonte L, Coenen A, Peters I, Visser M, van Gaalen K, Ligthart J, Drouet L, van der Heiden K, Gijsen FJH, Duncker DJ, van der Steen AFW, Wentzel JJ. The influence of shear stress metrics on plaque progression in an adult hypercholesterolemic pig model: multimodality imaging , biomechanics and histology. Zurich: Optics in Cardiology; 2018.

Kok AM, Hoogendoorn A, Hartman EMJ, Voorrecht DW, Chiastra C, van der Heiden K, Duncker DJ, van der Steen AFW, Gijsen FJH, Wentzel JJ. On the Prediction of Plaque Growth in Atherosclerotic Coronary Arteries in Pigs: which Hemodynamic Metric is the Best? Dublin: World Congress of Biomechanics; 2018.

De Nisco G, **Kok AM**, Chiastra C, Gallo D, Tomeo AF, Segreto G, Migliavacca F, Wentzel JJ, Morbiducci U. Helical flow assessment in coronary arteries in vivo and its instrumental role in suppressing disturbed shear stress features. An exploratory study. Dublin: World Congress of Biomechanics; 2018.

---

[1]Authors contributed equally

Hartman EMJ, **Kok AM**, Hoogendoorn A, Gijsen FJH, van der Steen AFW, Daemen J, Wentzel JJ. Near infrared positive regions are most often located at areas exposed to high shear stress. Munich: European Society of Cardiology; 2018.

PORTFOLIO

Courses	Year
Current Cardiac and Vascular Aging Research, COEUR, Erasmus MC, Rotterdam	2014
New imaging strategies for the detection of atherosclerosis, COEUR, Erasmus MC, Rotterdam	2014
Imaging of Cardiac Arrhythmias, COEUR	2014
Cardiovascular imaging and Diagnostics, COEUR, Erasmus MC, Rotterdam	2014
Basic course for clinical investigators (BROK), Erasmus MC, Rotterdam	2014
Openclinica, Erasmus MC, Rotterdam	2014
Research integrity course, Erasmus MC, Rotterdam	2015
Atherosclerotic and aneurysmal disease, COEUR, Erasmus MC, Rotterdam	2015
Biomedical English Writing and Communication	2016
Graduate Course Computational Fluid Dynamics I, JBMC, Delft	2016
Summer School on Biomechanics, Graz University of Technology, Graz	2016

Presentations at conferences	Year
Computer Methods in Biomechanics and Biomedical Engineering, 12th edition, Amsterdam (Oral presentation)	2014
Optics in Cardiology, 3th edition, Rotterdam (Poster presentation)	2015
International Symposium on Biomechanics in Vascular Biology and Cardiovascular Disease, 10th edition, Rotterdam (Poster presentation)	2015
Summer Biomechanics, Bioengineering, and Biotransport Conference, Salt Lake City, UT, USA (Oral presentation)	2015
International Symposium on Biomechanics in Vascular Biology and Cardiovascular Disease, 11th edition, Atlanta, GA, USA (Poster presentation)	2016
Virtual Physiological Human Conference, Amsterdam (Oral presentation)	2016
International Symposium on Biomechanics in Vascular Biology and Cardiovascular Disease, 12th edition, Rotterdam (Oral presentation)	2017
Optics in Cardiology, 4th edition, Rotterdam, (Oral presentation)	2017
Summer Biomechanics, Bioengineering, and Biotransport Conference, Tucson, AZ, USA, (Oral presentation)	2017

– continued from previous page

Presentations at conferences	Year
World Congress of Biomechanics, 8th edition, Dublin, Ireland, (Oral presentation)	2018

Attending conferences	Year
Computer Methods in Biomechanics and Biomedical Engineering, 12th edition, Amsterdam	2014
Optics in Cardiology, 3th edition, Rotterdam	2015
International Symposium on Biomechanics in Vascular Biology and Cardiovascular Disease, 10th edition, Rotterdam	2015
Summer Biomechanics, Bioengineering, and Biotransport Conference, Salt Lake City, UT, USA	2015
International Symposium on Biomechanics in Vascular Biology and Cardiovascular Disease, 11th edition, Atlanta, GA, USA	2016
Virtual Physiological Human Conference, Amsterdam	2016
International Symposium on Biomechanics in Vascular Biology and Cardiovascular Disease, 12th edition, Rotterdam	2017
Optics in Cardiology, 4th edition, Rotterdam	2017
Summer Biomechanics, Bioengineering, and Biotransport Conference, Tucson, AZ, USA	2017
World Congress of Biomechanics, 8th edition, Dublin, Ireland	2018

Teaching	
Supervision of two MSc students	2017
Supervision of a BSc student	2017-2018

Other	
Research Internship, Emory, Atlanta, GA, USA	2016-2017

CURRICULUM VITAE

Annette Monique Kok was born in Nijmegen on August 11th 1989. In 2008, she graduated from pre-university college at BC Broekhin in Roermond, the Netherlands. In the same year she started with the bachelor Biomedical Engineering at the Technical University in Eindhoven. Here, she obtained her Master degree in Medical Engineering in 2014. Her master's project was in collaboration with the University Medical Center of Maastricht. Her master's dissertation was titled: "Towards Ultrasound based 3D wall stress analysis of Abdominal Aortic Aneurysms".

In 2014, she started with her PhD the biomechanics group of the Biomedical Engineering Department at Erasmus University Medical Center. Here, she could continue her research on vascular diseases using computational modeling. The result of this work is described in this thesis. During her PhD, she did a three-month research internship at Emory University School of Medicine in Atlanta (GA, USA).

After her PhD, she will be employed as a technical software consultant at Alten Nederland in Eindhoven.